Characterization and structuration of piezoelectric ZnO-based composites : Toward medical applications

Xiaoting Zhang

▶ **To cite this version:**

Xiaoting Zhang. Characterization and structuration of piezoelectric ZnO-based composites : Toward medical applications. Electric power. Université de Lyon, 2022. English. NNT : 2022LYSEI006 . tel-03709331

HAL Id: tel-03709331
https://theses.hal.science/tel-03709331

Submitted on 29 Jun 2022

HAL is a multi-disciplinary open access archive for the deposit and dissemination of scientific research documents, whether they are published or not. The documents may come from teaching and research institutions in France or abroad, or from public or private research centers.

L'archive ouverte pluridisciplinaire **HAL**, est destinée au dépôt et à la diffusion de documents scientifiques de niveau recherche, publiés ou non, émanant des établissements d'enseignement et de recherche français ou étrangers, des laboratoires publics ou privés.

N°d'ordre NNT : 2022LYSEI006

THESE de DOCTORAT DE L'UNIVERSITE DE LYON
opérée au sein de
L'Institut National des Sciences Appliquées de Lyon

Ecole Doctorale N° ED160 EEA
ÉLECTRONIQUE, ÉLECTROTECHNIQUE, AUTOMATIQUE

Spécialité/ discipline de doctorat : Génie électrique

Soutenue publiquement/à huis clos le 01/ Février /2022, par :

Xiaoting ZHANG

Characterization and structuration of piezoelectric ZnO-based composites: Toward medical applications

---

Devant le jury composé de :

DEMOLY Frédéric	Professeur /UTBM	Rapporteur
GUIFFARD Benoit	Professeur /Université de Nantes	Rapporteur
BREMOND Georges	Professeur /INSA-LYON	Examinateur
LIANG Zhiyong	Professeur / Florida State University	Examinateur
PETIT Lionel	Professeur /INSA-LYON	Directeur de thèse
LE Minh Quyen	Maître de Conférences /INSA-LYON	Co-directrice de thèse
CONSONNI Vincent	HDR, Chargé de Recherche CNRS/LMGP	Invité
DELLA SCHIAVA Nellie	PhD., Praticien hospitalier /HCL Hôpital Edouard Herriot	Invité

Cette thèse est accessible à l'adresse : http://theses.insa-lyon.fr/publication/2022LYSEI006/these.pdf
© [X. Zhang], [2022], INSA Lyon, tous droits réservés

Cette thèse est accessible à l'adresse : http://theses.insa-lyon.fr/publication/2022LYSEI006/these.pdf
© [X. Zhang], [2022], INSA Lyon, tous droits réservés

Département FEDORA – INSA Lyon - Ecoles Doctorales – Quinquennal 2016-2020

SIGLE	ECOLE DOCTORALE	NOM ET COORDONNEES DU RESPONSABLE
CHIMIE	**CHIMIE DE LYON** **http://www.edchimie-lyon.fr** Sec. : Renée EL MELHEM Bât. Blaise PASCAL, 3e étage **secretariat@edchimie-lyon.fr** INSA : R. GOURDON	**M. Stéphane DANIELE** Institut de recherches sur la catalyse et l'environnement de Lyon IRCELYON-UMR 5256 Équipe CDFA 2 Avenue Albert EINSTEIN 69 626 Villeurbanne CEDEX **directeur@edchimie-lyon.fr**
E.E.A.	**ÉLECTRONIQUE, ÉLECTROTECHNIQUE, AUTOMATIQUE** **http://edeea.ec-lyon.fr** Sec. : M.C. HAVGOUDOUKIAN **ecole-doctorale.eea@ec-lyon.fr**	**M. Gérard SCORLETTI** École Centrale de Lyon 36 Avenue Guy DE COLLONGUE 69 134 Écully Tél : 04.72.18.60.97 Fax 04.78.43.37.17 **gerard.scorletti@ec-lyon.fr**
E2M2	**ÉVOLUTION, ÉCOSYSTÈME, MICROBIOLOGIE, MODÉLISATION** **http://e2m2.universite-lyon.fr** Sec. : Sylvie ROBERJOT Bât. Atrium, UCB Lyon 1 Tél : 04.72.44.83.62 INSA : H. CHARLES **secretariat.e2m2@univ-lyon1.fr**	**M. Philippe NORMAND** UMR 5557 Lab. d'Ecologie Microbienne Université Claude Bernard Lyon 1 Bâtiment Mendel 43, boulevard du 11 Novembre 1918 69 622 Villeurbanne CEDEX **philippe.normand@univ-lyon1.fr**
EDISS	**INTERDISCIPLINAIRE SCIENCES-SANTÉ** **http://www.ediss-lyon.fr** Sec. : Sylvie ROBERJOT Bât. Atrium, UCB Lyon 1 Tél : 04.72.44.83.62 INSA : M. LAGARDE **secretariat.ediss@univ-lyon1.fr**	**Mme Sylvie RICARD-BLUM** Institut de Chimie et Biochimie Moléculaires et Supramoléculaires (ICBMS) - UMR 5246 CNRS - Université Lyon 1 Bâtiment Curien - 3ème étage Nord 43 Boulevard du 11 novembre 1918 69622 Villeurbanne Cedex Tel : +33(0)4 72 44 82 32 **sylvie.ricard-blum@univ-lyon1.fr**
INFOMATHS	**INFORMATIQUE ET MATHÉMATIQUES** **http://edinfomaths.universite-lyon.fr** Sec. : Renée EL MELHEM Bât. Blaise PASCAL, 3e étage Tél : 04.72.43.80.46 **infomaths@univ-lyon1.fr**	**M. Hamamache KHEDDOUCI** Bât. Nautibus 43, Boulevard du 11 novembre 1918 69 622 Villeurbanne Cedex France Tel : 04.72.44.83.69 **hamamache.kheddouci@univ-lyon1.fr**
Matériaux	**MATÉRIAUX DE LYON** **http://ed34.universite-lyon.fr** Sec. : Stéphanie CAUVIN Tél : 04.72.43.71.70 Bât. Direction **ed.materiaux@insa-lyon.fr**	**M. Jean-Yves BUFFIÈRE** INSA de Lyon MATEIS - Bât. Saint-Exupéry 7 Avenue Jean CAPELLE 69 621 Villeurbanne CEDEX Tél : 04.72.43.71.70 Fax : 04.72.43.85.28 **jean-yves.buffiere@insa-lyon.fr**
MEGA	**MÉCANIQUE, ÉNERGÉTIQUE, GÉNIE CIVIL, ACOUSTIQUE** **http://edmega.universite-lyon.fr** Sec. : Stéphanie CAUVIN Tél : 04.72.43.71.70 Bât. Direction **mega@insa-lyon.fr**	**M. Jocelyn BONJOUR** INSA de Lyon Laboratoire CETHIL Bâtiment Sadi-Carnot 9, rue de la Physique 69 621 Villeurbanne CEDEX **jocelyn.bonjour@insa-lyon.fr**
ScSo	**ScSo*** **http://ed483.univ-lyon2.fr** Sec. : Véronique GUICHARD INSA : J.Y. TOUSSAINT Tél : 04.78.69.72.76 **veronique.cervantes@univ-lyon2.fr**	**M. Christian MONTES** Université Lyon 2 86 Rue Pasteur 69 365 Lyon CEDEX 07 **christian.montes@univ-lyon2.fr**

*ScSo : Histoire, Géographie, Aménagement, Urbanisme, Archéologie, Science politique, Sociologie, Anthropologie

Cette thèse est accessible à l'adresse : http://theses.insa-lyon.fr/publication/2022LYSEI006/these.pdf
© [X. Zhang], [2022], INSA Lyon, tous droits réservés

Acknowledgements

This thesis is the result of three years of research work conducted at the Laboratoire de Génie Electrique et Ferroélectricité of Institut National des Sciences Appliquées Lyon. This thesis work would not have been accomplished without the support and assistant of the people to whom I wish take this opportunity to express my sincere appreciation.

First of all, I would like to express my profound respect and gratitude to my supervisor, Prof. Lionel PETIT, for providing invaluable guidance throughout this research. Discussions with him have always been a learning experience and gave me another point of view for my result. I sincerely thank him for all the confirmation and encouragement he made to relieve my anxiety and motivate to another step.

Second, my deepest gratitude goes to my co-supervisor Dr. Minh Quyen Le, who was always there when I need assistance. She has taught me the methodology to carry out the experiment, data analysis, even presentation and scientific writing with endless patience, training me to be a qualified researcher. I warmly thank her for the suggestions she gave me, whether in the technical, scientific, professional and personal field.

Besides my supervisors, I would like to thank the rest of the jury members: Prof. DEMOLY Frédéric, Prof. GUIFFARD Benoit, Prof. BREMOND Georges, Prof. LIANG Zhiyong, Dr. CONSONNI Vincent and Dr. DELLA SCHIAVA Nellie, for their detailed reviews, insightful comments and present on my defense.

In addition, I wish to thank French National Research Agency for their financial support during my PhD period, providing precious opportunity to continue my academic study.

I am particularly grateful to Dr. Pierre-Jean Cottinet for his design and establishment of the d_{33} test bench and for providing constructive suggestions on my research. My sincere thanks go to Mr. Jose Villafuerte from LMGP laboratory, for constantly growing and preparing NWs samples to me. The frequently discussion and cooperation with him have been to be productive and substantially accelerated our project, especially during the hard times. I would like to thank Dr. Jean-Fabien Capsal for introducing composite fabrication process and efficiently helping solve several COMSOL simulation confusions at the beginning of my thesis. My thanks as well go to Dr. Gildas COATIVY for providing improved solution during the composite fabrication.

I would like to express my acknowledgments to staffs and colleagues in LGEF laboratory. Dr. Laurence SEVEYRAT, an experienced technician engineer, gave the introduction course in chemical room and guidelines in SEM. I am grateful for the assistance given by Ms. Véronique Perrin, a reliable electronic engineer, for the high voltage characterization. I would like to thank Mr. Frédéric DEFROMERIE, a skillful technician in LGEF, for manufacturing the desired masks, electrodes. A special thanks goes to Ms. Evelyne Dorieux for helping me deal with the complex administrative stuff.

I would like to extend my thanks to my colleagues and friends, who build a multicultural ambience in the office filled with smiles, rather than only a working place. Thanks to my dear Chinese girls: Dr. Yan ZHANG, Dr. Ziyin XIANG and Ms. Yuanyuan LIU for being always prepared to help for academical difficulties as well as accompany in my life. Thanks to Dr. Kritsadi Thetpraphi and Dr. Francesco Pedroli as the reliable and excellent seniors, who not only always gave helpful tips in my experiments but also

Cette thèse est accessible à l'adresse : http://theses.insa-lyon.fr/publication/2022LYSEI006/these.pdf
© [X. Zhang], [2022], INSA Lyon, tous droits réservés

organized lunch and beer time after our hard work. Thanks to Ms. Hiba Haissoune for her French help in administration works and wonderful short-term roommate. Thanks to Mr. Omar Zahaf for supporting the experimental observations in my first paper and to Mr. Van Cuong Nguyen for helping me with the mechanical characterization. Thanks to Ms. Giulia D'Ambrogio for patient help during my preparation of TP and to Mr. Amaury for enjoyable hiking experience. I am grateful for unforgettable and valuable time spent with Dr. Linjuan Yan, Dr. Mickaël Lallart, Dr. Giulia Lombardi, Dr. Bhaawan Gupta.

I would also take this chance to thank my friends Shuosi HUANG, who shares her amazing working experience and stories, Hui ZHOU, who gives criticism points of view and sets a self-discipline role model, Xiaojiao ZHANG, who is my sweet cousin and listener.

At last but not least, I would like to express my deepest gratitude to my parents, my lovely brother, sister in law, cute nephew and ninety-four years old grandfather for your unconditional love and cares. Thank you so much for always being with me.

Xiaoting ZHANG

11/11/2021

Cette thèse est accessible à l'adresse : http://theses.insa-lyon.fr/publication/2022LYSEI006/these.pdf
© [X. Zhang], [2022], INSA Lyon, tous droits réservés

Résumé

Grâce à ses multiples fonctionnalités, l'oxyde de Zinc (ZnO) est déjà utilisé dans de nombreuses applications du domaine de l'optoélectronique, des capteurs physico-chimiques, des composants électroniques ou encore des micro-dispositifs électromécaniques. Son excellente biocompatibilité et sa biosécurité permettent en particulier d'envisager des procédés technologiques innovants exploitant ses propriétés piézoélectriques en milieu biologique. Un matériau composite utilisant des charges ZnO incorporées dans une matrice polymère offre ainsi de nombreux avantages potentiels tels qu'une flexibilité élevée, un faible coût, une réelle recyclabilité et une intégration aisée, de plus adaptée à la fabrication additive sous toutes formes et dimensions. Ces composites se présente donc comme une intéressante alternative dans le domaine des capteurs flexibles compacts pour détecter les variations de pression ou de déformation élastique de tissus ou liquides biologiques. A terme, ces composites pourraient également cumuler la fonction de récupération d'énergie électrique extraite du gisement mécanique et vibratoire de l'environnement ambiant pour alimenter des nanodispositifs sans besoin de source d'alimentation externe ou de recharge de batterie interne, constituant ainsi de véritables dispositifs biomédicaux auto-alimentés.

L'objectif de ces travaux est de mener une caractérisation complète à l'échelle macroscopique de composites piézoélectriques intégrant des structures micro/nano ZnO afin d'aboutir à une meilleure compréhension du couplage électromécanique ainsi que des propriétés diélectriques, électriques et mécaniques intrinsèques de la matrice et de la charge, qu'elles soient individuelles ou combinées. Un autre point se concentre sur le développement de stratégies optimisées basées sur la caractérisation expérimentale et la méthode des éléments finis (FEM), dans le but d'augmenter les performances piézoélectriques des micro/nano composites ZnO. Les caractéristiques électriques, diélectriques, mécaniques et piézoélectriques des composites dépendent en premier lieu des propriétés intrinsèques de chaque élément constitutif mais également de la forme, de la taille, de la concentration et de la dispersion des charges ZnO. Aucune étude complète n'est pourtant disponible dans la littérature pour décrire l'influence de ses paramètres sur les propriétés du composite.

Dans ce but, la présente étude s'est d'abord orientée vers la mise au point d'un process de fabrication de composite, à faible cout, à l'élaboration simple et parfaitement maitrisée, basé sur l'utilisation des particules de ZnO encapsulées dans une matrice de polydiméthylsiloxane (PDMS). Les résultats expérimentaux ont montré qu'une concentration de particule élevée entraîne une augmentation de la permittivité diélectrique, de la conductivité, du module élastique de compression et de la constante piézoélectrique. Plus important encore, une amélioration significative de ces caractéristiques a été obtenue avec succès grâce à l'alignement diélectrophorétique de microparticules de ZnO à concentration plus faible. Une étude de l'influence de la forme et de la taille des charges sur les propriétés des composites a également été menée en utilisant des particules sphériques, des microtubes ou des nanofils. Les composites utilisant un réseau vertical ordonné de nanofils ZnO obtenu par dépôt en bain chimique présente au final le couplage piézoelectrique le plus élevé. Des simulations par la méthode des éléments finis ont été utilisées dans ce sens pour optimiser l'activité piézoélectrique d'un composite à nanofils ZnO en fonction du module d'élasticité et de la constante diélectrique des éléments constitutifs ainsi que de la densité et des dimensions des nanofils. Il a également été établi que l'apparition de défauts cristallins lors de la croissance des nanofils de ZnO génère des porteurs de charges électriques qui ont un effet masquant sur l'effet piézoelectrique. Cette dégradation peut être atténuée par un dopage à l'Antimoine (Sb) ou par un recuit thermique qui permet de diminuer la concentration de ces porteurs parasites.

Au final, des composites flexibles piézoélectriques à nanofils ZnO ont été developpé en utilisant un substrat de type polymère PDMS au lieu d'un substrat rigide silicium. L'ensemble des résultats expérimentaux obtenus confirme l'excellent potentiel des matériaux développés pour toute application de biodétection *in vivo* nécessitant impérativement des dispositifs médicaux flexibles et extensibles.

Mots clés : composites piézoélectriques ; nanofils de ZnO ; composites nano/micro ZnO ; application médicale ; caractérisations électriques, diélectriques et piézoélectriques ; méthode des éléments finis ; diélectrophorèse.

Cette thèse est accessible à l'adresse : http://theses.insa-lyon.fr/publication/2022LYSEI006/these.pdf
© [X. Zhang], [2022], INSA Lyon, tous droits réservés

Abstract

Due to the multiple functionalities of zinc oxide (ZnO), it has been used in a wide variety of applications such as optoelectronics, chemical sensors, piezoelectric transduces and varistors. Particularly considering the biocompatibility and biosafety of ZnO, exploring its excellent piezoelectricity in biological environment would be a new frontier with the development of innovative technological process. Composites of piezoelectric ZnO fillers embedded into a polymer matrix offer many potential benefits like high flexibility, low-cost, possible recyclability, tailored properties, adaptable to additive manufacturing, and easy integration to any shapes and dimensions. Hence, ZnO-based piezoelectric composites would be an alternative solution as flexible and compact implantable sensors, which can directly detect and monitor the mechanical stimulation or pressure change occurring in patient's organs. On the broader scale, these composites could harvest the mechanical energy from ambient environment to sufficiently supply nanodevices without the requirement of external power source and internal battery recharging and replacing, denoting as self-powered biomedical devices. The goal of this research is to investigate full characterizations of piezoelectric system based on ZnO micro/nano structure in a macroscopic scale. This allows to a better understanding of the electromechanical coupling as well as the intrinsic dielectric, electrical, and mechanical properties of the matrix and filler, when being individual or combined together. Another aspect focuses on the development of optimized strategies based on experimental characterization and finite element method (FEM), with the intention of boosting the piezoelectric performance of ZnO micro/nano composites.

The piezoelectric performance of composites could be tailored by varying the shape, size, concentration and dispersion of fillers, together with the intrinsic characteristics of the polymer matrix. To date, a full assessment of their influence on the effective properties of composites involving electric, dielectric, mechanical, and piezoelectric characteristics has been rarely reported in literatures, in spite of their crucial significance. Thus, a processive strategy was firstly proposed with ZnO particles incapsulated into polydimethylsiloxane (PDMS) matrix owning to their sample structure, low cost, easy process, and well-controlled elaboration. Experimental results revealed that a higher particle concentration gives rise to a substantial enhancement in the dielectric permittivity, the conductivity, the compressive elastic modulus, and the piezoelectric coefficient. More importantly, significant enhancements in those output performances have been successfully achieved via dielectrophoretic alignment of ZnO microparticles (MP) at moderate concentration. Additionally, a particular emphasis on the shape and size effect of the fillers (i.e., comprising spherical particles, microrods (MR) and nanowires (NW)) on the properties of ZnO composites was thoroughly explored via empirical characterization and numerical simulation.

It is pointed out that composites of vertically aligned ZnO NWs grown by chemical bath deposition (CBD) method exhibited the maximum piezoelectric efficiency. FEM modeling was employed to drive the optimization strategies through adjustment of the key parameters such as Young's modules and dielectric constant of the constituents, together with the density and dimension of NW itself. Furthermore, thanks to the investigation on the crystal defects from spontaneously grown ZnO NWs, two effective strategies including Sb-doping and thermal annealing were confirmed to decrease carrier concentration in ZnO, with the aim of weakening the undesired screening effect. Finally, flexible piezoelectric NWs composites based PDMS polymer substrate instead of the rigid silicon are investigated. Experimental results confirm high potential of the developed material in vivo biosensing and bio-detection applications, especially when flexible and stretchable devices are mandatory for medical uses.

Key word: piezoelectric composites; ZnO nanowires; nano/micro ZnO composites; medical applications; electrical, dielectric and piezoelectric characterizations; finite element method; dielectrophoresis.

Cette thèse est accessible à l'adresse : http://theses.insa-lyon.fr/publication/2022LYSEI006/these.pdf
© [X. Zhang], [2022], INSA Lyon, tous droits réservés

Résumé de mémoire

Introduction

Les travaux de thèse s'intègre de le projet ANR ROLLER réalisé en collaboration entre le LMGP, l'INL, Institut Néel. Les composites d'oxyde de zinc (ZnO) intégrés dans une matrice polymère ont attiré une attention considérable en raison de la combinaison des propriétés multifonctionnelles du ZnO et des avantages de la matrice polymère, tels que la flexibilité, la facilité de mise en œuvre, etc. Le ZnO présente des propriétés piézoélectriques sans nécessiter de processus de polarisation sous fort champ électrique, grâce à sa structure cristalline non centrosymétrique. De plus, l'effet de confinement quantique dans la nanostructure du ZnO donne lieu à une amélioration induite par la taille par rapport au matériau brut. En particulier, le ZnO est un matériau biocompatible et non toxique, ce qui ouvre la voie à des applications spécifiques pour la réalisation de dispositif médicaux, etc.

La contribution des travaux de thèse concerne une analyse des couplages multiphysiques dans des composites à base de ZnO, ainsi d'explorer leurs stratégies d'optimisation pour une application potentielle dans les dispositifs biomédicaux. Les composites à base de ZnO offrent des propriétés améliorées, qui sont plus flexibles que les matériaux piézoélectriques conventionnels (céramique) et peuvent être contrôlées par l'arrangement de la phase inorganique. Dans les composites à deux phases, ceux qui présentent un schéma de connectivité 1-3, défini comme des fibres continues alignées dans une dimension, présentent généralement de meilleures performances que ceux qui présentent un schéma de connectivité 0-3, où les charges sont dispersées de manière aléatoire. Par conséquent, les composites correspondants incorporant des charges avec différents facteur de forme de ZnO ont été élaborsé, caractérisés et simulés numériquement pour confirmer leur influence sur le couplage électromécanique. En raison de leur architecture simple, de leur processus de fabrication aisé, les composites particules de ZnO/polymère ont tout d'abord été étudiés afin de mieux comprendre leurs propriétés en termes de propriété diélectrique, piézoélectrique et mécanique en fonction de la taille et de la concentration de la charge. Cela a mis en avant que la capacité des particules sphériques à augmenter la constante diélectrique et piézoélectrique effective dans les composites 0-3 est assez limitée à faible teneur en charge, tandis que la concentration élevée en charge est difficile à atteindre en raison de l'effet d'agglomération. D'autre part, les composites à connectivité 1-3 conduisent à des performances plus élevées, malgré leur fabrication compliquée et leur coût plus élevé par rapport à leurs homologues 0-3. En conséquence, le composite quasi 1-3, développé par alignement diélectrophorétique des particules le long de la direction du champ, pourrait conduire à des propriétés améliorées à une concentration de particules plus faible. De plus, le processus de fabrication du matériau peut être optimisé en tenant compte du facteur de forme. Des charges sous forme de nano fil ont ainsi été réalisées pour produire des composites 0-3 et 1-3 diélectrophorétique. De plus les designs ont été modélisés par des méthodes des éléments finis (FEM) qui permet de vérifier les observations obtenues par les caractérisations expérimentales.

Cette thèse est accessible à l'adresse : http://theses.insa-lyon.fr/publication/2022LYSEI006/these.pdf
© [X. Zhang], [2022], INSA Lyon, tous droits réservés

Chapitre 1 – Etats de l'art

Les travaux se focalisent sur les matériaux piézoélectriques en mode capteur ; il s'agit l'effet piézoélectrique direct qui par définition implique la production d'une charge électrique en réponse à une stimulation mécanique appliquée. Le principe de la piézoélectricité peut être illustré par un modèle moléculaire simple. Un cristal centrosymétrique est incapable de générer une polarisation électrique sous une stimulation externe. Après application d'une force externe, les dipôles de polarisation p_i s'annulent toujours et donnent lieu à un moment dipolaire total nul en raison de l'existence du centre de symétrie. En revanche, pour un cristal non centrosymétrique, lorsqu'une contrainte externe est imposée, en raison de l'absence de centre de symétrie, la structure interne d'une cellule unitaire est déformée, ce qui entraîne la séparation des centres positif et négatif et produit un moment dipolaire. Même les demi-dipôles voisins portés par des signes de charge opposés s'annulent à l'intérieur du matériau. Mais ce matériau est polarisé et des charges nettes apparaissent à la surface évoquant un champ électrique, ce qui donne naissance au phénomèn piézoélectricité.

Il est possible de linéariser le comportement des matériaux et de les modéliser à l'aide d'équation phénoménologique

$$D_k = d_{kq} T_q + \varepsilon_{kp}^T E_p \tag{1.1}$$

$$S_m = s_{mq}^E T_q + d_{mp} E_p \tag{1.2}$$

où D et E sont le tenseur du déplacement électrique et le champ électrique, respectivement. ε_{kp}^T est le tenseur de permittivité sous contrainte constante, s_{mq}^E est le tenseur de compliance élastique sous un champ électrique constant et d est le coefficient de charge piézoélectrique. Le déplacement électrique total dans un matériau piézoélectrique est la somme du déplacement électrique induit dans les diélectriques et de la polarisation supplémentaire causée par l'effet piézoélectrique direct. De même, la déformation totale dans un matériau piézoélectrique est la somme de la déformation mécanique causée par la contrainte appliquée et de la déformation supplémentaire induite par l'effet piézoélectrique inverse.

Les matériaux piézoélectriques peuvent être classés en deux catégories : les matériaux naturels et les matériaux synthétiques fabriqués par l'homme, notamment les monocristaux, les céramiques et les polymères. Tous ces matériaux présentent certaines limites. Le principal inconvénient des matériaux piézoélectriques naturels est leur faible constante piézoélectrique. Les céramiques piézoélectriques telles que le titanate de plomb (PbTiO3) et le titanate de zirconate de plomb (PZT) présentent un grand potentiel de fabrication en raison de leur constante piézoélectrique supérieure à celle du quartz. Les polymères piézoélectriques, caractérisés par une grande flexibilité, sont limités par leur faible constante diélectrique et leur constante de charge piézoélectrique faible.

Par conséquent, afin de surmonter ces inconvénients, des charges piézoélectriques sont incorporées aux polymères pour développer des composites piézoélectriques présentant des avantages considérables tels

Cette thèse est accessible à l'adresse : http://theses.insa-lyon.fr/publication/2022LYSEI006/these.pdf
© [X. Zhang], [2022], INSA Lyon, tous droits réservés

qu'une ductilité élevée, une flexibilité et une facilité d'élaboration en différentes tailles et formes. Plus important encore, les propriétés des composites peuvent être adaptées aux formes, tailles et concentrations des charges. Le ZnO, choisi comme charge, est couramment utilisé dans une application piézoélectrique en profitant de l'effet piézoélectrique direct. De plus, le ZnO ne nécessite pas de processus de polarisation, contrairement aux autres céramiques piézoélectriques. En outre, le ZnO est également un matériau biocompatible et non toxique, ce qui élargit encore ses applications au domaine de la santé, notamment aux outils de biodétection et de détection in vivo.

La structure atypique du ZnO à savoir quatre anions oxygène et un cation Zn forment une unité tétraédrique qui présente une symétrie non centrale et un effet piézoélectrique lui confère ainsi des propriétés spécifiques. En outre, avec la diminution de la dimension du matériau à l'échelle nanométrique, les caractérisations mécaniques, électromécaniques, électriques et optiques deviennent très différentes de celles du matériau massif en raison des effets de surface et de confinement quantique. Des méthodes de calcul théoriques et des études expérimentales ont démontré la dépendance de la taille de la piézoélectricité, en particulier dans les nanostructures unidimensionnelles avec un rapport d'aspect élevé, comme les nanofils (NW), les nanotubes et les nanofibres. On pense que la réduction du diamètre des NWs de ZnO pourrait améliorer le coefficient piézoélectrique par rapport au ZnO massif. En outre, les nanostructures offrent la possibilité d'une miniaturisation, notamment dans un nanodispositif biomédical implantable.

Dans le système à deux phases, il existe dix modèles de connectivité différents selon la disposition des phases constitutives. Parmi eux, le modèle de connectivité 0-3, considéré comme le plus simple, présente une phase auto-connectée dans la direction zéro et une autre phase auto-connectée dans les directions tridimensionnelles, indiquant les particules non connectées dispersées de manière aléatoire dans une matrice entièrement connectée. Dans les composites multiphases, les propriétés physiques, notamment diélectriques, piézoélectriques, mécaniques et pyroélectriques, peuvent être contrôlées et améliorées en manipulant le modèle de connectivité. Dans les composites à phase de connectivité 1-3, la charge est connectée de manière unidimensionnelle et la matrice a une connectivité tridimensionnelle, ce qui signifie que la fibre ou la tige à phase continue est alignée dans la matrice polymère. Pour les composites 0-3, une teneur relativement élevée en charge est nécessaire pour obtenir des performances piézoélectriques prometteuses, tandis que les composites 1-3 peuvent stimuler le couplage électromécanique pour une concentration modérée, malgré leur fabrication compliquée et leur coût plus élevé. L'activité diélectrophorétique peut donc être largement utilisée pour créer un état intermédiaire entre un modèle de connectivité 0-3 et 1-3 en orientant les particules pour former une structure en chaîne.

Sur la base de la propriété électrique non linéaire du ZnO, l'une des applications potentielles des composites de ZnO est le développement d'un cathéter intelligent utilisé dans l'ablation par champ pulsé (PFA) pour traiter les arythmies cardiaques. Une telle conception permet de délivrer une série d'impulsions électriques ultracourtes pour ablater le tissu cardiaque. Sous un faible champ électrique, les composites à base de particules de ZnO se comportent comme un diélectrique avec une région à haute résistance, adjacente au tissu cardiaque où un champ électrique est imposé pour effectuer un traitement d'ablation normal. Une fois que le champ électrique imposé est excessif par rapport au tissu cardiaque, les composites à base de ZnO se comportent comme un conducteur variable qui attire un courant important à travers lui, ce qui entraîne un faible champ électrique dans le tissu adjacent. En ce qui concerne la propriété piézoélectrique, les composites à base de ZnO peuvent être utilisés pour deux types de fonctions en fonction des signaux électriques de sortie. Notre application cible pour le dispositif de détection développé est liée à la technique de réserve de flux fractionnaire (FFR) pour évaluer l'importance du rétrécissement des artères, en particulier

Cette thèse est accessible à l'adresse : http://theses.insa-lyon.fr/publication/2022LYSEI006/these.pdf
© [X. Zhang], [2022], INSA Lyon, tous droits réservés

dans les sténoses coronaires. Les composites piézoélectriques à base de ZnO sont supposés être une solution alternative comme capteur de pression flexible et sensible, et donc plus facilement implémentable sur un cathéter pour la mesure de la pression FFR.

Cette thèse est accessible à l'adresse : http://theses.insa-lyon.fr/publication/2022LYSEI006/these.pdf
© [X. Zhang], [2022], INSA Lyon, tous droits réservés

Chapitre 2 – Elaboration et méthode

Elaboration des composites piézoelectrique à base de ZnO

Pour les composites 0-3, élaborés durant la thèse, les particules utilisées sont de différentes tailles à savoir ~150 nm/~1 µm de diamètre. Elles ont été approvisionnées chez US Research Nanomaterials Inc, et des microrods (~ 3.9 µm de longueur et ~ 477 nm de diamètre) qui ont été synthétisé de façon spécifique par le LMGP. La matrice est élastomère de silicone de chez Dow Chemical Company. Les charges de ZnO ont été mélangées avec la solution de PDMS, puis dispersé par ultrason pour obtenir une dispersion homogène du mélange et dégazé pour évtier la préscence de bulle d'aire. Après avoir ajouté l'agent de durcissement, le mélange a ensuite été coulé sur un substrat en verre d'une épaisseur de 0,5 mm et a subi la réaction de thermodurcissement dans un four à une température de 100°c pendant 35 minutes. Enfin, des électrodes circulaires en or de 10 mm de rayon et de 25µm d'épaisseur ont été déposées sur les deux faces du film à l'aide d'une machine à pulvériser (Cressington, 208HR).

L'effet diélectrophorétique peut également être utilisé pour manipuler des particules dispersées dans un milieu fluide et développer des composites polymères « remplis » de particules alignées avec des propriétés anisotropes. Il est possible d'observer et d'enregistrer le mouvement des microparticules sous l'application d'une tension alternative (AC) en utilisant la microscopie optique. Ainsi, le degré d'alignement des particules a été surveillé et comparé en fonction des conditions appliquées afin de conclure à la magnitude et à la fréquence électriques externes optimales. En conséquence, le champ électrique de 1 V/µm et 2 Hz est considéré comme le choix le plus optimal pour fabriquer le composite structuré de microparticules de ZnO/PDMS. Le processus de fabrication des composites structurés par diélectrophorèse était similaire à celui du film aléatoire ZnO/PDMS décrit ci-dessus, sauf pour la dernière étape. Une couche constituée d'une plaque d'époxy isolante de 0,5 mm d'épaisseur avec un trou circulaire de 25 mm de diamètre au centre a été soigneusement remplie de la solution de ZnO/PDM non polymérisée. Ensuite, l'ensemble de l'échantillon et du support ont été placés dans un four (Votsch IndustrietechnikTM, VT7004) à une température constante de 100°C pendant 35 minutes, tandis qu'un champ électrique était appliqué pendant le processus de chauffage.

Afin d'améliorer encore les performances piézoélectriques, des composites constitués de réseaux de nanotubes de ZnO alignés verticalement et encapsulés dans une matrice polymère rigide ont été fabriqués au laboratoire de génie physique et des matériaux (laboratoire LMGP). Les nanotubes de ZnO ont été cultivés sur une couche d'ensemencement de ZnO de 40 nm d'épaisseur par la méthode de dépôt par bain chimique (CBD), puis une matrice de PMMA a été appliquée par centrifugation comme matériau isolant interstitiel entre les nanotubes et empilée sur les réseaux de nanotubes de ZnO. Dans cette recherche, des composites de NWs rigides et flexibles ont été préparés en utilisant respectivement du silicium et du PDMS comme substrat. En particulier, plusieurs améliorations ont été apportées à l'optimisation des propriétés des composites de NWs de ZnO flexibles afin d'augmenter les performances et l'efficacité globales : un traitement de recuit sous atmosphère d'O_2 a été mis en œuvre avant le revêtement par centrifugation de la couche supérieure en PMMA ; 1 % du rapport Sb/Zn a été ajouté à la solution de CBD pour obtenir des NWs de ZnO dopés au Sb.

Dispositif de caractérisation électrique, mécanique et de transduction

Cette thèse est accessible à l'adresse : http://theses.insa-lyon.fr/publication/2022LYSEI006/these.pdf
© [X. Zhang], [2022], INSA Lyon, tous droits réservés

Les propriétés diélectriques (permittivité, perte diélectrique) ont été mesurées à l'aide d'un analyseur de réponse en fréquence (Solartron, 1255) et d'une interface diélectrique (Solartron, 1296A) sur une gamme de fréquences allant de 0,1 Hz à 1 MHz. Les caractéristiques électriques sous des applications de niveau électrique élevé ont été analysées dans un montage expérimental composé d'un porte-échantillon, d'un générateur de forme d'onde, d'un amplificateur haute tension, d'un préamplificateur de courant à faible bruit et d'un oscilloscope. Il y avait trois catégories d'entrée, notamment des signaux DC, sinusoïdaux (bipolaires) et sinusoïdaux positifs (unipolaires). Afin d'évaluer et de comparer la distribution des particules des composites ZnO/PDMS structurés et aléatoires, une microscopie électronique à balayage (MEB) a été réalisée avec un microscope Hitachi Flex SEM 1000II. Des essais expérimentaux de traction et de compression monotones ont été réalisés à l'aide du TCE-N300 de Shimadzu pour évaluer les propriétés mécaniques des composites ZnO/PDMS. Ensuite, les modules de traction et de compression ont été déduits de la pente linéaire de la courbe contrainte-déformation. Le coefficient de charge piézoélectrique a été mesuré à l'aide d'un banc d'essai spécialement conçu à haute sensibilité, comme le montre la figure 1. L'excitation mécanique dynamique a été pilotée par un actionneur piézoélectrique à pile (PI 246-50) avec une amplitude et une fréquence accordables contrôlées par un générateur de forme d'onde (Agilent, 33500B) associé à un amplificateur de tension (Trek, modèle 20/20C). La charge électrique générée Q a été mesurée par un compteur de charge à haute sensibilité (KISTLER, Type 5015). Ainsi, le coefficient de charge d_{33} peut être estimé comme $d_{33} = \frac{Q}{A_{ative}} * \frac{A}{F}$, où A_{active} et A désignent la surface de l'électrode en or et la surface clapée, respectivement. D'autre part, les propriétés électriques des échantillons en termes de densité de courant par rapport aux caractéristiques du champ électrique peuvent être surveillées pendant le processus de sollicitation mécanique.

Enfin, un modèle simple bidimensionnel et tridimensionnel a été construit à l'aide de l'outil COMSOL Multiphysics pour simuler et estimer les comportements piézoélectriques dans les microparticules (MPs) et les nanofils (NWs) composites de ZnO, respectivement.

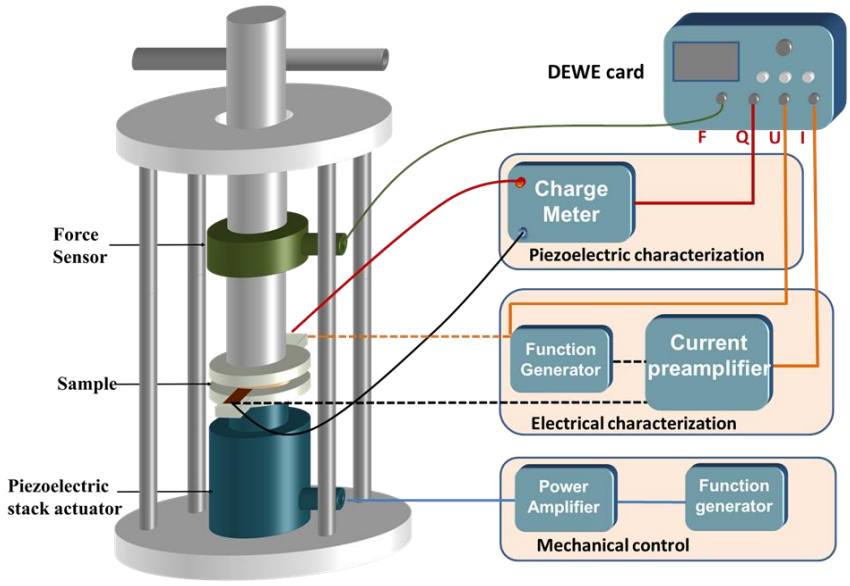

Fig. 1. Banc de mesure spécifique pour la caractérisation des propriétés piéozoelectrique

Cette thèse est accessible à l'adresse : http://theses.insa-lyon.fr/publication/2022LYSEI006/these.pdf
© [X. Zhang], [2022], INSA Lyon, tous droits réservés

Chapitre 3 – Structuration des composites ZnO PDMS à l'aide de la diélectrophorèse

Les caractérisations électriques des composites de microparticules de ZnO ont été effectuées au début pour étudier les différents modèles de connectivité. Les caractéristiques Densité de courant en fonction du champ électrique décrivent deux pentes différentes : la première pente présente un niveau très bas, correspondant au comportement isolant sous le champ de commutation ; la seconde pente, définie comme le coefficient non linéaire (α), augmente considérablement lorsque le matériau devient conducteur. Une concentration croissante de ZnO entraîne un champ de commutation plus faible et un α plus élevé, ce qui est attribué aux chemins de conduction incrémentaux dans les composites. De même, la structure 1-3 favorise le comportement non linéaire, conduisant à une augmentation de 10% de la valeur de α par rapport à la matrice 0-3, due à la création de chemins de conduction plus courts et plus droits. D'autre part, la caractéristique courant-tension AC a illustré deux mécanismes de conduction des composites dépendant du champ. Pour le champ appliqué inférieur à 0.4 V/µm, le courant capacitif est considéré comme la composante dominante et le courant de conduction obéit à la loi d'Ohm, pour extraire des paramètres tels que la permittivité et la conductivité. En augmentant le champ électrique jusqu'à 1V/µm, le courant de conduction devient dominant et présente un comportement non linéaire décrit par le modèle non-ohmique. Néanmoins, l'alignement diélectrophorétique sur les particules de ZnO améliore significativement la réponse conductrice des composites.

En termes de propriétés mécaniques, le module d'élasticité en traction et en compression augmente avec l'augmentation de la fraction volumique de ZnO au fur et à mesure de l'ajout de particules fragiles dans la matrice. Cependant, seulement dans le mode de compression, l'amélioration des propriétés mécaniques résultant du renforcement le long de l'orientation de la particule a été observée dans les composites structurés 1-3. De plus, le module d'Young des microparticules de ZnO a été estimé autour de 163.4 GPa grâce au modèle de Nielsen.

Indépendamment des composites incorporant des micro ou nanoparticules, la constante diélectrique expérimentale augmente substantiellement avec la teneur en ZnO. Mais la permittivité des microparticules (~125) est supérieure à celle des nanoparticules (~20), ce qui est basé sur les modèles analytiques. Ceci est probablement attribué à l'excès de métal et aux propriétés semi-conductrices du ZnO. Plus important encore, comme le montre la figure 2(a), la diélectrophorèse entraîne une meilleure amélioration de la permittivité dans les composites de microparticules en raison de l'introduction de la polarisation de l'interface ZnO/ZnO. Par exemple, à la fréquence de 1 kHz, une augmentation de 1,5 fois a été obtenue pour l'échantillon élaboré avec une fraction de 44% vol. de poudre de ZnO, alors qu'il y avait une augmentation de 2 fois pour l'échantillon de 14%. De même, en raison de la forte connectivité ZnO/ZnO, les composites alignés présentent des propriétés piézoélectriques nettement supérieures à celles des composites dispersés au hasard, comme le montre la figure 2(b). Plusieurs modèles analytiques ont été ajustés aux données réelles et une bonne cohérence a été observée pour permettre l'estimation de la constante piézoélectrique d_{33} (1.45 pC/N) des micro-particules de ZnO. De plus, un modèle COMSOL 2D a été développé pour prédire la constante diélectrique et le coefficient piézoélectrique du matériau ZnO en prenant en compte les différentes distances interparticulaires dans le composite structuré (Figure 2).

Cette thèse est accessible à l'adresse : http://theses.insa-lyon.fr/publication/2022LYSEI006/these.pdf
© [X. Zhang], [2022], INSA Lyon, tous droits réservés

La dernière partie de ce chapitre traite de la dépendance en température des caractéristiques densité de courant en fonction du champ électrique et des propriétés diélectriques afin de comprendre les mécanismes de fonctionnement. Deux facteurs concurrents, à savoir le transport des porteurs à travers les particules de ZnO et la résistance de contact entre les charges, peuvent dominer dans différentes plages de température dans les caractéristiques J-E ou différentes plages de fréquence dans les caractéristiques diélectriques.

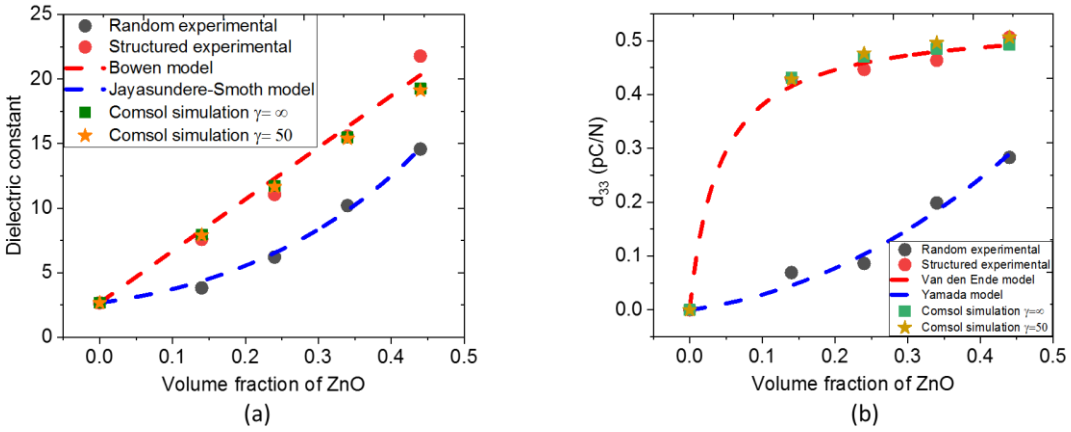

Fig. 2. Propriét diélectrique (a) et coefficient piézoélectrique (b) expérimentaux et théoriques des composites micro-ZnO/PDMS structurés et aléatoires en fonction de la concentration en ZnO.

Cette thèse est accessible à l'adresse : http://theses.insa-lyon.fr/publication/2022LYSEI006/these.pdf
© [X. Zhang], [2022], INSA Lyon, tous droits réservés

Chapitre 4 – Modélisation de réseaux de nanofils ZnO verticaux/composites PMMA

Dans ce chapitre, une approche « multiéchelle » allant de la structure de base, le NF individuel, aux réseaux de NF sera considérée pour simuler leurs comportements piézoélectriques. Ainsi, le premier objectif implique la modélisation analytique et la simulation COMSOL d'un NF unique fonctionnant à la fois en mode mécanique de flexion et de compression. Le schéma typique d'un nanofil de ZnO dans notre cas est représenté comme un cylindre avec un rayon (R) de 42 nm et une longueur (L) de 1031 nm. Le NF unique est fixé par le bas et poussé par le haut par une force latérale le long de la direction x (F_y=60 nN) ou comprimé par une force le long de la direction z (F_z=60 nN). Avec l'aide de la théorie des perturbations proposée par Gao et al, le potentiel piézoélectrique maximum d'un NF plié ($\varphi_{max\text{-}bend}$) ou comprimé ($\varphi_{max\text{-}com}$) est calculé analytiquement en fonction de la force externe appliquée, des paramètres géométriques et des propriétés du matériau (par exemple, la constante diélectrique, la constante piézoélectrique). Le potentiel électrique généré est uniforme le long de la direction z pour se comporter comme un "condensateur à plaques parallèles" dans un mode de flexion, par opposition à une tendance croissante le long de l'axe z dans le mode de compression. Une FEM complète basée sur le calcul numérique a été introduite en utilisant COMSOL Multiphysics pour confirmer la distribution du potentiel dans ces deux modes. Cependant, en raison de l'approximation du premier ordre et de la limitation de la théorie de Saint-Venant dans la modélisation analytique, les solutions analytiques ($\varphi_{max\text{-}bend}$ = 0,128 V, $\varphi_{max\text{-}com}$ = 2,006 V) présentent une divergence avec les valeurs dérivées des modèles FEM ($\varphi_{max\text{-}bend}$ = 0,13 V, $\varphi_{max\text{-}com}$ = 1,16 V). En outre, des paramètres tels que la force externe et les facteurs géométriques (forme et taille du NW) ont été balayés dans les deux modes afin de déterminer leur relation avec le potentiel de sortie, qui étaient cohérents avec la théorie analytique. Il a été souligné que, pour une force externe donnée, le mode de compression offrait une plus grande sensibilité piézoélectrique que le mode de flexion. Ce résultat montre l'intérêt de faire fonctionner la structure de NWs alignés sous l'excitation de compression afin de répondre aux besoins de la médecine, en particulier pour le développement de capteurs.

En réalité, les composites multicouches rigides basés sur les NFs sont illustrés dans la Fig. 3(a). Différents modèles analytiques correspondant à différents mécanismes de fonctionnement ont été construits pour avoir une estimation simple de la performance globale du système. La combinaison de modèles d'iso-déformation ou d'iso-contrainte reposant sur la mécanique linéaire classique a été introduite dans le modèle analytique mécanique, suggérant que la déformation du ZnO est uniquement déterminée par la force externe totale et la rigidité de la couche inférieure (K_{bottom}). L'effet piézoélectrique d'un seul NF peut être modélisé comme une source de tension en série avec une capacité C_{NW}, où la tension générée est déduite des équations constitutives piézoélectriques. L'étape finale consiste à transférer le potentiel au sommet des NFs de ZnO vers les électrodes supérieures. En considérant la couche composite inférieure comme un matériau homogène efficace possédant une propriété piézoélectrique, l'ensemble du dispositif peut être représenté par un circuit électrique équivalent composé de deux condensateurs connectés en série avec leur résistance de perte.

Cette thèse est accessible à l'adresse : http://theses.insa-lyon.fr/publication/2022LYSEI006/these.pdf
© [X. Zhang], [2022], INSA Lyon, tous droits réservés

Par souci de simplicité dans les simulations FEM, une cellule unitaire typique avec des conditions limites périodiques sur les parois latérales est définie pour être représentative du comportement de l'ensemble du dispositif, représenté sur la Fig. 3(b). Dans le but d'améliorer la performance piézoélectrique, nous nous concentrons sur l'optimisation des propriétés matérielles de la phase constitutive ainsi que sur la conception structurelle. La meilleure configuration, basée sur la prise en compte du module de Young et de la permittivité diélectrique, est une couche supérieure dure avec une permittivité élevée, et une couche inférieure souple avec une permittivité faible. Une densité modérée de NF d'environ 25-55 µm-2 semble être la configuration la plus optimisée, en raison de l'équilibre entre deux effets de tendance opposés relatifs au couplage électromécanique. Lorsque l'épaisseur de la couche supérieure de PMMA augmente, le rendement piézoélectrique diminue en raison de l'effet électrostatique classique, plutôt que de la variation de la déformation. Cependant, lorsque la fraction volumique de ZnO reste constante, la géométrie du NF a peu d'impact sur la sensibilité piézoélectrique d_{33} de l'ensemble du composite. Enfin, si l'environnement de l'air est considéré pour simuler le modèle réaliste, un réseau d'au moins 25×25 cellules est considéré comme un modèle approprié pour prédire la performance théorique en raison du fort effet de bord.

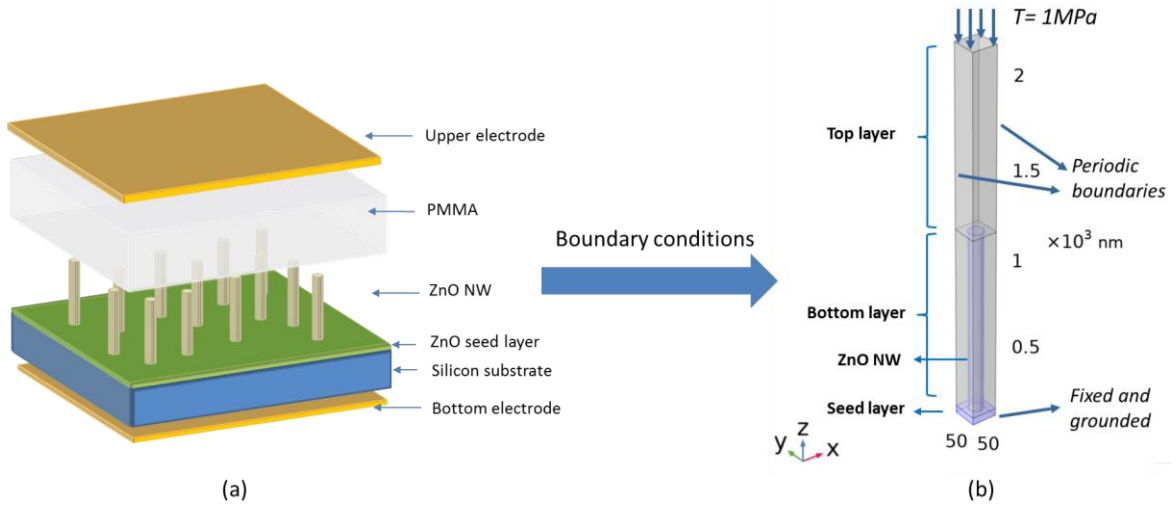

Fig. 3. (a) Structure schématique de réseaux rigides de NW ZnO/composites polymères ; (b) Structure schématique d'une cellule unitaire constituée d'une couche d'ensemencement de ZnO, d'une couche de matrice inférieure, d'une couche de matrice supérieure et d'un seul NW ZnO avec des conditions limites appropriées.

Cette thèse est accessible à l'adresse : http://theses.insa-lyon.fr/publication/2022LYSEI006/these.pdf
© [X. Zhang], [2022], INSA Lyon, tous droits réservés

Chapitre 5 – Composites piézoélectriques verticaux nano/micro matrices/PMMA

Dans ce chapitre, plusieurs configuration de connectivité de composite piézoelectrique ont été étudié comme l'illustre la Fig. 4. Il est intéressant de noter que la réponse piézoélectrique dépend du motif de connectivité. En commençant par le composite 0-3 ou à particules aléatoires dont la méthode de moulage basée sur le processus est facile, mais cette structure conduit à un coefficient piézoélectrique extrêmement faible (d_{33}). Par exemple, les composites de MPs de ZnO à 8% vol. présentent un d_{33} extrêmement faible (~0,0086 pC/N), comme le montre le tableau 1. Des charges de forme microrodale (MR) avec un rapport d'aspect (AR) plus élevé ont été substituées aux charges sphériques pour obtenir une réponse piézoélectrique relativement plus élevée (d_{33}~ 0.0173 pC/N). Afin d'améliorer encore leurs performances piézoélectriques sans changer la teneur en charges, la structuration des charges par diélectrophorèse est développée pour réduire la distance interparticulaire le long du champ. Les conditions diélectrophorétiques impliquant l'amplitude et la fréquence du champ électrique de structuration ont d'abord été étudiées et comparées entre les différentes charges. Pour toutes les particules AR, l'angle d'orientation moyen augmente avec une magnitude de champ électrique croissante et une fréquence décroissante, provoquant une augmentation de la constante diélectrique et donc du coefficient piézoélectrique. La dépendance de la constante diélectrique par rapport à l'amplitude du champ électrique est plus importante pour les particules MR à fort AR que pour les particules sphériques à faible AR. Par conséquent, sous le même champ électrique externe optimisé (0,6 V/μm, 2 Hz), les composites ZnO MRs/PDMS structurés à 8 % en volume présentent des améliorations substantielles des réponses diélectrique (~ sept fois) et piézoélectrique (~ six fois) par rapport à l'échantillon aléatoire, tandis qu'une amélioration de trois et cinq fois dans le cas des échantillons MP, respectivement.

Cependant, la structuration diélectrophorétique souffre toujours de la limitation de la saturation de la concentration de ZnO et de l'alignement non parfait comme dans le vrai motif 1-3. En fait, dans le composite 1-3, les fils sont encastrés verticalement dans une matrice polymère et créent une connexion continue des électrodes inférieures aux électrodes supérieures, ce qui donne lieu à la plus grande connectivité, et donc à la plus grande valeur d_{33}. Dans cette recherche, en fonction des matériaux de substrat, des composites rigides et flexibles de ZnO NWs sont fabriqués par la technique CBD pour améliorer la sensibilité piézoélectrique. Pour les composites rigides de réseaux de ZnO NWs, un des objectifs est d'identifier les caractéristiques de chaque couche ainsi que de l'ensemble de la structure complexe. Les caractérisations électriques ont été étudiées sur un ensemble de configurations conçues, permettant de confirmer que la couche d'ensemencement en Si et ZnO se comporte comme une résistance, tandis que les autres échantillons empilés avec une couche de PMMA se comportent comme un condensateur. De plus, les propriétés diélectriques de ces condensateurs étaient parfaitement stables sous une contrainte dynamique variant de 0,1 à 0,4 MPa. Un petit changement dans leur impédance électrique provenait de la variation d'épaisseur lorsque l'échantillon était soumis à une force de compression. Les mesures expérimentales ont mis en évidence que le composite de ZnO NWs avec une épaisseur plus faible de couche supérieure en PMMA a donné lieu à une sensibilité piézoélectrique accrue. Le coefficient de charge effectif (d_{33}) du composite fabriqué a atteint 3,4 pC/N lorsqu'il était empilé avec un PMMA de 1,5 μm d'épaisseur, par opposition à 0,86 pC/N dans le cas de la contrepartie en PMMA de 2 μm d'épaisseur. Cet effet était dans une certaine mesure corrélé au modèle prédit par COMSOL FEM. Par conséquent, des améliorations significatives du comportement

Cette thèse est accessible à l'adresse : http://theses.insa-lyon.fr/publication/2022LYSEI006/these.pdf
© [X. Zhang], [2022], INSA Lyon, tous droits réservés

piézoélectrique ont été obtenues en optimisant l'épaisseur de la couche supérieure (c'est-à-dire 1,5 µm). Malheureusement, l'échantillon Si/SL/NWs/PMMA (1 µm) n'a pas pu être mesuré en raison d'un problème de fuite électrique trop importante.

Dans un deuxième temps une matrice plus flexible à savoir le PDMS à été mise en œuvre à la pluce du Silicium (Si). Bien que le coefficient de charge piézoélectrique (d_{33}) soit inhibé, cette structure à haute flexibilité mécanique peut devenir un candidat prometteur dans les capteurs piézoélectriques pour des applications médicale, en particulier dans la technique FFR. En ce qui concerne la forte densité d'électrons libres des nanotubes de ZnO obtenus par la technique CBD, l'effet d'écran induit peut être réduit en appliquant un recuit thermique post-dépôt ou un dopage au Sb pendant le processus de fabrication. Les tests expérimentaux ont confirmé que le d_{33} du composite de NWs recuit et dopé est significativement amélioré (~1.055 pC/N) comparé à l'échantillon vierge (~0.288 pC/N).

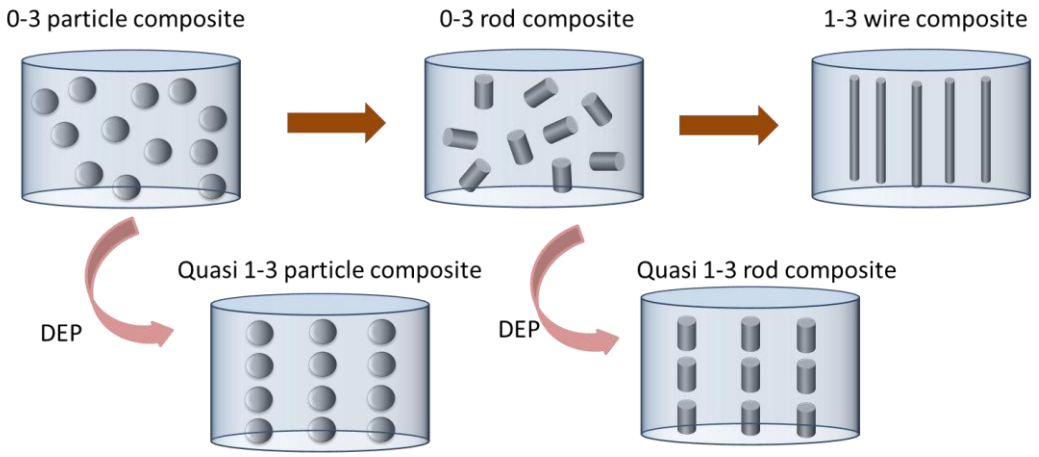

Fig. 4. Représentatif des modèles de connectivité utilisés dans les matériaux développés.

Table 1. Coefficient piézoélectrique (d_{33}) de la mesure expérimentale

	Random d_{33} (pC/N)	**R^2**	**Structured d_{33} (pC/N)**	**R^2**
8% vol. ZnO MRs/PDMS	0.0173 ± 0.0022	0.969	0.1040 ± 0.0079	0.989
2% vol. ZnO MRs/PDMS	0.0073 ± 0.0008	0.973	0.0371 ± 0.0015	0.997
8% vol. ZnO MPs/PDMS	0.0086 ± 0.0020	0.903	0.0399 ± 0.0049	0.970

Cette thèse est accessible à l'adresse : http://theses.insa-lyon.fr/publication/2022LYSEI006/these.pdf
© [X. Zhang], [2022], INSA Lyon, tous droits réservés

General Conclusion

Cette thèse porte sur l'exploration de l'amélioration de la performance piézoélectrique des composites à base de ZnO pour l'application potentielle d'un capteur biomédical implantable. Afin d'obtenir un capteur flexible, minuscule et efficace, adapté aux milieux biologiques à basse fréquence, des axes d'optimisation ont été développées en s'appuyant sur le meilleur réglage des propriétés matérielles des phases individuelles ainsi que sur la conception structurelle.

Tout d'abord, en partant de la structure de base où les particules de ZnO sont incorporées de façon aléatoire dans la matrice polymère (PDMS), les propriétés conductrices, mécaniques et diélectriques ont été étudiées séquentiellement en raison de leurs contributions aux propriétés piézoélectriques. La simulation COMSOL a permis de confirmer que la distribution du champ autour des charges était fortement affectée par deux facteurs, notamment la concentration des charges et la connectivité des particules (c'est-à-dire alignées ou dispersées de manière aléatoire). Des caractéristiques non linéaires densités de courant-champ électrique (J-E) ont été obtenues dans le cadre d'essais de champ élevé en courant continu et variable (sinusoïdal). D'une part, les caractéristiques J-E non linéaires en courant continu ont indiqué que le champ de commutation diminue avec l'augmentation de la concentration de la charge et des particules alignées par diélectrophorèse en raison de la création de courts chemins de conduction au sein de la matrice. D'autre part, sous différents niveaux de champ sinusoïdal, deux mécanismes de conduction différents ont été illustrés et corrélés avec des modèles d'analyse mathématique respectifs. Néanmoins, la conductivité dérivée d'une excitation à faible tension et le coefficient non linéaire extrait d'une tension d'entrée élevée ont montré l'amélioration des propriétés conductrices pour les composites à forte teneur en charge et à structure alignée. Par la suite, une tendance à l'augmentation du module d'Young avec la fraction volumique de ZnO a été vérifiée dans les tests de traction et de compression, conduisant à une estimation du module d'Young de ZnO (~342 GPa) à l'aide du modèle de Nielsen. En particulier, lors des tests de compression, le renforcement le long de l'orientation des particules des composites structurés a permis d'améliorer les propriétés mécaniques. Ensuite, les mesures diélectriques ont révélé qu'une concentration plus élevée de particules augmente la permittivité diélectrique des composites, surtout lorsque les particules sont alignées le long de la direction diélectrophorétique. Cela peut s'expliquer par le fait que les moments dipolaires interfaciaux à l'interface ZnO/ZnO contribuent à une augmentation de la constante diélectrique. Parallèlement, la constante diélectrique du ZnO a été dérivée à la fois de modèles analytiques (~125) et de simulations COMSOL (~ 250 avec $\gamma = 50$). Enfin, le coefficient de charge piézoélectrique (d_{33}) des composites structurés s'est avéré beaucoup plus important que celui des composites dispersés de manière aléatoire, en raison de la forte connectivité ZnO/ZnO. En outre, sur la base des paramètres (module de Young, constante diélectrique) extraits des mesures pertinentes précédentes, le coefficient piézoélectrique du ZnO a été prédit dans un modèle FEM ($d_{33} \approx 0{,}5$ pC·N^{-1}) et des modèles analytiques ($d_{33} \approx 1{,}45$ pC·N^{-1}) via l'ajustement aux données expérimentales.

Deuxièmement, la performance piézoélectrique peut être encore améliorée en ajoutant des charges en de type nanofils avec un facteur de forme plus important que les microparticules sphériques (MPs). Une amélioration significative du comportement piézoélectrique du composite MRs a été obtenue avec succès par l'alignement diélectrophorétique de la charge de ZnO. De plus, il a été confirmé que la constante

Cette thèse est accessible à l'adresse : http://theses.insa-lyon.fr/publication/2022LYSEI006/these.pdf
© [X. Zhang], [2022], INSA Lyon, tous droits réservés

diélectrique des composites MPs et MRs peut être améliorée en augmentant l'amplitude ou en réduisant la fréquence du champ diélectrophorétique. Sous le même champ électrique externe optimisé (E = 0,6 V/μm, 2 Hz), une augmentation de six fois de d_{33} a été obtenue pour le composite MRs aligné par rapport au composite aléatoire, tandis qu'une augmentation de cinq fois dans le cas des homologues MPs, sous la même teneur en charge (8% vol.). En dépit de la structure des charges (alignées ou dispersées de manière aléatoire), les composites avec des charges MRs présentent une réponse piézoélectrique plus élevée (deux fois) que ceux avec des charges sphériques.

Troisièmement, des NFs de ZnO alignés verticalement ont été mis en œuvre afin d'obtenir une structure 1-3 avec un facteur de forme optimal et un alignement complet parfait des charges. En couplant l'effet piézoélectrique et l'introduction électrostatique, une couche isolante a été empilée sur le dessus des NFs de ZnO et le polymère interstitiel entre les NFs. En partant d'un seul NF de ZnO, les calculs FEM analytiques et numériques ont suggéré que le fonctionnement de la structure de NFs alignés sous l'excitation de compression avait une efficacité élevée par rapport au modèle de flexion. Des stratégies d'optimisation ont ensuite été développées en ajustant les paramètres clés tels que les modules de Young et la constante diélectrique des phases constitutives, ainsi que la densité et la dimension des NF. Ainsi, un système multicouche sur un substrat rigide résistif en Si a d'abord été caractérisé dans les expériences pour identifier la fonction de chaque couche ainsi que de l'ensemble de la structure complexe. Le coefficient de charge effectif (d_{33}) du composite fabriqué a atteint 3,4 pC/N avec un PMMA de 1,5 μm d'épaisseur (11% vol.), par opposition à 0,86 pC/N dans le cas de la contrepartie en PMMA de 2 μm d'épaisseur (9,5% vol.), ce qui correspond bien aux résultats de la simulation FEM. Alternativement, un modèle variant dans le temps combinant les modules de piézoélectricité et de circuit électrique a permis d'estimer d_{33} pour les NFs de ZnO (16.5 pC/N). En raison de l'effet de fuite de charge, un substrat flexible en PDMS a remplacé le substrat rigide en Si, ce qui a donné une sensibilité piézoélectrique plus faible ($d_{33} \approx 0.288$ pC·N-1). En conséquence, elle peut être augmentée de près de 4 fois avec des post-dépositions (dopage au Sb et recuit thermique) en raison d'une diminution de la concentration en porteurs dans le ZnO. Du point de vue de l'application, la structure développée s'avère très prometteuse dans la réalisation de transducteur pour la technique FFR.

La contribution de cette thèse est de proposer une nouvelle façon d'augmenter la sensibilité piézoélectrique des composites à base de ZnO avec des considérations spécifiques pour les applications médicales. Les résultats sont prometteurs, montrant le potentiel des composites ZnO NF, avec l'avantage supplémentaire de ne pas nécessiter de polarisation, peuvent atteindre des performances piézoélectriques comparables aux alternatives conventionnelles des PVDF. À l'avenir, plusieurs aspects seront pris en compte, à savoir

- mener une caractérisation plus avancée pour évaluer pleinement la performance piézoélectrique. Par exemple, les paramètres impliqués dans l'excitation mécanique externe (par exemple, la fréquence et la direction) et l'environnement externe, en particulier les milieux biologiques ;
- améliorer la structure flexible selon les stratégies d'optimisation dérivées des simulations FEM, comme un substrat plus fin ;
- supprimer l'effet d'écran du semi-conducteur en diminuant les charges dans les NFs, par exemple en appliquant un polymère de type p ou en formant une jonction Schottky sur la surface du ZnO ;
- le revêtement de deux contacts métalliques à l'extrémité des NFs de ZnO pour maximiser leur effet piézoélectrique, en s'assurant qu'au moins une extrémité des NFs est un contact Schottky.

Cette thèse est accessible à l'adresse : http://theses.insa-lyon.fr/publication/2022LYSEI006/these.pdf
© [X. Zhang], [2022], INSA Lyon, tous droits réservés

Acronyms

%vol.	Volume fraction
1/2/3D	One-/two-/three-dimensional
AC	Alternating current
AFM	Atomic force microscopy
AR	Aspect ratio
$BaTiO_3$	Barium titanate
CBD	Chemical bath deposition
CF	Contact force
DC	Direct current
DEP	Dielectrophoresis
FEM	Finite element method
FESEM	Field emission scanning electron microscopy
FFR	Fractional flow reserve
GaN	Gallium nitrides
HMTA	Hexamethylenetetramine
MP	Microparticle
MR	Microrod
NP	Nanoparticle
NW	Nanowire
$PbTiO_3$	Lead titanate
PDMS	Polydimethylsiloxane
PFA	Pulsed field ablation
PFM	Piezoelectric force microscope
PMMA	Poly (methyl methacrylate)
PVDF	Polyvinylidene fluoride
PZT	Lead zirconate titanate
SEM	Scanning electron microscopy
Si	Silicon
SL	Seed layer

Cette thèse est accessible à l'adresse : http://theses.insa-lyon.fr/publication/2022LYSEI006/these.pdf
© [X. Zhang], [2022], INSA Lyon, tous droits réservés

SSA	Specific surface area
T_C	Curie temperature
WD	Working distance
$Zn(NO_3)_2$	Zinc nitrate hexahydrate
ZnO	Zinc oxide

Cette thèse est accessible à l'adresse : http://theses.insa-lyon.fr/publication/2022LYSEI006/these.pdf
© [X. Zhang], [2022], INSA Lyon, tous droits réservés

General introduction

Composites of Zinc oxide (ZnO) embedded into polymer matrix have drawn enormous attention owning to the combination of the versatile properties of ZnO and attractive merits of polymer matrix, such as flexibility, stability and, processability. ZnO exhibits excellent piezoelectric property with no requirement of high-voltage poling process, arising from its non-centrosymmetric crystalline structure. Moreover, quantum confinement effect in ZnO nanostructure gives rise to size-induced enhancement compared to bulk material. In particular, ZnO is further a biocompatible and non-toxic material, which paves the way for specifically energy harvesting and sensing applications adopted in the biological media, e.g., medical implants, health monitoring, and so on.

The motivation of this thesis is toward a better understand of the multiphysical coupling of ZnO-based composites and thus exploring their optimization strategies for the potential application in biomedical devices. ZnO-based composites afford ameliorated properties, which are more flexible than conventional piezoelectric materials (ceramic, polymer) and can be controlled by the arrangement of the constituent phase. In two-phase composites, those with 1-3 connectivity pattern, defined as continuous fibers aligned in one dimension, usually show better performance than that of 0-3 connectivity pattern, where fillers are randomly dispersed. Therefore, corresponding composites incorporated with ZnO spherical and wire-shaped dopants are experimentally fabricated, characterized, and numerically simulated to confirm their influence on the electromechanical coupling. Because of their simple architecture, easy process and cost effectiveness, ZnO particles/polymer composites are firstly investigated to have a better understanding of their properties in terms of conductivity, dielectric and piezoelectric as a function of filler's size and concentration. It is revealed that the ability of spherical particles to increase the effective dielectric and piezoelectric constant in 0-3 composites is quite limit at low filler content, while the high filler concentration is difficult to achieve due to the agglomeration effect. On the other hand, the 1-3 connectivity composites lead to higher performance, in spite of their complicated fabrication and higher cost compared to the 0-3 counterparts. Accordingly, quasi 1-3 composite, developed by dielectrophoretically aligning particles along the field direction, could lead to enhanced properties at lower particle concentration. Moreover, the material process can be further optimized via the consideration of aspect ratio (AR) factor. Microrod-shaped fillers, instead of particles, are integrated into polymer matrix to yield 0-3 together with dielectrophoretic 1-3 composites. Unfortunately, even with the help of dielectrophoretic techniques, the improvement is still limited due to the non-perfect connectivity of the quasi 1-3 pattern. Hence, a structure based on vertically aligned ZnO nanowire (NW) is designed to achieve a perfect 1-3 connectivity. Optimization architectures are performed with the help of finite element method (FEM) that allows to verify observations obtained through experimental characterizations. In addition, suppression of the semiconductor screening effect is an effective route for creating high piezoelectric response of flexible composites at a lower filler concentration.

In this thesis, there are three different types of ZnO fillers including microparticle (MP), microrod (MR), and nanowire (NW). Among them, ZnO MP and MR composites are elaborated at LGEF lab using a thin film casting method, while those incorporated with the vertically aligned ZnO NW, which are grown on either rigid or flexible substrate by chemical bath deposition (CBD) technique, are provided by LMGP lab. Regarding the evolution process described above, the thesis is split into five related chapters:

In Chapter 1, a background of piezoelectricity is introduced involving the definition and physical explanation of the piezoelectric effect, the derived general equations, and the categorical description about

Cette thèse est accessible à l'adresse : http://theses.insa-lyon.fr/publication/2022LYSEI006/these.pdf
© [X. Zhang], [2022], INSA Lyon, tous droits réservés

the piezoelectric materials. Subsequently, ZnO as an excellent piezoelectric material is proposed with a detail depiction towards the crystal structure, the crystal growth process, and the piezoelectric effect in ZnO nanostructure as well as the introduction of composites. According to the multifunctional characteristics of ZnO, the potential applications of the composites are proposed towards medical applications consisting of pulsed field ablation (PFA) and Fractional flow reserve (FFR) technique.

Chapter 2 presents the fabrication procedures of ZnO-based composites relying on the thin film casting method, CBD technique, and dielectrophoretic manipulation. Detailed descriptions on the experimental setups are given for obtaining a full characterization in terms of dielectric, conductive, piezoelectric and mechanical properties. A simple two-dimensional and three-dimensional model are built using COMSL Multiphysics tool to simulate and estimate the piezoelectric behaviors in ZnO microparticles (MPs) and nanowires (NWs) composite, respectively.

Chapter 3 focuses on the 0-3 and quasi 1-3 composites of ZnO particles embedded in a polydimethylsiloxane (PDMS) matrix. The conductivities with respect to different connectivity patterns inside the composite are characterized by performing the current density vs. electric field (J-E) curve under direct and alternating high voltage applications. Relative parameters such as permittivity, conductivity, and dielectric losses are extracted from the J-E curve through the identification of different component contribution with the help of analytical modeling. Mechanical and dielectric characterizations are carried out to confirm the influence of the filler's concentration as well as the structuration via dielectrophoresis. At last, piezoelectric and dielectric performances are empirically quantified and then being compared to those obtained via the analytical models and the numerical simulation.

Chapter 4 focusses on the optimization of vertically aligned ZnO NWs composites. Analytical calculation and numerical solution-based FEM are primarily performed on an individual NW, i.e., considered as a unit structure under a compressive or blending load. Both approaches suggest that the compressed NW yields higher piezoelectric efficiency as opposed to blended NW. An elementary cell-based ZnO NW arrays composites closed to the real developed structure are built, and its piezoelectric response is analyzed as a function of various parameters under a solicitation of a compressive load. Hence, the optimization guidelines are derived to enhance the piezoelectric sensitivity relying on the best tuning of the material properties as well as the geometric and structural design, such as mechanical and dielectric features of polymer matrix, NW density and dimension, and surrounding environment.

Chapter 5 firstly presents an experimental comparison between the 0-3 and quasi 1-3 composites with a spherical particles and rod-shaped fillers. The NW arrays composites are found to exhibit the optimal piezoelectric sensitivity. Thus, a rigid multi-layer structure based on NW arrays is experimentally tested to further identify the functionality of each individual layer. In accordance with the optimization guideline, a validation of thickness effect of the top insulating layer on the piezoelectric behavior is performed. From the application point of view, flexible NW arrays composites are proposed and further improved via the pretreatment of NWs including thermal annealing and Sb-doping.

Cette thèse est accessible à l'adresse : http://theses.insa-lyon.fr/publication/2022LYSEI006/these.pdf
© [X. Zhang], [2022], INSA Lyon, tous droits réservés

Table of Contents

Cette thèse est accessible à l'adresse : http://theses.insa-lyon.fr/publication/2022LYSEI006/these.pdf
© [X. Zhang], [2022], INSA Lyon, tous droits réservés

Cette thèse est accessible à l'adresse : http://theses.insa-lyon.fr/publication/2022LYSEI006/these.pdf
© [X. Zhang], [2022], INSA Lyon, tous droits réservés

Cette thèse est accessible à l'adresse : http://theses.insa-lyon.fr/publication/2022LYSEI006/these.pdf
© [X. Zhang], [2022], INSA Lyon, tous droits réservés

Cette thèse est accessible à l'adresse : http://theses.insa-lyon.fr/publication/2022LYSEI006/these.pdf
© [X. Zhang], [2022], INSA Lyon, tous droits réservés

Cette thèse est accessible à l'adresse : http://theses.insa-lyon.fr/publication/2022LYSEI006/these.pdf
© [X. Zhang], [2022], INSA Lyon, tous droits réservés

Chapter 1. State of arts

This chapter briefly elaborates the background knowledge of piezoelectricity involving the definition and physical explanations of the piezoelectric effect, together with the corresponding mathematical formulations as well as the categories of these materials. Among them, zinc oxide (ZnO) is especially investigated in detail (including the crystal structure and crystal growth) because of its multifunctional coupling and interesting physical properties. Particularly, the size effect on the piezoelectric coefficient is emphasized in ZnO nanostructure. Next, the piezoelectric composites consisting of two major constituent connectivity patterns are presented, with the aim of boosting the material performances. At last, a literature summary on the application of ZnO composites is carried out and two potential medical applications are proposed in the endocardial pulsed field ablation and fractional flow reserve techniques, respectively.

Cette thèse est accessible à l'adresse : http://theses.insa-lyon.fr/publication/2022LYSEI006/these.pdf
© [X. Zhang], [2022], INSA Lyon, tous droits réservés

1.1 Background on piezoelectricity

1.1.1 Piezoelectric effect

In 1880, Pierre Curie and Jacques Curie discovered that compressing and stretching the quartz can generate macroscopic polarization and hence the electric charges [1]. The Greek word “piezo” donates “to press or squeeze”, and thus “piezoelectricity” with the meaning of “electricity resulting from the press”, was utilized to explain this effect [2]. Until 1921, the first formal application of piezoelectric material was developed when quartz crystal was utilized in the transducer to detect submarines through echolocation. The appearance of piezoelectricity explored a new research field in crystal physics and rapidly created a perspective industry market since the invention of man-made piezoelectricity material. Particularly the discovery of ferroelectricity accelerated the investigation and application of piezoelectric material in modern engineering [3]. In 1969, a high piezoelectric effect in polyvinylidene fluoride polymer was found to satisfy the mechanical flexibility requirement in piezoelectric material [4]. Till now, piezoelectric materials including single crystal, ceramic and polymer have wide applications in medicine, telecommunications, information, and military.

The direct piezoelectric effect refers to the generation of electric charge in response to an applied mechanical stimulation. As seen in Figure 1.1(a)-(c), if an applied compressive stress causes the positive electric voltage, then an applied tension will result in negative electric voltage. Conversed piezoelectric effect is defined as the production of mechanical deformation in the material with response to electric stimulation, schematically shown in Figure 1.1(d)-(f). Applying a voltage on piezoelectric material drives compresive deformation while reversed voltage will cause tension.

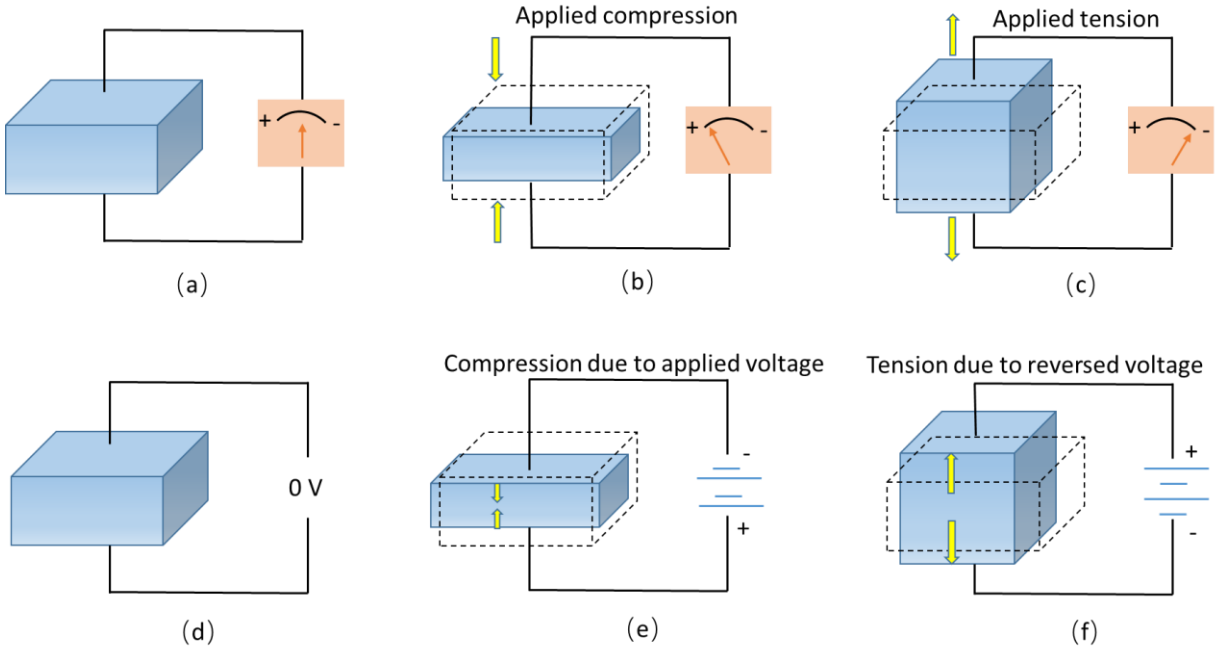

Figure 1.1. Direct piezoelectric effect: (a) at zero stress, (b) at applied compression, (c) at applied tension. Conversed piezoelectric effect: (d) at zero voltage, (e) at applied voltage, (f) at applied reversed voltage.

Cette thèse est accessible à l'adresse : http://theses.insa-lyon.fr/publication/2022LYSEI006/these.pdf
© [X. Zhang], [2022], INSA Lyon, tous droits réservés

Indeed, the principle of piezoelectricity can be illustrated with a simple molecular model displayed in Figure 1.2. Crystals can be classified as centrosymmetric and non-centrosymmetric material. Figure 1.2(a) shows that a centrosymmetric crystal is unable to generate electric polarization under external stimulation. In the original state without any external force, the centers of positive and negative charges coincide leading to an electrical neutral in the primitive unit cell. After applying an external force, the polarization dipole p_i always cancels each other and gives rise to a null total dipole moment due to the existence of the center of symmetry. Thus, there is no net polarization (P) inside the crystal, indicating that the centrosymmetric crystals are nonpolar and non-piezoelectric. On the other hand, similar to centrosymmetric crystal, the unperturbed non-centrosymmetric unit cell possesses electrically neutral state at the beginning (Figure 1.2(b)). When external stress is imposed, because of lacking a center of symmetry the internal structure in a unit cell is deformed, resulting in the separation of the positive and negative centers to produce a dipole moment. Even the neighboring half-dipoles carried with opposite charge signs cancel each other inside the material. But this material is polarized and net charges appear on the surface evoking an electrical field, which elaborates the origin of piezoelectricity [5].

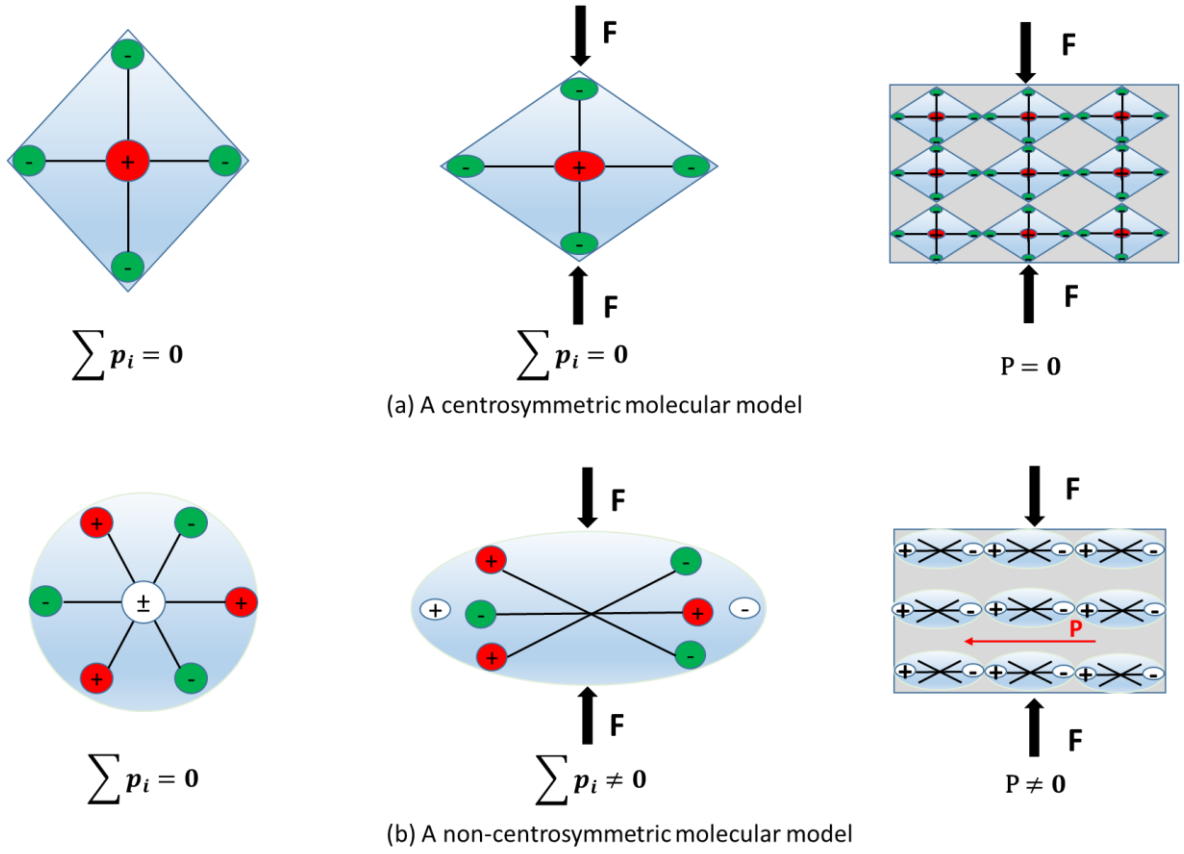

Figure 1.2. (a) A centrosymmetric molecular and (b) a non-centrosymmetric molecular model subjected to an external force [5].

1.1.2 Piezoelectric equations and coefficients

As we know, implement of stress on a piezoelectric material in a given direction will deform the material in the direction parallel and also perpendicular to the stress due to the Poisson effect. Thus, it is

Cette thèse est accessible à l'adresse : http://theses.insa-lyon.fr/publication/2022LYSEI006/these.pdf
© [X. Zhang], [2022], INSA Lyon, tous droits réservés

necessary to define the relative direction in the second-rank tensor of strain. Based on the Institute of Electrical and Electronics Engineers (IEEE) standard for piezoelectricity, an orthogonal coordinated system is applied to identify the axes as shown in Figure 1.3 [6]. In the piezoelectric material, 1 corresponds to x-axis denoting the stretch direction, 2 refers to y-axis representing the transverse direction and 3 corresponds to z-axis denoting the thickness direction. Shear planes 4,5,6 are defined perpendicularly to direction 1,2,3, respectively. Therefore, the electric polarization and mechanical strain generated by the piezoelectric effect can be described in mathematical formulation within three dimensions. While an assumption is proposed that piezoelectric materials are considered having a linear profile at low electric fields and low mechanical stress. If the external electric field or mechanical stimulation reaches a high level, the material will exhibit nonlinear piezoelectric properties. Following the linear theory, the relationship between the generated charge density and the applied stress is known as the direct piezoelectric effect. On the other hand, the relationship between resultant strain and the applied electric field is regarded as a conversed effect. Both phenomena can be expressed as:

$$D_i = d_{ijk} T_{jk} \qquad \text{Direct effect (1.1.1)}$$

$$S_{jk} = d_{ijk} E_i \qquad \text{Conversed effect (1.1.2)}$$

where *D* and *E* are the first-rank tensor of electric displacement and electric field, respectively. The second rank tensor of *T* and *S* represent the mechanical stress and strain respectively. d_{ijk} is the piezoelectric coefficient where tensor notation *i, j, k* refers to 1, 2, 3 directions, respectively.

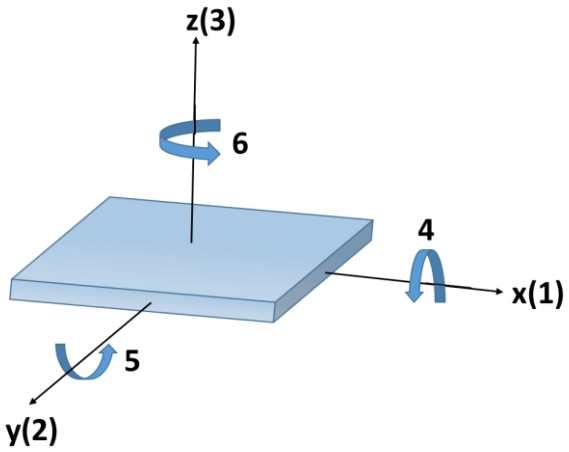

Figure 1.3. Tensor directions to define the constitute equation

To further simplify the equations, symmetry of the crystal material is utilized to compact the second rank tensor (T and S) into a first rank tensor with tensor notation ranging from 1 to 6. In the same way, the piezoelectric coefficient d_{ijk} can be transferred into a second rank tensor d_{ij} where the subscript *i* refers to the applied field direction limited from 1 to 3, and *j* is assigned to the applied stress direction ranging from 1 to 6. For instance, d_{33} denotes the resulting polarization in direction 3 under an applied stress in direction 3. So far, previous discussions are only concentrated on individual piezoelectric effects comprising the dielectric and elastic properties. Considering the electromechanical coupling effect in piezoelectric material, the linear electro-elastic constitutive equations can be derived in the following form:

Cette thèse est accessible à l'adresse : http://theses.insa-lyon.fr/publication/2022LYSEI006/these.pdf
© [X. Zhang], [2022], INSA Lyon, tous droits réservés

$$D_k = d_{kq}T_q + \varepsilon_{kp}^T E_p \quad (1.2.1)$$

$$S_m = s_{mq}^E T_q + d_{mp}E_p \quad (1.2.2)$$

where ε_{kp}^T is the permittivity tensor under constant stress, s_{mq}^E is the elastic compliance tensor under a constant electric field. The total electric displacement in a piezoelectric material is the sum of electric displacement induced in dielectrics and the additional polarization caused by direct piezoelectric effect. Also, the total strain in piezoelectric material is the sum of mechanical strain caused by the applied stress and the additional strain induced by the inverse piezoelectric effect. Similarly, the dielectric constant is a second-rank tensor donated by a 3 ×3 matrix, but it can be reduced to a matrix with 6 independent coefficients due to the symmetric ($\varepsilon_{mq} = \varepsilon_{qm}$). In fact, the piezoelectric coefficient *d* (see Eq. (1.2) is interpreted as induced polarization per unit stress. There are three more piezoelectric constants (*e*, *g*, *h*) derived from different constitutive equations including stress-charge, stress-voltage, strain-voltage forms. With the one-dimensional simplified assumption, the remaining mathematically-equivalent formulations can be written as follows [7]:

$$\mathrm{T} = c^E S - eE \quad \text{Stress-charge} \quad (1.3.1)$$

$$D = eS + \varepsilon^S E \quad (1.3.2)$$

$$S = s^D T + gD \quad \text{Strain-voltage} \quad (1.4.1)$$

$$E = -gT + \frac{D}{\varepsilon^T} \quad (1.4.2)$$

$$T = c^D S + hD \quad \text{Stress-voltage} \quad (1.5.1)$$

$$E = -hS + \frac{D}{\varepsilon^S} \quad (1.5.2)$$

where *c* is the elastic stiffness and D is the electric displacement of material, respectively; superscripts *s*, D means that the coefficients are measured at a constant strain and electric displacement, respectively. The relationship between the piezoelectric constants (*d*, *e*, *g*, *h*) can be derived as [7]:

$$d = \varepsilon^T g = s^E e \quad (1.6.1)$$

$$e = \varepsilon^S h = c^E d \quad (1.6.2)$$

$$g = \frac{d}{\varepsilon^T} = s^D h \quad (1.6.3)$$

$$h = \frac{e}{\varepsilon^S} = c^D g \quad (1.6.4)$$

1.1.3 Piezoelectric material

Before the discussion of the different types of piezoelectric materials, it is necessary to distinguish the relationship between dielectric, piezoelectric. pyroelectric and ferroelectric materials, as indicated in Figure 1.4.

Cette thèse est accessible à l'adresse : http://theses.insa-lyon.fr/publication/2022LYSEI006/these.pdf
© [X. Zhang], [2022], INSA Lyon, tous droits réservés

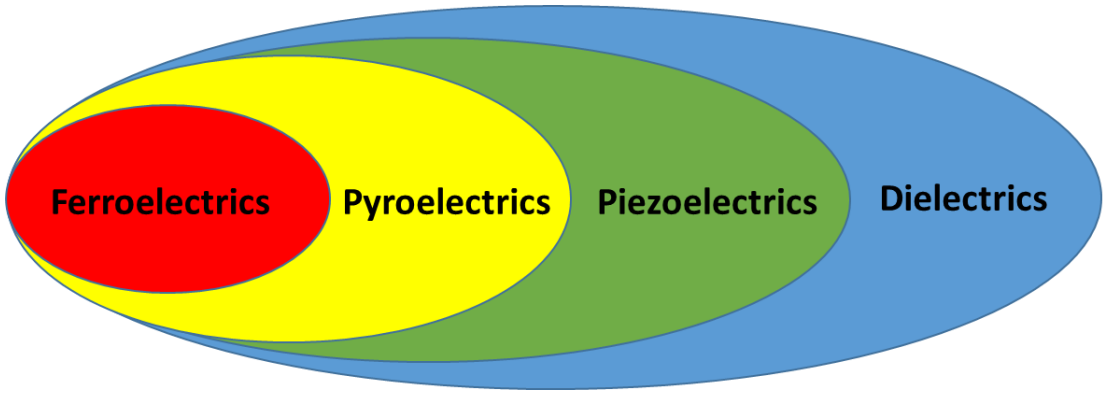

Figure 1.4. Classification of piezoelectricity [8].

A dielectric material is an electrical insulator that can be polarized under an external electric field. Among them, the piezoelectric material is a group of anisotropic dielectrics that exhibit the ability to generate the electric charge due to the application of stress or strain, or conversely the mechanical deformation due to the applied electric field. Pyroelectric materials belong to a subgroup of piezoelectrics, indicating the variation of polarization as a result of the change in temperature [9]. When the temperature changes, the positive and negative charge centers are displaced with respect to another one, changing the polarization inside the crystal. Ferroelectric material is a special case of pyroelectric material. Ferroelectrics have a spontaneous electric polarization which can be reversed by an opposed electric field [10]. Grains in ferroelectric crystals consist of multiple domains with their polarization direction inside. An electric field poling process is necessary to align all dipoles in the same direction, leading to a macroscopic net polarization. In general, piezoelectric material can be classified into 2 classes: natural material, and manmade synthetic materials including single crystals, ceramics, and polymers.

- Nature material

Piezoelectric materials can be natural existing crystals with non-centrosymmetric crystal lattice. Crystal materials like quartz, topaz, sucrose, Rochelle salt, and some organic substance as silk, wood, and so on. Rochelle salt has been widely used for various types of transducers meanwhile it possesses disadvantages such as the vulnerability to liquid and high temperature limitation [11]. The main drawback of the natural piezoelectric material is the low piezoelectric constant.

- Single crystal

In order to overcome the limitation of natural piezoelectric materials and enhance better piezoelectric properties, artificial piezoelectric materials have been developed. The piezoelectric effect occurs in single crystals which have no center of symmetry to exhibit piezoelectric property. There are 32 crystal classes that can be divided into seven categories according to their point groups: cubic, hexagonal, trigonal, tetragonal, orthorhombic, monoclinic and triclinic. Only 20 of the 32 classes have piezoelectric properties. Among them, 10 classes are polar, exhibiting a spontaneous polarization without mechanical excitation, and the remaining 10 classes are no polar which only create polarization after subjecting mechanical stress. Quartz, which is regarded as the typical single crystal, has wide application in transducers, high-frequency filter and frequency controlling oscillators [7]. It possesses excellent advantages like high mechanical

Cette thèse est accessible à l'adresse : http://theses.insa-lyon.fr/publication/2022LYSEI006/these.pdf
© [X. Zhang], [2022], INSA Lyon, tous droits réservés

strength of 2-3 GPa, temperature stability and high-voltage sensitivity, but exhibits low piezoelectric properties and dielectric constant [12].

- Ceramics

A ceramic is an inorganic solid material at room temperature. Indeed, the piezoelectric ceramics mainly belong to ferroelectrics with a polycrystalline structure that composes of mangy irregular small grains. The piezoelectric ceramics are prepared in several steps: fine powders with mixed metal oxides are heated to form a uniform powder. Then the powders are blended with an organic binder to form structural elements and finally sintered to attain a dense crystal structure. Normally the piezoelectric ceramics are binary or ternary mixtures with a perovskite crystal structure. The chemical formula of the perovskite crystal structure is ABO_3, where A is a large metal ion and B is a smaller metal ion. Barium titanate ($BaTiO_3$) was firstly synthetized as piezoelectric material after 1945 [13]. Piezoelectric ceramics such as lead titanate ($PbTiO_3$) and lead zirconate titanate (PZT) exhibit great potential in manufacturing due to higher piezoelectric constant as opposed to quartz. However, most ceramics are brittle, expensive, have a high electric loss, and low stability resulting in limitation in high-frequency systems [14]. Several studies have also reported that lead oxide as a component of PZT is toxic and adverse to the environment [15].

- Polymer

Polymer is large molecule, called macromolecules, composed of multiple chemicals unite [16]. These piezoelectric polymers mainly belong ferroelectric family and exhibit the piezoelectric effect through the attraction and repelling of long chains intertwined under an electric field. The piezoelectricity of polyvinylidene fluoride (PVDF) was firstly discovered by Kawai in 1969 [17]. PVDF is elastic and biocompatible to chemicals, which makes it widely applied in sensor, acoustic ultrasound measurements and biomedical fields [18]. Therefore, piezoelectric polymers attract more and more interest due to their environmentally friendly property and high flexibility, but are restricted by their low dielectric and relatively low piezoelectric charge constant [7,19,20].

1.2 ZnO based composites

Composites are materials that consist of at least two components that, when combined, produce a material with significantly modified physical or chemical properties. Among them, embedding fillers into the polymer is a special method for preparing a new class of composite with enhanced functionality and a wide range of applications in diverse fields [21,22]. Over the last twenty years, increasingly prominent researchers have made efforts to explore and commercialize those multicomponent polymer systems [23–25]. This method combines the unique electric, magnetic, optical, thermal, and piezoelectric properties of inorganic particles at the nanoscale or microscale level with the advantages of the polymer matrix, such as excellent processability, flexibility, and stability [26,27]. The selection of polymer and fillers depends on the purpose. Polymer can be categorized into polar or non-polar, determined by the chain geometry. For nonpolar polymers, under an alternating field, their dipole moments cancel each other which leads to a low polarization. Thus, nonpolar polymers usually have low dielectric constant (less than 3), e.g., polytetrafluoroethylene (PTFE), polyethylene (PE), and polystyrene (PS). By contrast, the dipole moments in polar polymers reinforce each other resulting a high dielectric constant, such as poly (methyl methacrylate) (PMMA), polyvinyl chloride (PVC). Besides the consideration of dielectric constant, the stiffness, viscosity,

Cette thèse est accessible à l'adresse : http://theses.insa-lyon.fr/publication/2022LYSEI006/these.pdf
© [X. Zhang], [2022], INSA Lyon, tous droits réservés

transparency, and curing condition should be carefully balanced for the selection of polymer matrix. Apart from polymers, fillers can be conductive [28], nonconductive [29], and magnetic [30]. Nonconducting fillers act as insulator, while conductive fillers are chosen to increase the effective dielectric constant of composites at low concentrations. Besides, properties of composites can be tailored by fillers shapes, sizes and concentration, which should verify in the experiment.

Piezoelectric ceramics exhibit high piezoelectric response, high thermal stability and low mechanical loss but are suppressed by their brittleness and complex process by sintering at very high temperature [31,32]. Nonetheless, the piezoelectric polymer is more flexible and environmentally friendly, but limited by its low dielectric constant and poor electromechanically coupling [33,34]. Therefore, in order to overcome these drawbacks, piezoelectric fillers incorporated into polymer are developed to form two phase systems, as shown in Figure 1.5. They are ductile, flexible, easy to shape and tailored properties.

In this thesis, Zinc oxide (ZnO) is selected as the filler with different sizes and shapes including nano/microparticle, microrod, and nanowire. ZnO, possessing non-centrosymmetric wurtzite structure, is commonly used in a piezoelectric application by taking advantage of the strong direct piezoelectric effect. Firstly, ZnO is one of the most significant II-VI semiconductor materials with a wide direct band gap of 3.39 eV, high excitation binding energy of about 60 meV at room temperature and high electron mobility [35–37]. By utilizing the coupling of semiconducting and piezoelectric properties, ZnO has achieved substantial applications in optoelectronic, electromechanical, electrochemical, photovoltaic devices, such as light-emitting diodes, solar cells, ultraviolet lasers, and piezoelectric nanogenerator [38–42]. Moreover, concerning the piezoelectric behavior, ZnO does not require high-voltage poling process as compared to PZT [14], $BaTiO_3$ [32], and PVDF films [18]. More importantly, ZnO is also a biocompatible, non-toxic material, which further broadens its applications to the healthcare area, especially in vivo biosensing and bio-detection tools [43,44]. In relation to polymers, for the lab-fabricated composites, polydimethylsiloxane (PDMS) is chosen owning to its stability, good transparency, low cost, and most importantly thermosetting property. Thermosetting effect is the crucial requirement for polymers during the dielectrophoresis technique.

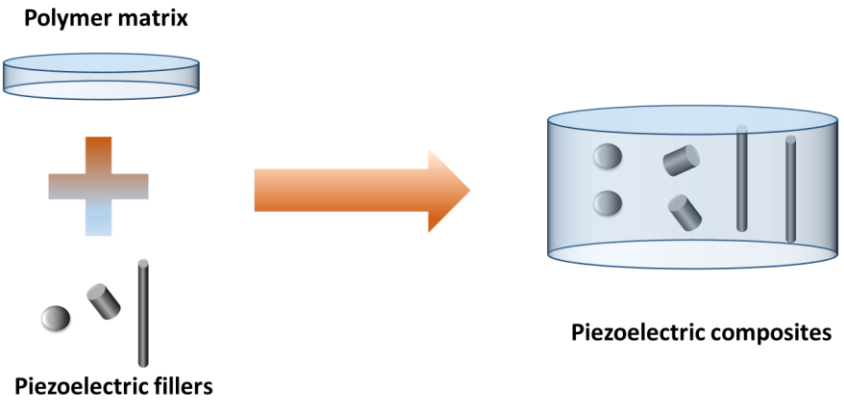

Figure 1.5. Schematic representation of piezoelectric composites.

Cette thèse est accessible à l'adresse : http://theses.insa-lyon.fr/publication/2022LYSEI006/these.pdf
© [X. Zhang], [2022], INSA Lyon, tous droits réservés

1.2.1 ZnO crystal

The ZnO crystal consists of three crystal structures: Wurtzite, Zinc blende and Rocksalt as schematically. Under an ambient environment, the thermodynamically stable phase is hexagonal Wurtzite structure, which is a non-centrosymmetric crystal [45]. As shown in Figure 1.6 (a), ZnO wurtzite structure has a hexagonal unite cell with lattice parameter *a* (~ 0.33 mm) in the basal plane and axial lattice parameter *c* (0.52 mm) perpendicularly to the basal plane [46]. In the wurtzite structure, four tetrahedrally coordinated Zn cations or oxygen anions spaced by parameter *a* form a basal plane to stack alternatively along the *c*-side direction. There are three types of fast growth directions structurally: ± [0001], ‹2 $\bar{1}$ $\bar{1}$ 0›, and ‹0 1 $\bar{1}$ 0›, resulting a range of structures along those directions with corresponding facets. The ZnO grown along c-axis with direction [0001] is the most common case. In that case, the surface plane is terminated entirely with positively charged Zn polar plane (0001), or negatively charged oxygen polar plane (000$\bar{1}$), resulting the formation of polar surface on the basal plane. The distribution of surface charges reduces the electrostatic energy of crystal and then influences the growing nanostructure with the domination of polar surfaces [47].

In spite of the growth direction, the basic unit is a tetrahedral unit formed by four oxygen anions and one Zn cation, as shown in Figure 1.6 (b). The negative charge center of the four oxygen anions locates at the equidistance with the positive Zn cation to precisely cancel each other, thereby resulting in an electrically neutral unite cell and zero net charge in crystal. As shown in Figure 1.6 (c), when a physical compressive force is applied to the unite cell, the distortion of the tetrahedral unite causes the displacement of the positive charge center from the negative charge center, which produces an electric dipole. Thus, a correspondingly macroscopic dipole generates and the overall crystal displays electric polarization inside. In that case, the mechanical energy is converted into electrical energy through the charge carriers, which exhibits excellent piezoelectric ability. Indeed, there is a difference in electronegativity of Zinc and oxygen atoms, giving rise to a shift of electron cloud to exhibit a nonzero charge in the repeated unit cell in their steady state. In addition, according to the classification of Tasker [48], the positively charged Zn poplar and negatively charged O polar surfaces along the c-axis belong to Type III [49]. In that case, a normal dipole moment is generated with spontaneous polarization field along the c-axis.

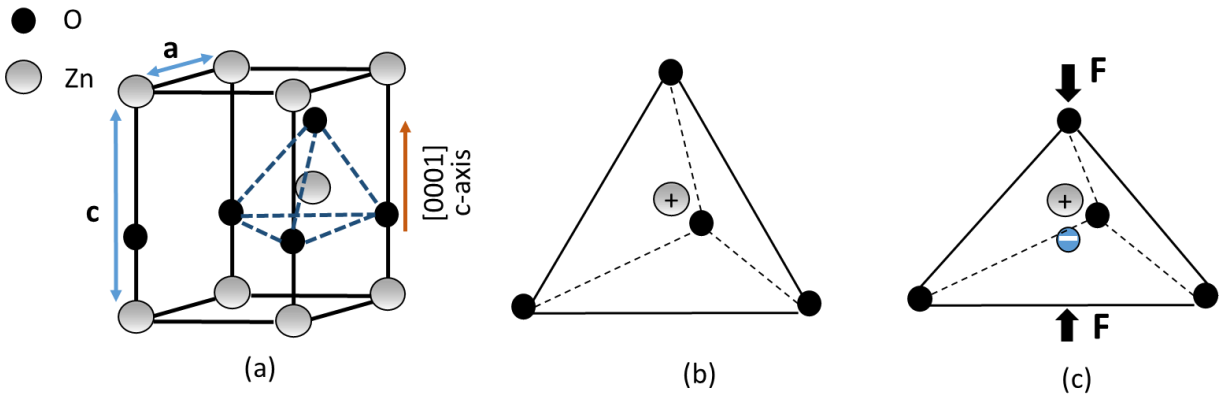

Figure 1.6. (a) Wurtzite structure model of ZnO where shaded gray and black spheres represent zinc and oxygen atoms, respectively. (b)Tetrahedral coordination between Zn and O in Wurtzite structure without external force, (c) the distortion of tetrahedral unit under an external compressive force [36].

Cette thèse est accessible à l'adresse : http://theses.insa-lyon.fr/publication/2022LYSEI006/these.pdf
© [X. Zhang], [2022], INSA Lyon, tous droits réservés

1.2.2 Piezoelectricity in ZnO nanostructure

In the last few decades, thanks to the development of nanotechnology synthesis, diverse and abundant configurations of ZnO nanostructures can be provided, such as nanoparticles, nanowires, nanobelts, nanorings, nanobows, and so forth. The definition of nanotechnology specifies the materials that have as least one dimension smaller than 100 nm and unique properties enabling novel applications [50]. With the material dimension decreasing to the nanoscale, mechanical, electromechanical, electrical and optical characterizations become quite different from those of bulk material due to the surface and quantum confinement effects [51]. Moreover, nanostructures provide the possibility of miniaturization capabilities, especially in an implantable biomedical nanodevice.

Among them, one-dimensionally (1D) nanostructures with high aspect ratio like nanowire, nanotube, nanofibers attract great attentions among the scientific communities with considerable superiorities. It has been reported that the diameter dependence of electrical and mechanical characteristics appeared in 1D nanowires (NWs) [52,53]. Chen *et al.* have revealed that Young's modulus in [0001] oriented ZnO NWs with diameter smaller than 120 nm (Figure 1.7a) dramatically increases with the decreasing diameter. This is attributed to the pronounced contribution of surface elasticity occurring at large surface-to-volume ratio structure, and tends to the value of bulk ZnO (140 GPa) with large diameter (>120 nm) [54]. The fracture strain of the ZnO NWs was found to increase from 5% to 15% when the diameter decreased from 475 to 225 nm [55].

Concerning the size dependence of the piezoelectric coefficient, theoretical computation method has been applied to estimate the variation tendency. Agrawal *et al*. have demonstrated that regarding the first principle-based density functional theory calculations, a giant piezoelectric size effect was identified for both ZnO and gallium nitrides (GaN) NWs due to the local polarization and surface relaxation induced volume reduction [56]. The piezoelectric coefficients of ZnO and GaN NWs decrease with respect to an increase in the diameter and coverage to bulk values with diameter larger than 1.5 nm and 2.5 nm (Figure 1.7b), respectively [56]. For the ferroelectric PZT nanowires, the reduction in size improves the dielectric constant, ascribed to the lowing of Curie temperature (T_C), and piezoelectric coefficient, assigned to the enhancement in dielectric constant and the decrease in lateral interaction [57]. While for the $BaTiO_3$ NWs, the piezoelectric coefficient increases and approaches the bulk value when the diameter is larger than 2.4 nm (Figure 1.7c) [58]. In addition, the aspect ratio of NW in terms of radius and length plays an important role in the piezoelectric properties. According to the FEM simulation of a deflected ZnO NW, the output voltage with a constant diameter of 50 nm (Figure 1.7d) increases as the aspect ratio increase and start to decrease above an aspect ratio of 80 resulting from excessive deflection [59]. Therefore, the size-dependences of piezoelectricity are not the same in different 1D nanomaterials.

It was thus believed that the ZnO NWs should have larger piezoelectric constants as opposed to the bulk ZnO. However, at such a nanoscale, experimental studies on the piezoelectric size effect of 1D nanostructure are supposed to be challenging. Those difficulties involve complicate manipulation at the nanoscale, high sensitivity requirement for measuring the generated voltage and current, simultaneously. Wang *et al.* firstly reported the experimental measurement of piezoelectric generation from bent ZnO NWs via atomic force microscopy (AFM) technique [60,61]. On the other hand, piezoelectric force microscope (PFM) has become a standard method to probe the piezoelectric effect at the nanoscale, which measures the sample's displacement by applying an electric field on the order of picometer [62]. A summary of the

Cette thèse est accessible à l'adresse : http://theses.insa-lyon.fr/publication/2022LYSEI006/these.pdf
© [X. Zhang], [2022], INSA Lyon, tous droits réservés

published piezoelectric strain coefficient (d_{33}) of typical 1D nanostructures has been provided in Table 1.1, with different diameters. The values of d_{33} of ZnO nanostructures are found to be lower than the bulk value, which might be due to the combination of the structural and compositional defects or impurity encapsulated in the nanorods [63].

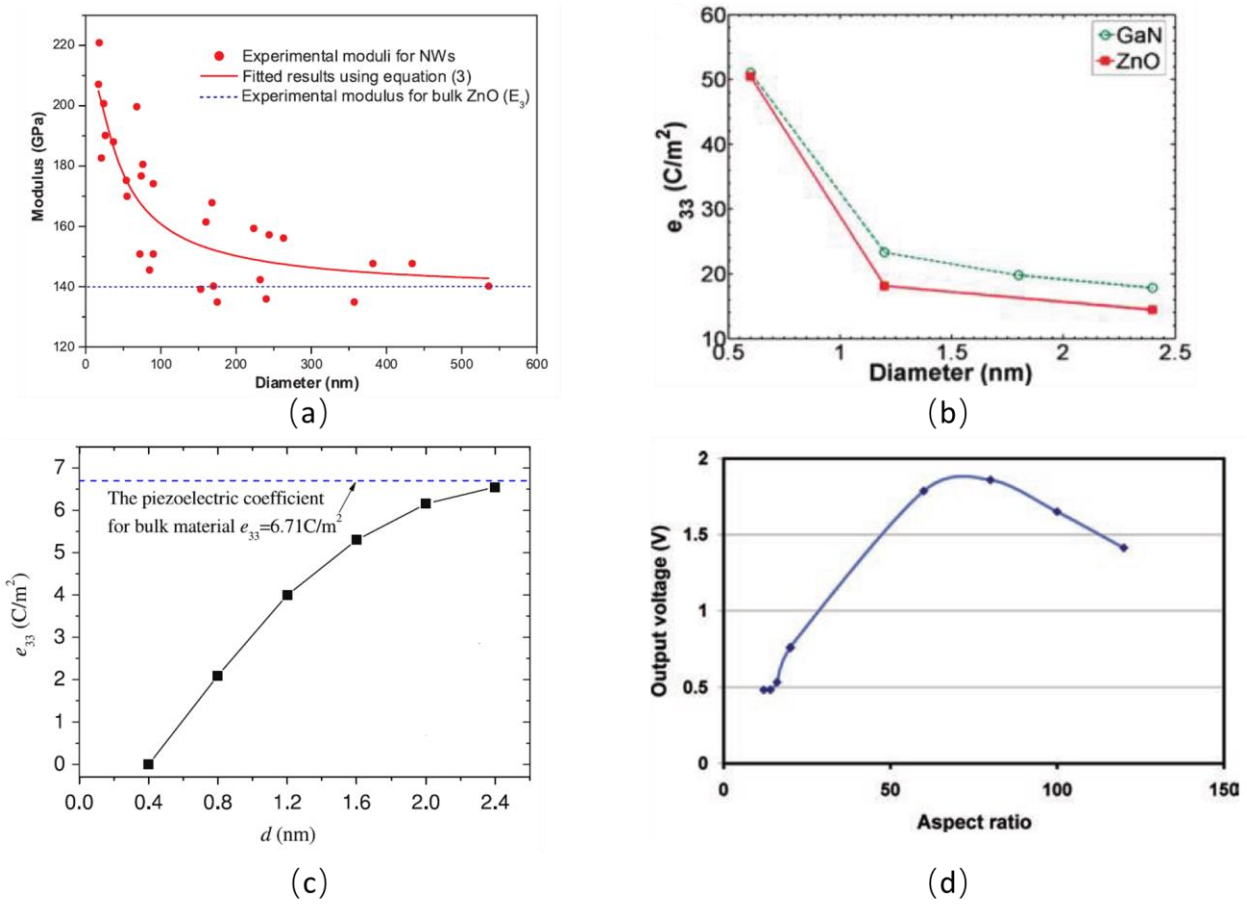

Figure 1.7. (a) Diameter dependence of effective Young's modulus in bended ZNO nanowires) [54]; (b) Piezoelectric coefficient of ZnO and GaN nanowires as a function of the diameter [56]; (c) The size dependent piezoelectric coefficient of $BaTiO_3$ [58]; (d) Output voltage as a function of aspect ratio of ZnO NWs controlled at a constant diameter of 50 nm [59].

Table 1.1. A summary of the piezoelectric properties of ZnO with different structures

Material	Diameter	d_{33} (pm/V)	Reference
ZnO film	Bulk	12.4	[64]
ZnO nanorod	150-500 nm	0.4-9.5	[63]
ZnO nanobelt	65 nm in thickness 360 nm in width	14.3-26.7	[62]
ZnO pillars	~300 nm	7.5±0.6	[65]
GaN nanowire	64-191 nm	~12.8	[66]

Cette thèse est accessible à l'adresse : http://theses.insa-lyon.fr/publication/2022LYSEI006/these.pdf
© [X. Zhang], [2022], INSA Lyon, tous droits réservés

$BaTiO_3$ nanowire	~280	~45	[67]
PZT fiber	10-50 µm	~127	[68]
PVDF nanowire	5-10 nm	10-20	[69]

1.2.3 NW growth process

With increasing developmental researches on nanostructures, ZnO nanowires have been synthesized by a wide range of techniques, such as vapor-solid growth process [70], wet chemical methods [71,72], pulsed laser deposition [73], electrospinning [74], and so on. Among them, the vapor-solid growth approach is simple, effective, fewer defects, but requires high temperature. Pulsed laser deposition gives out poor uniformity distribution of NW with low reproducibility whereas the electrospinning method is limited to polycrystalline fibers. Alternatively, nanowire grown by chemical process exhibit promising advantages such as low cost, relatively low temperature required, independence of the substrate and easily tailored by parameters.

Zinc nitrate hexahydrate ($Zn(NO_3)_2$) and hexamethylenetetramine (HMTA) components are mostly used for the hydrothermal synthesis of ZnO NWs [75,76], where Zinc nitrate hexahydrate salt provides Zn^{2+} ions and HMTA molecules supply OH- ions. The growth process of ZnO nanowires can be controlled by five chemical reactions as follows:

$$HMTA + 6H_2O \leftrightarrow 4NH_3 + 6HCHO \quad (1.7.1)$$

$$NH_3 + H_2O \leftrightarrow NH_4^+ + H_2O^+ \quad (1.7.2)$$

$$Zn^{2+} + 4NH_4 \leftrightarrow [Zn(NH_3)_4]^{2+} \quad (1.7.3)$$

$$Zn^{2+} + 2OH^- \leftrightarrow Zn(OH)_2 \quad (1.7.4)$$

$$Zn(OH)_2 \leftrightarrow ZnO + H_2O \quad (1.7.4)$$

The essential formation process for ZnO NW growth can be simply described as follows [37]. When a ZnO seed is prepared with an initial grown direction such as [0001] in the solution, a monolayer of precursor molecule compound is attracted on the polar surface of the seed layer to reduce the surface energy. Hence, an opposed polar surface is formed based on the above reactions and stacked on the original polar surface. Repeated chemical reactions process is continued to establish a number of alternating polar surfaces along the c-axis until a desired length is obtained. Finally, a wurtzite structured ZnO NW is terminated with a positively or negatively charged top surface and non-polar $(1\bar{1}00)$ side facets. In fact, the electromechanical properties of 1D nanostructure are correlated with their crystal structures and growth direction [77]. Three piezoelectric coefficients (e_{15}, e_{31} and e_{33}) were found to be in the ZnO nanostructures, emphasizing the importance of the crystalline phase [78].

1.2.4 Connectivity pattern of composites

Newnham *et al.* [79] demonstrated that in a multiphase composite system, electromechanical coupling and piezoelectric properties can be controlled by the arrangement of the constituent phase with various connectivity patterns. In the two-phase system, if each phase can be self-connected into zero, one, two and

Cette thèse est accessible à l'adresse : http://theses.insa-lyon.fr/publication/2022LYSEI006/these.pdf
© [X. Zhang], [2022], INSA Lyon, tous droits réservés

three dimensions, there are ten different connectives: 0-0, 1-0, 2-0, 3-0, 1-1, 2-1, 3-1, 2-2, 3-2 and 3-3 where the first and second number refers to the connectivity pattern of filler and polymer, respectively. In Figure 1.8, cubic is utilized as the basic building block and the white color represents the filler phase. In a basic 0-0 connectivity pattern, two phases have a zero-dimensional connection, which is impossible to achieve in particulate composites. While 0-3 connectivity pattern, regarded as the simplest type, has unshaded phase self-connected in zero-direction and shaded phase self-connected in three-dimensional directions, indicating the unconnected particles randomly dispersed in a fully connected matrix. In composite with 1-3 connectivity phase, the filler is one-dimensionally connected and the matrix has three-dimensional connectivity, meaning that fiber or rod with continuous phase is aligned in the polymer matrix.

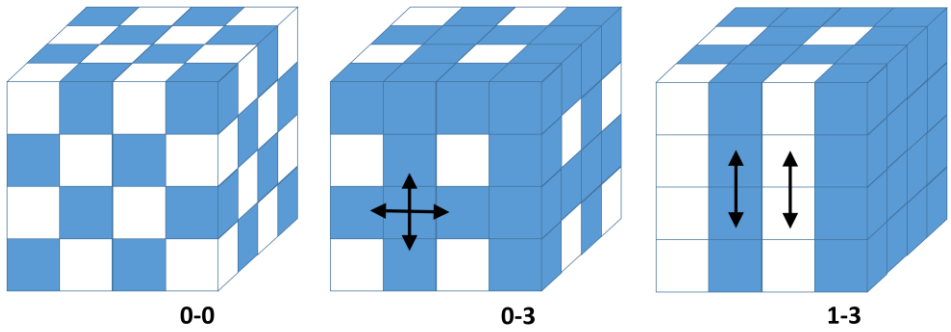

Figure 1.8. Representation of connectivity patterns for two-phase composites, where arrows indicate the connection directions [79].

The latter two connectivity patterns are the most commonly used. 0-3 composites (Figure 1.9a) have the advantages of simple fabrication, low production cost, high mechanical stability, and flexibility [79,80]. Nonetheless, below the percolation threshold, fillers cannot form a long-range continuous connected path in random systems to achieve higher connectivity. In fact, it was also mentioned that the charge coefficient (d_{33}) and the dielectric constant of the piezoelectric composites were strongly dependent on the connectivity [81–83]. For the piezoceramic composites, one major reason is that the high electric conductivity shortens the function time of the electric field applied to the ceramic fillers to cause a high poling efficiency [8]. For the piezoelectric ZnO particles without poling process, the interparticle distance and the interfacial polarization impacted by the connection pattern play a critical role in the property's improvement. Therefore, in order to pursue a great performance, the easiest way is to increase the volume fraction of filler to attain high connectivity in 0-3 composites. At low concentration, a large discrepancy in the dielectric properties of the two phases, including resistivity and permittivity, causes the unbalanced electric field distribution. In other words, electric charge is exerted more on the polymer than on the particles, resulting in low piezoelectric properties [84,85]. In a study reported by Yamada *et al.*[86], the ceramic phase was randomly dispersed within a polymer matrix, generally referred to as 0-3 composites, and exhibited only promising piezoelectric properties at very high filler content, i.e., around 67% volume fraction. However, large volumetric contents considerably deteriorate the mechanical properties and encounter the agglomeration problem during the fabrication process. A solution to this problem is to align the rod or fiber filler instead of particles in one direction within the matrix, defined as the 1-3 connectivity composites (Figure 1.9c). Those samples, allowing to boost the electromechanical coupling for a moderate concentration, seem to be an appropriate solution, despite its complicated fabrication and higher cost compared to the 0-3 composites [87,88]. Dielectrophoretic activity can be therefore widely employed to create an intermediate state between

Cette thèse est accessible à l'adresse : http://theses.insa-lyon.fr/publication/2022LYSEI006/these.pdf
© [X. Zhang], [2022], INSA Lyon, tous droits réservés

a 0-3 and 1-3 connectivity pattern by orienting particles [89–91], nanotubes [92,93], and micron rod [94] to form chain-like structure (Figure 1.9b) through an application of an AC electric field. It was demonstrated in [95] that significant enhancement in the dielectric and piezoelectric behavior has been achieved through dielectrophoretic manipulation of ZnO particles, as opposed to the 0-3 matrix.

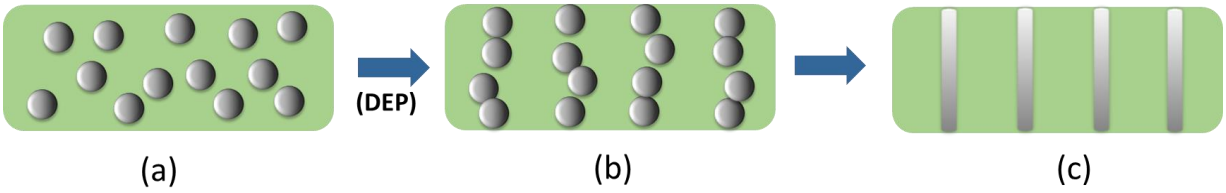

Figure 1.9. (a) Particles randomly in a polymer; (b) Particle chains in a polymer through dielectrophoresis (DEP); (c) Rods in a polymer.

1.3 Potential applications

1.3.1 Applications based electrical properties

1.3.1.1 ZnO varistor

Concerning the semiconducting and conducting mechanism, polycrystalline ZnO mixed with multiple metal oxides are sintered at high temperature to form conventional ZnO varistor. The ZnO varistor is a "diode-like" electronic component which exhibits nonlinear current-voltage characteristic above the switch field [96]. The root reason comes from the existence of the boundaries between ZnO grains. Those boundaries of nanometer thickness containing the lattice mismatch, defects and dopants form potential barriers with Schottky junctions [97]. When a small voltage is applied, electric charges are accumulated on the boundaries and only a small reverse leakage current goes through the junctions. Once the imposed voltage exceeds the switching field, the assembled charges avalanche to drive a large current. Usually, the ZnO varistor is used to conduct the high current to protect electric circuits or electronic components against overvoltage damage, e.g., surge protection devices and surge arresters [96]. The typical current-voltage curve of ZnO varistor can be classified into three regions, as seen in Figure 1.10 [98–100]:

1) Low current linear region (region I), which is below the switching field. The grain boundaries cause high resistance, thus the ohmic property is prominent compared to the nonohmic.
2) Intermediate nonlinear region (region II), between the switching voltage and the voltage at the current of about 100-1000 A cm^{-2}. The current drastically increases with the voltage, which can be described by the empirical equation:
$$I = kV^{\alpha} \tag{1.8}$$
where k is a constant, and α is the nonlinear parameter relating to the nonlinearly resistive changes.
3) High current linear region (region III), where the nonohmic property decays and the resistance of varistor drops to a low value. Thus, it returns to be ohmic property. The I-V characteristics in this region are usually measured with an impulse voltage, preventing heat generation and thermal breakdown.

Microvaristor is made of composite-based polymer matrix filled with semi-conductor (e.g. ZnO) powder. Such a device is widely used to minimize the localized field enhancement which could trigger

Cette thèse est accessible à l'adresse : http://theses.insa-lyon.fr/publication/2022LYSEI006/these.pdf
© [X. Zhang], [2022], INSA Lyon, tous droits réservés

corona and partial discharges in high voltage equipment. These beneficial properties give microvaristor compounds great potential to vary and adapt electrical characteristics. For conventional varistors, a high sintering temperature (around 1000 °C) is required to form stereotyped pattern. Contrarily, ZnO based microvaristor composites only need a curing temperature of around 100 °C and enable to be built on flexible substrates. Therefore, ZnO microvaristors are widely employed in high voltage application such as stator coils, polymer insulators, electric-field grading of bushing, cable accessories [101–104]. Recently, the electric nonlinear field-dependent conductivity has been characterized in ZnO-epoxy, ZnO-Linear low density PE, ZnO-Low density PE when the filler concentration is above the percolation threshold [105–107].

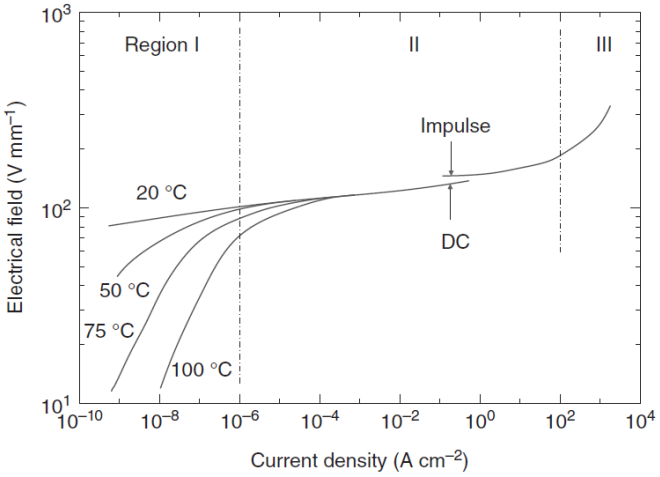

Figure 1.10. Current density-electric field curve of a ZnO varistor [100]

1.3.1.2 Pulsed field ablation technique

Catheter ablation is a technique employed to treat cardiac arrhythmias that result from abnormal or early activation of the myocardium through electrical triggers or aberrant conduction patterns in the myocardium [108]. Some of the technologies developed over the past three decades for cardiac ablation include radiofrequency microwave, high intensity focused ultrasound, lasers and cryogenics. These technologies, however, are often inadequate in eliminating lesion gaps which can lead to the recurrence of the arrhythmia and further complicate treatment strategy. Among these, endocardial pulsed field ablation (PFA) is particularly attractive as its non-thermal ablative mechanism is highly beneficial to myocardial tissue. This technique creates an instantaneous electrical field to open tiny doors (nano-pores) in nearby cells, a process called “electroporation”. PFA has the potential to completely avoid the collateral injury attendant with all other contemporary thermal energy sources. As reported in the review of F. D. Ramirez *et al.*, cardiomyocytes (heart tissues) have a particularly lower irreversible threshold of electroporation (~ 0.4 V/μm) than the other types of cellular like liver (~ 0.6 V/μm), kidney (~ 0.7 V/μm), vascular smooth muscle cells (~ 1750 V/μm), nervous system (~ 3800 V/μm) [109]. This makes PFA become selective, which can affect cardiomyocytes but not damage other surrounding non-heart tissue like nerve fibers or esophagus. Furthermore, unlike the standard ablation energy sources, the PFA catheter does not require actual physical contact but only needs proximity to the tissue to be ablated. As a result, it doesn’t cause scarring or char formation to the patients. In practical terms, this means that PFA is much safer than other current techniques.

Cette thèse est accessible à l'adresse : http://theses.insa-lyon.fr/publication/2022LYSEI006/these.pdf
© [X. Zhang], [2022], INSA Lyon, tous droits réservés

The company Farapulse has developed a specific catheter for this procedure, and obtained CE marking since October 2020 [110]. The developed device could generate sufficient electric field in seconds or minutes compared with hours for radiofrequency. The Farapulse generator, which creates the waveform, can be programmed to perform therapy through different catheters. This makes PFA not only very fast but very precise as well. Interestingly, the first functional device of Farapulse paves the way for numerous optimizations in order to enhance the development of such a new method. Also, multifunctional materials are an axis of innovation concerning the development of PFA devices. When designing smart catheter based PFE, several issues would be considered, such as 1) the bending angles achievable by the structure; 2) possibility of changing shape from 2D to 3D structure; 3) the degree of rotation needs to be reached and the capacity for miniaturization of the design; and 4) safety of the patients in case of electrical breakdown.

The objective of this section reports on the potential of ZnO composite for the development of a smart catheter used in PFA. The principal scheme of the proposed device is illustrated in Figure 1.11, where multiple electrodes are deposited above the composite surface. Such a design enables to deliver a series of ultra-short electrical pulses to ablate heart tissue. The overriding constraints of the fabricated materials were related to the following points: 1) Mechanical flexibility and biocompatibility; 2) electric protection for patients; 3) controlling electric field level; and 4) contact force sensing.

Concerning the first point, it has been demonstrated that PDMS and ZnO are biocompatible properties [111–113], and have the Young modulus and mechanical stiffness compatible with the specification of PFA [114–116]. Moreover, the mechanical properties of the fabricated composites can be somewhat adapted by varying the particle concentration. The second point is dedicated to patient safety where electric discharge within heart tissue must be avoided in case of dielectric breakdown of the composite. Indeed, ZnO powder whose electrical conductivity is voltage-dependent can be successfully exploited as a microvaristor. This effect is widely used to minimize the localized field enhancement which could trigger corona and partial discharges in high voltage equipment during the PFA procedure [109]. As seen in Figure 1.11, under a low electric field, the ZnO particles-based composites behave like dielectric with a high resistive region, adjacent to the heart tissue where an electric field is imposed to perform a normal ablation treatment. Once the imposed electric field is excessive to the heart tissue, ZnO composites act as a variable conductor to draw a large current through it, resulting in little electric field in adjacent tissue.

The third issue aims to point out that the electric field subjected to the treated tissue can be simply controlled by varying some relevant parameters. It should be confirmed that the microvaristor performance depends on various factors of the composites like particle concentration, percolation threshold, electric and dielectric properties. External condition like temperature, frequency and amplitude of voltage excitation has an important effect as well. Optimization of the material process through dielectrophoresis is thus of high benefit, which could lead to a similar performance by using lower particle concentration and voltage stimulation. Last but not least, the aim is to develop a smart PFA with multifunctionalities including not only electroporation effect but also sensing ability. One of the key points here involves performing the contact force (CF) between the ablation electrode and the atrial wall that is a major determinant of lesion size and durability [117]. On one hand, insufficient CF can result in inadequate lesion formation and higher rates of pulmonary vein reconnection [118]. On the other hand, excessive CF leads to complications, such as perforation of tissue. Consequently, monitoring CF would be expected to maximize ablation efficacy and improve safety. Until recent years, CF has been monitored indirectly using a combination of visual

Cette thèse est accessible à l'adresse : http://theses.insa-lyon.fr/publication/2022LYSEI006/these.pdf
© [X. Zhang], [2022], INSA Lyon, tous droits réservés

observation of catheter tip motion, tactile feedback, local electrogram attenuation, impedance monitoring, and in some laboratories, intracardiac echocardiography. Although widely used, these methods are a poor surrogate for a real-time recording CF. The previous works suggested that ZnO, due to its natural polarity, exhibited piezoelectric effect without requiring polarization process [95]. This makes ZnO as an adequate candidate for force sensor application. Even the piezoelectric sensitivity of ZnO is poor compared to the conventional materials (PZT, $BaTiO_3$, PVDF), a simple indicator representing the CF state (e.g. low, medium, high) would be a help to surgeons.

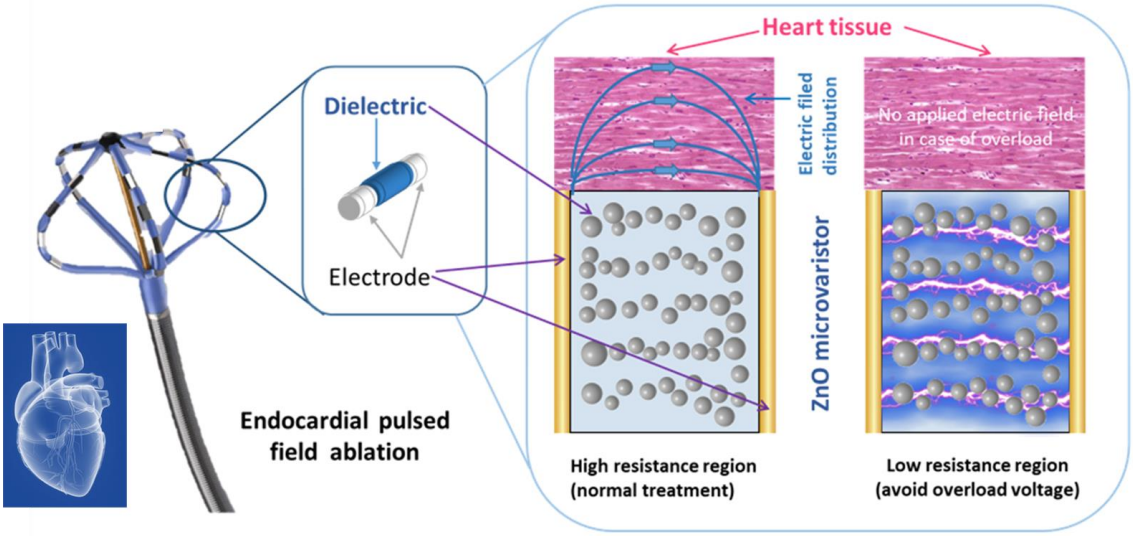

Figure 1.11. Principle scheme of catheter integrated with random or aligned ZnO/PDMS composite

1.3.2 Application based piezoelectric properties

Concerning the piezoelectric property, ZnO based composites have been explored in versatile applications. In fact, output electric signals converted from the mechanical input can be used in two ways. One is harvesting mechanical energy and storing the output electric energy as power supplies. Another is working as sensors which probe the magnitude and frequency of mechanical deformation based on the corresponding in-time electric signals.

1.3.2.1 Energy harvesting

Indeed, ambient energy such as solar, thermal and mechanical energies are wasted in our daily life. In order to reduce the energy burden and consumption from fuels and coal, it is necessary to harvest and scavenge green energy from the natural environment. Among them, mechanical energy is abundant and common in the environment. For instance, vibration from machine, air flow, body motion, etc., can be harvested by piezoelectric materials via the direct piezoelectric effect. Particularly, ZnO nanostructure-based structures certainly become promising options due to the high harvesting efficiency with respond to the small scale vibration [119][120]. Compared to the cantilever-based microelectromechanical systems which only work at several high resonance frequencies decided by the length of the cantilever, ZnO NWs-based devices can harvest mechanical vibration with a wide frequency range. Li and his co-workers have reported a micro-energy harvester integrated crystalline ZnO NWs that yield 22 mW/cm^3 volume-normalized power output with an acceleration of 1.4 g at 40 Hz [120].

Cette thèse est accessible à l'adresse : http://theses.insa-lyon.fr/publication/2022LYSEI006/these.pdf
© [X. Zhang], [2022], INSA Lyon, tous droits réservés

Moreover, their energy harvesting ability facilitates the revolutionary development of power supplies. Hence, the piezoelectric nanogenerator is developed to meet the low energy requirement in nanosystems or nanodevices [59,121,122]. Wang *et al.* have firstly estimated that nanoscale mechanical energy can be converted into electric energy via deflecting ZnO NWs with a conductive AFM tip (Figure 1.12a) [60]. In that case, a nanogenerator composing ZnO NW arrays of size 10 µm × 10 µm can drive a single NW/nanotube-based device with an efficiency up to 30% [60]. Yang *et al*. have also involved the development of flexible laterally integrated nanogenerators based on cyclic stretching-releasing movement where both ends are fixed (Figure 1.12b) [123]. Excellent energy harvesting properties have been found in the vertically integrated nanogenerators (VING) (Figure 1.12c) where one end is attached to substrate and the other is free to move [124]. Hu *et al*. have demonstrated the potential application of nanogenerator in energy harvesting from the motion of automobile tires (Figure 1.12d) [125]. Compared to conventional power supplies, those new generations can offer sustainable and long-term support without contaminating the environment once used up.

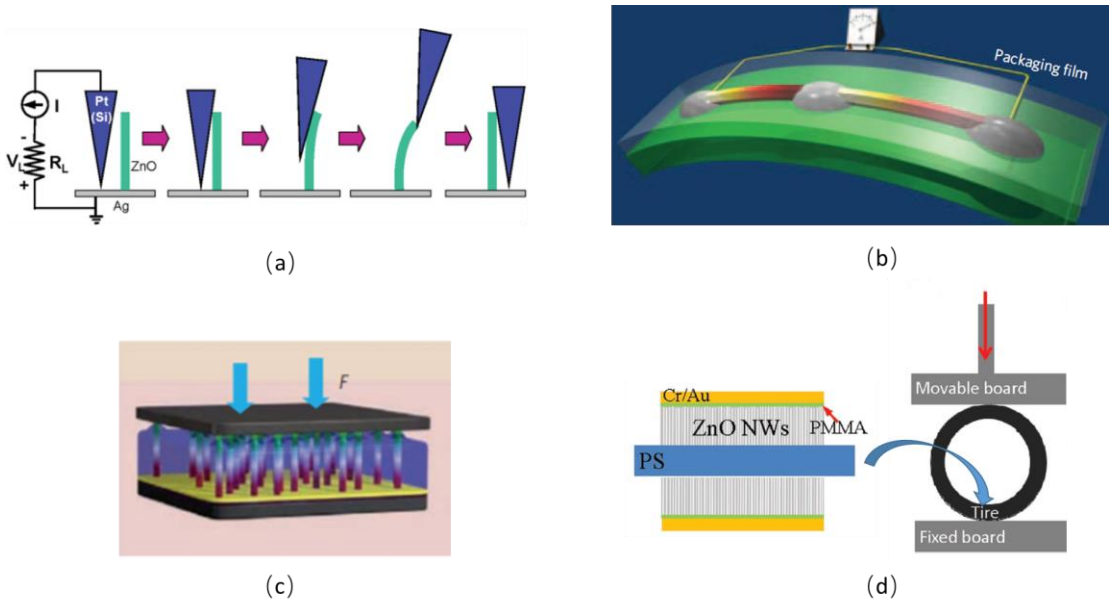

Figure 1.12. (a) Generating electricity by deforming a piezoelectric NW with a conductive AFM tip [60]; (b) A flexible power generator based on cyclic stretching-releasing of a piezoelectric fine wire create an oscillating output voltage up to ~ 50 mV [123]; (c) A three-layer integration of the vertical nanowire array integrated nanogenerator enhance the output voltage up to 0.243 V [124]; (d) Nanogenerators with a structure of a cantilever with five layers was integrated onto a tire's inner surface harvest energy from the motion of automobile [125].

1.3.2.2 Pressure sensor in biomedical field

Our target application for the developed sensing device is related to Fractional flow reserve (FFR) technique to evaluate the significance of artery narrowing, particularly in coronary stenoses. For a cardiac patient, a stenosis in the arteries blocks the amount of blood flowing through the blood vessels of heart. It probably causes the discomfort of the heart and breath, even a heart attack. Additionally, precise detection of the artery narrowing can help to determine the disease severity with corresponding treatment strategies. For instant, tight blockages could be treated in medicine to avoid unnecessary surgery and to save the cost. Compared to visual angiography, the pressure-derived FFR technique is an effective invasive assessment of coronary artery disease based on scientific evidence [126]. FFR index is defined as the maximum

Cette thèse est accessible à l'adresse : http://theses.insa-lyon.fr/publication/2022LYSEI006/these.pdf
© [X. Zhang], [2022], INSA Lyon, tous droits réservés

myocardial blood flow in the presence of stenosis divided by the theoretical maximum flow in the absence of the stenosis [126]. As shown in Figure 1.13(a), if a pressure sensing guidewire is inserted into a cardiac vessel to simultaneously measure the pressure on both sides of the arterial blockage, the FFR can be simplified to [126–128]:

$$FFR = \frac{P_d}{P_a} \tag{1.9}$$

where P_a is the proximal coronary pressure and P_d is the distal coronary pressure.

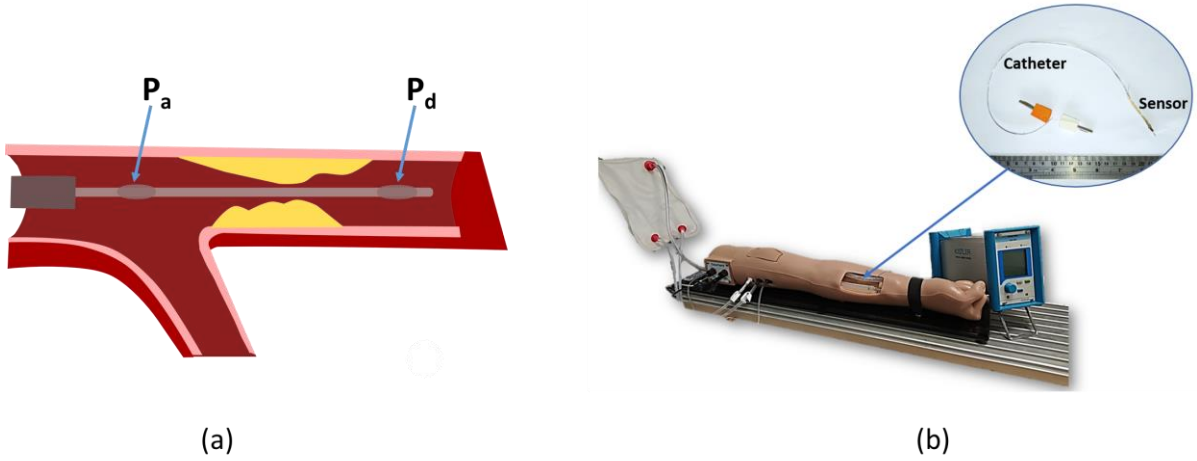

Figure 1.13. (a) Schematic illustration of FFR sensor implemented inside the vessel. P_a is the proximal coronary pressure while P_d is the distal coronary pressure; (b) Fabricated sensor implemented on a catheter was inserted into a cardiac simulation arm [129].

The current pressure sensor technologies employed in FFR marketing are [130]: optical fiber technology, microcatheter, and piezo-resistive sensor. Both optical fiber and microcatheter technologies require the incorporation of the fiber-optic sensor. An optical sensor benefits advantages such as small size, rapid response and being sensitive to the bending of the fibers. However, in the case of tortuous vessels, the optic fiber is rather fragile and limited by the minimum bend radius. It has been demonstrated that FFR measured using a microcatheter overestimates stenosis severity compared to a pressure wire [131]. The piezo-resistive sensor has good temperature sensing and mechanical stability, but possesses drawbacks like high power requirement, long-term instability in dynamic field conditions and non-linearity. Indeed, D'Ambrogio *et al.* have reported barium titanate nanoparticles/PDMS composite film integrated into a catheter was successfully simulated as a FFR sensor in a cardiac simulation arm [129]. Under an arterial pulse-shape stress, donated as 12 kPa pressure with a 66-bpm heart rate, a comparable and satisfactory sensitivity around 0.75 mV· kPa^{-1} is found in this piezoelectric film, showing high potential employed in the FFR tool with additional merits such as high flexibility, and ease of process and integration [129]. Therefore, we believe that ZnO-based piezoelectric composites would be an alternative solution as flexible and sensitive pressure sensor, and thus more easily implemented on a catheter for FFR pressure measurement.

Moreover, endovascular technology has been widely used for the treatment of vascular disease [132,133]. Especially in the surgery of arterial vascular trauma, remote vascular access could make the treatment rapidly and less tissue destruction and contamination, thus improving survival compared to

Cette thèse est accessible à l'adresse : http://theses.insa-lyon.fr/publication/2022LYSEI006/these.pdf
© [X. Zhang], [2022], INSA Lyon, tous droits réservés

conventional open surgery. For an acute and precise monitoring of the blood vessels, pressure sensors attached to the catheter can be employed to allow multiple points of pressure detection. Considering the working environment, internal space within the catheter must be kept for interventional apparatus. In that case, a thin and flexible pressure sensor is required to integrated on curved surfaces of catheters. Thus, the ZnO vertically aligned NWs composites would be suitable and popular due to their capability to achieve ultrathin thickness, even to several micrometers while the flexibility can be tuned by the material properties of encapsulating polymer matrix or the volume ratio between NWs and the polymer. Further, the devised ZnO sensor is biologically compatible and environmentally friendly, definitely showing the profound potential as implantable sensing under *in vivo* physiological conditions.

1.3.2.3 Self-powered systems adopted in the biomedical field

On the broader scale, it becomes much more attractive once the ZnO NW-based piezoelectric nanogenerators are employed in the biological environment, from natural to *in vitro* and *in vivo* acting as self-powered systems. These devices can be applied as medical implants or portable electronics with perspective advantages such as no requirement of external power source, no replacing or recharging process, miniaturization capabilities, biocompatibility, and non-toxicity [134]. Especially, there are various mechanical energy sources in living species, under vitro environment, e.g., muscle stretching, body movement, and vivo environment, e.g., blood flow, heartbeat. A single wire generator where both ends are fixed has been explored to detect and harvest the biomechanical energy from the movement of the human index finger and a live running hamster [135]. A portable self-powered biosensor based on ZnO NWs has been designed to monitor various swimming styles of swimmers [136]. Besides, NWs-based sensors are used to detect the human activities which are associated with skin deformation to monitor the health situation. Lee *et al*. have demonstrated an extremely thin film made of aligned ZnO nanowires was used to characterize the motion of the eyeball underneath, for the potential application in monitoring sleep behavior, tiredness and brain activity [137]. More importantly, ZnO NWs can be safely implanted into living species to harvest low-frequency mechanical energy. Li *et al*. have already reported the feasibility of implanting a single ZnO wire generator in a live rat to scavenge the mechanical energy generated by its breath and heartbeat [138]. Furthermore, self-powered systems can transduce human inner vibrations to drive smart nanodevices for drug delivery or monitor those vibrations for facilitating diagnosis [119].

Besides, it is well known that ZnO can be explored as a multifunctional material due to the versatile properties involving the optical, piezoelectric, electric, semiconductor and so on. Wang *et al*. have firstly introduced the principle of piezotronics and piezo-photonics in wurtzite structured material [139]. The overlap between piezoelectricity, piezoelectric and photoexcitation can result in multiple coupling effects. Piezotronics, based on the piezoelectricity-semiconductor coupling, is interpreted by using the piezoelectric potential as a gate to tune the charge transport process in fabricated electronic devices such as piezoelectric field effect transistor and piezoelectric gated diode based on a single ZnO nanowire [140,141]. Piezo-photonics is regarded as the piezoelectricity-semiconductor-photoexcitation coupling, where the electro-optical processes can be controlled by the strain induced piezopotential. Enhanced light emission efficiency has been found in ZnO micro-based diodes caused by the piezoelectric effect [142].

Cette thèse est accessible à l'adresse : http://theses.insa-lyon.fr/publication/2022LYSEI006/these.pdf
© [X. Zhang], [2022], INSA Lyon, tous droits réservés

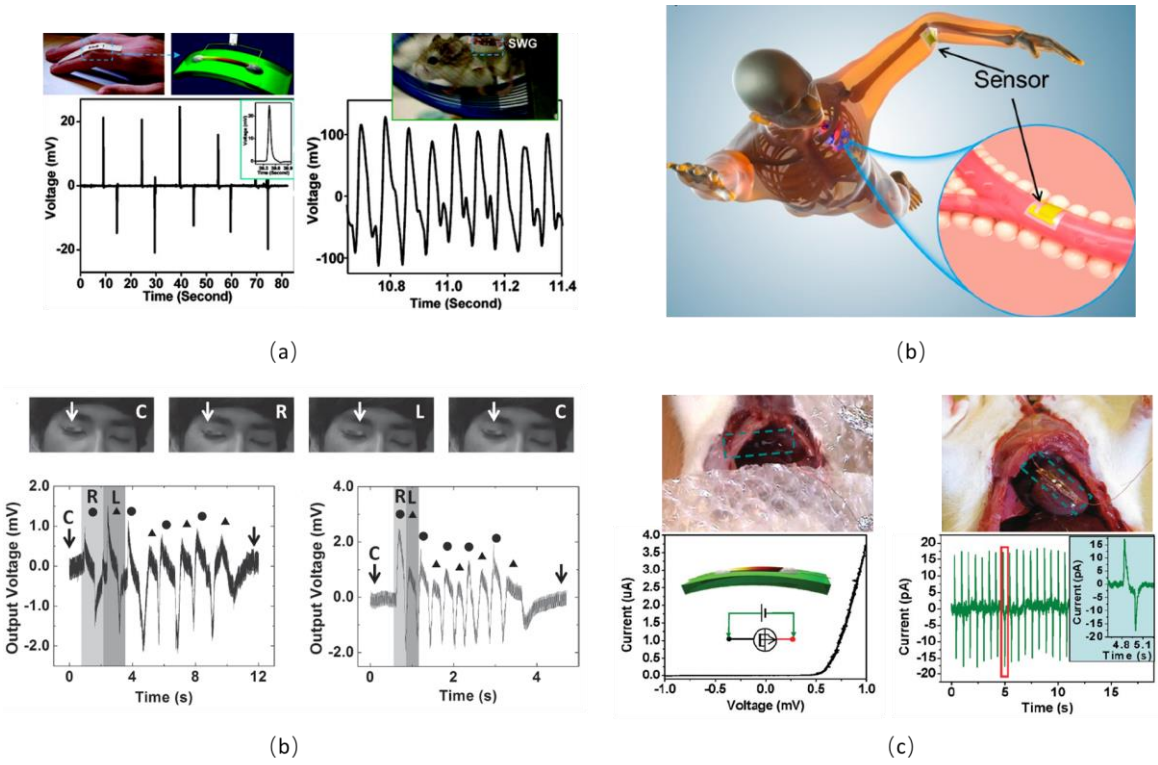

Figure 1.14. (a) Energy harvesting from an oscillating human index finger and a live running hamster using a single wire generator [135]; (b) Flexible self-powered biosensor based on ZnO NWs can be attached to the human's joint in vivo monitoring [136]. (c) A super- flexible ZnO NWs based sensor was used to detect the motion of a human eye ball [137]; (d) Energy harvesting from the breath and heart beats of a live rat using a single wire generator [138].

1.4 Summary

As a biocompatible semiconductor composed of abundant elements, ZnO has been receiving tremendous interest for a wide variety of electronic, optoelectronic, chemical, and biological sensing applications. This material exhibits numerous assets originating from its high crystalline quality, interesting physical properties (dielectric and semiconductor), cost-effective applicability into flexible devices, and possible recyclability. Consequently, the integration of ZnO into piezoelectric devices such as nano-generators, pressure/strain sensors, varistor has extensively been investigated in the last decade. Furthermore, the optimization of the electric potential generated under mechanical stress has mainly been addressed by considering technological matters including stack architecture, polymer matrix, alignment of ZnO fillers, etc. Full characterizations of ZnO composites in terms of dielectric, electrical, mechanical, and piezoelectric are thus necessary to confirm the potential and the reliability of the developed materials. Nonetheless, the investigation of these issues has been rarely reported in literature to some extent, despite their primary importance. Accordingly, the main objective of the thesis involves the optimized design via FEM simulation, enhanced material process, and advanced experimental characterization. The target application of this project is dedicated to the pressure bio-sensing device, with a particular focus on medical environment.

Cette thèse est accessible à l'adresse : http://theses.insa-lyon.fr/publication/2022LYSEI006/these.pdf
© [X. Zhang], [2022], INSA Lyon, tous droits réservés

Chapter 2. Materials and methods

Our main objective is to study the properties of the polymer-based composites with piezoelectric ZnO embedded. In this chapter, composites fabrication methods will be introduced including the conventional solution casting method for 0-3 particulate composites and chemical bath growth method for 1-3 nanowire composites. Moreover, the dielectrophoretic technology is developed to form quasi 1-3 particle composite to improve the performance. All characterization tools used in this work are described and the finite element method is followed in this chapter.

Cette thèse est accessible à l'adresse : http://theses.insa-lyon.fr/publication/2022LYSEI006/these.pdf
© [X. Zhang], [2022], INSA Lyon, tous droits réservés

2.1 Fabrication of ZnO particles-based composites

2.1.1 Material selection

In order to confirm the influence of filler size, two types of ZnO particles were chosen at the beginning. The nano- and micro-sized ZnO powders with an average particle size of approximately 150 nm and 10 µm, respectively, were purchased from US Research Nanomaterials company. A few properties of ZnO powders are listed in Table 2.1. The powders were stored at room temperature and directly used to prepare the composite without any chemical modification.

Table 2.1. Properties of ZnO powders from US Research Nanomaterials [143].

Purity	True density	Bulk density (g/cm^3)	Specific surface area (SSA) (m^2/g)	Boiling point	Melting Point
≥ 99.9%	5.606 g/cm^3	0.28-0.48 (nano-ZnO) 0.28-0.38 (micro-ZnO)	4.8-6.8 (nano-ZnO) 2-5.8 (micro-ZnO)	1800 °C	1975 °C

The commercial Sylgard-184 polydimethylsiloxane (PDMS) from Dow Corning is a non-expensive silicon-based elastomer and has been used for different applications. It is supplied as a two-component kit consisting of the base polymer and cross-linking agent. According to the recommendation of the manufacturer, the base polymer and the agent are blended at a mass ratio of 10 (base):1 (curing agent) to form a flexible elastomer. The silicone elastomer has good dielectric properties and high transparency regarding the inspection of fillers. The most important factor is that PDMS is a thermosetting polymer enabling to engineer dielectrophoretically structured composite. Versatile cure processing can be controlled by tuning the temperature within a rapid reaction time. The typical properties are displayed in Table 2.2.

Table 2.2. Typical properties of PDMS elastomer from Dow [144].

Thermal conductivity (W/m · K)	Volume resistivity (Ω · cm)	Dielectric constant at 100 Hz	Refractive index at 589 nm	Specific gravity (cured)
0.27	2.9E+14	2.72	1.4118	1.03

To fabricate different volume fractions of composites, ZnO particles and PDMS polymer contents were calculated based on the volume mixing law given by:

$$w_Z = \frac{M_z}{M_z+M_m} = \frac{\rho_z * V_z}{\rho_z * V_z+\rho_m * V_m} \quad (2.1)$$

$$V_z + V_m = 1 \quad (2.2)$$

where V and w represent, respectively, the volume fraction and mass fraction; and M and ρ denote the mass and mass density, respectively. The subscripts z and m correspond to the ZnO particles and polymer matrix, respectively.

Cette thèse est accessible à l'adresse : http://theses.insa-lyon.fr/publication/2022LYSEI006/these.pdf
© [X. Zhang], [2022], INSA Lyon, tous droits réservés

2.1.2 Random particle composites

As illustrated in Figure 2.1, the particles randomly dispersed composite films were fabricated using the classical thin film casting method, which is simple, low cost and straightforward.

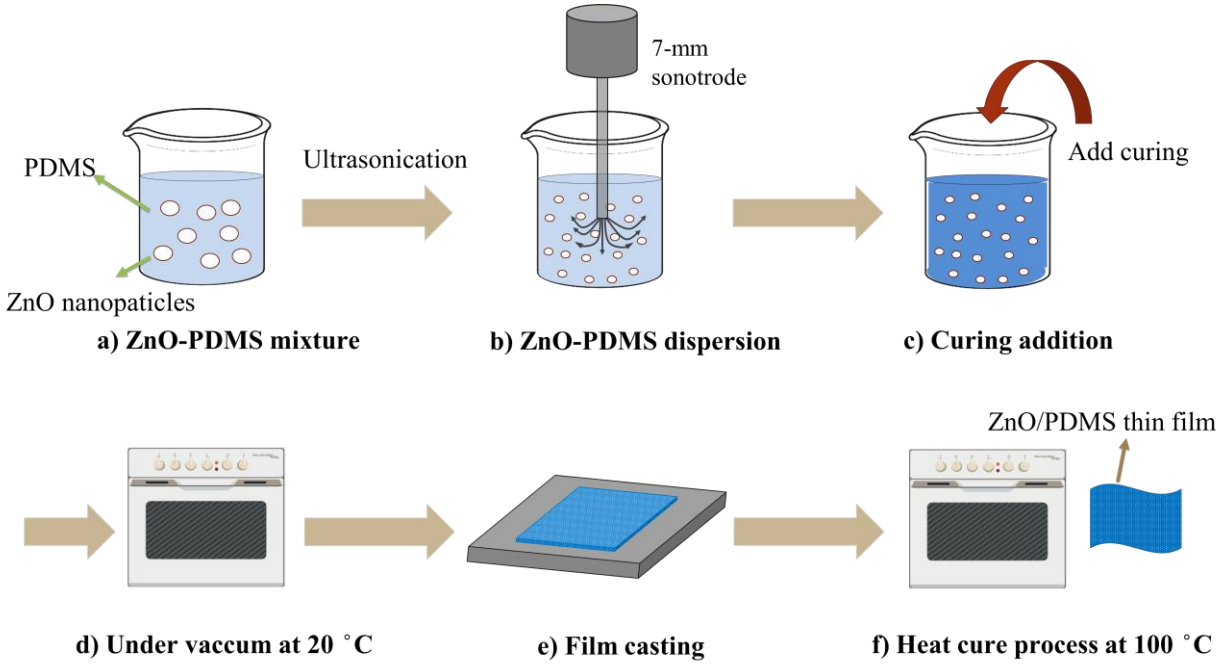

Figure 2.1. The fabrication process of nano- or micro-ZnO/PDMS composite.

It consists of 6 steps:

- (a) The particles were mixed with the PDMS solution at a given ratio according to the volume fraction of ZnO defined in Eq. (2.1).
- (b) 30-minute ultrasonication (Hielscher Ultrasound Technology, UP400S) was carried out for the whole solution (Figure 2.1b) under a laminar flow hood (ADS Laminaire, PPS12), allowing for the perfect uniform dispersion of ZnO powder in the PDMS polymer. The 7-mm sonotrode ultrasonic device was used with an amplitude of 60% and 1 cycle. During the whole process, the solution together with the beaker were immersed in an ice water bath to prevent overheating of the solution induced by the ultrasounds.
- (c) A curing agent was added to the solution at a mass ratio of 10 (base):1 (curing), which was then constantly stirred for 5 minutes until a homogenous substance was obtained (Figure 2.1c).
- (d) After that, the beaker of liquid composite was put in a vacuum drying oven (Memmert, VO 400) at 20°C for 30 minutes to completely evacuate the air bubbles trapped during the early mixing process (Figure 2.1d).
- (e) Subsequently, the uncured ZnO/PDMS mixture was poured into a specific mold to be cast as a film on a glass substrate (Figure 2.1e). The thickness of the film could be controlled by a specific blade. Normally, a 0.5mm thickness was required in this experiment.
- (f) Finally, the casting film was put into the oven at a temperature of 100°C for 35 minutes to speed the heat curing reaction (Figure 2.1f).

Cette thèse est accessible à l'adresse : http://theses.insa-lyon.fr/publication/2022LYSEI006/these.pdf
© [X. Zhang], [2022], INSA Lyon, tous droits réservés

Our objective is to fabricate composite with increasing filler content, maybe up to the maximum volume fraction with improved properties. However, after attaining a specific concentration, ZnO particles easily agglomerate and precipitate out of solution, resulting in a high viscosity and un-uniform dispersion that are unsuitable for composite film fabrication. Indeed, as opposed of microparticles, nanoparticles possess higher surface to volume ratio and high surface energy, making it much more difficult to achieve nanocomposite with high volume fraction. As a result, nanoparticles are usually used for fabrication of composite with low concentration (maximum 21% in our case), while micro particles can achieve a higher maximum volume fraction around 44%, leading to better dielectric and piezoelectric responses. Finally, we obtain different sample sets in nano- and micro ZnO particle composite:

- For nano-sized ZnO particles, 8%, 13%,17% and 21% volume fraction were achieved.
- For micro-sized ZnO particles, 14%, v 24%, 34%, 44% volume fraction were achieved.

Several examples of obtained nanocomposite and microcomposite are shown in Figure 2.2.

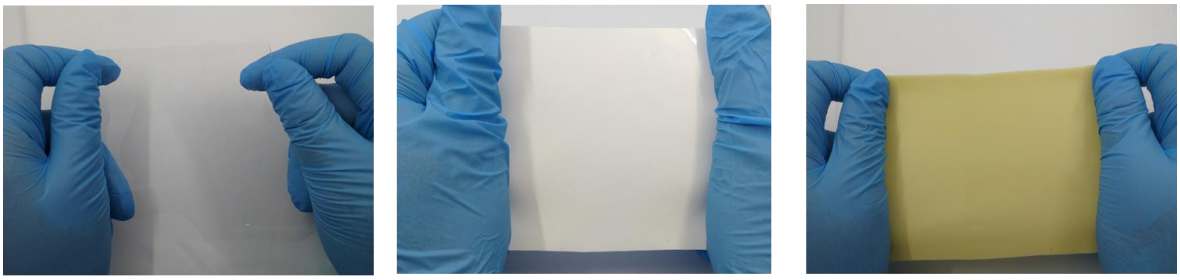

Figure 2.2. ZnO/PDMS composite films with a 0.5 mm thickness at different volume fraction: (a) 0% vol. ;(b) nanocomposite at 8% vol.; and (c) microcomposite at 14% vol.

Specimens were cut into circular samples of a 25 mm diameter by using a cylinder steel mold with a circular cavity of the same diameter. For electrical and electromechanical characterizations, normally conductive electrode coatings are deposited on the polymer films to improve the measurement accuracy. Thus, the composite samples were sputtered with gold electrodes on both sides using a sputter coater (Cressington, 208HR), as displayed in Figure 2.3(a). The gold thickness should be carefully considered because a thin gold layer will cause the decrease of the conductance of the electrode, meanwhile a thick gold coating could lead to high sample's rigidity that might impact its mechanical property. It has been reported that 26 nm would be the optimal thickness of the gold layer for experimental measurements [145,146]. As we know, during the operation process, the gold thickness is influenced by the current intensity, the sputtering time, and the distance between the sample and the target. Therefore, thin gold electrodes of 25 nm-thick and 20 mm-diameter were obtained under the condition of 0.6 mA current intensity, 90 seconds operation time and a 7 cm sample-target span. The electrode nano and micro composites are depicted in Figure 2.3 (b).

Cette thèse est accessible à l'adresse : http://theses.insa-lyon.fr/publication/2022LYSEI006/these.pdf
© [X. Zhang], [2022], INSA Lyon, tous droits réservés

(a) (b)

Figure 2.3. (a) Sputter coater for gold electrode coating; and (b) samples with circular gold electrode of 20 mm diameter.

2.1.3 Structured particle composites

2.1.3.1 Principle and theory of dielectrophoresis

Dielectrophoresis (DEP) refers to the induced movement of polarizable particles in a nonhomogeneous electric field [147]. Unlike electrophoresis, in which charged particles are separated with the suspension in a uniform electric field induced by a direct current polarization, dielectrophoretic motion occurs only for the polarizable particles under an alternating current field. When a dielectric particle is subjected to an external electric field, particles are polarized forming electric dipoles along the direction of the electric field. The dipole moments in the particle can be represented by macro dipoles consisting of equal and opposite charges on the interface of particle/medium [148]. In a uniform electric field (Figure 2.4a), the Columbic forces on each half of the dipole are equal with opposite direction. Then the resulting force on the dipoles, donated as DEP force (F_{dep}), is zero and there is no movement. Conversely, in a nonuniform electric field (Figure 2.4b), the force on either side of dipole are different and DEP force leads the movement of the particle. The movement of particles can be towards or away from the high electric field region depending on its polarization level compared to the surrounding medium [149].

DEP can be utilized for the manipulating, sorting, transporting and separating of particles due to the diverse dielectric properties of particles. In 1971, H.A.Phol observed the collectability of yeasts at the electrode tip under high-frequency alternating fields, thanks to the DPE technique [147]. Then DEP has been widely used in biotechnology to separate bacterial cells, viruses as well as biomacromolecules due to the advantages such as noninvasiveness, label-free [148]. Recently, dielectrophoresis, incorporated into the lab-on-a-chip devices, has developed into a separation technique that can be applied in medicine, molecular diagnostics because of the selectivity and accuracy [150].

The dielectrophoretic effect also can be operated to manipulate particles dispersed in a fluid medium and develop aligned particle-filled polymer composites with anisotropic properties. This process is based on the technique ‘dielectrophoretic assembly’ [151,152]. When an alternating electric field is applied to an uncured thermosetting polymer, the polarized particles experience mutually attractive force to align parallel to the direction of electric field. In other words, when the polarizability of particle is larger than the one of

Cette thèse est accessible à l'adresse : http://theses.insa-lyon.fr/publication/2022LYSEI006/these.pdf
© [X. Zhang], [2022], INSA Lyon, tous droits réservés

suspending medium, particles move towards the high intensity field which locates at the boundary of particles along the direction of electric field. Then the fluid polymer is solidified to fix chain-like structure between the electrodes through curing reaction [153]. In this thesis, dielectrophoretic alignment was utilized to form structured particles inside the polymer matrix and the dielectric, piezoelectric and electric properties were investigated in the next chapter.

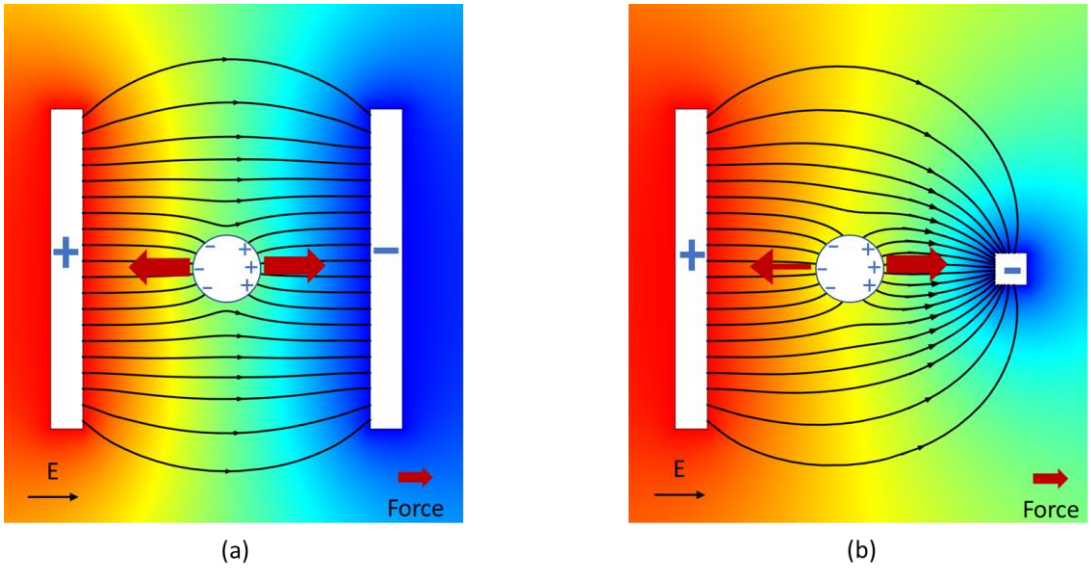

Figure 2.4. Diagram of dielectrophoresis principle: (a) when the polarized particle locates in a uniform electric field, the electrostatic forces on both side of the dipole are equal, and the net DEP force is 0. (b) When the particle exhibits a higher polarizability than the immersion medium and locates in a non-uniform electric field, an asymmetrical distribution of field on the opposed sides of dipole causes a non-zero net DEP force, driving the particle towards the stronger electric field.

Considering a dielectric sphere particle that suspends homogeneously in a fluid matrix under a non-uniform electric field, an electric dipole moment is formed with the positive and negative charges center displaced on the opposite sides of the particle. Accordingly, the dielectrophoretic force (F_{dep}) arising from the interaction between the induced dipole moment *p* and the field gradient is given by:

$$F_{\mathrm{dep}} = -\nabla U_E = (p\cdot\nabla)E \tag{2.3}$$

where U_E is the electric potential energy, *E* is the electric field.

Considering the spherical shape of particles, the induced dipolar moment is expressed by [154]:

$$p = 4\pi\varepsilon_0\varepsilon_m R^3\, \mathrm{CM}(f)\, E \tag{2.4}$$

where *R* is the radius of the particle, ε_m is the relative permittivity of the polymer matrix, and *CM(f)* denotes as a geometry- and frequency-dependent Clausius-Mossotti factor that can be explained as [155]:

$$CM(f) = \frac{\varepsilon_p^* - \varepsilon_m^*}{\varepsilon_p^* + 2\varepsilon_m^*} \tag{2.5}$$

Cette thèse est accessible à l'adresse : http://theses.insa-lyon.fr/publication/2022LYSEI006/these.pdf
© [X. Zhang], [2022], INSA Lyon, tous droits réservés

where subscripts *p* and *m* represent the property of the particle and the surrounding medium, respectively. ε^* refers to the complex permittivity, depending on the electric conductivity σ and angular frequency ω and permittivity ε:

$$\varepsilon^* = \varepsilon - \frac{j\sigma}{\omega} \tag{2.6}$$

When a stationary field is exerted on a dielectric spherical particle, the time-average DEP force is typically deduced as [148]:

$$F_{\mathrm{dep}} = 2\pi\varepsilon_0\varepsilon_{\mathrm{m}}R^3\ \mathrm{Re}[\mathrm{CM}(f)]|\nabla E_{\mathrm{rms}}^2| \tag{2.7}$$

where Re[*CM(f)*] denotes the real part of *CM(f)* and E_{rms} is the root-mean-square of the applied electric field. The force drives the particle towards or away from the high electric field regions depending on the sign of the Re[*CM(f)*]. Hence, in order to have dielectrophoretic orientation of particles along the applied electric field, Re[*CM(f)*] must be the positive. Above equation reveals that the DEP force is influenced by four parameters:

1) the dielectric properties of the suspending medium
2) the shape, volume of the particle, e.g. spherical or cylindrical tube geometries
3) the difference in polarizability between the particle and the surrounding medium
4) the magnitude and frequency of the applied electric field.

Among them, the first three parameters are determined by the intrinsic properties of the material, while the last term can be tuned and adjusted by the user to effectively exploit the piezoelectric effect of the ZnO particles.

However, since the dielectrophoresis is a multi-parameter influenced system, the DEP force should overcome the influential force including [153,156]:

1) gravity force leading the settling or sedimentation of particles, especially when the fillers have higher density than that of the surrounding fluid
2) viscous drag force, which is correlated to the viscosity of fluid and resists particles movement.
3) intra-particle
4) surface-particles adhesive force
5) electrothermal force due to the power density and heat generation during the high electric field application. The electrothermal fluid flow is formed when the increasing temperature inside the polymer matrix change the conductivity, permittivity and viscosity.

Actually, the drag force acting on the particles is regarded as one of the most important parameters and can be approximated using Stokes' law [85]:

$$F_{drag} = 6\pi\eta R\upsilon \tag{2.8}$$

where η is the viscosity of the matrix, *R* and υ are the radius, the velocity of the particle, respectively. The drag force is proportional to the viscosity which increases in the thermosetting polymer during polymerization process. Thus, the higher the viscosity, the longer time is required for dielectrophoretic alignment, resulting a lower particle velocity. Until the thermosetting matrix has fully solidified, the particles are immobilized and keep the formed chains inside the matrix.

Cette thèse est accessible à l'adresse : http://theses.insa-lyon.fr/publication/2022LYSEI006/these.pdf
© [X. Zhang], [2022], INSA Lyon, tous droits réservés

Besides the effect of influential forces, several parameters make the dielectrophoretic process impossible to have precise control. As particle fillers cannot possess exactly the same shape and size, the DEP forces exerting on different sized particles are always different. The viscous drag force is not constant caused by the increase of the viscosity with time. Simultaneously, the electrothermal effect leads a rise in the temperature to further decrease the viscosity and accelerate the curing reaction. Therefore, particle configurations with perfectly aligned chains are difficult to obtain because of these competing influences.

2.1.3.2 Preliminary observation on the dielectrophoretic process

The dielectrophoretic alignment process was observed through experimental setup depicted on Figure 2.5. Compared with nanoparticles, microparticles enables the facilitation of dielectrophoretic observation under a low-cost optical microscope which can be clearly visible at the microscale but not the nanoscale. Therefore, to clearly record the movement of particles, a low concentration mixture (i.e., 3% vol. of micro-sized of ZnO) after vacuum processing in the uncured state was filled up between two parallel copper electrodes through which high-voltage excitation was driven. The whole setup was then placed under a digital microscope (AVEN, Mighty Scope) and different magnitudes and frequencies of external electric field was applied on the electrodes. As we discussed in Eq. (2.7), the dielectrophoretic force is proportional to the amplitude of the applied electric field, while the speed movement of particles is determined by the balance between the dielectrophoretic force and other factors like drag force. Thus, the degree of particle alignment was monitored and compared according to applied conditions to conclude the optimal external electric magnitude and frequency.

As observed in Figure 2.6(a), under the same frequency of 2 Hz, different electric field magnitudes ranging from 0 to 2 V/μm were applied on the two copper electrodes. At low-voltage excitation corresponding to 0.5 V/μm, the ZnO particles still randomly separate, which is similar to the phenomenon obtained without the electric field. This result highlights the fact that the dielectrophoretic force exerted on particles under 0.5 V/μm is not sufficient to complete their orientation in 60 seconds. On the contrary, higher poling of 1 V/μm allows to form visible chain-like structure within polymer matrix along the field direction, i.e., a vertical direction from top to bottom. When the amplitude increases to 2 V/μm, the individual chains appeal to each other and consolidate to form substantial columnar structures [153]. As the DEP force is proportional to the gradient of squared electric field, the DEP force would be the maximum adjacent to the electrodes. An aggregation phenomenon of particles near copper electrodes occurs, leading to a considerable increase in the probability of short-circuiting, which perhaps results from air bubbles and/or a limited electrical breakdown of the PDMS polymer. It can be seen in Figure 2.6(b) that under the same amplitude of 1 V/μm, different frequencies of 0.2 Hz, 2 Hz, 20 Hz, and 200 Hz of electric field give out similar result in 60 s, suggesting that frequency is not the key factor influencing the degree of alignment. As a result, the electric field of 1 V/μm and 2 Hz is considered as the most optimal choice to fabricate the structured ZnO microparticles/PDMS composite.

Cette thèse est accessible à l'adresse : http://theses.insa-lyon.fr/publication/2022LYSEI006/these.pdf
© [X. Zhang], [2022], INSA Lyon, tous droits réservés

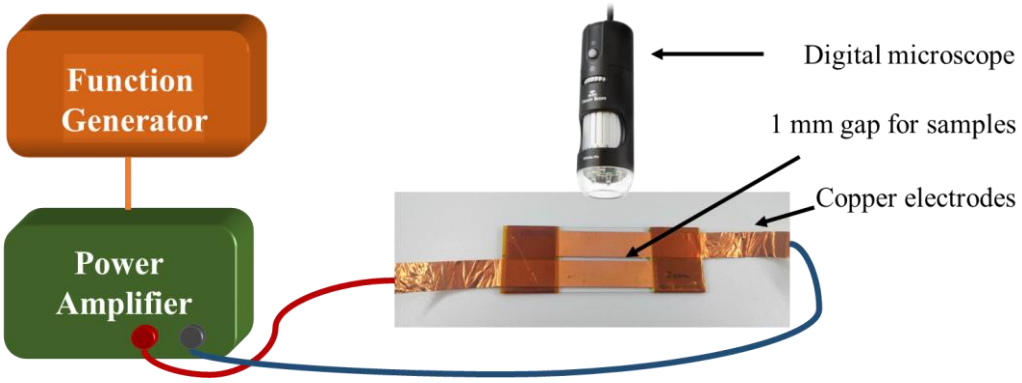

Figure 2.5. Experimental set-up for structuring PDMS solution filled with 3% vol. of ZnO particles performed under microscopic observation.

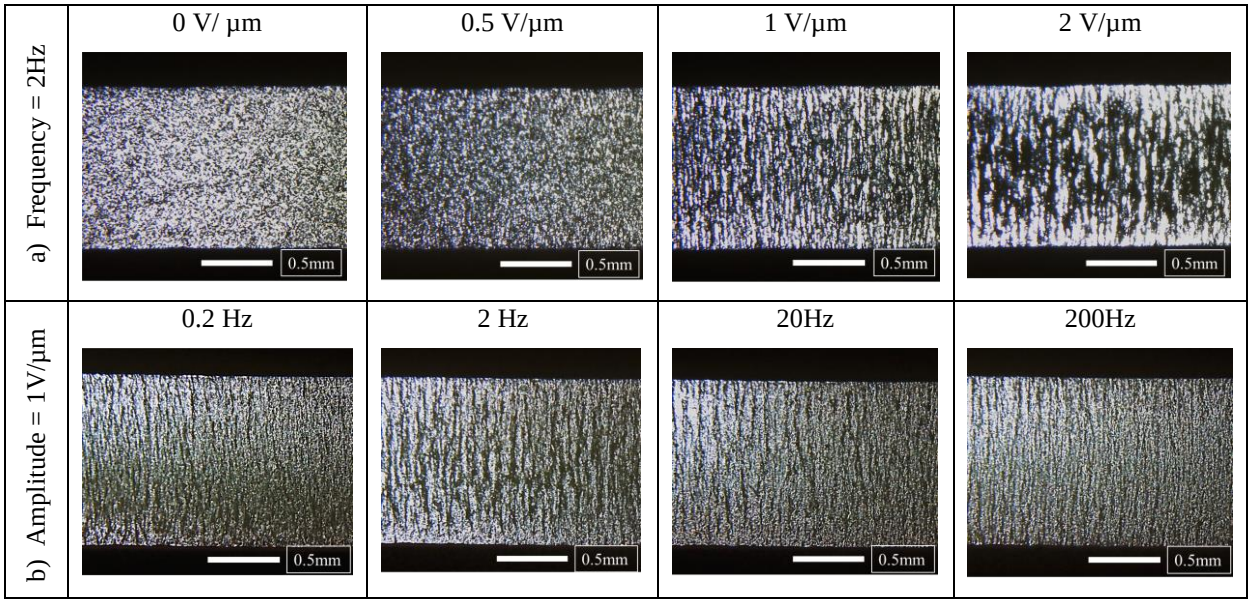

Figure 2.6. In-time microscope image of 3% vol. non-cured ZnO/PDMS composite at 60s after applying an external electric field with a) fixed frequency of 2 Hz and different amplitudes; b) fixed amplitude of 1V/µm and different frequencies.

2.1.3.3 Structured 1-3 composite via dielectrophoretic manipulation

The process of preparing the structured ZnO/PDMS composite was similar to the process of fabricating the random dispersed composite as previously described in Subsection 2.1.2, except for the last two steps, (f) and (g), of Figure 2.1. As illustrated in Figure 2.7, a layer consisting of a 0.5 mm-thick insulator epoxy plate with a circular 25 mm diameter hole in the center that was carefully filled with the uncured ZnO/PDM solution. The sample holder was then clamped between two parallel electrodes on which high voltage was applied. A thick, heavy circular brass plate was put on the top as the upper electrode to provide enough pressure for obtaining flat and compact samples. Afterward, the whole sample and support were placed into an oven (Votsch IndustrietechnikTM, VT7004) at a constant temperature of 100°C for 35 minutes. The

Cette thèse est accessible à l'adresse : http://theses.insa-lyon.fr/publication/2022LYSEI006/these.pdf
© [X. Zhang], [2022], INSA Lyon, tous droits réservés

electrodes were externally connected to a functional voltage generator (Agilent, 33210A) whose signal was amplified 1000 times via an amplifier (Trek, Model 20/20C). The detailed experimental set-up is displayed in Figure 2.8.

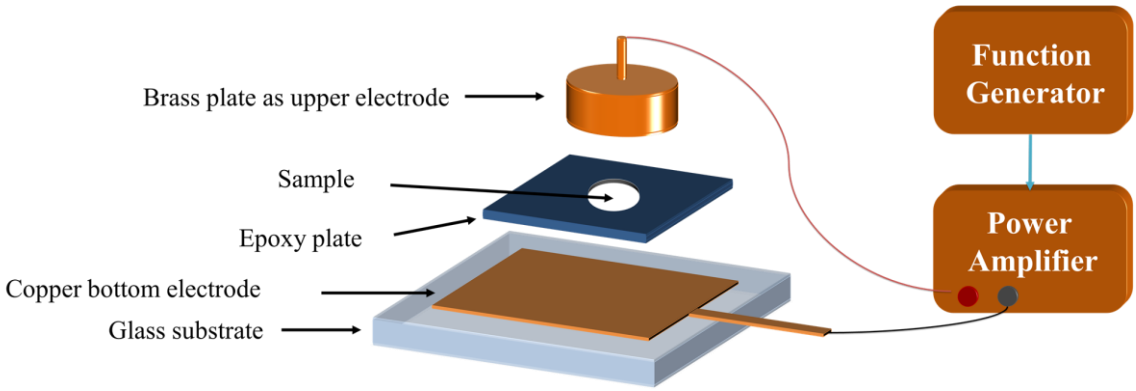

Figure 2.7. Schematic drawing of the mold used for the dielectrophoresis process under a high-amplitude electric field.

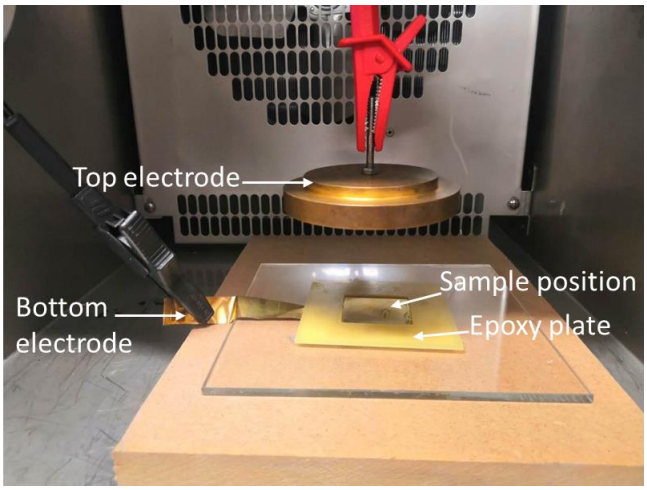

Figure 2.8. Experimental set-up for structured ZnO/PDMS composite fabrication.

2.1.3.4 Electric field distribution based 2D Comsol model

In order to have an idea about the distribution of the field within the particles and its surroundings, 2D Comsol model is carried out. In the FEM simulation, ZnO circular particles with a diameter of 10 µm are defined, embedded in PDMS polymer with 80 µm long × 70 µm wide. The bottom of the matrix is electrical ground whereas a potential of 35 V is applied on the top, allowing to drive an electric field of 0.5 V/µm to the whole matrix. The density of free charges in the materials is considered to be zero as the dielectric loss in ZnO composite under such an electric field is negligible. Figure 2.9 illustrates the electric field distribution in random and structured micro composites with a different ZnO volume fraction of 14% and 44%. For all samples, the electric field level is greatly higher in the polymer matrix than in the particles, especially around the particles, the electric field becomes maximum due to the polarizability contrast between polymer and particles. This result is consistent to the one reported on Pedroli et al. [157], where the electric field is always more significant in the material with lower dielectric permittivity (in polymer,

Cette thèse est accessible à l'adresse : http://theses.insa-lyon.fr/publication/2022LYSEI006/these.pdf
© [X. Zhang], [2022], INSA Lyon, tous droits réservés

for instance). Actually, there are two approaches proposed in the experiments to enhance the internal electric field on both matrix and particles:

- Increasing the filler content with higher dielectric constant will result in higher electric field on ZnO particles, when comparing between Figure 2.9 (a) and (c), Figure 2.9 (b) and (d). Meanwhile, a large number of particles gives rise to narrower polymer gaps, where electric field is concentrated and converged, rather than dispersing into other directions. Thus, this in turn improves the electric field level on the vicinity particles.
- In the structured materials (Figure 2.9b and d), as the axes of the particle chains are oriented perpendicular to the active surface (i.e. applied by an electric potential), the electric field would mainly affect the interparticle interactions within the same chain. This leads to homogenous electric field distribution of all particles and relatively higher electric level on particles, which is contrary to the case of the random matrix (Figure 2.9a and c).

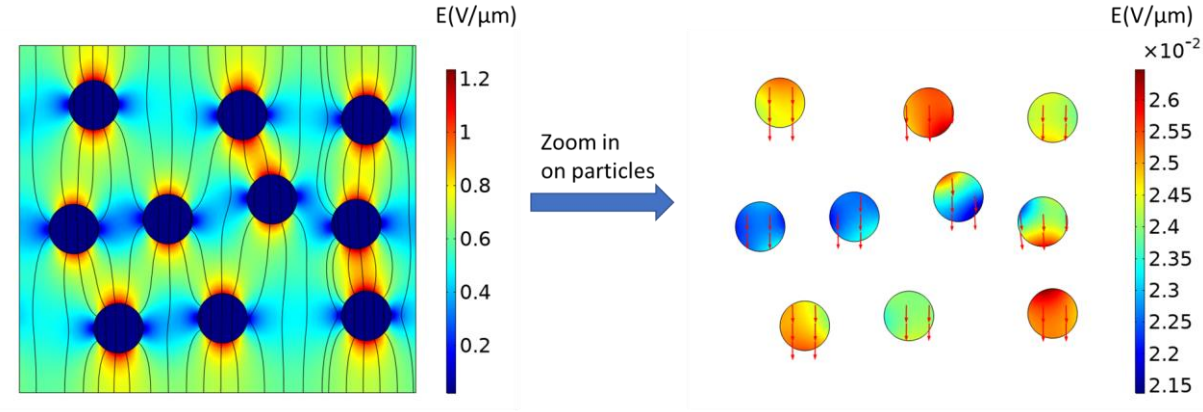

a) Random ZnO/PDMS composite with 14% volume fraction

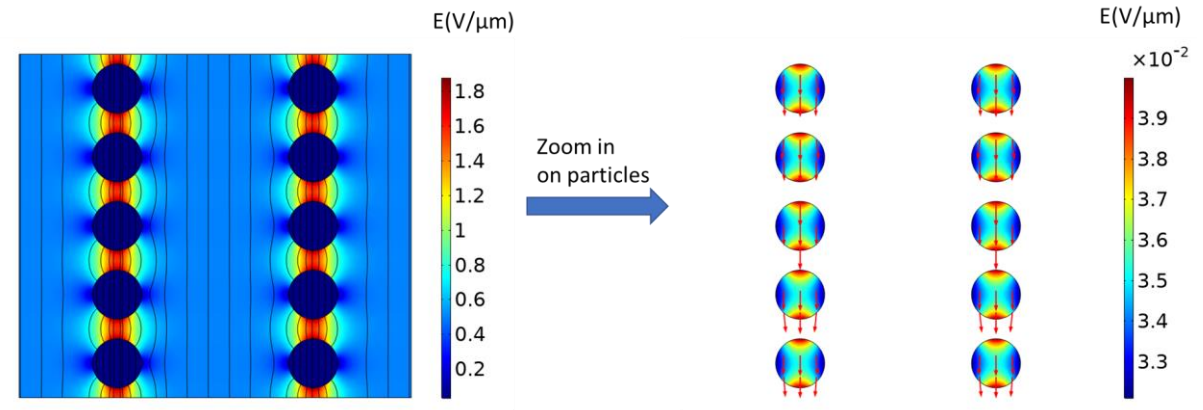

b) Structured ZnO/PDMS composite with 14% volume fraction

Cette thèse est accessible à l'adresse : http://theses.insa-lyon.fr/publication/2022LYSEI006/these.pdf
© [X. Zhang], [2022], INSA Lyon, tous droits réservés

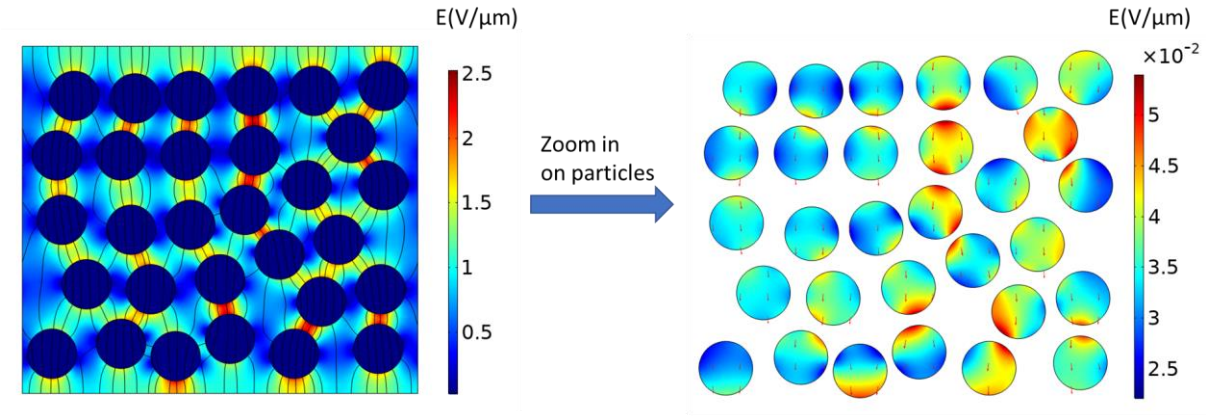

c) Random ZnO/PDMS composite with 44% volume fraction

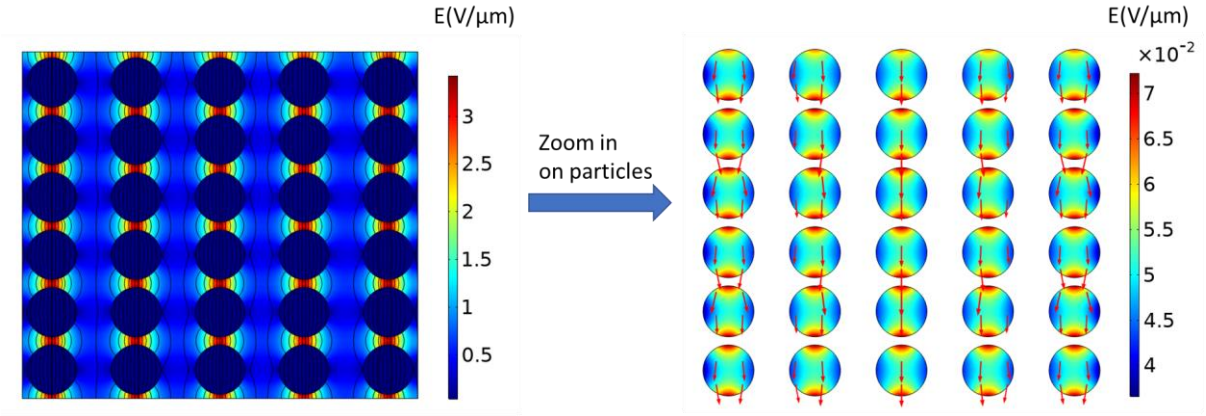

d) Structured ZnO/PDMS composite with 44% volume fraction

Figure 2.9. Electric field distribution in random and structured micro composites with a different ZnO volume fraction (on the left-hand side), and a closer view of the particles (on the right-hand side).

In addition, the results of Figure 2.9 allow to confirm that the ZnO particle is a dielectric isolation, as the electric field driven within the particles is significantly lower than the threshold value above which, ZnO passes from dielectrics to conductor. Several studies were investigated to characterize the electrical properties of ZnO material. In [158], current-voltage characteristics of a photo-conducting organic liquid-crystal film based Zinc octakis(b-decoxyethyl) porphyrin (i.e. ZnODEP) was performed, allowing to deduce the electric field threshold of around 0.15-0.2 V/μm. Alternatively, Ahmad et al. demonstrated that under low applied electric field, the relative permittivity of the ZnO powder was constant, and then drastically drop when the electric field attains the threshold value (i.e., approximately 0.15-0.9 V/μm) [159]. This confirms the semiconductor behavior of ZnO composite, which can be employed as microvaristor system. Based on these above results in literatures, it is obvious that in our case, the electric field applied on the particles (less than 0.1V/ μm) is not sufficient enough to make them conductive. As shown in Figure 2.10, a higher electric field of 2 V/μm is acted on the random and structured composite (44% vol.). Under higher input excitation, ZnO particles start manifesting the nonlinear conducting characteristics and sustain low voltage as a conductor. Hence, the short polymer gaps undertake most of the voltage and easily breakthrough to deliver the current. As a result, thorough conduction paths are formed in the whole composite and electric

Cette thèse est accessible à l'adresse : http://theses.insa-lyon.fr/publication/2022LYSEI006/these.pdf
© [X. Zhang], [2022], INSA Lyon, tous droits réservés

nonlinear properties are observed. Interestingly, when the composite is subjected to an intermediary level of 1 V/µm, the aligned particles become conductor whereas the random ones are still isolator, as its switching field is superior to the one of the 1-3 matrix.

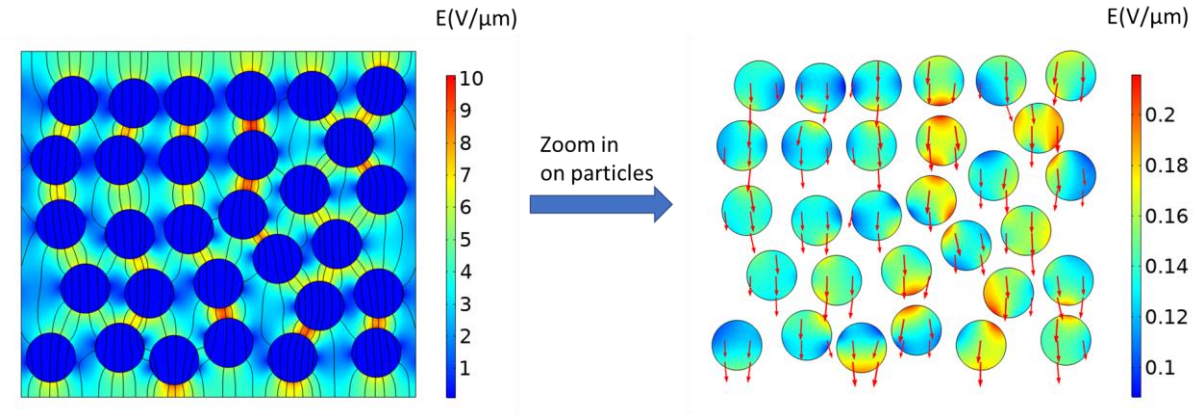

a) Random ZnO/PDMS composite under 2 V/µm

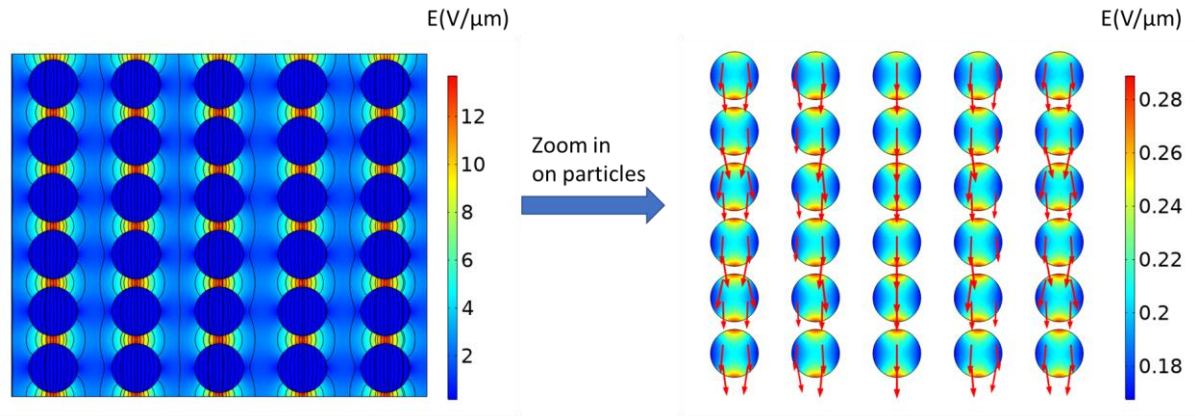

b) Structured ZnO/PDMS composite under 2 V/µm

Figure 2.10. Electric field distribution in random and structured micro-composites with 44% volume fraction under an electric field of 2 V/µm.

2.2 Fabrication of ZnO Nanowires (NWs) based composites

2.2.1 Rigid NWs composites

In this thesis, we designed a typical structure consisting of vertically aligned ZnO NW arrays encapsulated in a stiff polymer matrix, which were fabricated at the Materials and Physical Engineering Laboratory (LMGP laboratory). A ZnO thin seed layer (SL) was deposited on a silicon (Si) substrate above which the vertically aligned ZnO NWs grew. All fabrication steps were described in Figure 2.11. Firstly, the samples were prepared on a 675 ± 25 µm-thick (001) Si substrate, cleaned with acetone and isopropyl alcohol in an ultrasonic bath (Figure 2.11a). Secondly, a 40 nm-thick ZnO SL using a sol-gel process was prepared with 375 mM zinc acetate dehydrate ($Zn(CH_3COO)_2 \cdot 2H_2O$, Sigma-Aldrich) and 375 mM monoethanolamine (MEA, Sigma-Aldrich) mixed in pure ethanol (Figure 2.11b). Afterward, continuous

Cette thèse est accessible à l'adresse : http://theses.insa-lyon.fr/publication/2022LYSEI006/these.pdf
© [X. Zhang], [2022], INSA Lyon, tous droits réservés

stirring was performed for several hours at 60°C and then at room temperature. The Si substrates were dipped into the solution under a controlled atmosphere (< 15 % hygrometry). Consequently, they were annealed at 300 °C for 10 min on a hot plate for the evaporation of residual organic compounds, and at 500 °C for 1h in an oven under air for the crystallization of SL layers. Thirdly, ZnO NWs were grown by chemical bath deposition (CBD) in a sealed reactor containing an equimolar proportion of the precursors, 30 mM zinc nitrate hexahydrate ($Zn(NO_3)_2.6H_2O$, Sigma-Aldrich), and hexamethylenetetramine (HMTA, Sigma-Aldrich) mixed in deionized water (Figure 2.11c). The sealed reactor was kept for 3 hours in an oven at 85 °C. From each nucleation site created by a polycrystalline film deposition of both Zn- and O- polar seeds, there is a ZnO NW with the same polarity of the site from where it grew. The duality of colors represents the two different polarities. For instance, as described in Figure 2.11d, the light blue corresponds to the Zn-polarity while the dark blue denotes the O-polarity. It is noteworthy that this figure is used for illustration purpose only. A real scale and exact amount (or density) of NWs can be deduced from field emission scanning electron microscopy (FESEM) imaging. Next, different film thickness of poly(methyl methacrylate) (PMMA with 8% solids, All Resist) were spin coated on top of the different devices (Figure 2.11e). To improve the robustness and stabilize the NW structure, a PMMA matrix was spin coated as interstitial insulating material among NWs. With the aim of preventing electrical leakages and direct contact between NWs and top electrode, a dielectric top layer (e.g., made of PMMA polymer) was stacked on the ZnO NW arrays. Lastly, to create electric contact, a circular gold coating with a 10-mm diameter and approximately 25-nm thick was deposited on both sides by sputter coater (Cressington, 208HR) (Figure 2.11f).

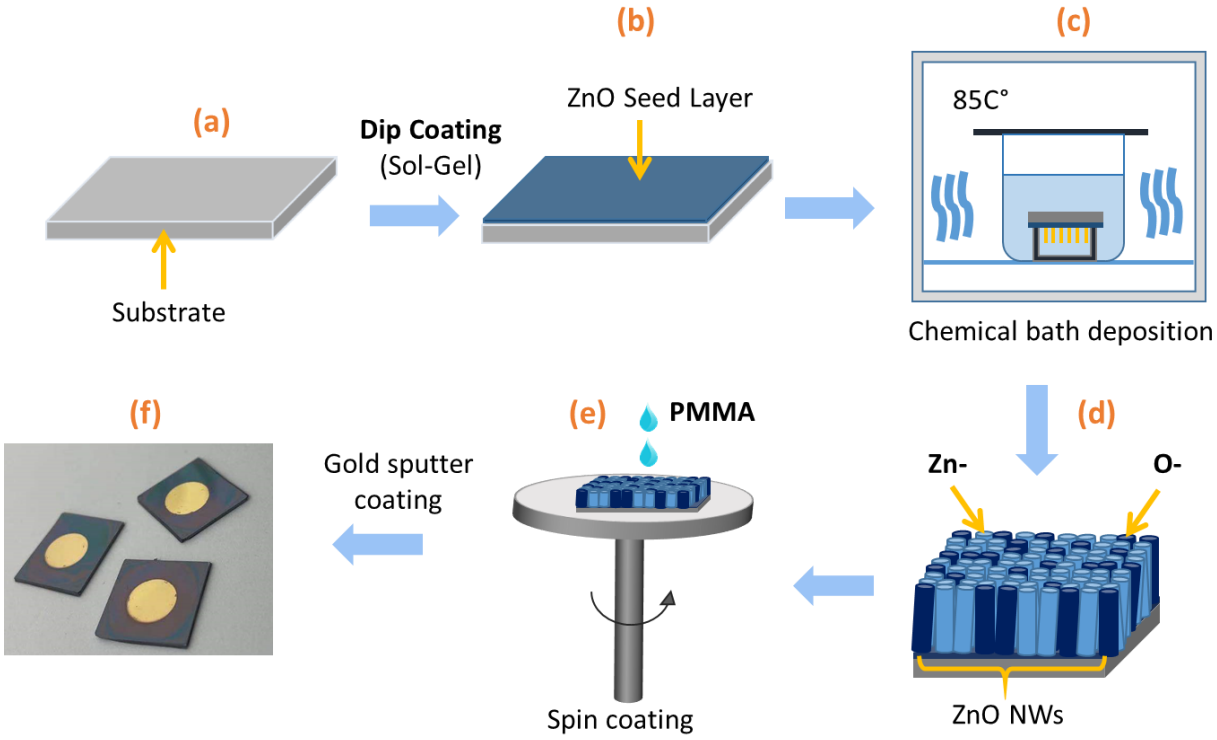

Figure 2.11. Fabrication steps of ZnO NW arrays/PMMA composite.

Cette thèse est accessible à l'adresse : http://theses.insa-lyon.fr/publication/2022LYSEI006/these.pdf
© [X. Zhang], [2022], INSA Lyon, tous droits réservés

2.2.2 Flexible microrods and nanowires composites

2.2.2.1 Flexible microrods composite

Structured spherical particle composites were fabricated via dielectrophoretic technique as described in Subsection 2.1.3. In order to further achieve a high level of alignment, particles with highly anisotropic geometric (e.g., cylinder) were used instead of those with spherical form. So, in the thesis, ZnO microrods (MRs) were employed to synthesize the composites of aligned MRs in PDMS through dielectrophoresis.

ZnO MRs were developed by LMGP through CBD technique, in which MRs were grown on the ZnO nanoparticles seed layer [160]. This method possesses high flexibility for ex-situ thermal annealing and relatively fast production of ZnO MRs, with homogeneous nucleation. At the end, ZnO MRs with a 3.9 μm length and a 477 nm diameter were obtained. However, due to the relatively low growth rate during fabrication process, such as collecting only 1.8 gram from 1 L mixture liquid, only tens gram of ZnO MRs were obtained. As a result, 0-3 and quasi 1-3 composites elaborated via the casting method (see Figure 2.1 and Figure 2.8), is limited at low volume fraction of 2% and 8%. The 8%. vol oriented sample is shown in Figure 2.12(a). Indeed, 10% vol. is failed to achieve because of the microrods agglomeration problem. For an easier comparison, ZnO microparticles/PDMS composites with an 8% concentration were also fabricated, as displayed in Figure 2.12(b).

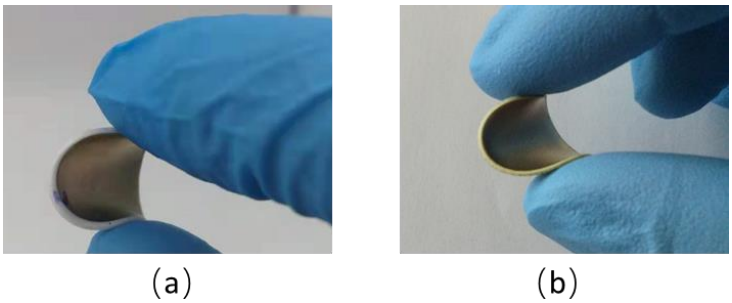

Figure 2.12. Samples with 8% vol. of quasi 1-3 (a) ZnO MRs/PDMS composite and (b) micro-ZnO particles/PDMS composite.

2.2.2.2 Flexible NWs composite

In Figure 2.11(a), the rigid silicon was replaced by an elastic 0.5 mm-thick PDMS as the substrate used to develop the flexible 1-3 NWs composites, provided by LMGP laboratory. Several improvements in the optimization of the properties of ZnO NWs were conducted to boost the whole performance and efficiency.

1) A post-growth treatment was implemented before the top layer PMMA spin coating (Figure 2.11e). ZnO NWs were annealed at 220°C under O_2 atmosphere for 2 hours.
2) During the growth of NWs (Figure 2.11c), 1.0% of Sb/Zn ratio was added on CBD solution to obtain Sb-doped ZnO NWs finally. Both pristine and doped samples are shown in Figure 2.13.

Accordingly, there are total four sample sets for the piezoelectric evaluation, as displayed in Table 2.3.

Table 2.3. Specimens of flexible 1-3 NWs composites

N°	Thermal annealing	Doping	Sample
1	No	No	PDMS/pristine NWs

Cette thèse est accessible à l'adresse : http://theses.insa-lyon.fr/publication/2022LYSEI006/these.pdf
© [X. Zhang], [2022], INSA Lyon, tous droits réservés

2	Yes	No	PDMS/annealed NWs
3	No	Yes	PDMS/Sb-doped pristine NWs
4	Yes	Yes	PDMS/Sb-doped annealed NWs

(a) (b)

Figure 2.13. Photographs of obtained (a) PDMS/pristine ZnO NWs and (b) PDMS/Sb-doped annealed NWs composite

2.3 Characterization methods

2.3.1 Dielectric characterization

Broadband dielectric spectroscopy was measured utilizing a frequency response analyzer (Solartron, 1255) together with a dielectric interface (Solartron, 1296A) at ambient temperature as shown in Figure 2.14. Each composite was clamped in a sample holder (AMETEK, 12962a). An alternating voltage with an RMS value of 200 mV was applied to drive the precise measurement in the frequency ranging from 1 Hz or 0.1 Hz to 1 MHz.

Figure 2.14. Experimental setup for dielectric characterization

Cette thèse est accessible à l'adresse : http://theses.insa-lyon.fr/publication/2022LYSEI006/these.pdf
© [X. Zhang], [2022], INSA Lyon, tous droits réservés

The principle of the dielectric spectrometer is measuring the magnitude and phase relationship between output and input signals as a function of frequency. More specifically, an alternative voltage $u(t) = Ucos(\omega t)$ is subjected on the sample and the responded current density $i(t) = I\cos(\omega t + \phi)$ is measured, where ϕ is the phase shift, I and U are the current and voltage amplitude, respectively. For a parallel-plate capacitor, the capacitance C can be calculated as

$$C = \frac{A\varepsilon_0\varepsilon_r}{d} \tag{2.9}$$

where A is the surface, d is the thickness, $\varepsilon_0 = 8.854 \cdot 10^{-12}$ F/m is the vacuum permittivity, $\varepsilon_r = \varepsilon_r' - i\varepsilon_r''$ is the relative complex permittivity of the material, in which ε_r' is the real part and ε_r'' is the imaginary part of permittivity. Therefore, according to known parameters, the complex impedance Z for a capacitive medium can be calculated as

$$\underline{Z} = \frac{u(t)}{i(t)} = \frac{U}{I}(cos\phi - j\sin\phi) = \frac{1}{jC\omega} \tag{2.10}$$

Combining equation (2.9) and (2.10), it can be derived that

$$\varepsilon_r' = \frac{Id}{UA\varepsilon_0\omega}\cos(\frac{\pi}{2} - \phi) \tag{2.11}$$

$$\varepsilon_r'' = \frac{Id}{UA\varepsilon_0\omega}\sin(\frac{\pi}{2} - \phi) \tag{2.12}$$

and the electric loss tangent is defined as

$$\tan\delta = \frac{\varepsilon_r''}{\varepsilon_r'} = \tan(\frac{\pi}{2} - \phi) \tag{2.13}$$

There are two different experimental conditions subjected on the dielectric spectroscopy measurements for various purposes:

(1) Characterization of frequency-dependent behaviors under a wide frequency range from 0.1 Hz up to 1 MHz in an ambient environment.
(2) Characterization of temperature-dependent behaviors range from -10 ºC to 110 ºC, thanks to a cryogenic controller (ITC503). To create the low temperature, liquid nitrogen was employed by placing it in a vacuum chamber driven by a vacuum pump.

2.3.2 Electrical characterization

In order to study the nonlinear electric properties of ZnO particles/polymer composites, experimental characterizations under high electric level applications were carried out using varying or direct current (DC) tests, displayed in Figure 2.15. A film of 25 mm diameter was clamped in a sample holder between two copper electrodes. Firstly, a high voltage was applied on the electrodes of the film using a waveform generator (Agilent, 33210A) coupled with a high voltage amplifier (Trek, Model 20/20C). Secondly, the resulting was sent to an overload protection current and detected by a low-noise current preamplifier (Stanford Research Systems, SR570) with a gain setting from 10-500 µA/V. Lastly, these signals were monitored and recorded in digital storage oscilloscope (KEYSIGHT, DSOX1102G). There were three categories of input, including DC, sinusoidal (bipolar) and positive sinusoidal (unipolar) signals. To obtain a point-to-point curve in J-E characteristics, all samples were subjected to a number of DC voltage levels until 2 V/µm so as to avoid initiation of breakdown, which eventually caused damage to the test samples.

Cette thèse est accessible à l'adresse : http://theses.insa-lyon.fr/publication/2022LYSEI006/these.pdf
© [X. Zhang], [2022], INSA Lyon, tous droits réservés

For each measured point, after a 10-minute waiting, current across the sample attained the steady state that was measured through the current amplifier. For both unipolar and bipolar cases, electric field with frequency of 1 Hz and amplitude increasing from 0.2 V/μm to 1 V/μm were applied to the composites. It is noteworthy that an application of sinusoidal waveform allows to achieve polarization loop of all samples. Analytical model was then carried out so as to distinguish the conduction, the dielectric, and the ferroelectric responses. On the other hand, under DC electric field application, only conduction behavior got involved, making it possible to accurately determine the electric conductivity.

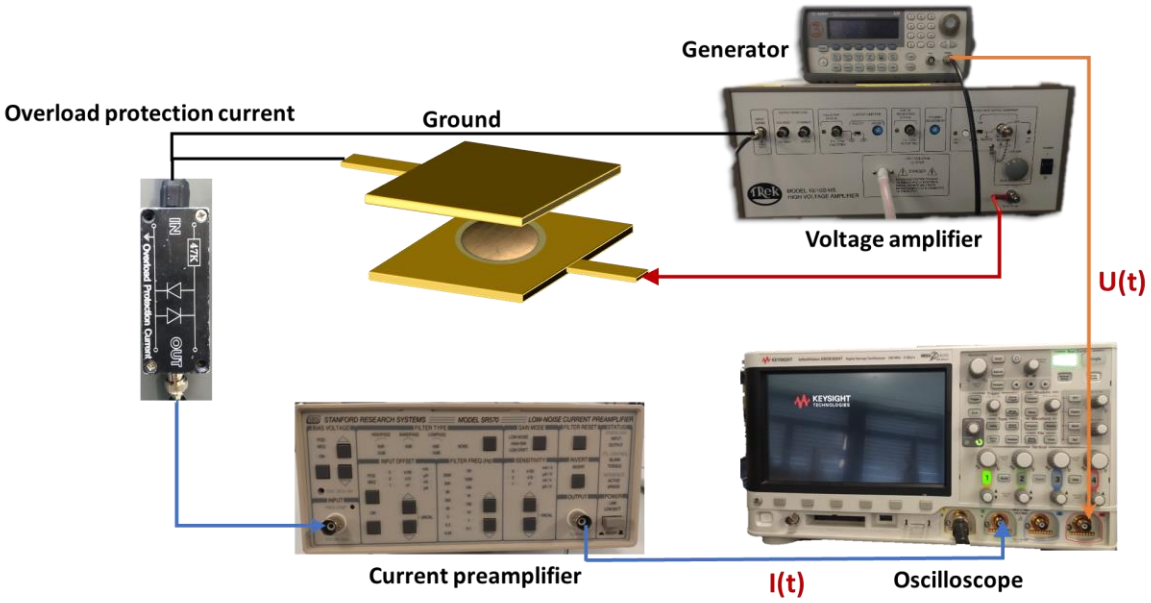

Figure 2.15. Schematic illustration for the high electric field characterization

To investigate the influence of temperature on the switch field and electric polarization loop, the entire sample holder was placed into an oven (Votsch IndustrietechnikTM, VT7004), allowed the control of temperature with high precision. Samples were exposed to a large temperature range, increasing from -10 ºC to 110 ºC. For each temperature variation, 10 minutes waiting time was required to achieve a stable temperature environment. Voltage and current measurements were descripted previously. Experimental tests were carried out under DC voltage excitation, considering that the conduction property (i.e. dominant at static regime) is strongly temperature dependent.

2.3.3 Piezoelectric characterization

The piezoelectric charge coefficient was measured using a specially designed setup with high sensitivity, as shown in Figure 2.16. The sample was clamped between upper and lower sample carrier board Figure 2.17. It should be noted sample carrier board with different copper electrodes are used according to that different gold electrode sputtered on the specimens. Dynamic mechanical excitation was driven by a piezoelectric stack actuator (PI 246-50) with tunable amplitude and frequency controlled by a waveform generator (Agilent, 33500B) together with a voltage amplifier (Trek, Model 20/20C). In this experimental test, a mechanical frequency equal to 1 Hz was chosen, whereas the voltage amplitude varied to obtain different levels of force exerted on the sample. The charge coefficient d_{33} can be estimated as:

Cette thèse est accessible à l'adresse : http://theses.insa-lyon.fr/publication/2022LYSEI006/these.pdf
© [X. Zhang], [2022], INSA Lyon, tous droits réservés

$$d_{33} = \frac{D}{T} = \frac{\frac{Q}{A_{ative}}}{\frac{F}{A}} \tag{2.14}$$

where A_{active} and A denote the surface of the gold electrode and the clapmed surface, respectively; Q denotes the electric charge; D is the electric displacement (or charge density); and T and F, respectively, denote the mecanical stress and applied force. To avoid measurements of parasitic deformations, the clamping electrodes should have the same diameter as the gold electrode (i.e., around 20 mm). During the movement, the force F was quantified via a load sensor (HBM) and the electrical charge Q was measured through a high-sensitivity charge meter (KISTLER, Type 5015). The charge density D and the mechanical stress T can therefore be easily deduced, allowing for obtaining the value of the piezoelectric coefficient d_{33}. Finally, real-time signals were simultaneously recorded using DEWE software (Sirius 8XSGT). Post-data treatment was performed with the Origin software.

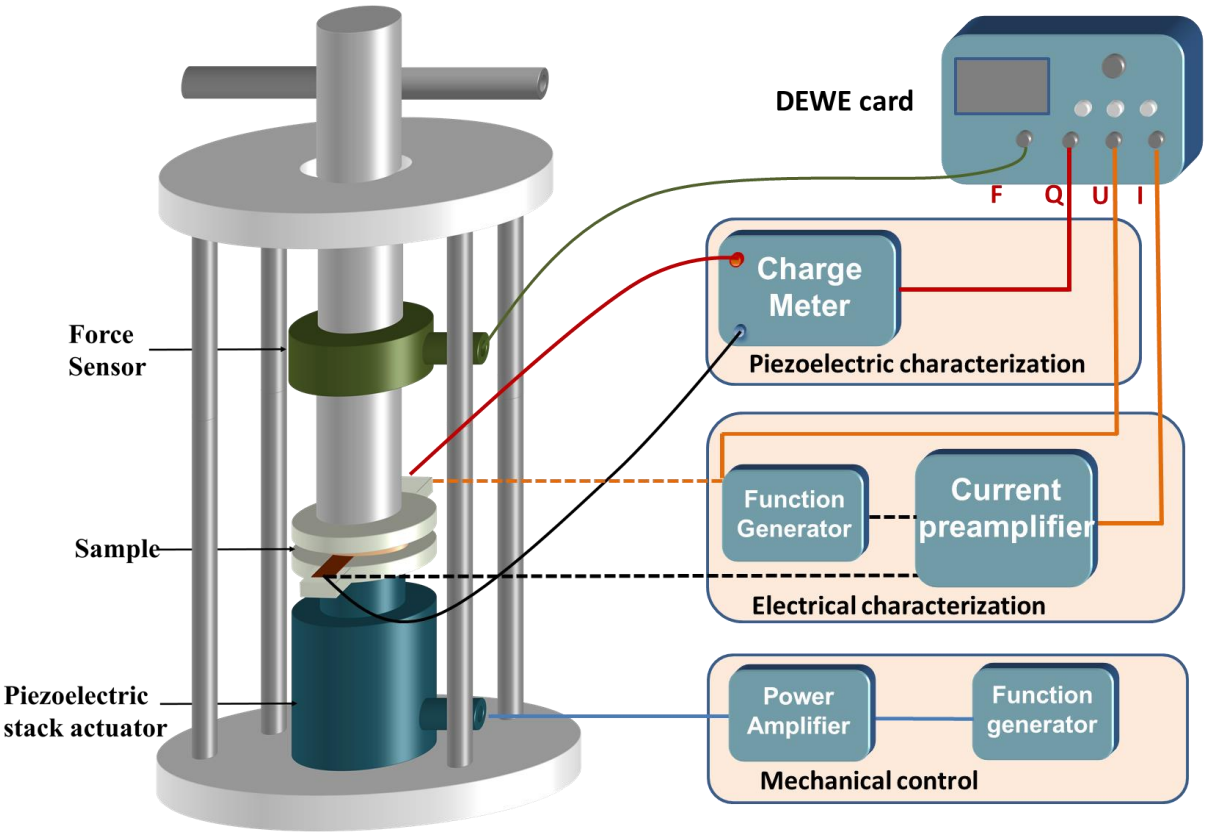

Figure 2.16. Experimental setup dedicated to electromechanical characterization

To perform the electrical properties of sample subjected to a mechanical solicitation, both current and voltage signals were simultaneously recorded, as shown in Figure 2.16. Firstly, an alternating current (AC) input voltage with a frequency of 1 kHz was applied on the electrodes of the sample by means of a waveform generator (Agilent, 33210A). Secondly, the resulting current was detected by a low-noise current preamplifier (Stanford Research Systems, SR570) with a gain setting from 100 - 500 µA/V. Finally, the characteristic loop of current density versus electric field was monitored with the corresponding force through the DEWE interface. Post-data treatment was performed via the Origin software.

Cette thèse est accessible à l'adresse : http://theses.insa-lyon.fr/publication/2022LYSEI006/these.pdf
© [X. Zhang], [2022], INSA Lyon, tous droits réservés

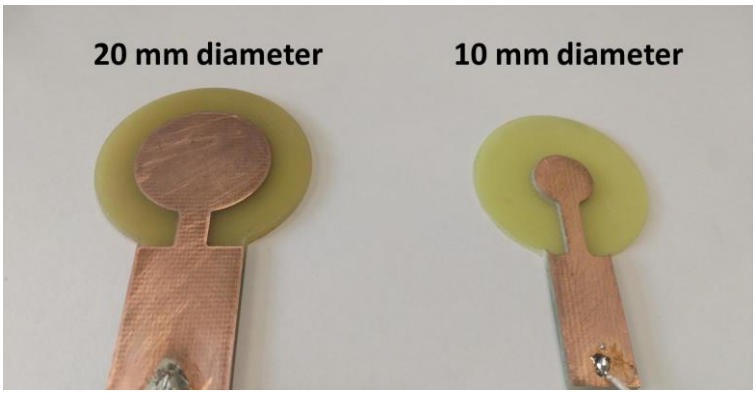

Figure 2.17. Sample carrier board with different copper diameter (20 mm and 10 mm).

2.3.4 Mechanical Characterization

Experimental monotonic tensile and compression tests were performed with the help of Shimadzu TCE-N300 to evaluate the mechanical properties of the ZnO/PDMS composites. Specimens were cut into two different dimensions according to the type of mechanical characterization. As shown in Figure 2.18, rectangular-shaped specimens with size of around 30 × 2 mm² were used in the tensile tests, while those with circular shape of 20 mm diameter were applied in the compression mode. The thickness of all samples was precisely measured using a mechanical comparator (Florenza) and remnant dimensions were measured by calipers before testing. In the tensile mode (Figure 2.18a), two boundaries of sample were fixed in the upper and lower non-shift wedge grips (model MWG-20kNA) and a ramp-up tensile load at rate of 0.1 mm. s^{-1} was applied to obtain a stress-strain pattern. The composites were subjected to an increasing force until breakdown occurs. This test allowed to determine the ultimate tensile strength (T_{MAX}) that the material can withstand while being stretched before breaking.

On the other hand, the compressive behavior was studied under a complete mechanical cycle, consisting of loading the sample to the maximum strain and unloading it until recovering to the initial position. As shown in Figure 2.18(b), samples were clamped between the compression plate kit and compressed at a speed of 5 μm. s^{-1} under a displacement-controlled mode. Four compressive strain cycles (20, 40, 60, 70%) were exerted on the composite and thus the peak stress (occurred at the maximum strain) can be measured for a given strain. During both types of tests, the axial force (F) and the deformation data (ΔL) of either expansion or contraction were recorded at a sampling frequency of 100 Hz through a TRAPEZIUM software. Hence, the stress (i.e., $T = F/A$ with A being the cross area perpendicular to the force), and the strain (i.e., $S = \Delta L/L_0$ with L_0 being the initial length) were calculated to plot the stress-strain curves. Based on elastic deformation behavior, it was possible to derive the elastic modulus of the materials corresponding to the slope of the stress-strain curve in linear regime [161].

Cette thèse est accessible à l'adresse : http://theses.insa-lyon.fr/publication/2022LYSEI006/these.pdf
© [X. Zhang], [2022], INSA Lyon, tous droits réservés

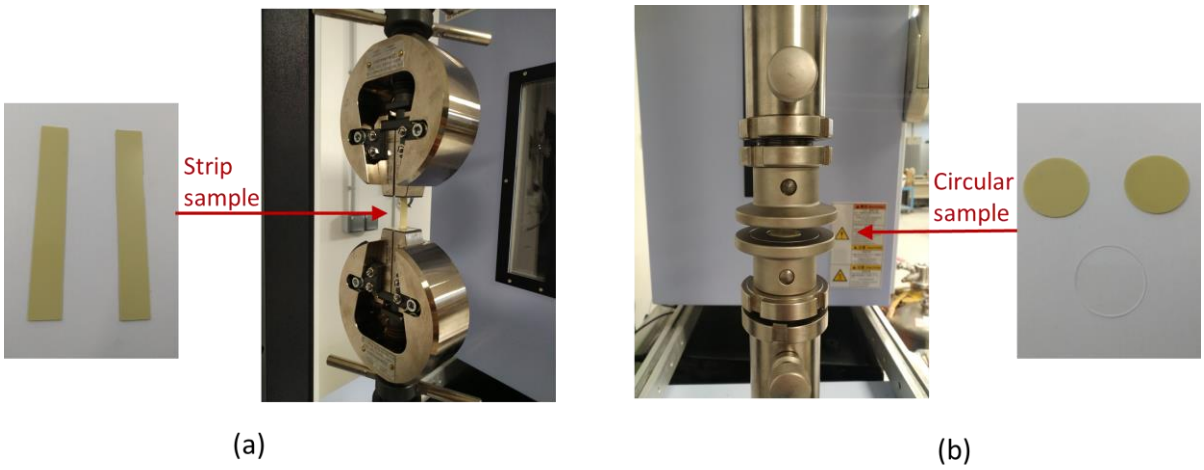

Figure 2.18. Different load frames for (a) tensile test and (b) compression test in terms of two types of sample dimensions.

2.3.5 Morphology characterization

In order to evaluate and compare the particles distribution of aligned and random ZnO/PDMS composites, scanning electron microscopy (SEM) was carried out with a Hitachi Flex SEM 1000 Ⅱ microscope. No conducting layer was coated on the samples as the low voltage application. The operation was performed under a vacuum of 30 Pa, working distance (WD) of 6 mm, and accelerating voltage (Vacc) of 15 kV.

Figure 2.19. The Flex SEM 1000 Scanning Electron Microscope.

2.4 Simulation method based finite element

2.4.1 Structured ZnO particles/PDMS composites

In this work, finite element analysis (FEA) was applied to provide a better understanding of electrophoretic effect on the dielectric and piezoelectric properties of ZnO particles/PDMS composite. A 2D anisotropic model was built using COMSOL Multiphysics tool as described by the 3 following steps:

Cette thèse est accessible à l'adresse : http://theses.insa-lyon.fr/publication/2022LYSEI006/these.pdf
© [X. Zhang], [2022], INSA Lyon, tous droits réservés

a) Geometry creation

As illustrated in Figure 2.20, the composites consist of a rectangle-shaped PDMS polymer embedded with ZnO spherical particles with a 5 μm radius. Particles are vertically aligned and stacked to each other to form a chain-like structure. In order to avoid edge effects, it is necessary to stack at least 20 particles in a column. Different volume fractions of 14%, 24%, 34%, and 44% were respectively designed by keeping the same concentration of ZnO (cf. Figure 2.20a-d), but with a different volume of polymer matrix. The ratio (γ) of particle size to interparticle distance (d) is one of the relevant parameters that strongly affects the piezoelectric response. Thus, two configurations are performed in this study, including:

- the particles touch each other with $\gamma = \infty$ ($d = 0$);
- the particles are spaced equally of 0.2 μm distance with $\gamma = 50$.

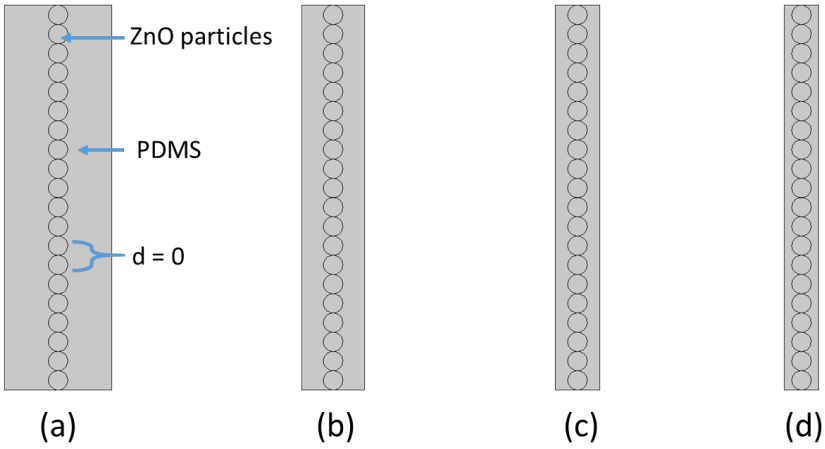

Figure 2.20. Geometric design for ZnO particles/PDMS composite at a volume fraction of (a) 14%, (b) 24%, (c) 34%, and (d) 44%.

b) Model setting

Electrostatics module was used to simulate the effective permittivity of ZnO/PDMS composite, while the effective piezoelectric response was evaluated by coupling the Piezoelectricity module with Electrical circuit module under proper terminal condition. The material properties of ZnO and PDMS were initially taken from the COMSOL material Library, such as the Poisson's rate of PDMS (0.49). But the permittivity, dielectric loss and Young's modulus will be measured and derived in the dielectric and mechanical characterization. For the boundary conditions within the electrostatics module, as shown in Figure 2.21a, the bottom was maintained at ground, while a floating potential of 1 V was applied on the top. In addition, periodic electric conditions were acted on the side walls of the matrix to form a tangential continuous electric field across the periodic boundary. Hence, this simple 2D geometry can be regarded as the repeating unit to represent the whole composite material. Similarly, for the piezoelectric module, the side walls were maintained with periodic electric and mechanical continuity conditions. Meanwhile, the bottom was set with grounded and fixed constrain and a compression stress of 1 MPa in the vertical direction was applied on the top. A capacitor was connected in parallel to the composite so as to collect and accumulate the piezoelectric charges in response to the compressive stress.

Cette thèse est accessible à l'adresse : http://theses.insa-lyon.fr/publication/2022LYSEI006/these.pdf
© [X. Zhang], [2022], INSA Lyon, tous droits réservés

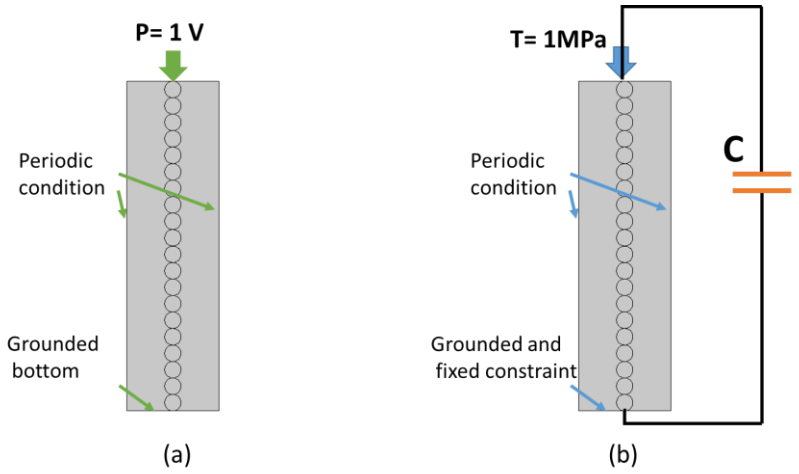

Figure 2.21. Boundary conditions for (a) permittivity; and (b) piezoelectric response prediction.

c) Model solving

The accuracy of solution is impacted by the size, shape number of mesh elements. In our model, fine physics-controlled mesh was sufficient and created. The study for dielectric and piezoelectric prediction were carried out in the frequency domain.

The effective permittivity (ε_{eff}) of the composite can be calculated according to the following formula [162]:

$$\varepsilon_{eff} = \frac{D}{\varepsilon_0 E} \tag{2.15}$$

where D and E are the electric flux density and the electric field of the whole material, respectively. On the other hand, the effective piezoelectric constant (d_{33}) along the vertical direction can be simply estimated as the ratio of charges, collected in the external capacitor, to the force acting on the composites.

2.4.2 Vertically ZnO NWs/PMMA composites

In order to estimate the d_{33} of single ZnO nanowire, the FEM under an arbitrary compression was performed through fitting the simulated piezoelectric response of composite with the experimental effective d_{33}. The model of vertically ZnO NWs/PMMA composites can be simplified into a 3D elementary cell. As seen in the Figure 2.22(a), a single ZnO NW with a radius of 42 nm and a length of 1031 nm stacked on a 40 nm-thick seed layer was incorporated in a PMMA matrix with different thicknesses. The width of the elementary cell was defined to satisfy the realistic NW density (51 ± 7 μm^{-2}). Similar to the model of structured ZnO particles/PDMS composites, a fixed and grounded condition was applied on the bottom, while the top was subjected a stress of 1MPa. The different point is in order to decrease the discrepancy of d_{33} between the FEM model and experimental results, air condition was considered. In the Figure 2.22 (b), a simulation involves 25 ×25 periodic unit cells embedded in the finite air were built to avoid the edge effects, which we will discuss in detail in the chapter 4. Then the piezoelectricity module and Electrical circuit module were coupled with each other by applying proper terminal condition. Specifically, a capacitor

Cette thèse est accessible à l'adresse : http://theses.insa-lyon.fr/publication/2022LYSEI006/these.pdf
© [X. Zhang], [2022], INSA Lyon, tous droits réservés

was connected in parallel to the composite so as to collect and accumulate the piezoelectric charges in response to a compressive stress. This method allows to easily estimate the effective piezoelectric constant (d_{33}) along the vertical. It should be noticed that the value of permittivity and dielectric losses of polymer in the COMSOL are extracted from the experimental result measured in the dielectric spectrometer. The study was carried out in time domain in which the composite was excited on the top by a positive sinus compressive stress of 1 MPa amplitude.

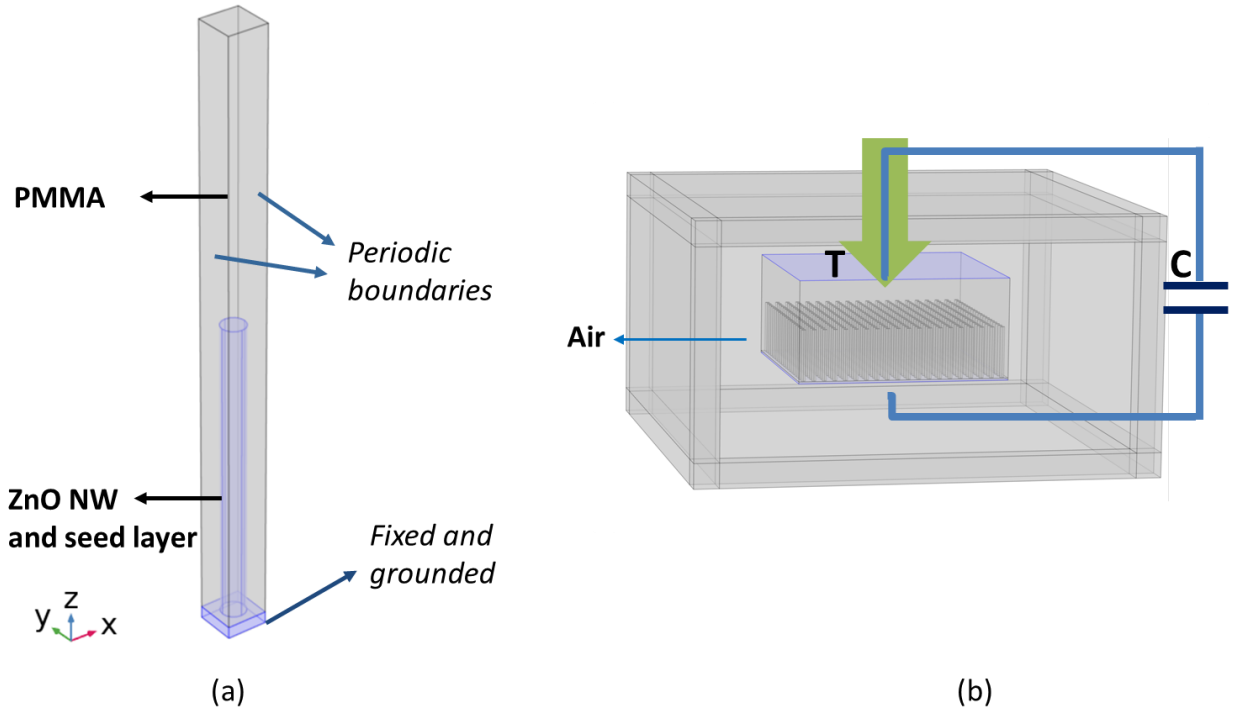

Figure 2.22. (a) Geometric design and boundary condition of one elementary cell. (b) Schematics of ZnO NWs composite in parallel with an external capacitor of 100 nF subjected to a compressive stress of 1 MPa magnitude considering air condition.

2.5 Summary

Composite thin films of ZnO particles and microrods randomly dispersed inside the polymer were fabricated using the classic solution blending method. Alignment of fillers in PDMS to form chain-like structure can be achieved via dielectrophoresis technology, which was controlled by the magnitude and frequency of applied alternating field. In addition, vertically aligned ZnO NWs-based composites were prepared with the help of CBD technique. The electric, mechanical, dielectric, piezoelectric, thermal and morphology characterization approaches were described in this chapter. Besides, a simple two-dimensional and three-dimensional model were built using COMSL Multiphysics tool to simulate and estimate the piezoelectric behaviors in ZnO microparticles (MPs) and nanowires (NWs) composite, respectively.

Cette thèse est accessible à l'adresse : http://theses.insa-lyon.fr/publication/2022LYSEI006/these.pdf
© [X. Zhang], [2022], INSA Lyon, tous droits réservés

Chapter 3. Enhancing properties of ZnO particles/PDMS composites via dielectrophoresis

Broad practical applications have been developed for polydimethylsiloxane (PDMS) polymer filled with multifunctional zinc oxide (ZnO) powders. From a practical application point of view, a full characterization is critically important, which can lead to a better understanding on their electrical, mechanical dielectric and piezoelectric properties. In this chapter, we will confirm the feasibility of ameliorating those properties by varying the filler's size, filler's concentration, and filler's structuration. Especially, the dielectrophoretic method will be introduced to form oriented particle-filled polymer composites in order to further enhance the piezoelectricity, dielectric and electric performance. Meanwhile, analytical approaches, simulation models will be established to correlated to the experimental characterizations, making a possibility to possess a thorough analysis.

Cette thèse est accessible à l'adresse : http://theses.insa-lyon.fr/publication/2022LYSEI006/these.pdf
© [X. Zhang], [2022], INSA Lyon, tous droits réservés

3.1 Material morphology

Microscopic evaluations were conducted to examine the homogeneity of particle distribution within the polymer matrix, together with the chain-like structure of the aligned composites elaborated with various ZnO volume fraction. Figure 3.1 displays the SEMs image of specimens with a volume fraction increasing from 14% to 44%, and the micro-sized particles dispersion is either random or structured.

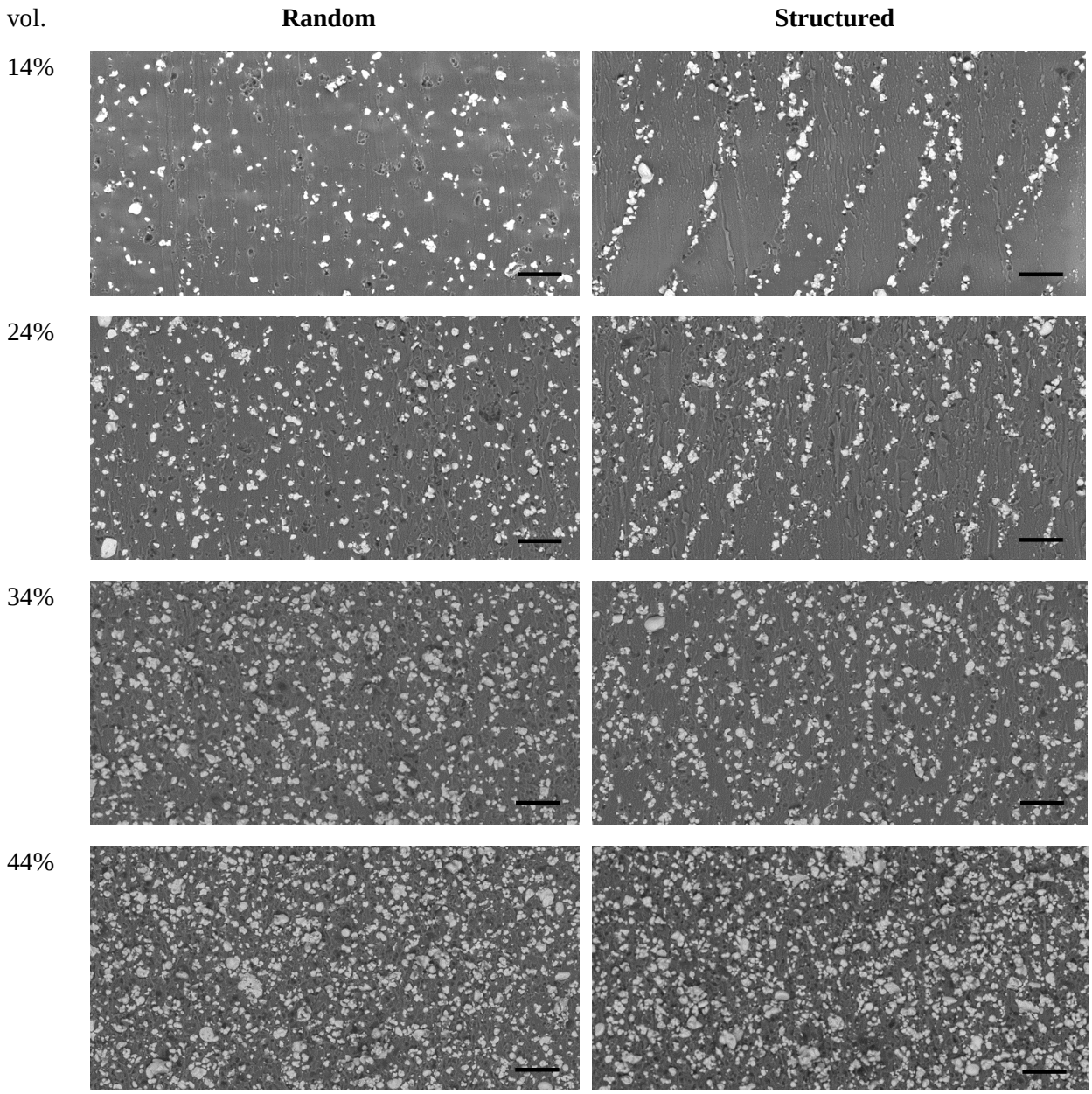

Figure 3.1. SEM images of random and structured micro composites at different volume fraction (the scale bar is of 400 µm).

Cette thèse est accessible à l'adresse : http://theses.insa-lyon.fr/publication/2022LYSEI006/these.pdf
© [X. Zhang], [2022], INSA Lyon, tous droits réservés

For the non-aligned 0-3 samples, ZnO particles were randomly distributed within PDMS polymer matrix, implying a homogeneous dispersion of samples. Inversely, an anisotropic spatial arrangement of reinforced particles was clearly visible in case of the structured composites treated with dielectrophoresis. It is noticed that the lower the filler content, the easier the alignment effect can be observed [163]. For instance, in case of the 14% vol. random composite, particles have enough space to create chain-like structure along the field direction. When the filler content is increased, inter-chain interactions are getting stronger and compete with their interaction with the external field. Consequently, that chains tend to merge together to form a network-like structure, due to greater impact of interactions between particles, caused by their smaller distances. In other words, this behavior is attributed to the fact that at high density composites, interactions between laterally adjacent particles overwhelms the dielectrophoretic force [99]. Consequently, in the 34% and 44 % aligned samples, observation of particle alignment is not evident with respect to the one of 14% and 24%.

3.2 Electric characterization

In the multiphase composites, physical properties including the dielectric, piezoelectric, mechanical, pyroelectric can be controlled by arrangement of the constituent phase, allowing for an increase in the number of connectivity patterns [79]. It has been reported that the charge coefficient (d_{33}) of the piezoelectric composites was strongly improved by manipulating on the pattern of connectivity, which elaborated on the interspatial relationships between two phases [85,164]. Thus, the electrical conductivity of the composites should be investigated at the beginning to have a better comprehension on the connectivity patterns. Alternatively, with the aim of efficiently exploiting potential of ZnO based PDMS polymer in microvaristor application, more detailed analysis of their electrical properties is involved in this study. It should be understood that when the applied input excesses the switching field, ZnO becomes more a conductor than a capacitor, which is manifested by its semiconductor properties.

Thus, in this study, the current-voltage characteristics of samples were firstly measured with DC voltage, concentrating on the intermediate nonlinear region. Then AC voltage was applied mainly in the low current linear region and partial intermediate nonlinear region due to the existence of high resistance in this range. However, the resulting current of ZnO sample can be modeled by three components including ferroelectric, dielectric, and conduction mechanisms. The weighting given to each component strongly depends on the material properties and essentially on the applied voltage level. Consequently, exploring behavior of polarization hysteresis loop of ZnO microvaristor under large range of electric field becomes mandatory to further understand its nonlinear characteristics.

3.2.1 DC current density-electric field characterization

For a better visualization of the isolator-semiconductor transition, which is situated around the percolation threshold characterized by the switching field, different samples subjected to different fields are displayed in the J-E curve. Actually, the percolation depends on the sample's concentration and structuration (0-3 or 1-3 connectivity). The J-E characteristics described in Figure 3.2 clearly show the semi-conductor property of the ZnO composites, which consists of two different slopes: the first slope exhibits very low level, corresponding to the insulating behavior below the switching field. The second slope, on the other hand, drastically increase when the material becomes conductor. In that case, the charge carriers get enough

Cette thèse est accessible à l'adresse : http://theses.insa-lyon.fr/publication/2022LYSEI006/these.pdf
© [X. Zhang], [2022], INSA Lyon, tous droits réservés

energy to freely move through the material, resulting in significantly enhanced current density. The root cause of the sharp increase in the current density around the switch field could be originated from the charge accumulation on the grain boundaries of ZnO crystals. Due to the arrangement of oxygen atoms, Schottky barriers are formed on the grain boundary and a depletion layer is formed within the ZnO grains [98]. Therefore, charges are accumulated in the depletion layers until the Schottky potential barrier is reached, which elaborates the conduction mechanism in the ZnO material [159].

Moreover, Figure 3.2 explains how the nonlinear conductions behaviors vary with the filler concentration. As reported by Yang et al., this issue can be justified by considering influence of the conduction path made by ZnO/ZnO connectivity [165]. When the filler concentration is below the percolation threshold, the composite behaves as an insulator. As soon as conduction paths develop above the percolation threshold, the composite manifests nonlinear properties. Some of the conduction paths are mainly straight, while others are curved. The shortest conduction paths are those with the greatest current density, because the conductivity of the paths is the largest [166]. Thus, the main conduction paths are shorter and straighter at higher filler concentrations, leading to lower switching field. Inversely, the conduction paths in low filler concentration are mostly roundabout and curved, because of predominant resistive connectivity between particles and polymer, giving raise to higher switch field. The switching fields (E_s) of the composites are shown in Table 3.1.

It is expecting in Figure 3.2, that whatever the applied electric field, the 0-3 composites with low ZnO content (14% and 24% vol.) always perform as an insulator where no switching field exists. Nonetheless, the 1-3 aligned structures doped with the same concentration allows the creation of the conduction path, being confirmed by apparition of the switching field. The result demonstrates that the dielectrophoretic alignment on ZnO particles successfully enhances the electric response of the composite. For instance, the 1-3 matrix with 24% vol. exhibits higher current density than the 0-3 matrix with 44% vol.

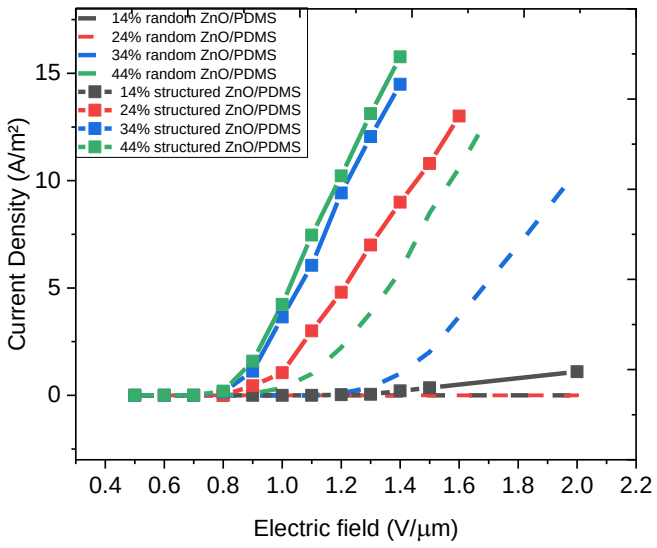

Figure 3.2. Nonlinear J-E characteristics of random and structured-ZnO/PDMS composites at filler content of 14%, 24%, 34%, 44%. Dotted lines represent the 1-3 aligned samples whereas dashed line depict the 0-3 random samples.

Cette thèse est accessible à l'adresse : http://theses.insa-lyon.fr/publication/2022LYSEI006/these.pdf
© [X. Zhang], [2022], INSA Lyon, tous droits réservés

Table 3.1 describes the nonlinear coefficient α of random and structured composites elaborated with ZnO concentration of 14%, 24%, 34%, 44%. The nonlinear coefficient α is calculated as [100]:

$$\alpha = \frac{\log\frac{J_2}{J_1}}{\log\frac{E_2}{E_1}} \tag{3.1}$$

where J_1 and J_2 are the measured current densities with amplitude of 1 A/m² and 10 A/m², respectively; E_1 and E_2 are the corresponding DC applied electric field. In case of the 14% and 24% random composites, as well as the 14% structured composite, it is not possible to calculate α as their current densities cannot go up to 10 A/m². The nonlinear coefficient α gradually increases with the increasing ZnO concentration, which is attributed to the incremental conduction paths in composites. Also, the 1-3 structure favors the nonlinear behavior, leading to 10% increase in the value of α with respect to the 0-3 matrix. Interestingly, for the 34% and 44% composites with aligned structure or not, the nonlinear coefficients are almost identical. This can be explained that in such high concentration composites, the amount of active short conduction paths almost saturates, and little discrepancy was observed.

Table 3.1. Nonlinear coefficient (α) of random and aligned composites at 14%, 24%, 34%, 44% volume fraction

	$\mathbf{14\%_{vol}}$	$\mathbf{24\%_{vol}}$	$\mathbf{34\%_{vol}}$	$\mathbf{44\%_{vol}}$
$\boldsymbol{E_{s-random}}$ (V/μm)	-	-	1.39	1.09
$\boldsymbol{E_{s-structured}}$ (V/μm)	1.93	0.98	0.88	0.85
$\boldsymbol{\alpha_{random}}$	-	-	6.51	6.52
$\boldsymbol{\alpha_{structured}}$	-	5.96	7.21	7.24

3.2.2 Time-varying electric field characterization

The main feature differentiated the ferroelectric materials from the dielectric materials is the presence of spontaneous polarization, retaining the intrinsic electrical polarization in the absence of external field. Thus, the ferroelectricity can be characterized by measuring the intersection of the D-E hysteresis loop with the electric displacement axis, denoted as remnant polarization in response to a high AC electric field [167]. For the dielectric film, when being doped with impurities the dielectric has a finite resistivity, leads to a leakage current. If a varying electric field is applied on the composites, the electric energy losses can be divided into two parts: dissipation of dielectric energy from pure dielectric material, and energy losses associated with leakage current inducing from dopant fillers [168]. From a practical application viewpoint, energy loss may cause significant heat generation in electromechanical devices under strong field driving condition, leading to device failure [169]. This subsection aims to distinguish different losses mechanisms of ZnO composites, at the same time to verify the piezoelectricity and semiconductor of ZnO particles. Tests are performed under a large range of electric field, with two configurations comprising bipolar and unipolar polarizations.

3.2.2.1 Bipolar polarization

The measured total current density (J_{tot}) through the ZnO/PDMS composite can be decomposed into three components: conduction (J_{con}), dielectric (J_{die}), and ferroelectric (J_{ferro}) [170]. Figure 3.3 displays the J-E hysteresis loops of both random and aligned ZnO composites elaborated with the same volume fraction.

Cette thèse est accessible à l'adresse : http://theses.insa-lyon.fr/publication/2022LYSEI006/these.pdf
© [X. Zhang], [2022], INSA Lyon, tous droits réservés

For a sake of simplicity, only those filled with 24% vol. of ZnO were presented. Under a maximum amplitude of 1V/µm delivered by an external high-voltage source, these samples were revealed to be the most appropriate choice to better highlight the dielectrophoresis effect. As indicated in Figure 3.3(a), the 0-3 matrix exhibits a near-capacitive behavior for a whole range of the applied electric field, which is confirmed by a circular-shaped J-E curve. It is generally believed that the dielectric current density (J_{die}) has circular relationship with the electric field while the conduction one (J_{con}) exhibits a linear response relating to Ohm's law. Concerning the aligned composite shown in Figure 3.3(b), a transition from capacitive to conductive behavior is observed with increasing electric field, which is proven by the disappearance of the circular-shape. Beyond the switching field, the resulting current intensity drastically enhances, reflecting the semiconductor properties of the ZnO materials. As demonstrated by COMSOL simulation (seen in subsection 2.1.3.4), the aligned particles are driven by higher field level than the random particles. This justifies why the 1-3 structured composites exhibits lower switching voltage than the 0-3 isotropic sample. Consequently, dielectrophoresis of the ZnO/PDMS composite improves the probability of forming conduction paths, thereby increasing the electrical conductivity of material.

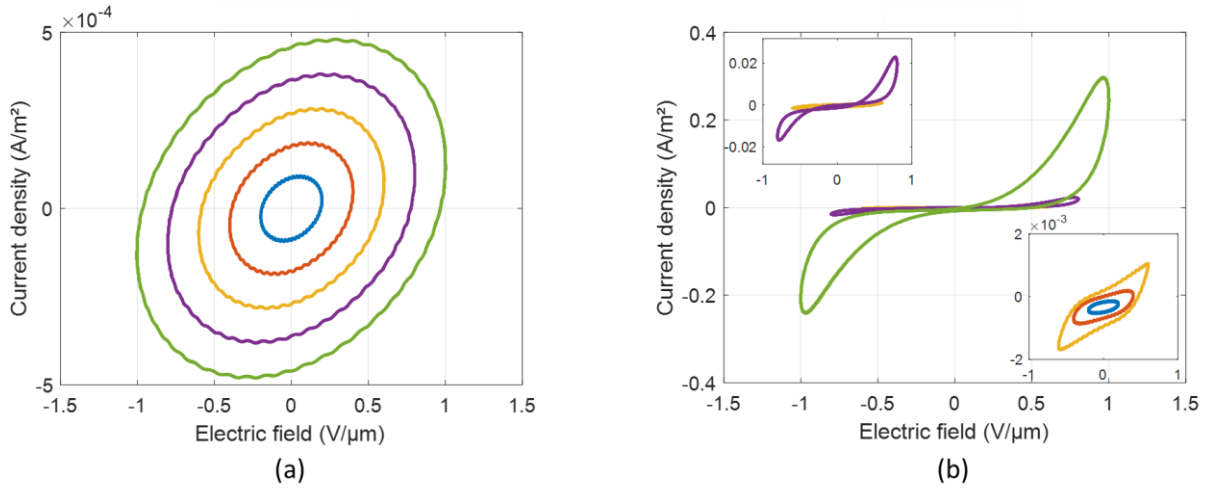

Figure 3.3. Representative current density vs. electric field of (a) random composite; and (b) structured composite. Both samples are filled with 24% vol. of ZnO microparticles and are subjected to different levels of electric field

Figure 3.4(a)-(b) illustrates the variation of J-E hysteresis loop for the 0-3 and 1-3 ZnO/PDMS composites elaborated with various concentrations (i.e. 14%, 24%, 34%, and 44%) under a given electric field of 0.4 V/µm amplitude. This value is chosen in order to ensure that either structured or random samples behave as quasi-capacitive like structure, allowing to easier identify the three components of current density (J_{con}, J_{die}, and J_{ferro} [170]). As expected, higher ZnO particle content leads to superior J-E slope. Actually, the conductivity and dielectric of these materials are boosted, giving raise to enhanced J_{con} and J_{die}. A comparison between Figure 3.4(a) and (b) clearly shows that the aligned samples exhibit higher current density as opposed to those randomly dispersed. This result is in consistent to the one performed in subsection 3.2.1.

Cette thèse est accessible à l'adresse : http://theses.insa-lyon.fr/publication/2022LYSEI006/these.pdf
© [X. Zhang], [2022], INSA Lyon, tous droits réservés

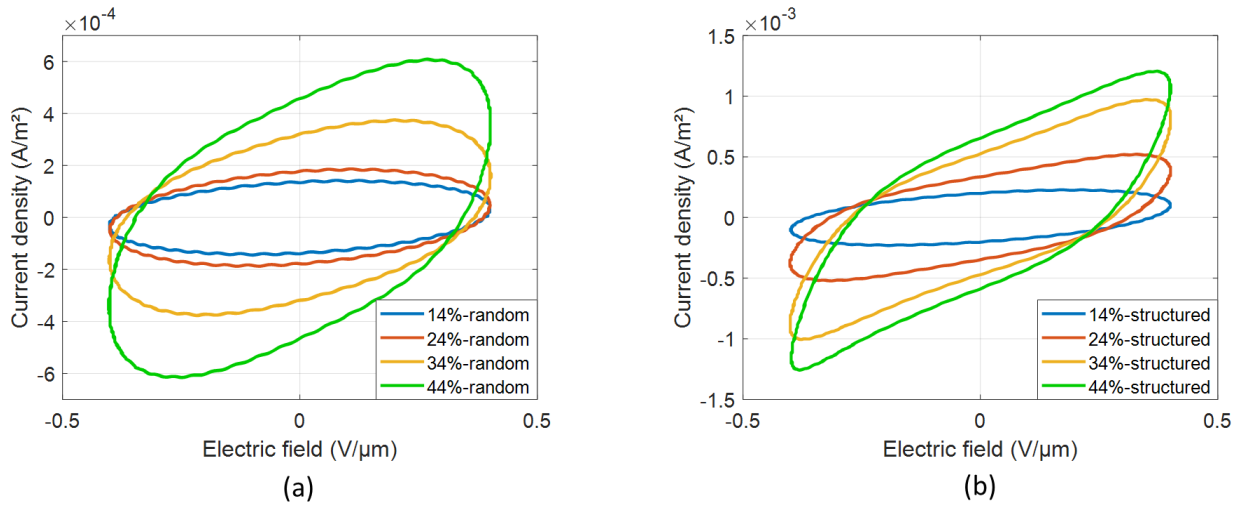

Figure 3.4. Hysteresis current density loops for ZnO/PDMS composites of different concentrations (a) without and (b) with dielectrophoretic alignment. All samples are excited by the same amplitude of electric field.

In order to further explore the mechanism inside the ZnO/PDMS composites under varying electric field, a simple way to estimate the permittivity and conductivity is introduced. The conduction mechanisms in the dielectric film can be divided into electro-limited conduction, which depends on electrode-dielectric contact, and bulk-limited conduction relating to the dielectric itself [105]. In this case, for simplification only bulk-limited conduction mechanisms are considered. Among them, the capacitive current (J_{die}) is assumed to be more dominant than the Ohmic conduction current (J_{con}) under low voltage application. In addition of these current densities, ferroelectric property of ZnO fillers should be getting involved (J_{ferro}). Taking 44% vol. of randomly dispersed sample as a typical example, the analysis result depicted in Figure 3.5 consists of several steps:

- Firstly, as shown in Figure 3.5(a), the conduction current density J_{con} is extracted and assumed to be linear to the electric field (E) according to the Ohm's law. The electrical conductivity (σ) can be inferred from:

$$J_{con} = \sigma E \tag{3.2}$$

- Secondly, the charge density or the polarization (D_T) can be determined by integrating the current density over time after subtracting the conduction element. The polarization only consists of the dielectric (D_{die}) and ferroelectric properties (D_{ferro}) that can be expressed as:

$$D_T = D_{die} + D_{ferro} = \int (J_{tot} - J_{con}) dt \tag{3.3}$$

Figure 3.5(b) describes the linear polarization-versus-electric-field (D-E) characterization, allowing to conclude that the relative permittivity (ε_r)) is almost constant under low input voltage range. Considering the dielectric loss factor (denoted as ε_r'', the imaginary part of ε_r)) is negligible, only the real part of ε_r (denoted as ε_r')) is taken in consideration. In other words, ε_r' attributed to the dielectric charge (D_{die}) can be obtained by fitting with the following linear model:

$$D_{die} = \varepsilon_0 \, \varepsilon_r' \, E \tag{3.4}$$

Cette thèse est accessible à l'adresse : http://theses.insa-lyon.fr/publication/2022LYSEI006/these.pdf
© [X. Zhang], [2022], INSA Lyon, tous droits réservés

Therefore, a relative permittivity approximately 22.53 for the 44% vol. random composite is derived, which is highly in agreement with the one measured via the dielectric spectrometer in the following (seen in subsection 3.4.1). It is noteworthy that the polarization (D_T) displays very small hysteresis area, demonstrating poor ferroelectric property of the ZnO composites.

- Thirdly, the fitted polarization D_{die} can be subtracted from the total polarization, allowing to draw the ferroelectric polarization (D_{ferro}, yellow line in Figure 3.5(b)). The remnant polarization, corresponding to the D_{ferro} value when the electric field turns back to zero, is very closed to zero, confirming the weak ferroelectric effect of the ZnO material. Actually, ZnO is considered as a non-ferroelectric material due to the unite cell configuration [171]. Since the covalent bonds between tetrahedrally coordinated O^{2-} and Zn^{2+} ions are too strong that the spontaneous polarization cannot switch by an external electric field [51,172]. The ferroelectric behavior can be observed only in the case of structural modifications occurring on the unite cell. For instance, the ZnO is doped with substitutional atoms (e.g. Sb) or un-doped ZnO nanorods grown vertically on a Pt substrate [171,173].
- Lastly, the dielectric current and ferroelectric current densities are carried out through the gradient of the capacitive polarization ($\frac{dD_{die}}{dt}$) and the ferroelectric polarization ($\frac{dD_{ferro}}{dt}$), respectively shown in Figure 3.5(a). Figure 8 (c)-(d) describes the time varying behavior of the electric field together with the resulting current density, and the charge density. On one hand, the electric field lags the current density, which is corelate to the dominant capacitive property represented by the circular-shaped J-E curve. On the other hand, the electric field and the charge density are in-phase, confirming linear relationship between D_T and E.

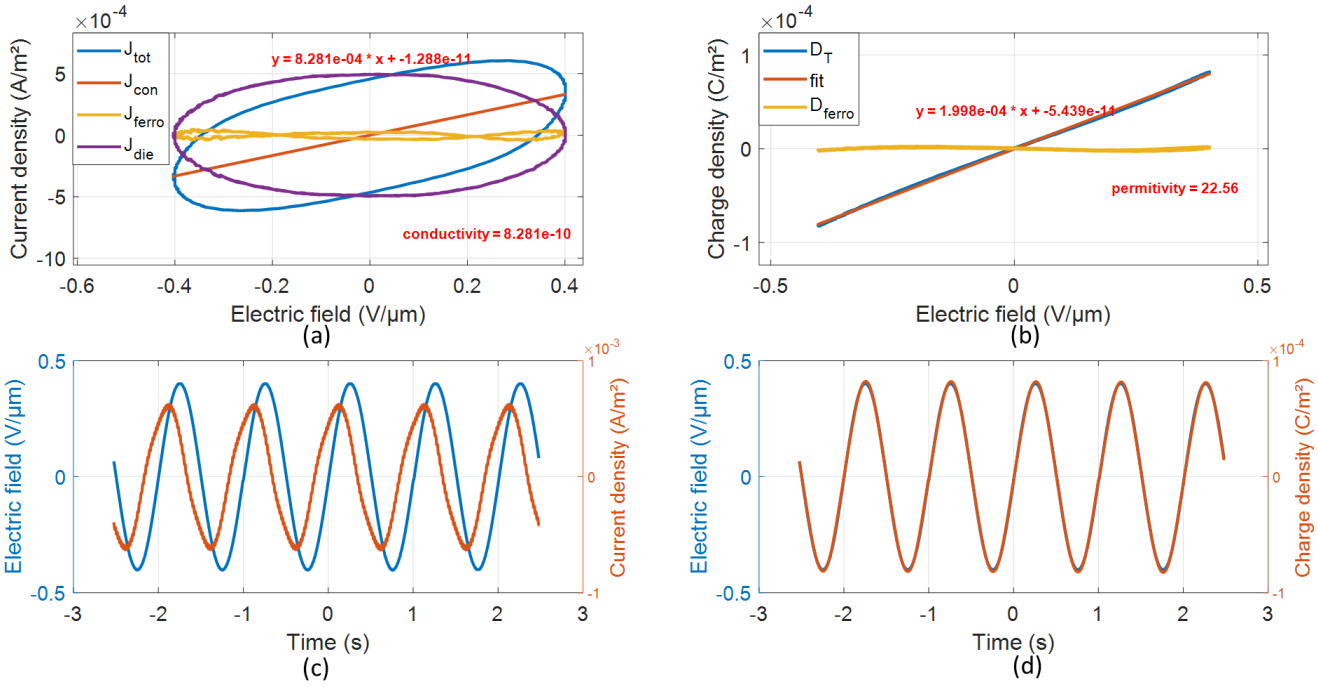

Figure 3.5. Electrical characterization of the 44% vol. random ZnO/PDMS composite under input electric field of 0.4 V/μm amplitude. (a) Decomposition of the total measured current densities into three components (J_{con}, J_{die}, and J_{ferro}), the conductivity is deduced using the Ohm's law. (b) Polarization loop of charge density versus electric field,

Cette thèse est accessible à l'adresse : http://theses.insa-lyon.fr/publication/2022LYSEI006/these.pdf
© [X. Zhang], [2022], INSA Lyon, tous droits réservés

allowing to determine the dielectric permittivity and ferroelectric properties of the composite. Time evolution of electric field and resulting (c) current density, and (d) charge density.

The relative permittivity, with corresponding coefficient of determination (R^2) and the electrical conductivity of the 0-3 and 1-3 composites at different ZnO content have been calculated and summarized in Table 3.2. Clearly, the higher the volume fraction of ZnO, the better the relative permittivity and the conductivity. Meanwhile, an improvement of the permittivity assigned to the introduction of ZnO/ZnO interface polarization has been achieved with the 1-3 matrix. Furthermore, a substantial increase of 3 to 6 times in the conductivity resulted from enhanced short-conducting paths were observed for the composite embedded with aligned ZnO particles.

It is worth noting that using experimental measurement to derive three unknown parameters, even with the advantages of fitting it with analytical model, leads to inevitable errors. Especially for the material with low ferroelectricity like ZnO, i.e., generally considered non-ferroelectric. However, the purpose here is not to accurately quantify the ferroelectricity level of ZnO composites, which is usually characterized by estimating the remnant polarization based on ferroelectric-current-versus-electric-field loop [170]. The objective involves in using the resulting D-E hysteresis responses as a qualitative indicator to confirm the piezoelectric behavior of the developed composites. As suggested, small hysteresis in ferroelectric polarization loop clearly manifests low piezoelectricity, which in turn makes it difficult and challenging to extract the ferroelectric current in comparison with the other dominant current components (leakage and capacitive). Accordingly, to confirm in a more rigorous manner the piezoelectric properties of ZnO composites, we designed in a special experimental setup to measure the piezoelectric charge coefficient with a higher sensitivity in the section 3.5.

Table 3.2. Calculation results for random and aligned ZnO/PDMS at different filler concentrations.

Volume fraction	ε_{random}	R^2 for ε_{random}	$\varepsilon_{structured}$	R^2 for $\varepsilon_{structured}$	σ_{random} (S/m)	$\sigma_{structured}$ (S/m)
14%	6.16	0.999	9.34	0.999	0.397E–10	2.442E–10
24%	8.05	0.999	17.01	0.998	1.153E–10	8.594E–10
34%	15.07	0.999	25.52	0.995	3.924E–10	18.69E–10
44%	22.56	0.999	30.87	0.994	8.281E–10	24.09E–10

3.2.2.2 Unipolar polarization

To further investigate the electric response where the ferroelectric behavior was excluded, a positive sinusoidal wave (unipolar) was used. The electric field amplitude was chosen to be equal 1 V/µm (i.e., above the switching field), at which the conduction mechanism turned to be the dominant component with respect to the capacitive one. The material behaves as a semiconductor that enables the flow of current as soon as the electric field is above the switching value. Hence, only 0-3 composites with 44% vol., and 1-3 composites with filler content above 24% exhibit nonlinear J-E characteristics under a high electric field (Figure 3.6). The results point out a significant hysteresis curve caused by dielectric losses, which is drastically increase with the voltage level. The following analysis will clarify this issue.

Cette thèse est accessible à l'adresse : http://theses.insa-lyon.fr/publication/2022LYSEI006/these.pdf
© [X. Zhang], [2022], INSA Lyon, tous droits réservés

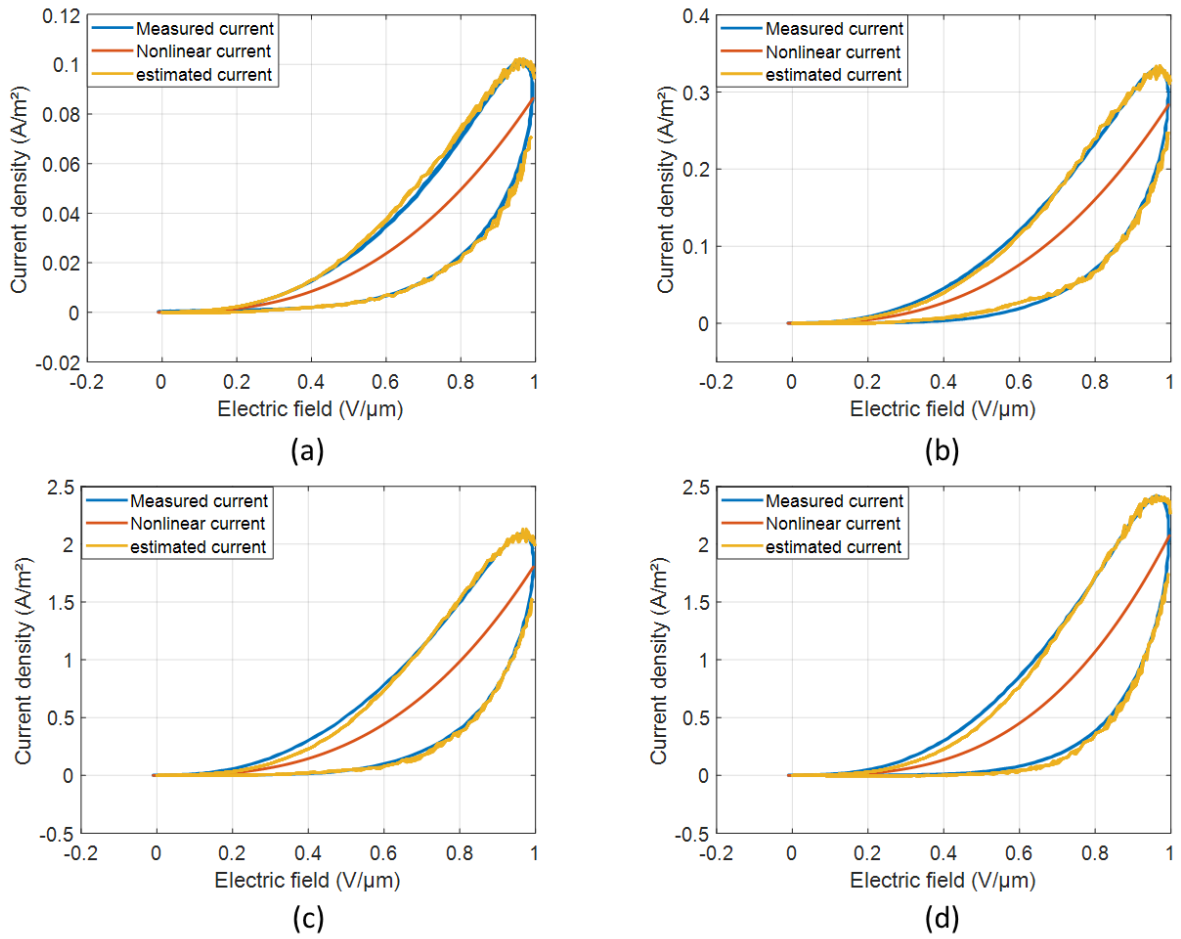

Figure 3.6. Nonlinear J-E characteristics that is powered by a high unipolar voltage at 1 Hz frequency and 1 V/μm amplitude. Experimental measure and theoretical model of J-E curve at sample of (a) random composite with 44% vol., and structured composite of (b) 24%vol., (c) 34% vol., (d) 44%vol.

The measured total current density (J_{tot}) is supposed as the sum of the conduction current (J_{con}) and the dielectric current (J_{die}):

$$J_{tot} = J_{con} + J_{die} \tag{3.5}$$

When a relatively high electric field was applied, the abrupt increasing of current density within composite is essentially attributed to the charge accumulation on grain barriers, which is the same cause of ZnO varistors effect [97,98]. Therefore, considering the empirical relation between current I and voltage V in ZnO varistors, the nonlinear properties of ZnO composites can be expressed by:

$$I = KV^{\alpha} \tag{3.6}$$

where K is a constant and α is a nonlinear coefficient varying with voltage. The non-ohmic parameter α depends on the type of boundary junctions between the grains and reveals the nonlinear variation of resistivity with the voltage [174]. Table 3.3 shows the values of α fitted from the nonlinear model under a 1 V/μm external electric field. Eq (3.1) can be derived from Eq (3.6) and the nonlinear coefficient α appears in both equations is same parameter. The discrepancy of the values calculated in two cases can be explained

Cette thèse est accessible à l'adresse : http://theses.insa-lyon.fr/publication/2022LYSEI006/these.pdf
© [X. Zhang], [2022], INSA Lyon, tous droits réservés

to the fact that different applied voltages give rise to different α. Interestingly, under same filler content (44% vol.), α of structured composite is higher than of random composite, indicating the distribution of the ZnO particles contribute to the nonlinear effect. Highly connections of ZnO particles entail narrow insulting gap of PDMS, thus resulting high electric level on the boundary of particles, which in turn facilitate the nonlinear conducting behaviors. On the other hand, α increases as the concentration of the ZnO phase increases. Indeed, the more ZnO particles, the more conduction paths appearing within the composites.

Table 3.3. Fitting results of variable α from the nonlinear model with different samples

Samples	α	R^2
$\mathbf{44\%}_{random}$	2.598	0.837
$\mathbf{24\%}_{structured}$	2.646	0.828
$\mathbf{34\%}_{structured}$	2.836	0.810
$\mathbf{44\%}_{structured}$	3.05	0.791

In addition to the nonlinear conduction current, the dielectric current density associated to the pure dielectric can be expressed as:

$$J_{die} = \frac{dE}{dt}\,\varepsilon_0 \times \varepsilon_r(E) \tag{3.7}$$

where $\varepsilon_r(E)$ is the relative permittivity as a function of the electric field E. Generally, ε_r can be described as a complex number $\varepsilon_r = \varepsilon_r' - i\varepsilon_r''$, consisting of a real component ε_r' and an imaginary component ε_r''. The dielectric loss is defined as the dissipation of electrical energy induced in an alternating electric field due to the movement or rotation of dipoles. At low frequency and high electric field, more free charge motion in the composites causes that ε_r'' is far larger than ε'_r. Hence, Eq. (3.7) becomes:

$$J_{die} = -\frac{dE}{dt}\,\varepsilon_0 \times i\varepsilon_r''(E) \tag{3.8}$$

where i is the imaginary number. In the sinusoidal regime, $\frac{dE}{dt} = i\omega E$, which allow to infer that J_{die}, J_{tot} and E are perfectly in phase. Accordingly, the estimated current density ($J_{estimated}$) is estimated by:

$$J_{estimated} = J_{con} + \frac{dE}{dt}\,\varepsilon_0\varepsilon_r''(E) \tag{3.9}$$

As seen in Figure 3.6, the estimated current density is well coherent with the measured one, suggesting high reliability of the theoretical model depicted in Eq. 3.9. The fitted loss factor of all 0-3 and 1-3 matrix deduced from Eq. (3.8) is illustrated in Figure 3.7, reflecting nonlinear electric field effect of the dielectric loss. Such a nonlinear behavior is consistent to the approach reported on Yang *et al*., which is deduced from polynomial relationship between the dielectric loss and the applied electric field [107]. The increasing trend of ε_r'' versus E shown in Figure 3.7 is completely different to the model under low electric field, where the dielectric loss is supposed to be stable and small under a given frequency. The fact is that at high polarization of 1 V/μm, the conduction mechanism is the dominant contribution, whereas at low polarization of 0.4 V/μm, the dielectric mechanism is regarded as the primary behavior. Moreover, it was revealed that the simulated dielectric loss factor increases with the increasing ZnO content. Additionally, ε''_r is impacted by the distribution of particles due to the increase trend of the free charges and the dipole oscillation in ZnO at

Cette thèse est accessible à l'adresse : http://theses.insa-lyon.fr/publication/2022LYSEI006/these.pdf
© [X. Zhang], [2022], INSA Lyon, tous droits réservés

low frequency. Interestingly, the dielectric loss shown in Figure 3.7 under low electric field is relatively high compared to the value measured in dielectric spectrometer in the following, suggesting this model is more applicable for the high electric field case.

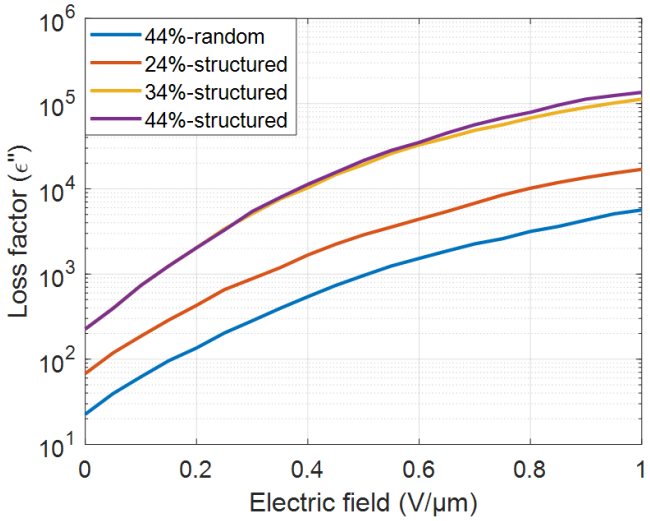

Figure 3.7. The simulated loss factor derived from the dielectric current for the samples of a random and structured distribution with different volume fractions.

3.3 Mechanical characterization

As known in the piezoelectric constitutive equations, the piezoelectric coefficient is related to the dielectric properties and mechanical properties of piezoelectric material. Additionally, ZnO composites can be considered as an effective homogeneous piezoelectric material. Thereby the evaluation of the Young's modulus (Y) and permittivity (ε) in composites should be important and necessary. Moreover, in our case, an estimation of the corresponding parameters in ZnO microparticles (e.g. Y_{ZnO}, ε_{ZnO}) via respective analytical approach is beneficial to predict the piezoelectric behavior in ZnO.

In this study, mechanical properties are investigated on both 0-3 and DEP 1-3 composites with different particles volume fraction. Actually, in most applications of ZnO composites like varistors, energy harvesting devices, piezoelectric sensor, moderate stress solicitation is usually employed so as not to deteriorate the materials [161][96,175]. Because the composite materials experience tensile and compressive deformation depending on the application environment, it is necessary to evaluate the tensile and compressive behaviors, as well as the impact of dielectrophoresis.

3.3.1 Tensile mode

These materials are subjected to monotonic tensile testing, and their stress-strain response is displayed in Figure 3.8 a and b, respectively for the random and aligned samples. A typical stress-strain curve of a polymer as well as its composite consists of 3 phases: 1) a linearity at elastic strain region, 2) a nonlinear behavior in plastic regime, and 3) final fracture [176].

Table 3.4 summarizes the average tensile modulus ($Y_{tensile}$) of ZnO/PDMS film obtained through the linear fitting of the initial elastic stress-strain region near the origin (10%) (Figure 3.8). The tensile modulus

Cette thèse est accessible à l'adresse : http://theses.insa-lyon.fr/publication/2022LYSEI006/these.pdf
© [X. Zhang], [2022], INSA Lyon, tous droits réservés

of pure PDMS obtained in our experiment (~2.111 MPa) is close to the value reported by Johnston et al. (~1.32 MPa) employing same commercial PDMS (Sylgard 184)[177], confirming the accuracy of our experiments. A significant enhancement of tensile modulus is observed with the increasing volume fraction of ZnO, verifying the possibility of tailoring the mechanical properties through the control of the filler content. Indeed, increasing ZnO content makes the film less flexible as more brittle particles added into the matrix. Therefore, the failure strain decreases with ZnO concentration, whereas the failure stress increases. Interestingly, there is no distinct different of tensile modulus between the 0-3 and the 1-3 composites. It is probably due to the fact that the dielectrophoretic field direction is not the same as the mechanical tensile stress.

It is possible to estimate the ultimate tensile strength (T_{max}) of the composites by continuously increasing the applied stress until breakdown occurs (see Figure 3.8 and Table 3.4). With the increasing volume fraction, the ultimate tensile strength coherently enhances while the ultimate failure strain decreases, simultaneously. This behavior can be explained due to the defect function of ZnO particles [96].

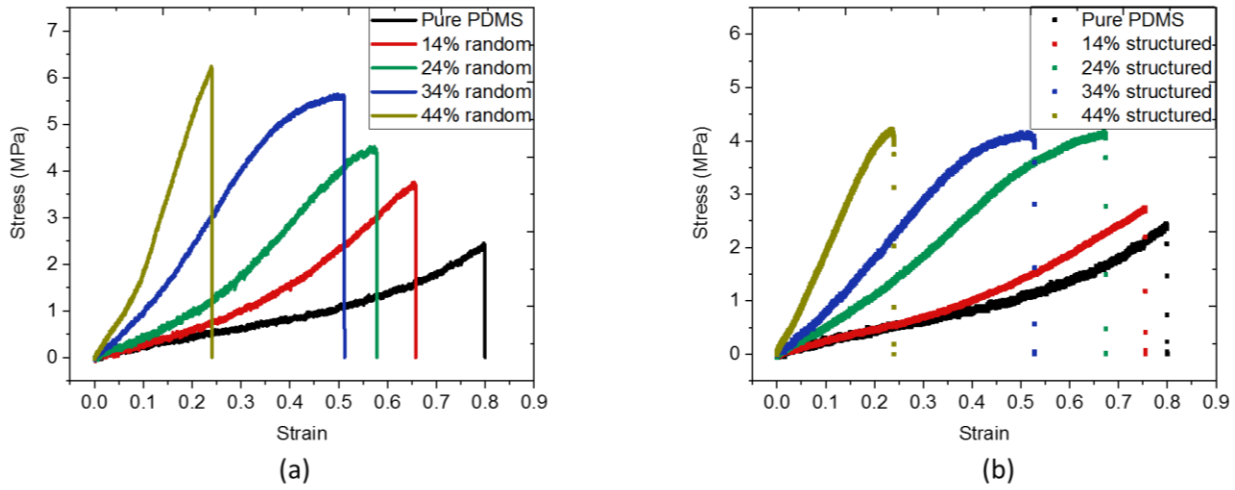

Figure 3.8. The tensile stress-strain response of (a) random, and (b) aligned-ZnO/PDMS composites with different particle concentrations.

Table 3.4. The average tensile elastic modulus from the fitting data in the linear region

Parameter	Pure PDMS	$14\%_{vol}$	$24\%_{vol}$	$34\%_{vol}$	$44\%_{vol}$
Y_{random} (MPa)	2.111 ± 0.106	2.364 ± 0.053	4.576 ± 0.027	8.769 ± 0.020	18.140 ± 0.046
$Y_{structured}$ (MPa)	-	2.606 ± 0.009	5.127 ± 0.018	8.793 ± 0.021	18.593 ± 0.022
$T_{max(random)}$(MPa)	2.435	3.751	4.518	5.628	6.243
$T_{max\ (structured)}$(MPa)	-	2.749	4.166	4.162	4.218

Reinforcement mechanisms in polymeric composites are influenced by the dispersion and distribution of fillers and the interfacial interaction between polymer and fillers [178]. The mechanical properties of composites can be predicted using different theoretical models. For a two-phase material, the rule of mixture

Cette thèse est accessible à l'adresse : http://theses.insa-lyon.fr/publication/2022LYSEI006/these.pdf
© [X. Zhang], [2022], INSA Lyon, tous droits réservés

is the simplest way to predict the Young's modulus based on the arrangement of phases (series or parallel). According to these models, the effective Young's modulus of composites (Y_{eff}) should locate between the upper bound given by parallel model [179]

$$Y_{eff} = Y_f V_f + Y_m V_m \tag{3.10.1}$$

and a lower bound from series model

$$Y_{eff} = \frac{Y_f Y_m}{Y_f V_m + Y_m V_f} \tag{3.10.2}$$

where Y and V represent the Young's modulus and volume fraction, respectively, whereas subscripts f and m denote the filler and matrix, respectively. Above models are usually applied in composites with aligned fibers. It is assumed that the fibers are distributed uniformly and deformed under uniform stress/strain. It seems that the reinforcement effect of the filler is independent of its size and aspect ratio from above equations.

The Halphin-Tsai model is a commonly used model by considering the geometry and orientation of filler (e.g. aspect ratio) [180][181]. It is a semi-empirical model based on the self-consistent method. This model have successfully predicted in short-fiber composites [182]. However, the Halpin-Tsai model is preferred to fit the results at low volume fraction of filler ascribed the underestimation of values at high volume fraction [183]. It is later modified by Nielsen to estimate the modulus of composite reinforced with particles and short fibers at high volume fraction. Compared to Halpin-Tsai model, Nielsen model considers an additional parameter which is the type of packing for a two-phase system. Then the modulus of elasticity in Nielsen model can be described as [183]

$$Y_{eff} = Y_m\left(\frac{1+A\eta_N V_f}{1-\psi\eta_N V_f}\right) \tag{3.11.1}$$

where

$$A = K_E - 1 \tag{3.11.2}$$

$$\eta_N = \frac{\frac{Y_f}{Y_m} - 1}{\frac{Y_f}{Y_m} + A} \tag{3.11.3}$$

$$\psi = 1 + \left(\frac{1-\zeta_{max}}{\zeta_{max}^2}\right)V_f \tag{3.11.4}$$

where A and ψ are parameters related to Einstein coefficient (K_E) and the maximum packing fraction of filler (ζ_{max}). K_E depends on the aspect ratio and orientation of the filler, giving a value of 2.5 for spherical particles [184]. Whereas ζ_{max} is defined as the true volume of the fillers divided by the volume they appear to occupy when packed to their maximum extent [185]. As seen in Figure 3.9, experimental tensile modulus of random micro-ZnO/PDMS composites are plotted as a function of ZnO concentration. By the fitting between the measured data and Nielsen model, the fitted curve is displayed in Figure 3.9 with analytical parameters summarized in Table 3.5. The Young's modulus of ZnO is estimated as ~163.4 GPa, which is reasonable compared to the value of ~144 GPa reported for bulk ZnO [186,187] and value of 61-125 GPa reported for ZnO thin films [188,189]. Alternatively, the value of maximum packing fraction (ζ_{max}) has been demonstrated to be 0.524 for spherical fillers with a simple cubic packing and 0.601 for the case that

Cette thèse est accessible à l'adresse : http://theses.insa-lyon.fr/publication/2022LYSEI006/these.pdf
© [X. Zhang], [2022], INSA Lyon, tous droits réservés

spherical fillers are packed randomly loose [178]. Thus, the value of ζ_{max} is found to be 0.508 in our case is reasonable with a high coefficient of determination (R^2).

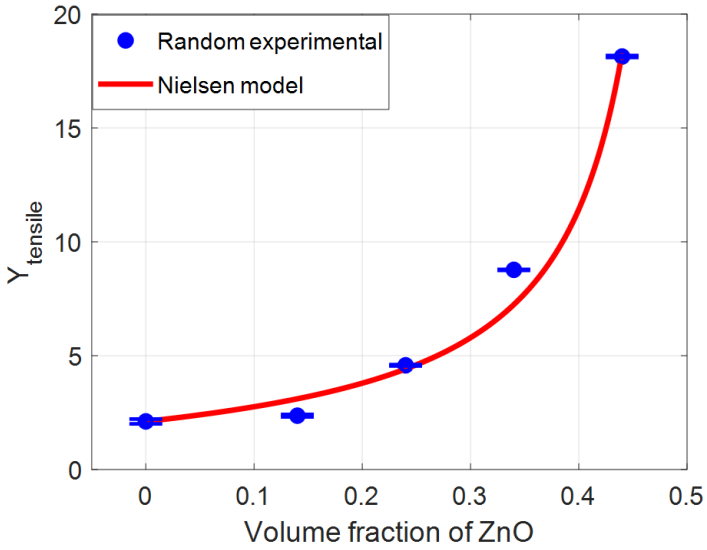

Figure 3.9. Experimental and fitting tensile modulus of random micro-ZnO/PDMS composites as a function of ZnO concentration.

Table 3.5. Fitting data from Nielsen model for random micro-ZnO/PDMS composites

Parameter	Y_f (GPa)	Y_m (MPa)	ζ_{max}	R^2
Y_{random} (MPa)	163.4	2.111	0.508	0.984

3.3.2 Compressive mode

The compressive stress-strain curves of the random and structured 44% vol. composite are plotted in Figure 3.10(a), (b), respectively. The composites firstly experience a stepped loading profile in which a series of fixed strains (including 0.2, 0.4, 0.6, 0.7) were exerted. After reaching the maximum, unloading processes were conducted for a given deformation of the specimen. Both random and structured composite undergo a complete recovery, demonstrating how strong and flexible mechanical characteristics the developed composites are. Interestingly, the structured composite exhibits somewhat larger hysteresis area, reflecting higher mechanical losses caused by structuration of particles. For a better evaluation of the compressibility, the peak magnitude of stress with associated peak strain are illustrated in Figure 3.10(c). The stiffness (slope of the stress-strain) is increased after alignment of particles in the direction of compressive force. The compressive elastic modulus ($E_{compressive}$) is calculated and displayed in Table 3.6. It can be pointed out that the structured composites provide reinforcement along the particle's orientation, giving raise to improves mechanical properties. To some extent, the values of elastic moduli vary with the mechanical tests, and higher in the compression mode than in the tensile mode [190], whatever the material connectivity (0-3 or 1-3).

Cette thèse est accessible à l'adresse : http://theses.insa-lyon.fr/publication/2022LYSEI006/these.pdf
© [X. Zhang], [2022], INSA Lyon, tous droits réservés

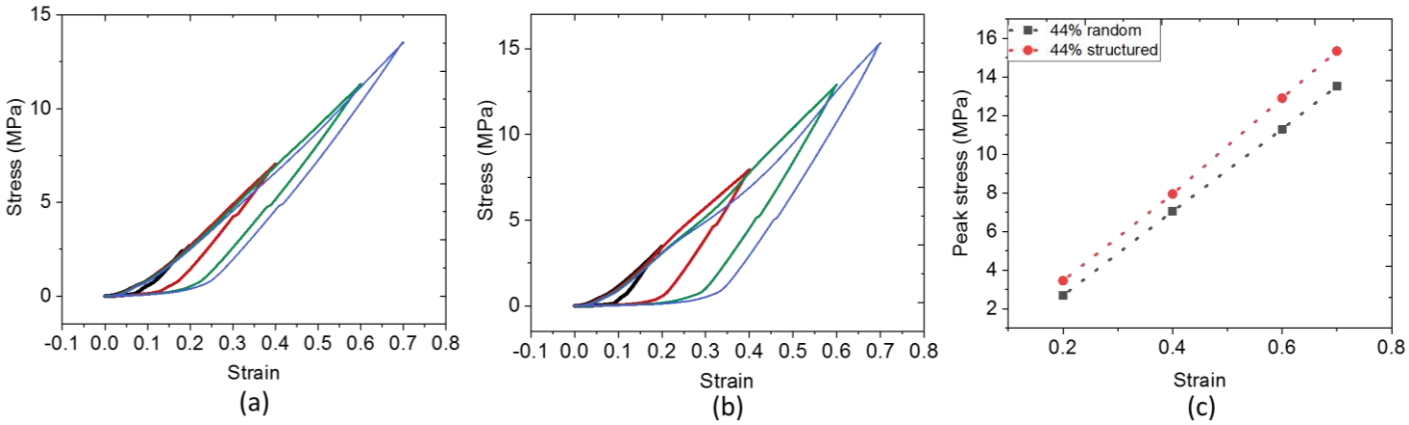

Figure 3.10. The compressive stress-strain curve of the 44% vol. (a) random and (b) structured ZnO/PDMS composite; (c) peak stress *vs*. strain for the random and structured composites.

Table 3.6. The average compressive elastic modulus from the fitting data in the linear region

Parameter	**Pure PDMS**	$\mathbf{14\%_{vol}}$	$\mathbf{24\%_{vol}}$	$\mathbf{34\%_{vol}}$	$\mathbf{44\%_{vol}}$
E_{random} (MPa)	11.155 ± 0.302	13.062±0.069	13.612±0.090	18.252±0.594	21.620±0.103
$E_{structured}$ (MPa)	-	13.372±0.889	15.001±0.343	19.209±0.386	23.842±0.398

3.4 Dielectric characterization

3.4.1 Effect of particle size

3.4.1.1 Random nano-ZnO/PDMS composites

Figure 3.11(a) displays the variation of the dielectric constant versus frequency for the PDMS polymer incorporated with different volume fractions of ZnO nanoparticles. For all samples, decreasing trend of dielectric constant with increasing frequency at a given temperature can be attributed to the dielectric relaxation mechanism of the ZnO-PDMS composite. Specifically, at high frequency, dipoles are not sufficiently rapid to orient themselves, provoking a lag between the oscillating dipole and the applied field dynamics, hence dielectric constant is decreased with the increase of frequency [191,192]. Moreover, it can be seen that the dielectric constant of the pure PDMS and the composites with low concentrations (e.g., 8% or 13%) is somewhat stable for a large range of frequency. On the other hand, when the ZnO volume content is increased to 17% or 21%, the dielectric constant significantly increases under low dynamic excitations (i.e., 0.1Hz-1Hz) and decreases with higher frequency. This phenomenon can be ascribed to the interfacial polarization, also known as the Maxwell-Wagner-Sillars effect. The increase in the interfacial area between polymer and nanoparticles leads the interfacial polarization being the predominant physical effect for their dielectric performance at lower frequencies [192]. Subsequently, the decreasing trend in dielectric constant is particularity more visible at materials with higher content of ZnO. Conversely, with higher dynamic excitation, i.e., above 1 kHz, the permittivity can be considered to be frequency-independent.

Cette thèse est accessible à l'adresse : http://theses.insa-lyon.fr/publication/2022LYSEI006/these.pdf
© [X. Zhang], [2022], INSA Lyon, tous droits réservés

As observed in Figure 3.11(b), the experimental dielectric constant of nano-ZnO/PDMS composite substantially increases with the ZnO content at 1 kHz. Various theoretical models developed by Maxwell-Garnett, Lichtenecker, and Jayasundere-Smith were used to predict the dielectric constants plotted in Figure 3.11(b). For the sake of simplicity, these approaches are supposed to be frequency-independent. As a result, a deeper analysis of the dielectric property is performed under a dynamic of 1 kHz, above which frequency-variation of the permittivity is relatively moderate.

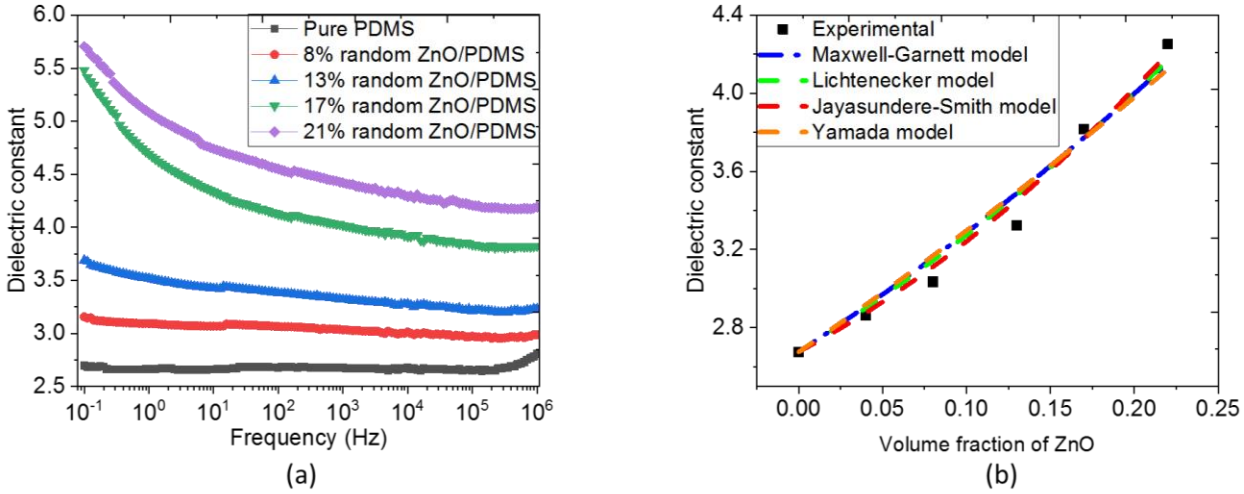

Figure 3.11. Variation of the dielectric constant of nano-ZnO/PDMS composites as a function of (a) frequency and (b) ZnO concentration measured at 1 kHz together with a comparison of associated models.

The Maxwell-Garnett model is suitable for a two-phase composite with spherical particles in a continuous medium given by [193]:

$$\varepsilon_{eff} = \varepsilon_m \frac{2\varepsilon_m+\varepsilon_p +2V_p(\varepsilon_p-\varepsilon_m)}{2\varepsilon_m+\varepsilon_p-V_p(\varepsilon_p-\varepsilon_m)} \tag{3.12}$$

where V_p is the volume content of ZnO in composite; and ε_m, ε_p , and ε_{eff} represent the dielectric constant of the polymer matrix, particles, and composites, respectively. The relative permittivity of PDMS (ε_m) is known as 2.68, according to technical Data sheet of "SYLGARD™184 Silicone Elastomer". This result is also confirmed by dielectric spectroscopy using SOLARTRON (Figure 3.11(a)) where the dielectric constant of the pure PDMS sample is almost frequency dependent.

Lichtenecker logarithmic law is described for a two-component system based on the logarithmic dielectric constants of each component [194]:

$$\log \varepsilon_{eff} = V_p \log(\varepsilon_p) + V_m log\varepsilon_m \tag{3.13}$$

where V_m is the volume fraction of the polymer matrix in the composites. Jayasundere and Smith developed an equation to calculate the effective dielectric constant, including interactions between neighboring spheres [195]:

Cette thèse est accessible à l'adresse : http://theses.insa-lyon.fr/publication/2022LYSEI006/these.pdf
© [X. Zhang], [2022], INSA Lyon, tous droits réservés

$$\varepsilon_{eff} = \frac{V_m\varepsilon_m+\varepsilon_p V_p\left[\frac{3\varepsilon_p}{\varepsilon_p+2\varepsilon_m}\right]\left[1+\frac{3V_p(\varepsilon_p-\varepsilon_m)}{\varepsilon_p+2\varepsilon_m}\right]}{V_m+V_p\left[\frac{3\varepsilon_p}{\varepsilon_p+2\varepsilon_m}\right]\left[1+\frac{3V_p(\varepsilon_p-\varepsilon_m)}{\varepsilon_p+2\varepsilon_m}\right]} \quad (3.14)$$

Yamada *et al.* studied a binary system composed of the continuous medium and ellipsoidal particles and proposed a dielectric model that can be expressed as [86]:

$$\varepsilon_{eff} = \varepsilon_m\left[1+\frac{nV_p(\varepsilon_p-\varepsilon_m)}{n\varepsilon_m+V_m(\varepsilon_p-\varepsilon_m)}\right] \quad (3.15)$$

where *n* is a shape-dependent parameter, relating to the morphology of ellipsoidal particles. It is noticed that such a parameter is considered only for the Yamada model, as opposed to the other models, in which the shape of particles has not been considered for the estimation of the dielectric constant.

The fitting between experimental data and theoretical models allows for the obtaining of the relative permittivity ε_p of the PDMS polymer filled with ZnO nanoparticles as summarized in Table 3.7. Interestingly, different analytical models give slight variations of the dielectric constant, e.g., from 13.4 to 22. However, as highlighted in Figure 3.11(b), all models lead to an excellent trend with respect to experimental data, reflecting high reliability of the theoretical approach for PDMS composite with the volume content of ZnO particles up to 20%. Compared to the other models, that of Jayasundere-Smith results in the highest coefficient of determination (i.e., R-squared or R^2 equals 0.985). Furthermore, this approach allows for considering of the interactions between the neighboring particles as opposed to the Maxwell-Garnett and Lichtenecker estimations. Thus, the expected dielectric constant of the nano-ZnO composite is chosen equal to approximately 13.4. This value is used in the Yamada equation (Eq. 3.15) to determine the shape factor *n* (cf. Table 3.7).

Table 3.7. Fitting parameters from various models of nano-ZnO/PDMS composite

Model	ε_m	ε_p	n	R^2
Maxwell-Garnett model	2.68	22.06 ± 2.92	-	0.969
Lichtenecker model	2.68	20.12 ± 1.56	-	0.974
Jayasundere-Smith model	2.68	13.40 ± 0.65	-	0.985
Yamada model	2.68	13.40	4.97± 0.71	0.962

3.4.1.2 Random micro-ZnO/PDMS composites

Figure 3.12(a) illustrates the dielectric spectroscopy of the micro-ZnO/PDMS composites with a different volume fraction from 0% to 44%. As expected, the relative permittivity ε_p is greatly enhanced as a function of particle concentration, where the 44% vol. sample leads to a dielectric content of 19 under a low frequency of 0.1 Hz, which is six times increased as opposed to the pure one. A multiple factor of five times has been achieved at a higher dynamic of 1 kHz. As discussed before, interfacial dipole moments contribute to the frequency-dependent behavior of the dielectric site, this effect is prominent when the concentration is above 34% volume (cf. Figure 3.12(a)).

Cette thèse est accessible à l'adresse : http://theses.insa-lyon.fr/publication/2022LYSEI006/these.pdf
© [X. Zhang], [2022], INSA Lyon, tous droits réservés

Figure 3.12(b) plots the measured and theoretical dielectric constants of PDMS polymer filled with different volume content of ZnO microparticles. Analytical parameters found by fitting the experimental data with theoretical models of Eqs. (3.12) - (3.15) are summarized in Table 3.8. It can be noticed that the Lichtenecker and Jayasundere-Smith models yield a similar prediction of ε_p around 125 with a coefficient of determination R^2 very close to 1, reflecting an excellent correlation between empirical data and estimated values. Substituting the relative permittivity ε_p = 125 in the Yamada model produces the shape-dependent parameter of n = 6.62 ± 0.55, which is higher than the one obtained in the case of nano ZnO particles (cf. Table 3.7). Unlike the other models, the Maxwell-Garnett approach fails to match the experimental data of the micro-ZnO/PDMS composite, especially at a volume fraction over 24%. This result is consistent with the one reported on previous publications [196,197].

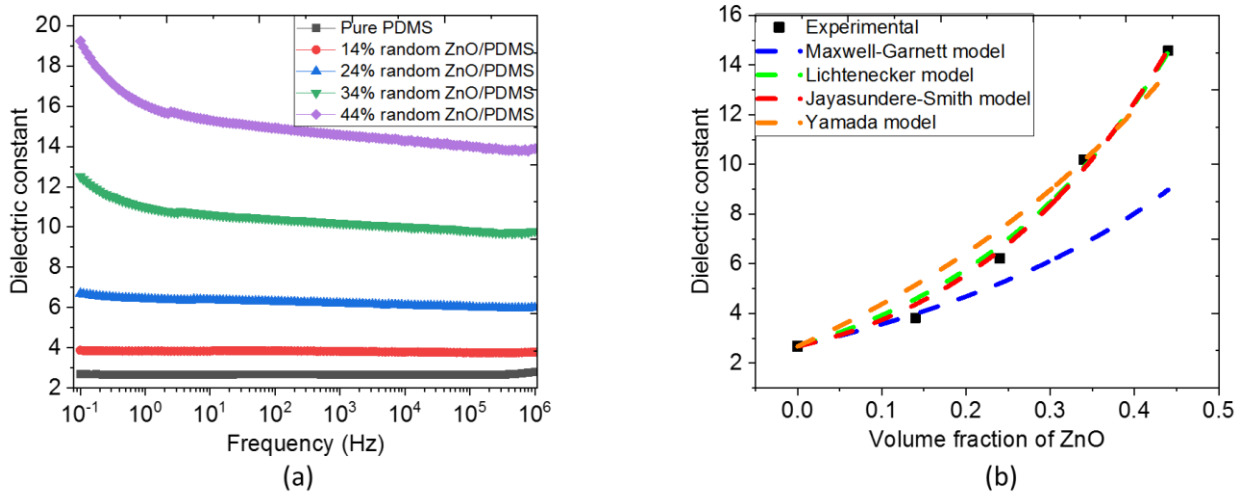

Figure 3.12. Variation of the dielectric constant of the random micro-ZnO/PDMS composite as a function of (a) frequency and (b) ZnO concentration measured at 1kHz together with a comparison of associated models.

Table 3.8. Fitting data from various models of the micro-ZnO/PDMS composite

Model	ε_m	ε_p	n	R^2
Maxwell-Garnett	2.68	-	-	0.543
Lichtenecker	2.68	125.07 ± 8.19	-	0.990
Jayasundere-Smith	2.68	125.48 ± 18.22	-	0.994
Yamada	2.68	125	6.62 ± 0.55	0.960

All above results allow to confirm further advantage of micro-ZnO composites with respect to the nano-ones. Concretely, micro-ZnO composites allow to:

- higher dielectric permittivity. The dielectric permittivity (at 1kHz) of the micro-sample and nano-sample respectively equals to 4.5 and 7, for a volume fraction of around 21%-24%. It is due to the fact that the permittivity of the micro-particles (ε_p ~125) is higher to the one of the nanoparticles (ε_p ~20), which is based on the analytic models. Indeed, when the filler size

Cette thèse est accessible à l'adresse : http://theses.insa-lyon.fr/publication/2022LYSEI006/these.pdf
© [X. Zhang], [2022], INSA Lyon, tous droits réservés

decreases, the dielectric constant of composite should be enhanced ascribed to the large surface-area-to-volume. That can induce more interface polarizations to increase the overall polarization response, meanwhile reduce the particles interdistance to strengthen the polarization in the region between the adjacent fillers [198]. However, the inversely tendency in our case is possibly attributed to the metal excess and semiconductor properties of ZnO. More specifically, oxygen is absorbed on the ZnO surface leading the construction of Schottky barriers with a high resistivity [199,200]. Therefore, the micro-particles with lower surface area per volume ratio indicate less resistance and thus higher dielectric constant as opposed to nanoparticles;

- higher maximum volume fraction (44% compared to 21% as in the case of the nanocomposite, leading to better dielectric and piezoelectric responses);
- simpler observation of particle chains during dielectrophoretic process under a low-cost digital microscope, which is impossible for the nanocomposite, considering the limited magnification.

Considering above reasons, the following studies will focus on the effect of dielectrophoretic structuring on dielectric, piezoelectric and other properties of the micro-ZnO composites.

3.4.2 Effect of particle structuration

High volume fractions of ZnO can cause an increase in the dielectric constant of composites. But saturation on the filler content (44% in the case of the micro composites) as well as a lower electrical breakdown strength and rigid mechanical properties also occurs in high concentration composite. Therefore, dielectrophoretic activity can be widely employed to manipulate particles in composite through application of an AC electric field.

This subsection aims to demonstrate that the dielectrophoretic effect with oriented particles in the early curing stages has a significant impact on the dielectric properties of micro-ZnO/PDMS composites. Figure 3.13a depicts the dielectric constant of structured micro-ZnO/PDMS composites at a large frequency range of 0.1 Hz to 1 MHz. Samples were elaborated with different concentrations of piezoelectric ZnO particles, which are similar to the study reported in subsection 3.4.1. The results of Figure 3.12(a) and Figure 3.13(a) demonstrate that the structured composites lead to significantly improved dielectric permittivities with respect to the random composites. Usually, in the structured 1-3 composites, the filler particles are oriented in the direction of external field and start to touch each other forming interface between ZnO particles. Then interface dipoles moments are considered to origin from the electrons trapped at ZnO/ZnO interface electronic states. As a result, the ZnO/ZnO interfacial dipoles, rather than ZnO/PDMS interfacial dipoles, give rise to significant improvement in the dielectric permittivity under low frequencies [201,202]. Actually, at a low frequency of 0.1 Hz, a two-fold increase has been achieved for the sample elaborated with a 44% vol. fraction of ZnO powder, whereas there was a 3.5-fold increase for the 14% sample. In the event of a higher dynamic, e.g., at 1 kHz, enhancement in dielectric property between the aligned and random mixtures is less significant, corresponding to 1.5-fold and two-fold improvement for the 44% and 14% composites, respectively. Consequently, regardless of the frequency range, dielectrophoresis results in better permittivity enhancement for lower-concentration composites compared to those with a higher filler content.

To better assess the influence of the dielectric response versus the ZnO volume fraction, Figure 3.13(b) illustrates the experimental data of oriented and random materials at 1 kHz, above which their relative

Cette thèse est accessible à l'adresse : http://theses.insa-lyon.fr/publication/2022LYSEI006/these.pdf
© [X. Zhang], [2022], INSA Lyon, tous droits réservés

permittivity is supposed to be frequency-independent. To determine the physical parameters related to the ZnO/PDMS composite, two approaches have been investigated, consisting of a Comsol modeling/simulation as well as the analytic theory developed by Bowen et al. [89]. The Bowen model is applied on 2-D structured composites where chains of cubic particles and matrix are oriented as capacitor in parallel. The equation of the dielectric constant is given by:

$$\varepsilon_{eff} = V_p\left(\frac{\gamma\varepsilon_p\varepsilon_m}{\varepsilon_p+\gamma\varepsilon_m}\right) + V_m\varepsilon_m \tag{3.16}$$

where γ is the ratio of the average particle size to the effective inter-particle distance; ε_m denotes the relative permittivity of PDMS (2.68); and ε_p denotes the relative permittivity of ZnO microparticles (i.e., ~ 125, as previously determined in subsection 3.4.1.2). Based on the best correlation between the experimental data to the Bowen model, γ is estimated as being approximately 24.3, displayed in Table 3.9.

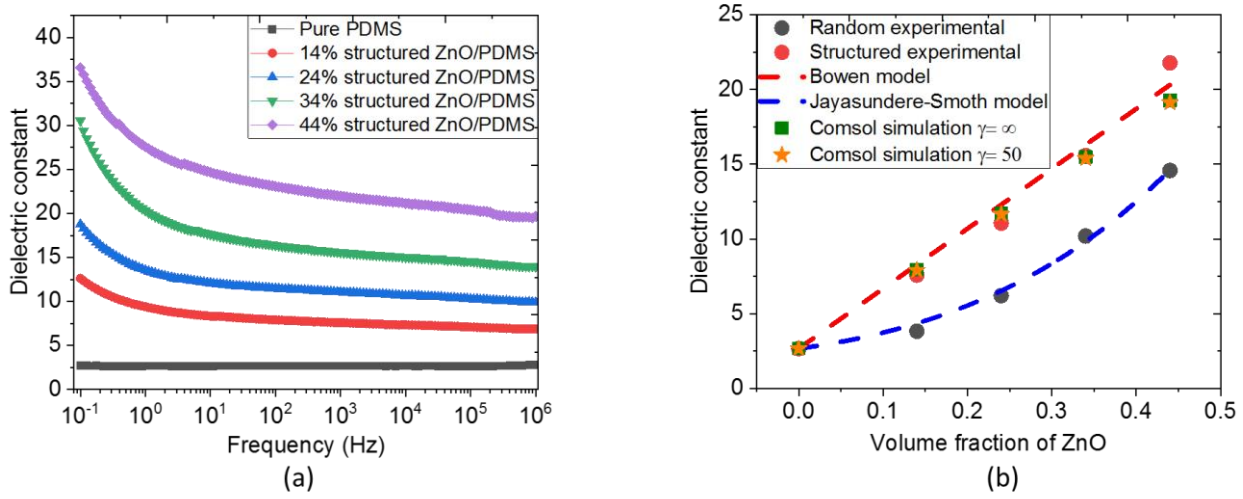

Figure 3.13. a) Variation of the dielectric constant as a function of frequency for structured PDMS composites filled with different content of ZnO microparticles. (b) Experimental and theoretical dielectric constant versus ZnO concentration under an AC applied voltage of 1 kHz and 1 V amplitude.

Table 3.9. Fitting data in the structured micro-ZnO/PDMS composite

Model	ε_m	ε_p	γ	R^2
Bowen	2.68	125	24.3 ± 1.5	0.978
COMSOL γ= ∞	2.68	70	∞	0.968
COMSOL γ = 50	2.68	250	50	0.965

In order to predict the dielectric properties of PDMS polymer incorporated with aligned microparticles, a 2D COMSOL model was built only in the electrostatic module. There are two configurations are performed in this study, including: the particles touch each other (γ = ∞); and the particles are spaced equally of 0.2 µm distance (γ = 50). The PDMS's permittivity (ε_{PDMS}) is measured equal to 2.68, whereas

Cette thèse est accessible à l'adresse : http://theses.insa-lyon.fr/publication/2022LYSEI006/these.pdf
© [X. Zhang], [2022], INSA Lyon, tous droits réservés

the one of ZnO (ε_{ZnO}) is determined based on the fitting between the simulation and experimental results. Seen in Figure 3.13(b), under two different configurations, the dielectric constant of the composite (ε_{eff}) derived from the 2D model increases with increasing ZnO volume fraction, which faithfully correlate to the empirical data (green and yellow dots, respectively). As summarized in Table 3.9, ε_{ZnO} depends on the interparticle distance. For instance, increasing the distance between ZnO particles to 0.2 µm lead to increase the dielectric constant of ZnO up to 250. Good estimation of the determination coefficient (R^2) allows to confirm excellent consistence between theoretical model and experimental result of the structured composite. As a conclusion, the FEM simulation leads to a much superior dielectric constant (ε_p) of ZnO microparticles (~ 250) than the Bowen calculation (~ 125). The main difference between these two approaches stems principally from the fact that different particles shapes (cubic for Bowen and circle for FEM) are used, and boundary edge effect is considered in FEM.

In order to see whether or not losses in dielectric material (the so-called tanδ) remain small over the considered frequency range (i.e. 1 Hz–1 MHz), Figure 3.14 illustrates frequency-dependent tanδ of the 1-3 and 0-3 microcomposites with different percentage of ZnO piezoelectric particles. As expected, the loss tangent in dielectric polymer increases with the piezoelectric concentration as higher ZnO content leads to increase conductivity of the composite. It can be seen that the pure PDMS exhibits very low and constant losses, which are mainly due to the dielectric losses, and not to the conduction losses. Similar behavior is observed for all ZnO composites at high frequencies (i.e., from 100 Hz), confirming that losses can be negligible in the Comsol simulation as well as in the analytical model (i.e. studied at 1 kHz). At low frequencies (0.1-10 Hz), on the other hand, tanδ is more considerable because of dominant conduction effect. Obviously, the 1-3 piezocomposite causes higher losses compared to the 0-3 random structure, since the aligned particle chains facilitate the conduction mechanism, giving raise to increase leakage current in the dielectric material. Although the structured composites with high ZnO content leads to increase conduction losses at low frequencies, all samples performed in this study behave as good dielectric materials with stable permittivity and insignificant losses.

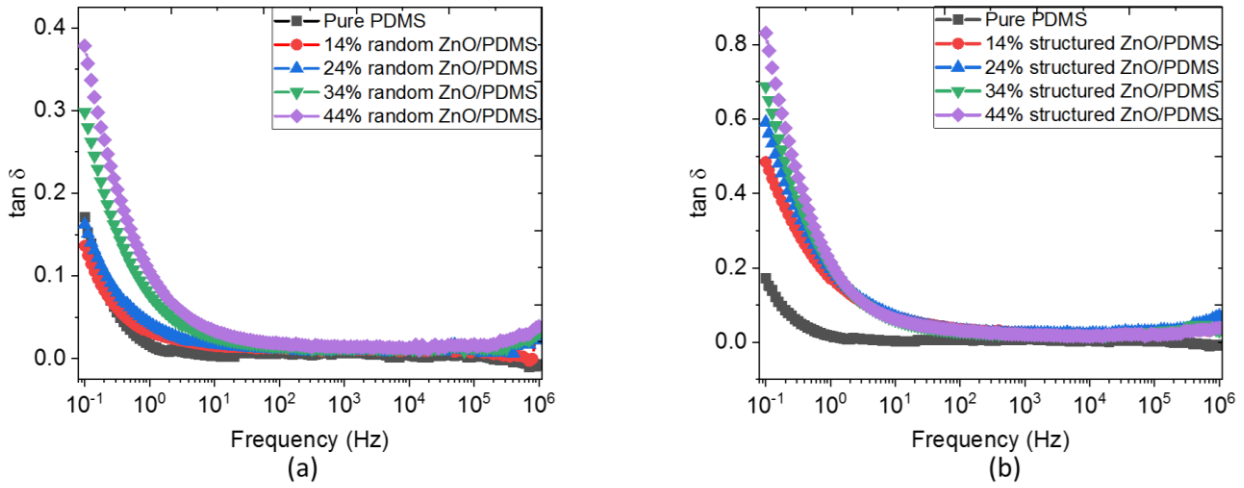

Figure 3.14. (a) Evolution of dielectric losses of ZnO-PDMS microcomposites with different volume fraction as a function of frequency: (a) without dielectrophoresis process, and (b) with dielectrophoresis process.

Cette thèse est accessible à l'adresse : http://theses.insa-lyon.fr/publication/2022LYSEI006/these.pdf
© [X. Zhang], [2022], INSA Lyon, tous droits réservés

3.5 Piezoelectric characterization

The measured dielectric permittivity can be the indication to assess how well the particles get aligned and form chains. As the piezoelectric electric displacement is proportional to the permittivity, the measurement of the piezoelectric coefficient is also a method to evaluate the orientation level. In addition, ZnO composites have the promising potential to be piezoelectric sensor for measuring pressure or strain, for instant in heart or blood vessels, thanks to its biocompatibility. Therefore, piezoelectric characterization is of interest to efficiently exploit ability of ZnO composite, which is revealed to be promising in piezoelectric devices.

As described in Figure 2.16, by applying a dynamic mechanical stress on the sample in a short circuit, the electric charge can be collected and the piezoelectric coefficient d_{33} was then evaluated. Figure 3.15(a) describes the piezoelectric behavior of the 14% vol. random and structured ZnO/PDMS composite where the periodic variation of the generated charge density is in accordance with the applied stress. This result confirms the piezoelectric effect of the ZnO NW array/PMMA composite described in Eq. 2.14, where the electric charge density (D) was perfectly in phase and exposed similar trend with respect to the input mechanical stress (T). In addition, within the same volume fraction and dynamic stress, significant enhancement of generated charge density has been recorded in structured samples as opposed to random samples. A comparison of the d_{33} value between structured and random ZnO/PDMS composites elaborated with different concentrations is revealed in Figure 3.15(b). The result confirms that the dielectrophoretic orientation on ZnO particles successfully enhances the piezoelectric response of the structured composite as opposed to the 0-3 composite. At above 20% vol. of ZnO content, the d_{33} value of the oriented sample slowly increases and seems to attain the saturated regime, which is contrary to the random material whose d_{33} significantly improved with high filler concentration. Nonetheless, at a 44% vol. volume fraction, the 1-3 composite still achieved an almost two-fold increase in the charge coefficient (i.e., 0.50 pC/N) with respect to the 0-3 one (i.e., 0.27 pC/N).

The saturation effect appearing in the composite with high piezoelectric-particle content can be explained by the fact that such materials already exhibit sufficient connection between ZnO/ZnO interfaces, which cannot be much of an increase anymore, even when being treated with dielectrophoresis. On the other hand, the weak connectivity pattern of the 0-3 composite with low piezoelectric concentration can be significantly enhanced after the dielectrophoretic alignment of particles.

Analytical approaches have been investigated to predict the charge coefficient d_{33} of the composites. The Yamada model [86] is utilized in 0-3 composites to estimate the d_{33} value along the external electric direction:

$$d_{33\,random} = \frac{V_p n \alpha \varepsilon_{eff} d_{33\,p}}{(n-1)\varepsilon_{eff} + \varepsilon_p} \tag{3.17}$$

where n is a shape-dependent parameter, α is the poling ratio of the particles, and $d_{33\,p}$ is the piezoelectric charge constant of the particles.

The Bowen model can be expanded to the Van den Ende model [85] to calculate the charge coefficient d_{33} of 1-3 composite with particle-matrix alternations in the chains. The equation for d_{33} of such a design architecture is given by:

Cette thèse est accessible à l'adresse : http://theses.insa-lyon.fr/publication/2022LYSEI006/these.pdf
© [X. Zhang], [2022], INSA Lyon, tous droits réservés

$$d_{33\ structured} = \frac{(1+\gamma)^2 \varepsilon_m V_p d_{33\ p} Y_p}{(\varepsilon_p + \gamma\varepsilon_m)[(1+\gamma V_p)Y_p + V_m Y_m \gamma]} \quad (3.18)$$

where γ is the ratio of the average particle size to the effective inter-particle distance and Y_p and Y_m are, respectively, the elastic moduli of the particles and matrix. As discussed in the section 3.3, all materials are treated as isotropic materials with Y_p and Y_m estimated as 163.4 GPa and 2.11 MPa, respectively.

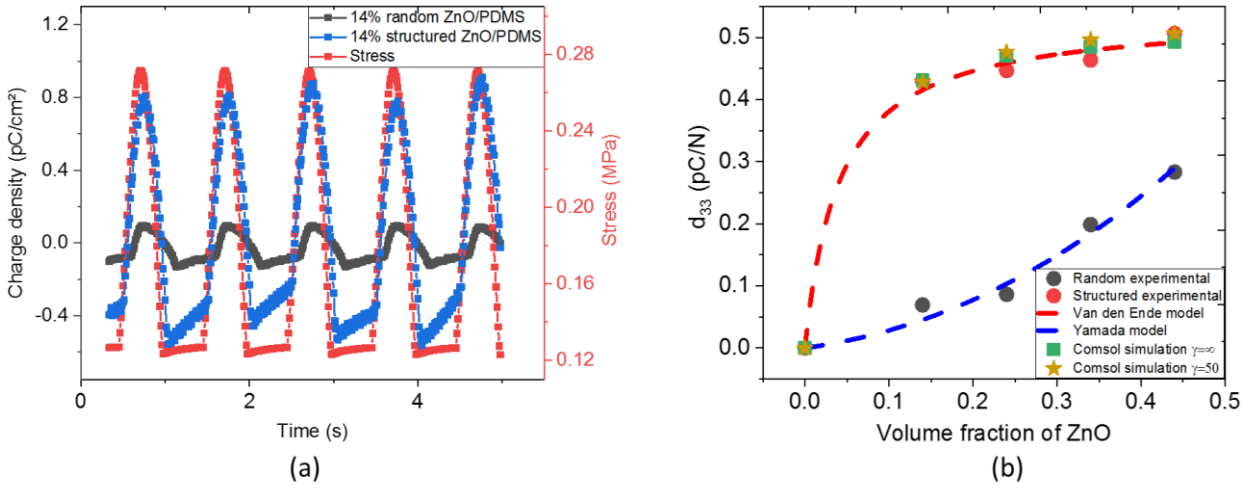

Figure 3.15. Piezoelectric characterization performed under a dynamic stress of 1 Hz. (a) Time evolution of stress and charge density of the 14% vol. random and structured ZnO/PDMS composite. (b) Experimental and fitting piezoelectric coefficients (d_{33}) of structured and random micro-ZnO/PDMS composites as a function of ZnO concentration. The red and black dotted lines represent the empirically measured values, the green and yellow dotted lines correspond to the Comsol simulation, and the dashed lines depict the theoretical models.

Besides the analytical approaches and experimental measurement, FEM simulation was applied to predict the piezoelectric performance. Figure 3.16(a-d)-based Comsol simulation highlights the piezoelectric effect, by which the material generates an electric potential and corresponding electric charge density in response to an application of mechanical stress.

The analytical parameters of Yamada, and Van den Ende models, together with those used in the FEM simulation are displayed in Table 3.10, based on which theoretical estimation faithfully matches the empirical measurement, as illustrated in Figure 3.15(b). Indeed, the best fit between the experimental data and the Van den Ende models allows for the determination of the piezoelectric constant d_{33} of the micro-ZnO particles with a value of approximately 1.45 pC/N (Eq. 3.18). Injecting this value in the Yamada model leads to an estimation of the poling ratio α and the shape-dependent parameter n (Eq. 3.17). The quality of all theoretical models was verified by the coefficient of determination R^2, which almost equals 1.

Interestingly, Comsol simulation leads to very different values of d_{33p}, i.e. 0.58 pC/N and 3 pC/N, corresponding to the ratio γ equals ∞ and 50, respectively. These values (d_{33p}) are not the same to the one found from the analytical equations (i.e., 1.45 pC/N). This is probably because different geometric and boundary considerations imposed in a 2D Comsol. Another impact parameter is the inter-particle distance or coefficient γ, which is not easy to be determined in a 2D architecture. With γ decreasing with longer distance between particles, the predicted value of d_{33p} should increase to compensate the energy loss (electric

Cette thèse est accessible à l'adresse : http://theses.insa-lyon.fr/publication/2022LYSEI006/these.pdf
© [X. Zhang], [2022], INSA Lyon, tous droits réservés

and mechanical loss) in the polymer gap. But if the inter-particle distance is too large in the FEM simulation, no matter how high the d_{33p} is, the resultant d_{33} of composite has already reached the saturation state and cannot fit well with experiment data. Therefore, in the 2D simulation, γ is chosen to be 50, rather than 24.28 derived from the Van den Ende model. As a result, the average inter-particle distance, which significantly affects to the piezoelectric response, causes the discrepancy of d_{33p} between the analytical model and the 2D Comsol simulation.

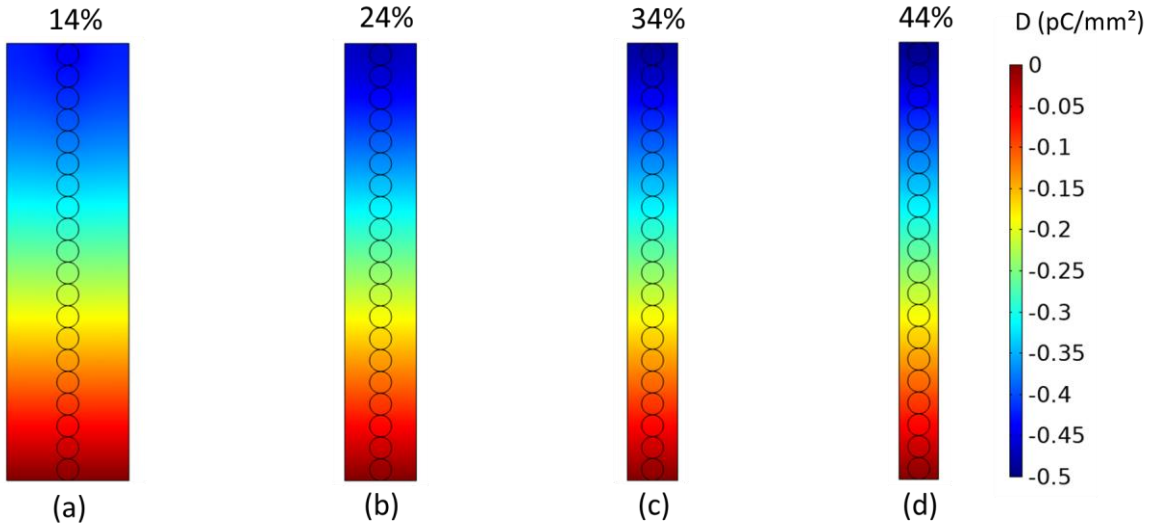

Figure 3.16. A 2D model of the structured ZnO/PDMS composite with a volume fraction of (a) 14%, (b) 24%, (c) 34%, and (d) 44%, which produce various charge density under an applied compression stress of 1MPa in the vertical direction.

Table 3.10. Fitting data based various models for structured and random micro-ZnO/PDMS composites

Model	ε_m	ε_p	d_{33p} (pC/N)	α	n	γ	Y_p(GPa)	Y_m(MPa)	R^2
Yamada	2.68	125	1.45	1.01 ± 0.05	6.63	-	-	-	0.978
Van den Ende	2.68	125	1.45 ± 0.02	-	-	24.28	163.4	2.11	0.995
Comsol	2.68	70	0.61	-	-	∞	163.4	2.11	0.998
Comsol	2.68	250	3.05	-	-	50	163.4	2.11	0.997

3.6 Thermal stability

From a practical application viewpoint, the thermal stability is an inevitable consideration during the implementation. In addition, temperature has considerable influence on the dielectric relaxation and the electric conductivity of nonlinear composites. Thus, the investigation of the impact of temperature promotes a better understanding of the working mechanisms inside of composites.

Cette thèse est accessible à l'adresse : http://theses.insa-lyon.fr/publication/2022LYSEI006/these.pdf
© [X. Zhang], [2022], INSA Lyon, tous droits réservés

3.6.1 Dielectric characterization under temperature variation

Regarding the dielectric characterization under temperature variation of a typical dielectric composite, Ramajo *et al*. and Hadik *et al.* identified three major mechanisms [203,204], that can be cited as following:

1) The dielectric response of the filler is temperature dependent, which is due to the changes in the filler structure (below Curie temperature). It has been reported that the dielectric constant of ZnO increases with temperature increasing, meanwhile the electrical conductivity increases also with temperature [205]. Thus, the dielectric properties of semiconductor/polymer composites are greatly affected by the conductivity of fillers.

2) The segmental mobility of polymer with temperature: The higher the temperature, the greater the freedom of the dipole molecular movement. This leads to improvement of dielectric constant.

3) The contact between the ZnO particles is interrupt due to the thermal expansion of PDMS matrix, results in decrease in electrical conductivity, thus reducing the dielectric constant.

Figure 3.17 showed the temperature dependence of the dielectric constant (ε_r') and the loss tangent with frequency in the range 0.1 Hz–1 MHz of the 44% vol. random and aligned samples. As the frequency-dependent behavior is more observable in the case of ZnO composite filled with 44% vol., as opposed to the other containing lower fraction content. Hence, in this study, the 44% sample is considered be the most representative for temperature-stability analysis of the dielectric properties.

Under an excited electric field, particles of ZnO in micro size act as dipoles and obtain high freedom of movement to reach high dielectric constant [206]. Therefore, the dielectric constant and electrical conductivity of semiconductor fillers usually increases with the increase of temperature. However, a decreasing trend of ε_r' with temperature was discovered in composites (Figure 3.17a and c) at high frequency, which may be attributed to the temperature dependence of PDMS or the interaction between two constituent phases. On one hand, at a high temperature, the interruption of the conduction path in ZnO/PDMS composite makes it difficult for dipoles to arrange at a certain direction when subjected to electric field. On the other hand, increasing the mobility of the dipoles in PDMS molecular chain with temperature could favor the dielectric constant, to some extent. Thereby, the first assumption has much more convince according to the experimental trend. Based on the result of Figure 3.17a and c, another possible reason is mainly attributed by the thermal expansion of PDMS matrix. Eventually, similar observation is reported in the literature, where the dielectric constant of PDMS decreases with increasing temperature, i.e. above its glass transition temperature (175 °K) [207]. In addition, as shown in Figure 3.17 (a) and (c), there is an unusual improvement on dielectric constant between a low frequency range of [0.1 Hz, 10 Hz] compared to other high frequency ranges. This phenomenon probably stems from the interface polarization of composites and the conductivity of fillers at low frequency, where an increase in temperature could improve the dielectric constant (ε_r') by facilitating the polarization process and the filler's conductivity.

It has been demonstrated in Figure 3.17(b) and (d) that at low frequency, the dielectric loss tangent increases as a function of the temperature, whereas almost unchanged at higher frequency. Actually, increasing temperature at low frequency favors segmental mobility of polymer as well as the friction of the rotating dipoles. Also, it makes the degree of dipole orientation increase, causing increase dielectric loss [192]. Interestingly, the dielectric loss is stable between a frequency range of [50 Hz ,100 kHz]. Besides, an upward trend occurs at higher frequency (i.e. beyond 100 kHz), which is ascribed to the relaxation of dipolar

Cette thèse est accessible à l'adresse : http://theses.insa-lyon.fr/publication/2022LYSEI006/these.pdf
© [X. Zhang], [2022], INSA Lyon, tous droits réservés

orientational polarization [208,209]. It is reveled in Figure 3.17(b) and (d) that a peak in the tanδ loss might be observed beyond 1 MHz, i.e., similarly to the one reported in [210]. Generally, dipole relaxation in a dielectric material (e.g. PDMS) is undesirable for capacitor applications because this process is usually accompanied by great variations in permittivity (ε_r') and tanδ.

It is worth noting that the estimation of (ε_r') via Solartron is less accurate for the sample measured at 110 °C, as its tanδ value is higher than 1. Actually, in reality, the permittivity of the sample subjected to 110 °C should be smaller and somehow close to the one with other temperature conditions. This is a limitation of Solartron spectrometer, where measurement in the relative permittivity is problematic with a bad dielectric material (i.e. high conduction loss with tan$\delta > 1$)

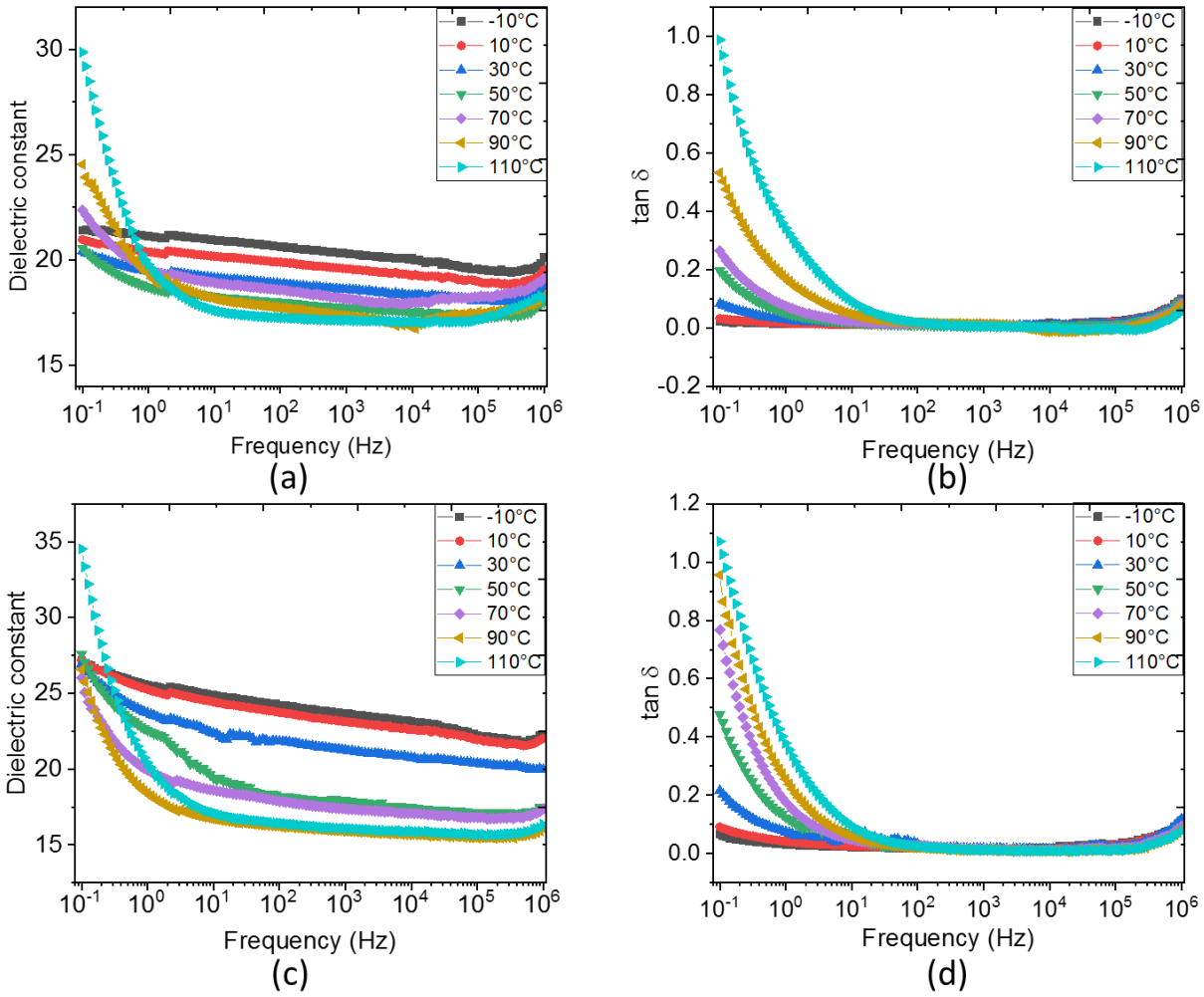

Figure 3.17. Broadband dielectric spectroscopy including dielectric constant, and dielectric loss tangent of the 44% vol. (a), (b) random and (c), (d) aligned samples at different temperature.

3.6.2 J-E characteristics under temperature variation

In this section, the influence of temperature on the electric properties of developed materials was investigated. Figure 3.18 displays the nonlinear J-E characteristics of the random and structured composites

Cette thèse est accessible à l'adresse : http://theses.insa-lyon.fr/publication/2022LYSEI006/these.pdf
© [X. Zhang], [2022], INSA Lyon, tous droits réservés

elaborated with 44% of ZnO content, which were measured at various temperatures in the range -10 °C to 110 °C. It can be seen in that for both 0-3 and 1-3 structures, the switching field gradually increases with increasing temperature from 10 °C to 110 °C. The primary reason is that growing temperature facilitates the contact resistance between the fillers, leading to higher switch field [165]. More specifically, because of the large discrepancy of thermal expansion coefficient between ZnO particles (around $4.3\times 10^{-6}K^{-1}$) [189] and PDMS polymer (around $9.6\times 10^{-4}K^{-1}$) [211], the expansion of matrix may block the formation of conduction path and also transform a thin insulation gap into thick gap between ZnO particles. Additionally, enhancing temperature makes the interaction force between fillers increase, resulting in large face contact interfaces and resistance [212]. Therefore, an increment of switching field is expected in composite measured at increasing temperature.

Interestingly, it was observed a decreasing trend of switch field from negative temperature (-10 ºC) to positive temperature (10 ºC), which may be ascribed to the temperature effect on carrier transport between ZnO particles and segmental mobility of polymer. The energy bandgap of semiconductor tends decrease electron concentration in the conduction band with increasing temperature, resulting in lower switch field and sharper increase in current density when a high voltage is applied [105,213]. Also, the liberation of charge carriers from traps to greater mobility at high temperature improves the conductivity and thereby decreases the switch field [214]. It therefore seems that the increase of carrier transport through the ZnO particles dominates the conductivity of the composites at low temperatures between -10 °C and 10 °C, but the increase in contact resistance dominates between 10 °C and 110 °C. Consequently, the temperature dependence of the J-E characteristics is a result from two competitive effects, i.e., contact resistance and carrier transport.

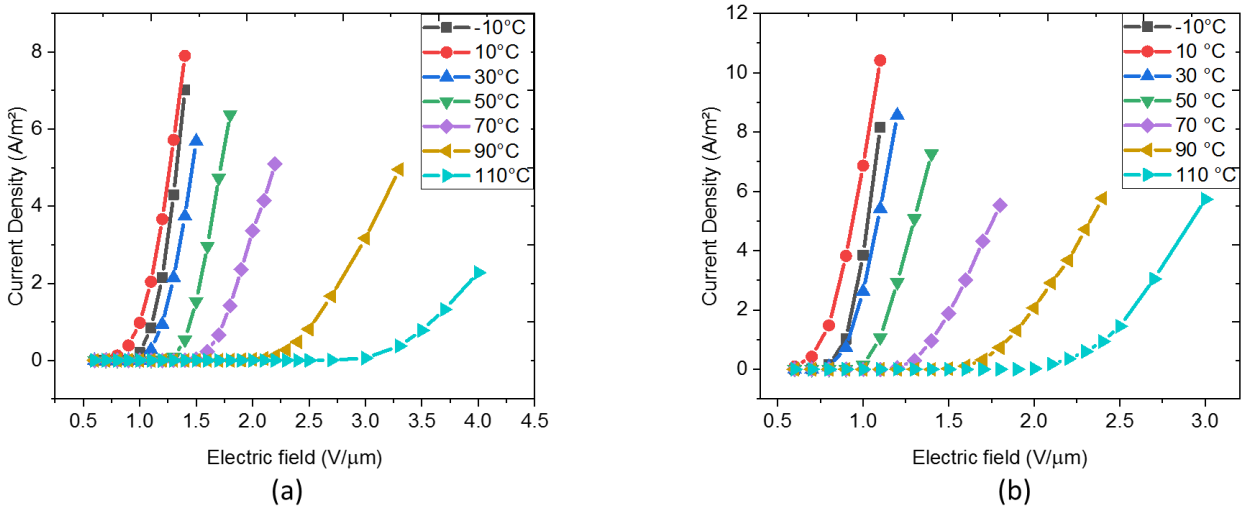

Figure 3.18. Nonlinear J-E characteristics of (a) random, and (b) structured ZnO/PDMS composite with filler content of 44% at different temperatures.

3.7 Summary

In this work, a dielectrophoretic structuring technique was explored for micro-ZnO/PDMS composites and it was confirmed that this technique can be used to induce directional materials properties. Indeed, the

Cette thèse est accessible à l'adresse : http://theses.insa-lyon.fr/publication/2022LYSEI006/these.pdf
© [X. Zhang], [2022], INSA Lyon, tous droits réservés

structuration of particles is considered to be one of the key factors governing the dielectric, mechanical and piezoelectric properties of composites, which were demonstrated to be significantly improved through experimental tests as well as theoretical work.

First, the SEM images indicated a uniform dispersion of micro ZnO particles in the PDMS matrix and showed the formation of aligned particle chains in preferred direction via dielectrophoretic. The conductive, mechanical and dielectric properties were sequentially investigated due to their contributions to the piezoelectric properties. For the high electric field characterization, DC nonlinear J-E characteristics indicated that the switch field decreases with increasing filler concentration. Moreover, dielectrophoretic alignment on the particles clearly enhances the electric response, which is manifested by creation of short conduction paths within the matrix. When a bipolar electric field was applied, for the applied field less than 0.4 V/µm, capacitive current is regarded as the dominant component and conduction current is linear to the electric field according to the Ohm's law. Thus, a new mathematical analysis method based on J-E hysteresis loop was developed to identify the three main components (leakage, capacitive and ferroelectric) contributed to the measured current. Another conducting nonlinear model was developed for the unipolar electric field at 1 V/µm. Based on this model, it is possible to quantify the loss factor, which is electric-field dependent and cannot be neglected under high voltage excitation. Nonetheless, significant improvements in the permittivity and conductivity were achieved for the structured composites via dielectrophoretic technique. Also, stress-strain curves were performed using the tensile and compression tests, suggesting an increasing trend of Young modulus of composite with increasing volume fraction of ZnO. An estimation of Young's modulus of ZnO (~163.4 GPa) was performed with the help of Nielsen model. In particularly, during the compressive tests, reinforcement along the particle's orientation from structured composites gave rise to improved mechanical properties.

Both ZnO nanoparticles and microparticles were used to prepare piezoelectric composites and a comparison of their dielectric responses was carried out. The experimental results revealed that a higher particle concentration gives rise to the increased dielectric permittivity of composites, especially when particles are aligned in the poling-direction-based dielectrophoretic process. Hence, the microparticles were chosen instead of the nano ones because the microscale facilitates the fabrication process of the composites, especially with high filler content. Significant improvement in the dielectric and piezoelectric behavior of the proposed composite has been successfully achieved via dielectrophoretic alignment of ZnO microparticles. The dielectric constant, as well as the charge coefficient of the ZnO particles, were estimated thanks to analytical models. Besides 2D FEM simulation models were fitted to the real data and good coherent was observed, reflecting a high reliability of the proposed approaches. Finally, the temperature dependence of J-E characteristics and dielectric properties were investigated to figure out the working mechanisms.

To sum up, characteristics of ZnO composites can be controlled by enhancement of material properties like filler concentration and particle structuration. Experimental characterizations together with theoretical models developed in this work were of interest to efficiently exploit ability of ZnO composites, which was revealed to be promising in piezoelectric and semiconductor devices. For instance, a potential of ZnO composite as piezoelectric sensor was explored to measure pressure in heart or blood vessels. In addition, excellent nonlinear electric behavior proved the high potential of ZnO composites for new design of medical tools, e.g. cardiac catheter ablation where multifunctional modules can be combined. However, the

Cette thèse est accessible à l'adresse : http://theses.insa-lyon.fr/publication/2022LYSEI006/these.pdf
© [X. Zhang], [2022], INSA Lyon, tous droits réservés

piezoelectric sensitivity of ZnO composite (d_{33}≈0.5 pC.N^{-1}), despites its optimized configuration (high particle concentration, good anisotropic structure through dielectrophoresis), is dramatically smaller than the one of the conventional counterparts like PZT (d_{33}≈20 pC.N^{-1}) [215] or $BaTiO_3$ (d_{33}≈5 pC.N^{-1}) [216]. Therefore, in the following chapters, ZnO nanotubes and nanowires with a 1-3 structure configuration will be introduced to further improve the device efficiency and performance

Cette thèse est accessible à l'adresse : http://theses.insa-lyon.fr/publication/2022LYSEI006/these.pdf
© [X. Zhang], [2022], INSA Lyon, tous droits réservés

Chapter 4. Modeling of vertically ZnO nanowires arrays/PMMA composites

In order to understand the working mechanisms, and further to optimize the performance of ZnO nanowires (NWs) based piezoelectric devices, simulations consisting of analytical model and finite element method (FEM) are investigated. A progressive approach considering from individual NW, which is the basic structure, to NW arrays will be performed to stimulate their piezoelectric behaviors. Thus, the first objective involves the analytical modeling and COMSOL simulation of a single NW operating in both mechanical bending and compression modes. Second, the corresponding equivalent models are developed for a better understanding of the multiphysical couplings manifested by vertically ZnO NW arrays within polymer matrix and also proposed a simple electric model of the sensor. Last, FEM is employed to drive the optimization strategies through the adjustment of key parameters such as Young's modules, dielectric permittivity, together with density and dimension of NW itself.

Cette thèse est accessible à l'adresse : http://theses.insa-lyon.fr/publication/2022LYSEI006/these.pdf
© [X. Zhang], [2022], INSA Lyon, tous droits réservés

4.1 Single nanowire (NW)

Regardless of constitution structure of ZnO NWs devices, for instance, single-wire nanogenerator [217], aligned ZnO NW arrays nanogenerator [60], etc., a single NW is the basic construction building cell in the diverse applications. Therefore, to better understand the working mechanisms in ZnO NW based device, an investigation of single NW is of prime importance. In this section, a theoretical and finite element method (FEM) analysis of a laterally defected and an axial compressive single NW are performed and compared. In addition, external force and geometric parameters are sequentially considered due to their great impact on the device performance.

4.1.1 Analytical method

It is fundamental to develop analytical equations to quantitatively identify the potential difference along the NW in order to further predict and promote the efficiency of the system. There are numerous theories of NW piezoelectricity that have been demonstrated, such as first-principles calculations, molecular dynamic simulation, and continuum models [218–220]. But the first principle calculations and molecular dynamics simulations are more suited in small amount of atom (diameters up to 2.8 nm) and the continuum model is only valid in one-dimensional structure. Considering that the strain and electrostatic potential distribution on the nanowire cross section are also significant in piezotronics systems, a continuum model with a perturbation technique has been proposed by Gao *et al*. This technique allows to solve the coupled differential equations and gives a result of 6% discrepancy with respect to those obtained from the full numerical calculation [221]. Thus, the details about the theoretical derivation will be introduced based on our own model configuration.

The typical schematic of a ZnO nanowire in our case is represented as a cylinder with a radius (R) of 42 nm and a length (L) of 1031 nm (see Figure 4.1a). The NW is epitaxially grown along with the z-axis (i.e., revolution central axis) on a crystal substrate and thus modeled along the z axis (i.e., length direction). The single NW is bottom fixed and top pushed by a laterally force along the y-direction (Figure 4.1b) or compressed by a force along the z-direction (Figure 4.1c). Normally, there are three categories of equations corresponding to different physical couplings: pure mechanical equations, electromechanical coupling equations, and pure electrical equations.

Firstly, the mechanical equations include of:

$$\nabla \cdot \mathrm{T} = 0 \tag{4.1}$$

$$e_{ikr} e_{jls} S_{ij,kl} = 0 \tag{4.2}$$

where T is the stress tensor, e_{ikr} and e_{jls} are the Levi-Civita antisymmetric tensors and S is the strain tensor. Eq. (4.1) represents the mechanical equilibrium regime where the resulting force applied on the NW is zero [222]. Eq. 4.2 describes the geometrical compatibility equation when a geometrical constrain condition is imposed in continuum mechanics [223].

Cette thèse est accessible à l'adresse : http://theses.insa-lyon.fr/publication/2022LYSEI006/these.pdf
© [X. Zhang], [2022], INSA Lyon, tous droits réservés

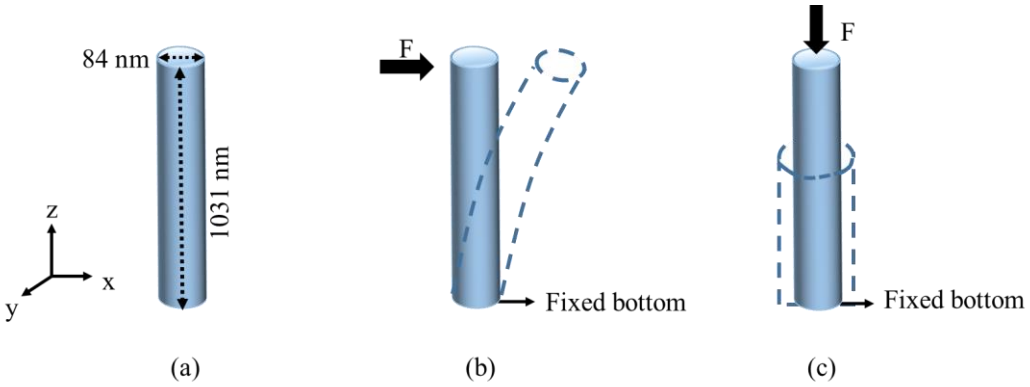

Figure 4.1. (a) Typical configuration of a ZnO NW with an 84-nm diameter and a 1031-nm length; (b) Bending force in the y-direction; and (b) Compressive force in the z-direction.

Next, constitutive equations for electromechanical coupling can be written as:

$$T_m = c_{mq} S_q - e_{pl} E_p \tag{4.3}$$

$$D_k = e_{kq} S_q + \varepsilon_{kp} E_p \tag{4.4}$$

where E_p is the electric field and D_k is the electric displacement, c_{mq} is the linear elastic constant, e_{pl} is the linear piezoelectric coefficient, and ε_{kp} is the dielectric constant. Those constants can be further simplified when considering the symmetric wurtzite structure of ZnO crystal.

Finally, assuming there is no free charge in the NW, the electric relationship can be expressed by the following Gauss equation:

$$\nabla \cdot \vec{D} = 0 \tag{4.5}$$

Eqs. (4.1) to (4.5) combined with boundary conditions fully describe a static piezoelectric system. Our objective is to solve these equations and derive the piezoelectric potential generated in NW as a function of the input applied force. The perturbation method consists of a power series divided into "solvable" part and "perturbation" part, which indicates the deviation from the solvable problem [224]. In the piezoelectric coupled differential equations, a perturbation parameter λ is introduced by defining $\widetilde{e_{pl}} = \lambda e_{pl}$ to confirm the contribution from different orders of effects [221]. Therefore, by substituting the perturbation expressions into Eqs. (4.3), (4.4) with same order of λ, constitutive equations can be rewritten as [221]:

Zero order:

$$T_m{}^0 = c_{mq} S_q{}^0 \tag{4.6}$$

First order:

$$D_k{}^1 = e_{kq} S_q{}^0 + \kappa_{kp} E_p{}^1 \tag{4.7}$$

where the superscripts 0 and 1 donate the order of perturbation. For the zeroth solution, the NW is subjected to an elastic strain without piezoelectric effect, which is also explained as the Hook's law. The first order solution elaborates the process of direct piezoelectric effect, where the generation of charges is induced by the applied strain. The second order describes that the generated charges in return impact the mechanical

Cette thèse est accessible à l'adresse : http://theses.insa-lyon.fr/publication/2022LYSEI006/these.pdf
© [X. Zhang], [2022], INSA Lyon, tous droits réservés

deformation in the material. For the ZnO nanowire under bending or compression model, the first order approximation is sufficient and thus the effect of the electric field (E) on T is neglected. To further simplify the analytical solution, the material was treated as an isotropic elastic medium whose Young's modulus Y = 127 GPa, Poisson ratio υ = 0.358, and the relative tensors can be written as:

$$e = \begin{bmatrix} 0 & 0 & 0 & 0 & e_{15} & 0 \\ 0 & 0 & 0 & e_{15} & 0 & 0 \\ e_{31} & e_{31} & e_{33} & 0 & 0 & 0 \end{bmatrix} \tag{4.8.1}$$

$$\varepsilon = \begin{bmatrix} \varepsilon_{11} & 0 & 0 \\ 0 & \varepsilon_{11} & 0 \\ 0 & 0 & \varepsilon_{33} \end{bmatrix} \tag{4.8.2}$$

$$\mathrm{c} = \begin{bmatrix} c_{11} & c_{12} & c_{13} & 0 & 0 & 0 \\ c_{12} & c_{11} & c_{13} & 0 & 0 & 0 \\ c_{13} & c_{13} & c_{33} & 0 & 0 & 0 \\ 0 & 0 & 0 & c_{44} & 0 & 0 \\ 0 & 0 & 0 & 0 & c_{44} & 0 \\ 0 & 0 & 0 & 0 & 0 & \frac{(c_{11}-c_{12})}{2} \end{bmatrix} \tag{4.8.3}$$

Back to our bending mechanical model (Figure 4.1b) in which one end of NW is fixed while the other is free and subjected to a bending force F_y. At the free end, there is no bending moment and only a small displacement exists, while at the fixed base part, a bending moment and a force arise as a response of the applied force. Assuming the force is exerted uniformly on the top, Saint-Venant theory is applied in the determination of stress to simplify the boundary condition [225]. It demonstrates that the elastic fields, caused by two different but statically equivalent loading conditions, are approximately the same everywhere at sufficiently large distance from the load. Therefore, the stress distribution of a deflected NW without piezoelectric effect can be expressed as [221]:

$$T^0 = \begin{bmatrix} T_{xx} \\ T_{yy} \\ T_{zz} \\ T_{yz} \\ T_{xz} \\ T_{xy} \end{bmatrix} = \begin{bmatrix} 0 \\ 0 \\ -\frac{4F_y}{\pi R^4} y(l-z) \\ \frac{\mathrm{F_y}(3+2\upsilon)}{2\pi \mathrm{R}^4(1+\upsilon)} (r^2 - y^2 - \frac{1+2\upsilon}{3+2\upsilon} x^2) \\ -\frac{F_y}{\pi R^4} \frac{(1+2\upsilon)}{(1+\upsilon)} xy \\ 0 \end{bmatrix} \tag{4.9}$$

where R is the radius of the NW. Then, following the Hook's law, the strain can be given as [221]:

$$S^0 = \begin{bmatrix} \frac{4\upsilon F_y}{c_{13}\pi R^4} y(l-z) \\ \frac{4\upsilon F_y}{c_{13}\pi R^4} y(l-z) \\ -\frac{4\upsilon F_y}{c_{33}\pi R^4} y(l-z) \\ \frac{\mathrm{F_y}(3+2\upsilon)}{c_{44}\pi \mathrm{R}^4} (r^2 - y^2 - \frac{1+2\upsilon}{3+2\upsilon} x^2) \\ -\frac{2F_y}{\pi R^4} \frac{(1+2\upsilon)}{c_{44}} xy \\ 0 \end{bmatrix} \tag{4.10}$$

Cette thèse est accessible à l'adresse : http://theses.insa-lyon.fr/publication/2022LYSEI006/these.pdf
© [X. Zhang], [2022], INSA Lyon, tous droits réservés

It should be noted that due to the limitation of Saint-Venant theory, the above equations are only utilized in the regions far away from the constrained end. Next, according to the direct piezoelectric effect of Eq. (4.7), the remnant electric displacement D^R and a corresponding remnant body charge ρ^R can be introduced as [221]:

$$D_k^R = e_{kp} S_q^0 = \begin{bmatrix} e_{15} \cdot 2S_{xz} \\ e_{15} \cdot 2S_{yz} \\ 2e_{31} \cdot S_{xx} - e_{33} \cdot S_{zz} \end{bmatrix} \tag{4.11}$$

$$\rho^R = -\nabla \cdot D_k^R = \frac{4F_y}{\pi R^4}\left[2(1+\upsilon)\frac{e_{15}}{c_{44}} + 2\upsilon\frac{e_{31}}{c_{13}} - \frac{e_{33}}{c_{33}}\right] y \tag{4.12}$$

Then, combing Eq. (4.5) and the first order Eq. (4.7), the Poisson equation without any free carriers is given:

$$\nabla \cdot (\varepsilon_{kp} {E_p}^1) = \rho^R \tag{4.13}$$

Finally, the electric potential φ(r, θ) in cylindrical coordinates can be solved as [221]:

$$\varphi = \frac{1}{2\varepsilon_{11}} \frac{F_y}{Y\pi}[2(1+\upsilon)e_{15} + 2\upsilon e_{31} - e_{33}]\left[\frac{\varepsilon_0+3\varepsilon_{11}}{\varepsilon_0+\varepsilon_{11}}\frac{r}{R} - \frac{r^3}{R^3}\right] R^3 sin\theta \quad (r < R) \tag{4.14.1}$$

$$\varphi = \frac{1}{2\varepsilon_{11}} \frac{F_y}{Y\pi}[2(1+\upsilon)e_{15} + 2\upsilon e_{31} - e_{33}]\left[\frac{2\varepsilon_{11}}{\varepsilon_0+\varepsilon_{11}}\frac{R}{r}\right] R^3 sin\theta \quad (r \geq R) \tag{4.14.2}$$

Regarding Eq. (4.14), the maximum potential occurs at r = R and θ = 90º (at the compressive surface side) or θ= - 90º (at the tensile surface side). The φ_{max} is expressed as [221]:

$$\varphi_{max} = \left|\frac{1}{\varepsilon_0(\varepsilon_{11}+1)} \frac{F_y}{Y\pi}[2(1+\upsilon)e_{15} + 2\upsilon e_{31} - e_{33}]\frac{1}{R}\right| \tag{4.15}$$

From Eq. (4.14), the electric potential is related to the external applied force and the material properties (e.g., dielectric constant, piezoelectric constant). These parameters are invariant in z direction, implying the uniform electric potential along that direction and the NW behaves like a 'parallel plate capacitor'. Meanwhile, the maximum piezoelectric potential in Eq. (4.15) is inversely proportional to the radius (R) and irrelevant to the length. Similarly, for the case of the compressive mode, a force (F_z) is applied on the top but parallel to the growth axis, as seen in Figure 4.1c. Assuming that the compressive deformation within the NW generates uniform uniaxial strain along the c-axis, the strain tensor can be rewritten as:

$$S^0 = \begin{bmatrix} S_{xx} \\ S_{yy} \\ S_{zz} \\ S_{yz} \\ S_{xz} \\ S_{xy} \end{bmatrix} = \begin{bmatrix} \frac{\upsilon F_Z}{Y\pi R^2} \\ \frac{\upsilon F_Z}{Y\pi R^2} \\ \frac{F_Z}{Y\pi R^2} \\ 0 \\ 0 \\ 0 \end{bmatrix} \tag{4.16}$$

The magnitude of the maximum electric potential is deduced by [226]:

$$\varphi_{max} = \left|\frac{1}{\varepsilon_{11}\varepsilon_0} \frac{F_z}{Y\pi}[e_{33} - 2\upsilon e_{31}]\frac{L}{R^2}\right| \tag{4.17}$$

The maximum compressive potential is related to both length and radius. Utilizing the material properties in the COMSOL Library, the analytical solutions can derive the maximum piezo-potential

Cette thèse est accessible à l'adresse : http://theses.insa-lyon.fr/publication/2022LYSEI006/these.pdf
© [X. Zhang], [2022], INSA Lyon, tous droits réservés

magnitude of a laterally defected NW (φ_{max} = 0.128 V) and a compressive NW (φ_{max} = 2.006 V) with the same geometry and amplitude of the applied force. As the mathematical computation involves several approximation and assumption steps (e.g., the simplification of piezoelectric model to the first order equation, the neglection of the bending force at the bottom of NW), the analytical results are believed to be a little discrepant to the reality. But this method gives an indication about what and how relative parameters influence the generated piezoelectric potential. Eventually, COMSOL model is introduced in the next subsection, for a better comparison.

4.1.2 3D FEM simulation

Another approach to predict the electric potential distribution of a single ZnO nanowire (NW) is finite element method (FEM) using COMSOL Multiphysics. The FEM simulations can provide a clear understanding of the working principle, and in turn, facilitate the optimization of the output efficiency through relevant parameters. Hence, in order to obtain a more accurate NW model undergoing a lateral defection and vertical compression, the FEM program was applied with a combination of Solid Mechanics and Electrostatics modules that describe the piezoelectric coupling. There are five main steps in the COMSOL to simulate the single NW:

1) In the geometry part, we defined a 3D cylinder-shaped ZnO NW with a 42 nm diameter and a 1031 nm length (see Figure 4.2a), which keeps consistence to the realistic NW.
2) The material parameters used in the simulation are listed in Table 4.1 from the COMSOL's library in the strain-charge form. Noted that, in the simulation, ZnO NW was treated as a bulk material, even it has been proved that the piezoelectric coefficient of nanomaterial is higher than those in the bulk ZnO [62].
3) In the Solid mechanics and Electrostatics module, several boundary conditions were defined in order to achieve a converge solution. The bottom of ZnO NW was fixed and electrically grounded. The density of free charges in the NW was zero and side walls were free to move. The force-exerted surface was determined by the mechanical module, as shown in Figure 4.2b-c. Additionally, the semiconductor effect of ZnO were not considered in the electrical module of COMSOL, which will be introduced in subsection 4.3.
4) The mesh is a critical step in the COMSOL simulation as the solution accuracy is related to its size and shape. Small mesh size can improve precision but involve high computational space and time. In our simulation, a tetrahedral mesh with element size between 40 pm and 40 nm seems to be the best compromise.
5) Finally, a stationary mode was utilized without considering the geometric nonlinearity.

Cette thèse est accessible à l'adresse : http://theses.insa-lyon.fr/publication/2022LYSEI006/these.pdf
© [X. Zhang], [2022], INSA Lyon, tous droits réservés

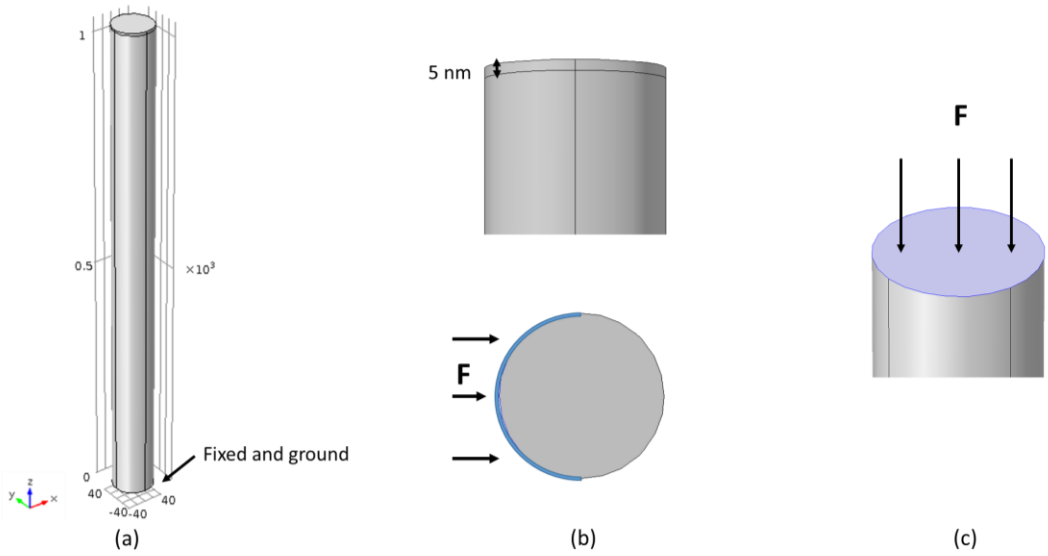

Figure 4.2. 3D NW in COMSOL Multiphysics with a radius R = 42 nm and length L = 1031 nm. (b) The upper part of the NW with 5 nm from the top side is laterally bent by a force *F*. (c) The top of the NW is compressed by a vertical force in compression mode.

Table 4.1. List of ZnO material parameters used in the simulation.

Constant	Value	Unite
Density	5680	kg/m³
Elasticity matrix	$\begin{bmatrix} 2.09714e+11 & 1.2114e+11 & 1.05359e+11 & 0 & 0 & 0 \\ 1.2114e+11 & 2.09714e+11 & 1.05359e+11 & 0 & 0 & 0 \\ 1.05359e+11 & 1.05359e+11 & 2.11194e+11 & 0 & 0 & 0 \\ 0 & 0 & 0 & 4.23729e+10 & 0 & 0 \\ 0 & 0 & 0 & 0 & 4.23729e+10 & 0 \\ 0 & 0 & 0 & 0 & 0 & 4.42478e+10 \end{bmatrix}$	Pa
Coupling matrix	$\begin{bmatrix} 0 & 0 & 0 & 0 & -0.480508 & 0 \\ 0 & 0 & 0 & -0.480508 & 0 & 0 \\ -0.567005 & -0.567005 & 1.32044 & 0 & 0 & 0 \end{bmatrix}$	C/m²
Relative permittivity	$\begin{bmatrix} 8.5446 & 0 & 0 \\ 0 & 5.5446 & 0 \\ 0 & 0 & 10.204 \end{bmatrix}$	1

4.1.2.1 Bending mode

To bend the nanowire, a lateral force is exerted on the top NW. For instance in the literature, the NW was usually bent by an AFM tip that is indicated as a point force [60]. However, a point force in COMSOL is not realistic and maybe cause a non-converging problem. As solution here is to introduce a thin 5nm-heigh cylinder stacked on top of the NW (cf. Figure 4.2(b)). Hence, the lateral force F_y = 60 nN is exerted on the upper part of the NW, 5 nm below the top side.

Figure 4.3(a) shows the mechanical stress (T_z) evolution of the NW in the z-direction. As expcted, the distribuion of T_z is concentrated at the bottom NW and decreases gradually along that direction. The bending mode shows a positive stress, which is cotrary to the compressive mode. In both case, the zero stress is obtained at the middle of the NW. The maximum and minimum stresses appear at the campled bottom

Cette thèse est accessible à l'adresse : http://theses.insa-lyon.fr/publication/2022LYSEI006/these.pdf
© [X. Zhang], [2022], INSA Lyon, tous droits réservés

owing to the binding reaction to the external bending force. Opposedly, the discussion on the field distribution of the NW's bottom part is absent in the analytical model due to the fact that the Saint-Venant principle is only valid in the regions far away from the affixed end. As shown in Figure 4.3(b), the strain distribution is similar to that of the stress where the maximum deformation also locates at the bottom. Furthermore, according to Eqs.(4.4), the generated electric displacement is caused by the stress and can be directly drived from the mehcanical strain. Thus, the electric displacement (Figure 4.3c) in the Z component (D_z) has the similar evolution profile compared to the strain distribution, while in the X and Y components the values are too small to be compared.

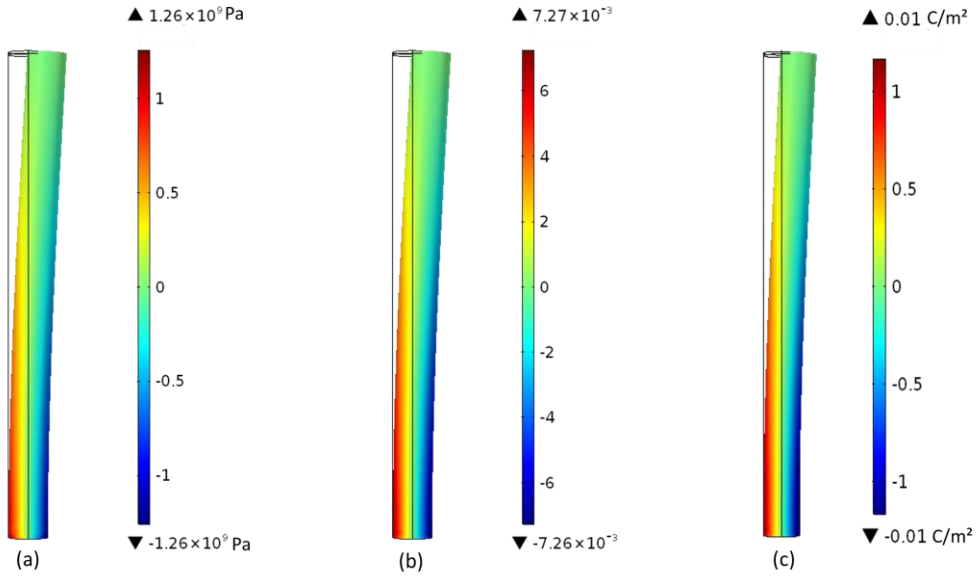

Figure 4.3. FEM calculation of a ZnO nanowire bending induced by a 60 nN lateral force on the top. Distribution of z component of (a) mechanical stress (T_{zz}), (b) mechanical strain (S_{zz}), and (c) electric charge displacement (D_z).

As it can be seen, the piezoelectric potential created by the polarizations within NW is displayed in Figure 4.4a. The electric potential on the extension surface is positive while negative on the compressive surface with equal absolute value, except at the end area near the affixed boundary. More specifically, as shown in Figure 4.4b, the cross-sectional outputs at z = 1031 nm and z = 15 nm have total inverted electric field distribution. And at the position of z = 1031 nm, where force is applied, the electric potential reaches the maximum value. The evolution of electric potential along the tensile and compressive side walls of NW as a function of the arc length are plotted in Figure 4.4c. Firstly, at the bottom cylinder within height smaller than 30 nm, a potential reverse region is observed. For the middle cylinder with height between 100 to 1000 nm, the absolute value of maximum potential (0.13 V) is almost same as the value of minimum potential (-0.13 V) at the opposite position. Therefore, the bending ZnO nanowire can be regarded as a "parallel-plate capacitor". At the free end of the NW, the output potential increase little compared to that of the middle cylinder due to the exertion of external force. In addition, the maximum potential in a "parallel-plate" region derived from the FEM simulation shows high consistent with the value (0.128 V) calculated from analytical modeling (Eq. 4.15) with a small discrepancy of 2%.

Cette thèse est accessible à l'adresse : http://theses.insa-lyon.fr/publication/2022LYSEI006/these.pdf
© [X. Zhang], [2022], INSA Lyon, tous droits réservés

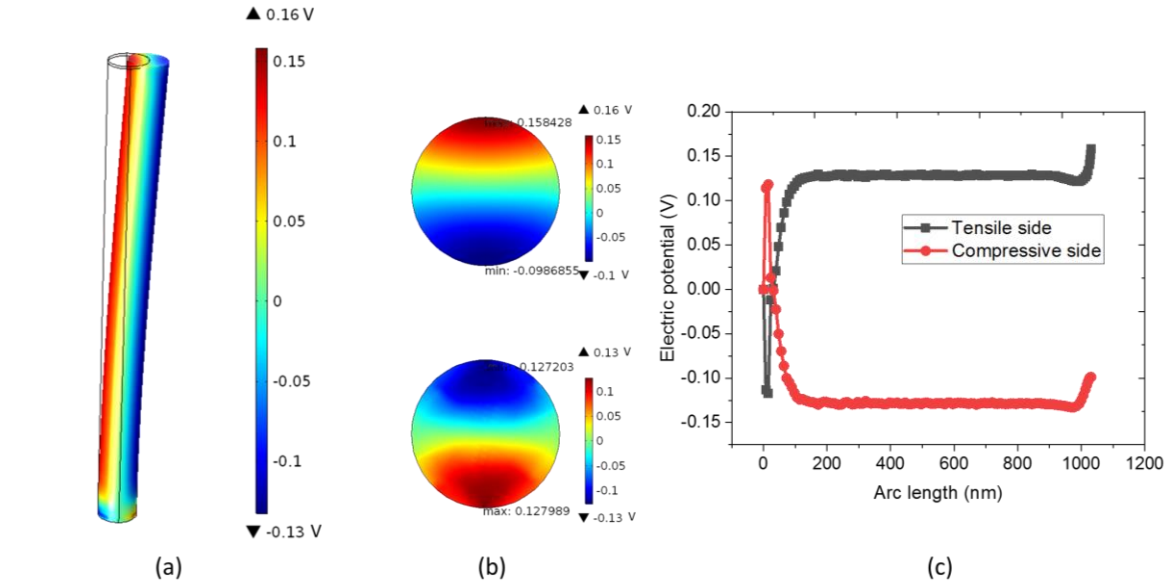

Figure 4.4. (a) 3D electric potential generated in NW under a lateral force, and (b) cross-section electric potential profile at z =1031 (upper panel) and z =15 nm (bottom panel). (c) Evolution of the electric potential along the tensile and compressive side walls of NW at the y-z plane as a function of the z axis.

4.1.2.2 Compression mode

For the compression mode, a NW with the same geometry and boundary condition is submitted to an axial compressive force F_z = 60 nN along the z-axis (Figure 4.2c). Generally, the NW experienced by a compressive force has a contraction deformation in the z-axis and an expansion deformation in the x and y directions due to the Posson effect. As expected in Figure 4.5(a), the stress tenser in z component (T_{zz}) shows a negative uniform distribution on the whole nanowire, except the bottom part, where a fixed constrain is limit. Similar phenomenon is observed for the X and Y components (Figure 4.5(b), (c)), but with positive values of the stress tenser.

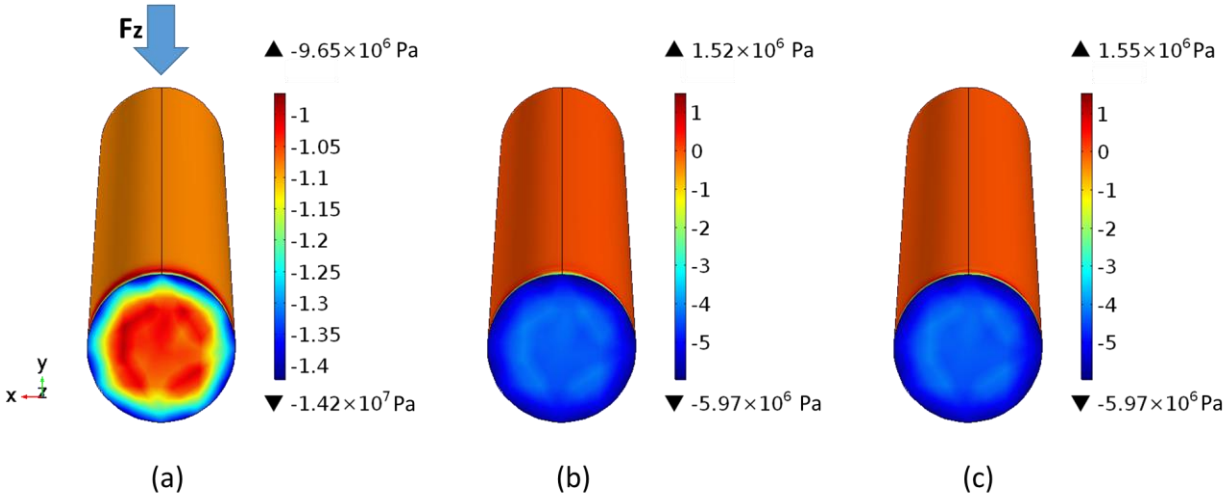

Figure 4.5. FEM calculation of a ZnO NW compressed by an axial force of F_z = 60 nN on the top surface. Distribution of the mechanical stress of (a) Z component, (b) X component and (c) Y component.

Cette thèse est accessible à l'adresse : http://theses.insa-lyon.fr/publication/2022LYSEI006/these.pdf
© [X. Zhang], [2022], INSA Lyon, tous droits réservés

Figure 4.6(a) shows a 3D electric potential profile of the NW under an axial compression. A maximal value (~ 1.16 V) of the generated potential at the top linearly decreases along the z direction and attains zero at the bottom NW (Figure 4.6(b)).

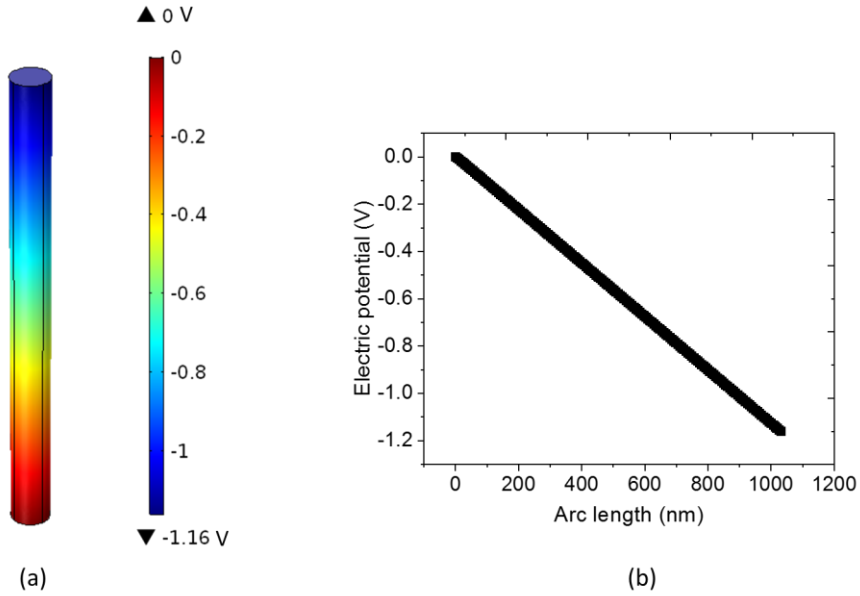

Figure 4.6. (a) 3D electric potential generation in the ZnO NW under compression model. (b) Evolution of the electric potential along the side wall of NW at the y-z plane as a function of the length.

4.1.3 Parameters influencing the output performance

To improve the NW performance, the impact of parameters on the generated piezoelectric potential should be studied. As we discussed in Eqs. (4.15) and (4.17), the piezoelectric potential is related to the excitation mode of external force, the geometric parameter (NW's size and shape), and the intrinsic material properties such as the piezoelectric coefficient (e_{pl}), Young's modulus (Y), etc. Usually, the intrinsic properties are difficult to modify, while the first two parameters can be tuned and tailored by the user in experimental tests and synthesis process, respectively. For instance, the length of the NW can be easily controlled by the growth time. Hence, we investigate the influence of three main parameters including excitation mode, NW size, and NW shape.

4.1.3.1 Excitation mode

Figure 4.7 illustrates the piezoelectric potential (in absolute value) versus the external force resulted from a perpendicular compressive force and a parallel bending force. As expected in Figure 4.7, the output potential increases with the increasing applied force, whatever its direction. Interestingly, under the same force magnitude, the output voltage is almost tenfold higher in the compressive mode as opposed to the bending mode. Actually, for a single ZnO crystal, the piezoelectric coefficient along the length direction has the highest value (d_{33} = 11.67 pC/N) while on other direction, d_{31} for example, has lower value of 5.43 pC/N. High d_{33} allows to enhance the energy conversion, giving raise to higher electric potential under a given input force along the c-axis. Therefore, the compressive mechanism is preferred in the application of the piezoelectric ZnO NWs.

Cette thèse est accessible à l'adresse : http://theses.insa-lyon.fr/publication/2022LYSEI006/these.pdf
© [X. Zhang], [2022], INSA Lyon, tous droits réservés

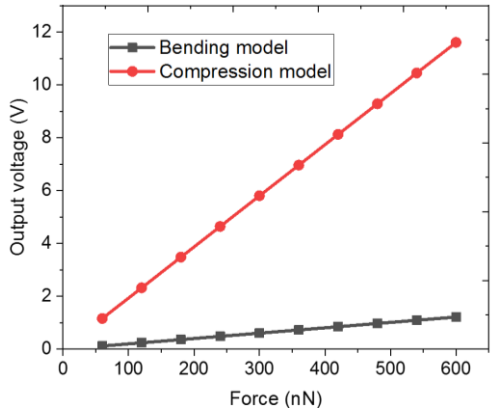

Figure 4.7. Generated piezoelectric output potential as a function of the exerted force along the z-direction (compression model) and x-or y-direction, defined as bending model.

4.1.3.2 NW size

Figure 4.8(a) illustrates the piezoelectric response of a deflected NW under an external *F*= 60 nN. when the radius (R) of the NW is constant, the average electric potential at "parallel plate region" does not change with the increasing aspect ratio (L/R). Only the binding reaction effect at the bottom of the NW reinforces, which is not presented here. On the contrary, the average output voltage is linearly increasing when fixing the length but decreasing the radius. As the diameter is reduced, the deflection of the NW increases; resulting in enhanced piezoelectric performance. Therefore, a smaller NW is preferred in the deflected mode, but the fraction failure should be more considered with smaller radius [227]. In the compression mode (Figure 4.8b), the output voltage is linear proportional to the length (while the radius is fixed of 42 nm) and reaches approximately 8 V with the length of around 7100 nm. Similar behavior is found with the decreasing radius at a fixed length (L=1031 nm), but linearity is somewhat less perfect. Interestingly, the maximal value of the generated potential substantially boosts (~ 58 V) when the radius reduces to 6 nm. Therefore, with the same aspect ratio, decreasing the NW diameter has much more impact on the improvement of the piezoelectric properties than increasing its length. In practice, the aspect ratio under compression model, to some extent, should be reasonably limited so as not to weaken the NW strength [227].

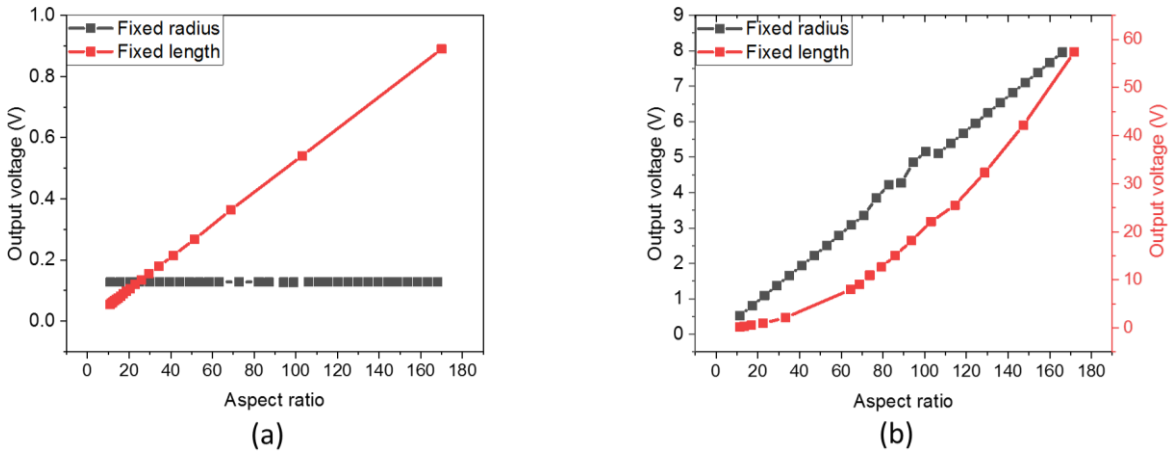

Figure 4.8. Output electric potential versus aspect ratio under an external *F* = 60 nN with (a) bending and (b) compressive directions.

Cette thèse est accessible à l'adresse : http://theses.insa-lyon.fr/publication/2022LYSEI006/these.pdf
© [X. Zhang], [2022], INSA Lyon, tous droits réservés

Accordingly, the results of the COMSOL simulation allows to confirm the relationship between the output potential and the NW size. These findings correlate to the analytical predictions of Eqs (4.15) and (4.17) for bending and compression model, respectively.

4.1.3.3 NW shape

In order to simplify the computations of the FEM simulation, the individual NW is designed as a cylinder with a perfect circular cross-section. In reality, ZnO wurtzite structure has a typical hexagonal shape. Thus, we should distinguish the difference outputs between cylindrical and hexagonal NW. Under a boundary lateral force F_y = 60nN on the top, a 3D electric potential distribution of the ZnO nanowire with a hexagonal cross-section shape is displayed in Figure 4.9(a). A side length of 46.17 nm in the hexagon and an axial length of 1031 nm were set, ensuring an equal surface and volume as compared to the cylinder drawn on Figure 4.2a. The piezoelectric potential profile of the hexagonal-shaped NW is similar to that of circular shape, where a potential inversion region appears on the bottom and a "parallel-plate capacitor" exists in the middle part. However, under the same boundary lateral force, the maximum piezoelectric potential of the hexagonal NW is around 0.15 V, which is slightly higher (~ 6.1%) compared to the circular NW. In the meantime, when the hexagonal NW is submitted to an axial compressive fore (F_z=60nN), both NWs reach the same maximal value of the electric potential (~ 1.16 V). Therefore, for the compression mode, modeling a hexagonal NW by a circular NW seems to be reasonable. For the bending mode, a small discrepancy (6.1%) between them can be neglected as other factors in the realistic samples (e.g., NW size) have more significant impact on the piezoelectric performance [175,228].

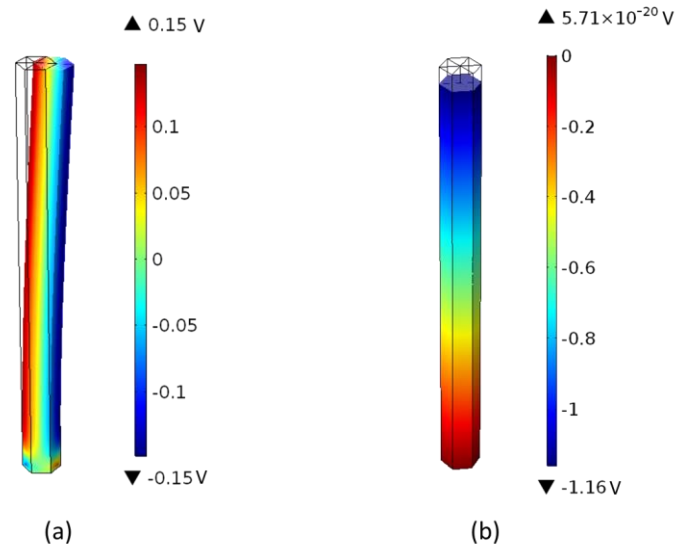

Figure 4.9. 3D electric potential distribution of ZnO NW with a hexagonal cross-section shape under (a) a boundary lateral force F_y = 60nN on the top, and (b) an axial compressive force F_z = 60nN.

4.2 Analytical model of ZnO NW arrays-based composite

As discussed in the previous section, the individual ZnO NW subjected to a compressive force has higher output voltage and efficiency compared to the one applied by a lateral bending force. Thus, piezoelectric ZnO NWs based structures in the compressive mode are highly promising in the medical and health applications such as ex vivo and in vivo flexible sensors. In our work, a novel structure where

Cette thèse est accessible à l'adresse : http://theses.insa-lyon.fr/publication/2022LYSEI006/these.pdf
© [X. Zhang], [2022], INSA Lyon, tous droits réservés

vertically aligned ZnO NW arrays encapsulated in polymethyl-methacrylate (PMMA) matrix is investigated. As illustrated in Figure 4.10, the developed multi-layer composite consists of two thin electrodes, a substrate layer, a ZnO seed layer, a NWs-PMMA composite layer, top PMMA layer above the NWs. The top PMMA polymer is employed to enhance the stability, mechanical robustness of the whole device, as well as to avoid the electrical leakages and short circuit. The working principle of the ZnO NWs/PMMA composite can be explained based on the electromechanical coupling of a piezoelectric material: 1) an axial force is subjected on the top electrode to compress the NWs along the z-axis; 2) positive charges and negative bound charges are generated at two ends of the NWs and create a dipole-like potential along the z-axis, according to the piezoelectric effect; 3) due to the electrostatic induction effect, opposite charges appear at upper and bottom electrodes driving a flow of electrons is through the external circuit.

For the modeling of the ZnO NW-based device, analytical models relying on the equivalent mechanical and electric circuits are crucial to simplify the estimation of the overall system performance. Besides, the upper and bottom gold electrodes are omitted as its thin thickness (around 25 nm) has little impact on the mechanical behavior. Thus, only electrical condition limit is assigned to the whole structure, where the bottom is grounded, and the top is defined with a floating potential. Moreover, the silicon substrate normally behaves like a resistor and possesses much higher Young's modulus than the PMMA matrix itself. Hence, the substrate can be also neglected and only regarded as the clamping condition at the bottom of the ZnO NWs/PMMA composite.

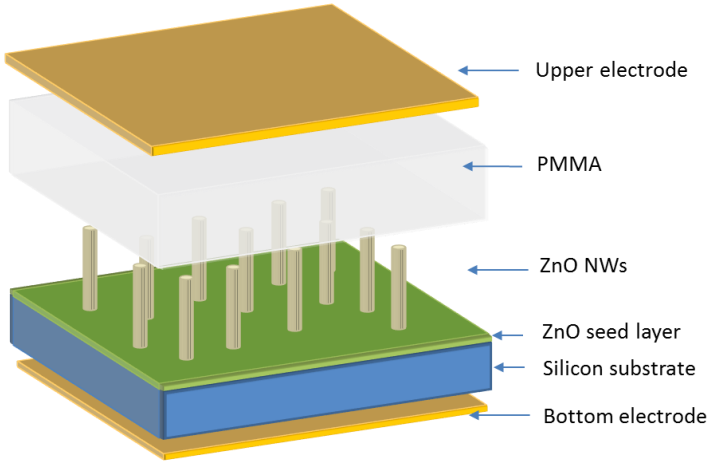

Figure 4.10. Schematic structure of ZnO NW arrays/ polymer composites

4.2.1 Mechanical equivalent model

To simplify the mechanical analytical model, two cases for the idealized fiber-reinforced composite material including the iso-strain or iso-stress models were introduced [229]. Several assumptions were taken in account: each layer was assumed as isotropic material and the Hooke's law was valid under small elastic deformations. Figure 4.11(a) describes the material structure where the arrangement of two elements (ZnO and matrix) is considered to be perpendicular with respect to the external applied stress (T). Considering the stress distribution is homogeneous to transfer to each layer within an external stress T, the iso-stress condition can be derived as:

$$T = T_{ZnO} = T_{PMMA} \tag{4.18}$$

Cette thèse est accessible à l'adresse : http://theses.insa-lyon.fr/publication/2022LYSEI006/these.pdf
© [X. Zhang], [2022], INSA Lyon, tous droits réservés

The effective Young's modulus Y_{Pe} of the composite with the stress perpendicular to direction of the fiber is given as:

$$\frac{1}{Y_{Pe}} = \frac{V_{ZnO}}{Y_{ZnO}} + \frac{V_{PMMA}}{Y_{PMMA}} \tag{4.19}$$

where V is the volume fraction. For the case that stress applied parallel to the fiber direction, the fibers cannot be pulled out from the matrix. Thus, iso-strain (S) condition is defined as:

$$S = S_{znO} = S_{PMMA} \tag{4.20}$$

Then, the effective Young's modulus Y_{Pa} of the composite can be deduced as:

$$Y_{pa} = Y_{ZnO} * V_{ZnO} + Y_{PMMA} * V_{PMMA} \tag{4.21}$$

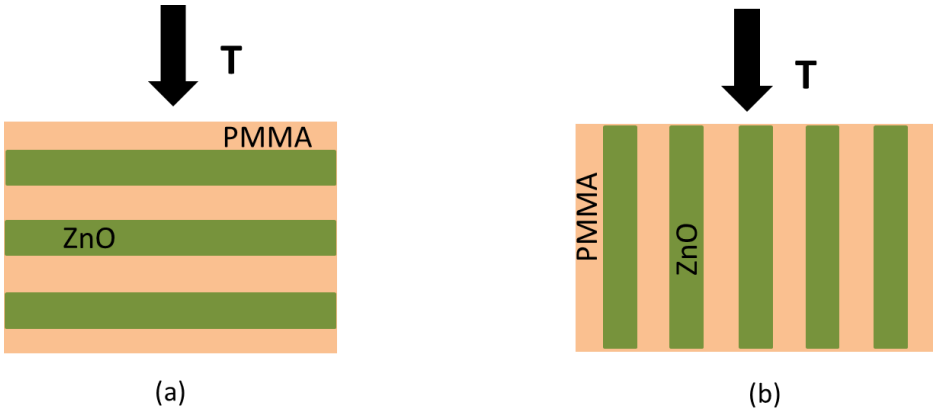

Figure 4.11. Schematics of idealized fiber-reinforced composite subjected to stress (a) perpendicular or (b) parallel to the fiber direction.

Combing the above iso-strain or iso-stress models, the ZnO NWs within PMMA matrix composite can be described as an ideal fiber composite material shown in Figure 4.12(a). Bottom layer consists of the ZnO fibers and interstitial PMMA matrix between nanowires with direction parallel to the stress, and a top layer composed of insulating polymer (PMMA in our case) is stacked above the bottom layer. The effective Young's modulus Y_{Eff} of the composite is given as:

$$\frac{1}{Y_{Eff}} = \frac{V_{Top}}{Y_{Top}} + \frac{(1-V_{Top})}{Y_{matrix}*V_{matrix}+Y_{ZnO}*V_{ZnO}} \tag{4.22}$$

Furthermore, we demonstrate that the mechanical structure of the composite can be featured as the spring model displayed in Figure 4.12b. A spring K_{top} is in series to a spring K_{bottom} which involves 2 parallel springs of ZnO (K_{ZnO}) and matrix (K_{matrix}). Regarding the stress expression of the bottom layer:

$$S_{bottom} = S_{ZnO} = S_{matrix} = \frac{\Delta L_{bottom}}{L_{bottom}} = \frac{T}{Y_{bottom}} \tag{4.23}$$

where L_{bottom} denotes the height of the bottom layer, and ΔL_{bottom} refers to as its deformation, which is deduced by:

$$\Delta L_{bottom} = \frac{T \times L}{Y} = \frac{F}{\frac{A*Y}{L}} \tag{4.24}$$

Cette thèse est accessible à l'adresse : http://theses.insa-lyon.fr/publication/2022LYSEI006/these.pdf
© [X. Zhang], [2022], INSA Lyon, tous droits réservés

Given that $K_{bottom} = \frac{A*Y}{L}$, where K_{bottom} is the stiffness of the bottom layer and A is the surface, it follows:

$$\Delta L_{ZnO} = \frac{F}{K_{bottom}} = \frac{F}{K_{matrix}+K_{ZnO}} \quad (4.25)$$

Consequently, under small elastic deformation, the strain of ZnO is only determined by the total force, Young's modules, surface area and thickness of ZnO and matrix.

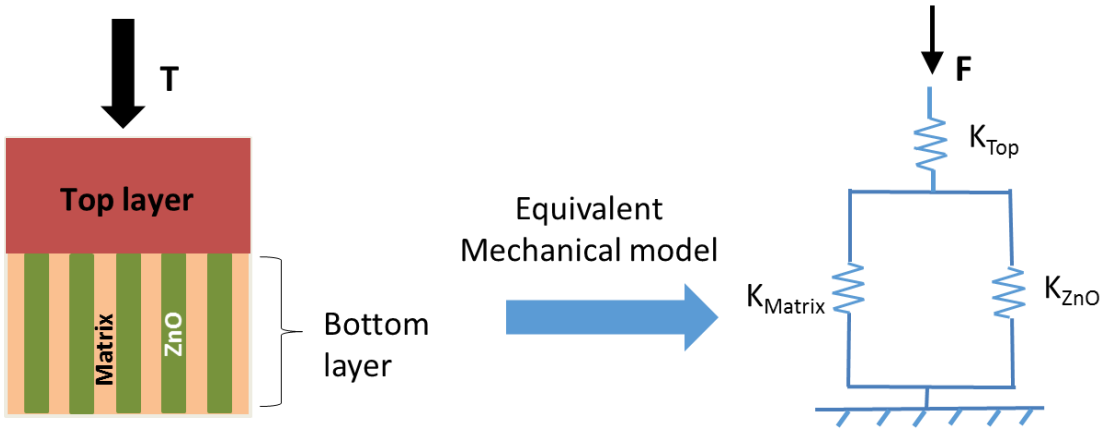

Figure 4.12. Equivalent mechanical schemes: (a) ideal fiber composite material; and (b) equivalent spring model

4.2.2 Piezoelectric equivalent model

In this study, the material is operated at low mechanical frequency, as the final objective is to adopt the NWs-based device as a pressure sensor for FFR (fractional flow ratio) measurement during coronary angiography. In comparison with the resonance frequency of one NW (above 1 MHz), it is assumed that ZnO NW arrays/PMMA composites are compressed under a quasi-static force. To further simplify the model, transverse deformations due to the Poisson's ratio and relative d_{31} piezoelectric coefficient are neglected. As the piezoelectric NW only generates charge under a stress, it operates as a charge generator, rather than a voltage source. But with the help of the Thevenin's theorem, a piezoelectric ZnO NW can be modeled as a voltage source in series with a capacitance C_{NW}. As seen in Figure 4.13, this combination is in return parallel with a resistance R_{NW}, i.e., representing the internal resistance of NW that is dedicated to the conduction leakage, particularly under low frequency [230].

In reality, the ZnO NWs are doped semiconductors with a typical resistivity (ρ) of 0.01-10 Ω cm [231], so $R_{NW} = \rho * L_{ZnO}/A_{ZnO}$. $C_{NW} = \varepsilon_0\varepsilon_{ZnO} * A_{ZnO}/L_{ZnO}$ donates the capacitance of the NW. According to the piezoelectric constitutive equation, the piezoelectric potential across the nanowire can be calculated as:

$$U_{NW} = \frac{T_{ZnO}*L_{ZnO}*d_{33}}{\varepsilon_{ZnO}*\varepsilon_0} \quad (4.26)$$

From the above equation, the piezoelectric voltage U_{NW} is determined by the dielectric property, the piezoelectric coupling, the NW length, and the stress applied on it. Besides, the real sample is made of a large number (denoted n) of NWs that are considered to be connected in parallel. In that case, the resulting capacitor is n times higher but the output voltage is unchanged.

Cette thèse est accessible à l'adresse : http://theses.insa-lyon.fr/publication/2022LYSEI006/these.pdf
© [X. Zhang], [2022], INSA Lyon, tous droits réservés

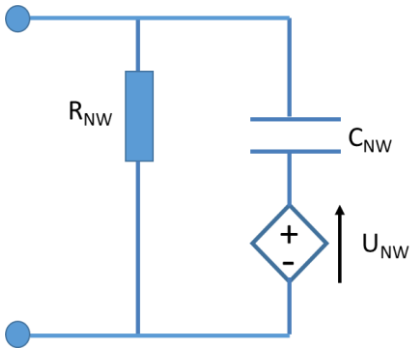

Figure 4.13. Equivalent electrical circuit of a compressive ZnO NW along the direction of c-axis.

4.2.3 Electrical equivalent model

In general, the bottom layer with 1-3 phase distribution can be considered as an effective homogeneous material with piezoelectric property [232]. Thus the effective dielectric permittivity of bottom layer can be calculated as [233]:

$$\varepsilon_{bottom} = V_{ZnO}\left(\varepsilon_{33}^{ZnO} - \frac{2V_{matrix}\left(e_{31}^{ZnO}\right)^2}{V_{ZnO}\left(c_{11}^{matrix}+c_{12}^{matrix}\right)+V_{matrix}\left(c_{11}^{ZnO}+c_{12}^{ZnO}\right)}\right) + V_{matrix}\varepsilon_{11}^{matrix} \quad (4.27)$$

where V is the volume fraction, the superscript "ZnO" and "matrix" stand for the corresponding material properties of ZnO and interstitial matrix, respectively. Thus, the effective capacitance of the bottom (C_{bottom}) can be derived as a function of ε_{bottom} as $C_{bottom} = \varepsilon_0\varepsilon_{bottom} * A_{bottom}/L_{bottom}$. By adding an insulting top layer with a capacitance ($C_{top} = \varepsilon_0\varepsilon_{top} * A_{top}/L_{top}$), the equivalent electric circuit is displayed in Figure 4.14 [234].

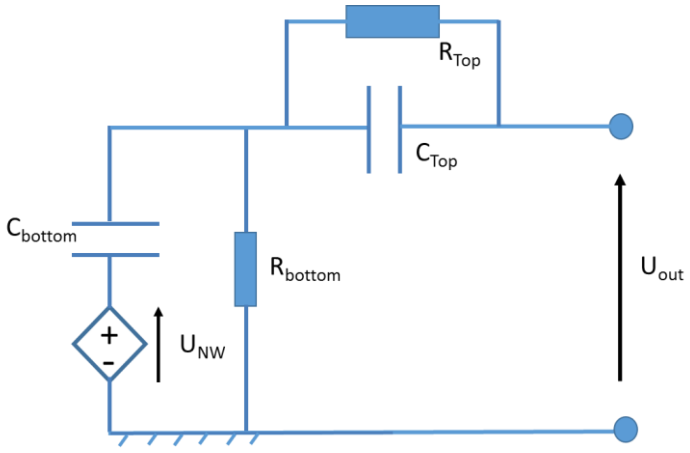

Figure 4.14. Equivalent electrical circuit of a ZnO NW within PMMA composite.

Furthermore, in case of perfect dielectric materials (low leakage) where if the resistance of the bottom and the top layers can be removed, the effective capacitance (C_{total}) of composite consisting of ZnO NWs integrated in polymer matrix is given by:

$$C_{total} = \frac{C_{bottom} * C_{top}}{C_{bottom}+C_{top}} \quad (4.28)$$

Cette thèse est accessible à l'adresse : http://theses.insa-lyon.fr/publication/2022LYSEI006/these.pdf
© [X. Zhang], [2022], INSA Lyon, tous droits réservés

As a consequence, the analytical approach derives different analytical expressions to estimate the device behavior. Moreover, optimization routes can be concluded based on three analytical models. There are two categories of parameters which can be tuned to improve the performance: 1) material properties involving the dielectric, piezoelectric, and mechanical characterizations; and 2) design of the structural design like the NW's density, the NW's geometry, etc. However, some parameters not only impact one physical process, but also the interplay from coupled mechanisms. For instance, the density of NW influences the mechanical and electrical process, simultaneously. Thus, this situation leads to a complicated and non-straightforward analysis result. Besides, the simple analytical model lacks the consideration of 3D complex effects like extreme deformation, air influence, and so on. The COMSOL Multiphysics based FEM therefore should be used to simulate a fully coupled electromechanical system and investigate the optimization trends. At the end, this approach will permit to propose a simple equivalent electric model of the sensor for the future design of the complete measurement interface stage.

4.3 Simulation model of ZnO NW arrays-based composite

As seen in Figure 4.15(a), simulation of ZnO NW arrays/PDMS composite is a complicated numerical model with repeated NWs structure. In order to simplify the numerical model and reduce the computational time and resources, a typical unit cell with periodical boundary conditions on the sidewalls is defined to be representative of the whole device behavior, as depicted in Figure 4.15(b). In the bottom layer, a 3D cylinder shape representing a ZnO NW with 42 nm radius and 1031 nm length was grown on a 40 nm thick seed layer (SL) and embedded in a PMMA matrix. A dielectric top layer, with a varying thickness initially set to 1000 nm, was stacked above the bottom layer to create a unit cell with size of 141 × 141 × 2071 nm^3 that matches the realistic NW density (51 ± 7 μm^{-2}). The material properties of ZnO and PMMA were taken from the COMSOL material library. To consider the dielectric loss in the insulating matrix layer, the real part and imaginary part of the relative permittivity of PMMA matrix were respectively set as 4.8 and 0.2 at 1 Hz, measured through experiment. Regarding the boundary conditions, a fixed mechanical constraint and electrical ground condition were applied at the bottom of the SL, while the top of PMMA was subjected to a boundary stress T = 1 MPa along the z-axis and an electrical floating condition. Finally, the study was carried out in the frequency domain at 1 Hz to simulate the experimental situation where the mechanical excitation was 1 Hz (i.e., similar to human's pulse).

The electrical potential profile generated in a unit cell is displayed in Figure 4.16(a) with a cross section view, and evolution of potential along the central axial is shown in Figure 4.16(b). Under application of a compressive stress, the output piezoelectric potential generated along the NW becomes negative and its absolute value gradually increases from the bottom (connected to the ground) to the top. This potential difference in the unite cell occurs mainly along the NW and SL due to the piezoelectric effect in ZnO material. Interestingly, a very small variation (decreasing from 0.182 V to 0.180 V) of the potential occurs in the dielectric top layer, which probably results from the permittivity difference on the interface of two materials.

Cette thèse est accessible à l'adresse : http://theses.insa-lyon.fr/publication/2022LYSEI006/these.pdf
© [X. Zhang], [2022], INSA Lyon, tous droits réservés

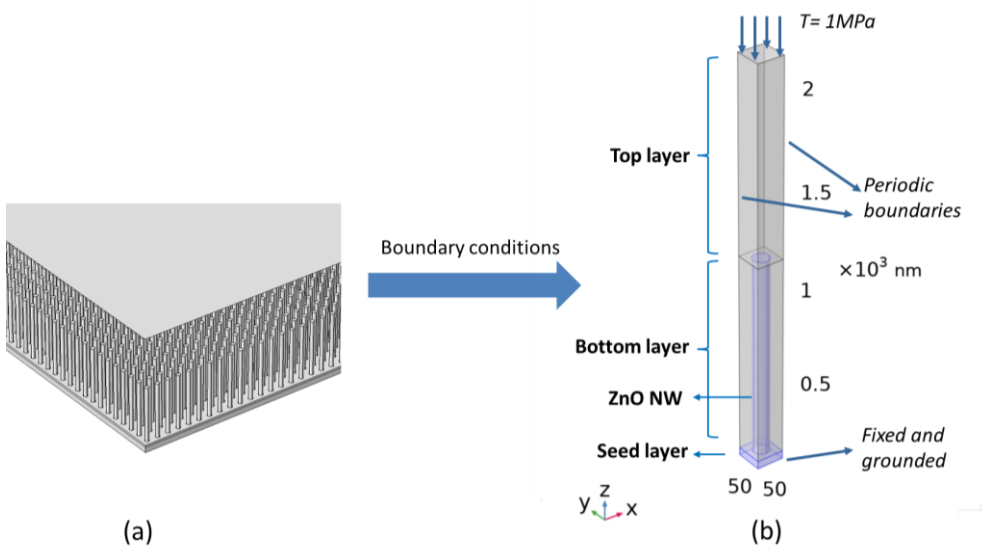

Figure 4.15. (a) COMSOL model of ZnO NW arrays in reality. (b) Schematic structure of a unit cell consisting of ZnO seed layer, bottom matrix layer, top matrix layer, and single ZnO NW with proper boundary conditions.

In order to simulate the actual working environment of ZnO NW arrays composite, Electrical Circuit module was coupled with Piezoelectricity module by applying proper terminal condition to form an electric loop. As indicated in Figure 4.16(c), a capacitor is connected in parallel to the composite so as to collect and accumulate the piezoelectric charges in response to a compressive stress. The electric potential on the top part of the NW is relatively low as the electrons in the external circuit are driven to cancel the voltage difference inside NW. This method allows to easily estimate the collected charge displacement (D), thus the effective piezoelectric constant ($d_{33} = D/T$) along the vertical direction. Since in a linear regime (i.e. subjected to a moderate mechanical stress), the effective piezoelectric coefficient of composite does not depend on the input compression, but rather on the intrinsic properties such as designed structure and material properties. Meantime, charge meter was used in the experimental setup to estimate the effective d_{33} of ZnO NWs/PMMA composites. Therefore, the FEM under an arbitrary compression was performed to describe the effective piezoelectric response of composite to have a comparison with the experimental results. With the aim of optimizing the material design and architecture, in the next steps, we focus on the influence of essential parameters such as Young's modulus and relative permittivity of the dielectric polymer, together with the density and dimension of the ZnO NW.

Cette thèse est accessible à l'adresse : http://theses.insa-lyon.fr/publication/2022LYSEI006/these.pdf
© [X. Zhang], [2022], INSA Lyon, tous droits réservés

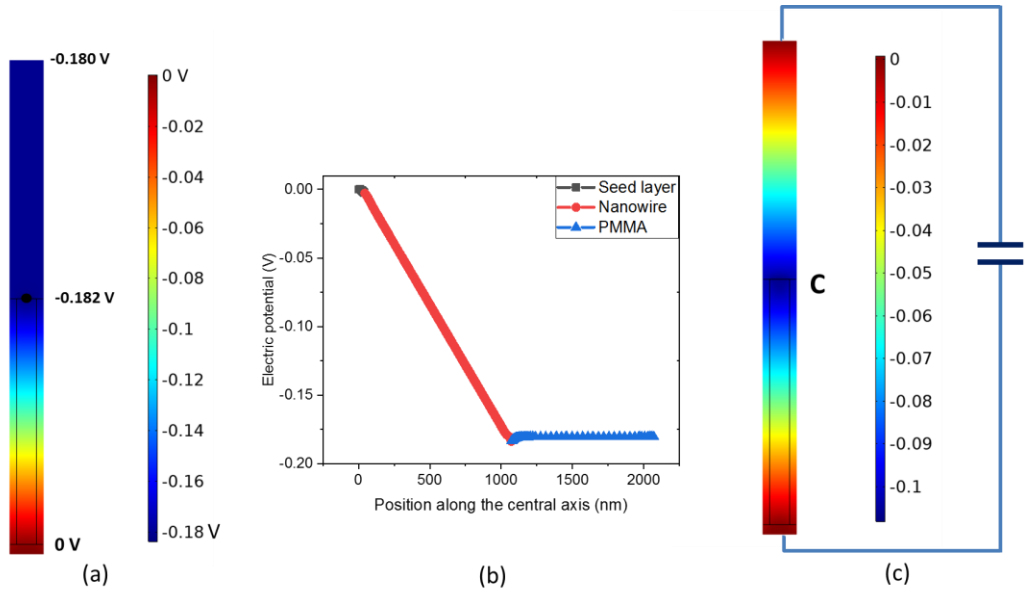

Figure 4.16. Electric potential longitudinal profile of unit cell subjected to an axial compression (a) viewed in a 2D YZ cut plane and (b) along the central axis. (c) Electric potential distribution of one unite cell electrically connected with an external capacitor.

4.3.1 Influence of Young's modulus

As shown in Figure 4.17(a), when increasing the Young's modulus of the bottom matrix (Y_{matrix}) from 1 to 500 GPa, the effective piezoelectric coefficient d_{33} of whole structure drastically decreases under a 1 MPa compressive stress (T). This phenomenon coincides with what we expected in the mechanical equivalent model (section 4.2.1) based on the combination of iso-strain or iso-stress models. This 2D model illustrates that stress is considered to be identical for top and bottom layers, and the strain is the same for the interstitial polymer matrix between NWs and the ZnO NWs. According to Eq. (4.23), the higher the Young's modulus of the bottom composite layer (Y_{bottom}), the lower the strain (S_{bottom}) can be observed. The strain S in the following sections always refers to the strain in the Z component (S_{ZZ}) for the sake of simplicity. This result is also confirmed in Figure 4.17(c) where S_{bottom} and S_{ZnO} are identical and inversely proportional to Y_{bottom}. The behavior of the strain response with respect to the Young's modulus of the bottom layer allows to explain the decreasing trend of the output charge shown in Figure 4.17(a). As expected, no change in the strain of the top layer (S_{top}) is revealed, as its Young's modulus is remained constant.

In Figure 4.17(b) and (d), we fix the Young's modulus of the bottom matrix while varying the value of the top layer. Logically, increasing Y_{top} leads to a decrease in the strain response of the top layer (S_{top}), i.e., tends to zero when Y_{top} is high enough. According to the Eq. (4.24) and (4.25), the deformations of the ZnO and matrix layer are independent to the top layer. Unexpectedly in Figure 4.17(d), there are some variations in S_{ZnO} and S_{matrix} , influenced by the variation of the Young's modulus of the top layer. Such variations are only obvious when a soft matrix top layer is made (low Y_{top}) with a large deformation where the ideal mechanical equivalent model is not valid. This phenomenon is attributed by the non-homogeneous distribution of the strain nearby the NW and of the stress of each layer, particularly in the 3D model [235].

Cette thèse est accessible à l'adresse : http://theses.insa-lyon.fr/publication/2022LYSEI006/these.pdf
© [X. Zhang], [2022], INSA Lyon, tous droits réservés

In case of hard top layer (high Y_{top}), the composite can be assumed as ideal model where the strain responses S_{ZnO} and S_{matrix} are close together and remind constant, despite the important change in the Young's modulus of the top layer. These observations explain why the piezoelectric response slightly increases with a soft top layer but unchanged otherwise (Figure 4.17(b)). As the voltage variation is very small (~ 1%), it is reasonable to conclude that Y_{top} has no noteworthy consequence on the piezoelectric output. From above two simulations, considering the same variation range of the Young's modulus for the top and the bottom matrix layers, a decrease in Y_{matrix} gives much higher efficiency for the optimization of the output d_{33} as compared to an increase in Y_{top}.

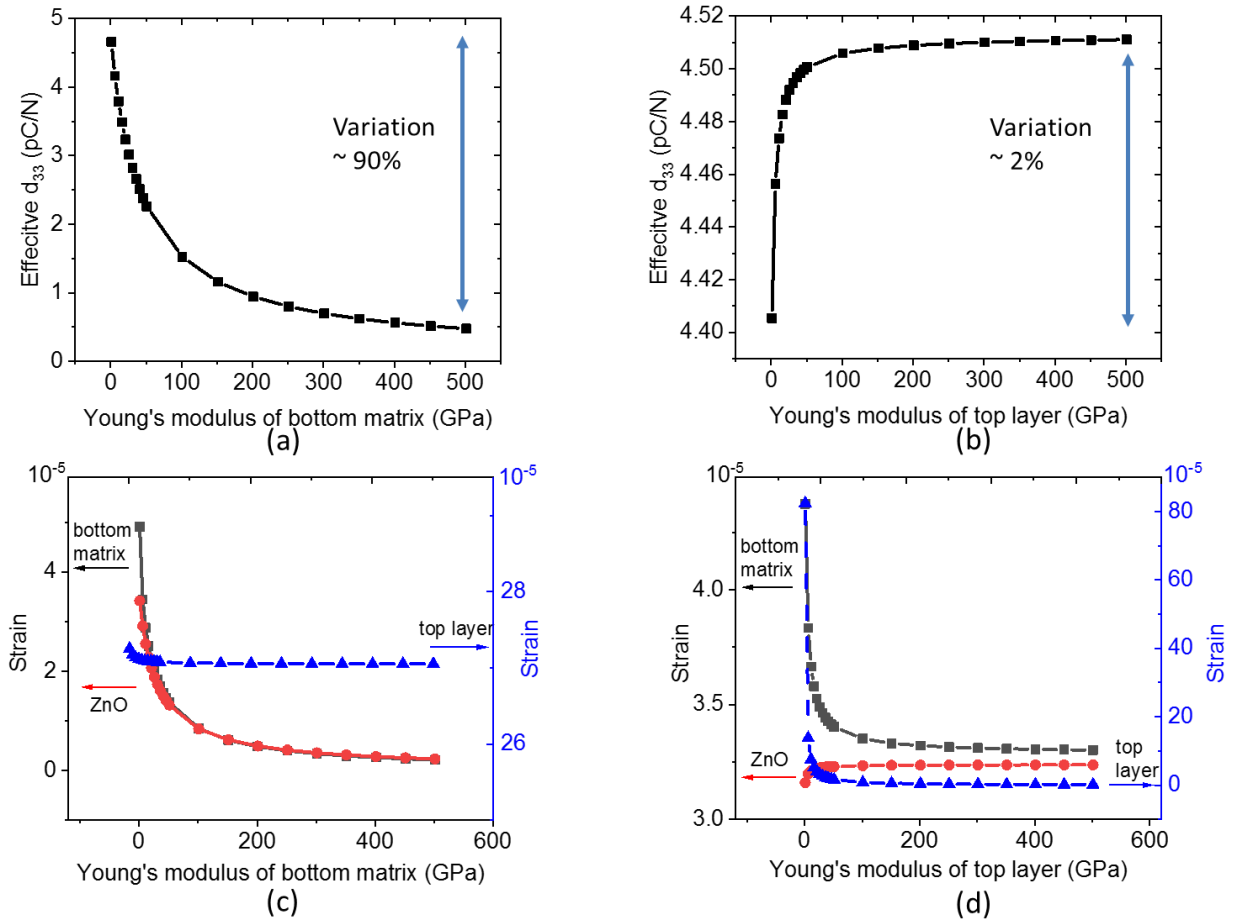

Figure 4.17. Effect of Young's modulus of (a) the bottom matrix and the top layer (respectively) on: (a) and (b) the piezoelectric response; (c) and (d) the resulting strain along the stress direction of different layers.

4.3.2 Influence of dielectric permittivity

The influence of relative permittivity on the effective piezoelectric coefficient is illustrated in Figure 4.18. Indeed, as we discuss in the section 4.2.3, the ZnO NWs and interstitial PMMA between NWs can be treated as an effective homogeneous piezoelectric material with relevant effective parameters [233]. A higher permittivity of isotropic bottom matrix layer can lead a large value of the effective dielectric permittivity of bottom composite. Meanwhile, the piezoelectric voltage of bottom composite is inversely proportional to the effective dielectric permittivity in Eq (4.26), causing a decrease of generated charges.

Cette thèse est accessible à l'adresse : http://theses.insa-lyon.fr/publication/2022LYSEI006/these.pdf
© [X. Zhang], [2022], INSA Lyon, tous droits réservés

As expected in Figure 4.18(a), the output piezoelectric sensitivity (d_{33}) significantly decreases with the increased relative permittivity of the bottom matrix layer (ε_{matrix}). Figure 4.18(b) shows the evolution of the effective d_{33} as a function of the relative permittivity of the top layer (ε_{top}). When increasing the permittivity of top insulating layer, decreasing dielectric loss and impedance from electric circuit equivalent model ($Z=1/(j\omega C)$), discussed in the section 4.2.3, are induced during the charge transmission process. Finally, the output charges collected on the top electrodes are boosted with an increasing piezoelectric sensitivity d_{33}.

As a conclusion, the best configuration based on the consideration of Young's modulus and dielectric permittivity, is a hard-top layer with high permittivity, and a soft bottom layer with low permittivity. It has been demonstrated that Si_3N_4 and Al_2O_3 are regarded as promising candidates for top insulating layers in vertical integrated nanogenerator structure [235,236]. Concerning the bottom layer, PMMA seems to be the favorable polymer thanks to its easy process, interesting dielectric and mechanical characteristics, as well as its high biocompatibility that makes it fascinating for medical applications. It is pointed out in this study that the properties of the top layer have relatively less effect on the piezoelectric response of the composite. Thus, in the fabrication process, we employed directly PMMA as a top layer, for the sake of simplicity.

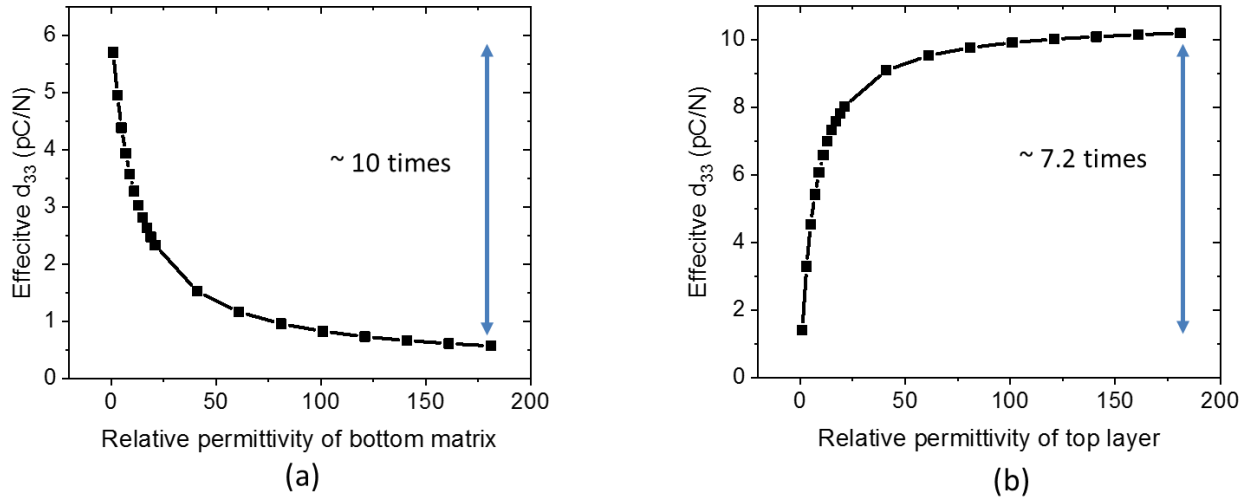

Figure 4.18. Effect of relative permittivity of the (a) bottom matrix layer, (b) top layer on the effective d_{33}

4.3.3 Influence of NW density

Simulation test performed in Figure 4.19(a) allows to assess the relationship between the NW density and the piezoelectric response. The NW density is modified by changing the width of the unit cell. A peak effective d_{33} of 4.45 pC/N is reached for the density of around 37 μm^{-2}, as a result of the balance between two main effects relating to the electromechanical coupling.

The first effect stems from the strain variation of the ZnO/matrix bottom layer (S_{bottom}), which substantially decreases as the NW density increases (cf. Figure 4.19(b)). Actually, increasing the density gives rise to an enhanced ZnO fraction content of the bottom layer composite, whose effective Young's modulus significantly boosts because of large differences in the mechanical properties between ZnO and PMMA ($Y_{ZnO} = 127\ GPa$ as opposed to $Y_{PMMA} = 3\ GPa$). The piezoelectric charge, i.e. ultimately related to the strain variation, drastically drops, particularly with a density higher than 50 μm^{-2}. It is

Cette thèse est accessible à l'adresse : http://theses.insa-lyon.fr/publication/2022LYSEI006/these.pdf
© [X. Zhang], [2022], INSA Lyon, tous droits réservés

noteworthy that the addition of NWs in particular, or fillers in general within polymers can lead to significantly change of their mechanical properties, which depend on the filler percentage.

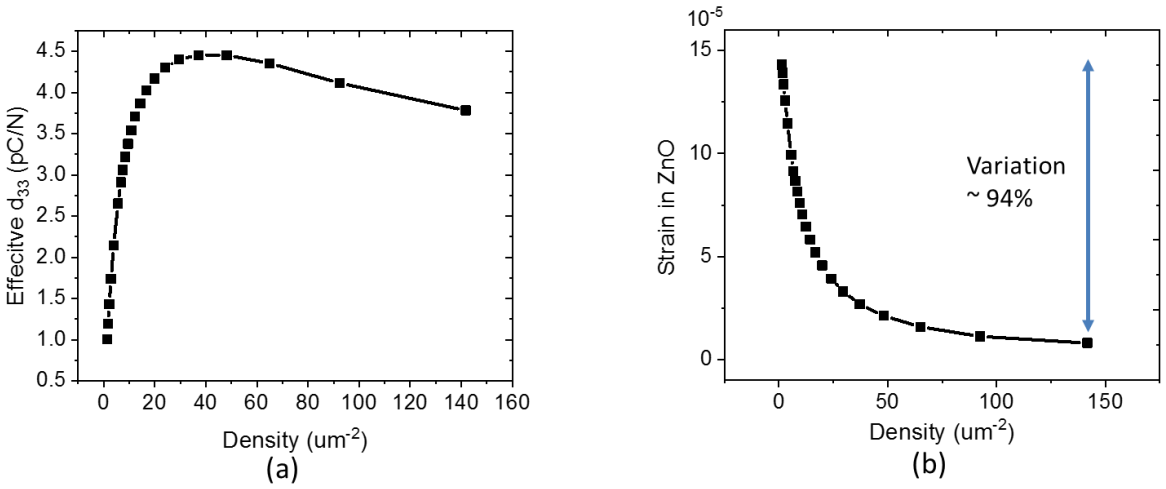

Figure 4.19. Effect of ZnO NW density on: (a) the effective d_{33}; (b) the strain in ZnO along the stress direction.

The second effect is dedicated to classic electrostatic effect [237]. More specifically, as the density increases, the volume of polymer matrix where ZnO NW is immersed reduces, resulting in a weak electrostatic effect inside the matrix. Besides, due to the increasing proportion of piezoelectric ZnO NW, the resulting piezoelectric response of whole device is significantly improved. As a consequence, a rise trend of the relative effective d_{33} with density is observed at low density. To summarize, the optimization of the piezoelectric response should consider and balance those opposed tendency effects. From the COMSOL simulation, a moderate density of around 25-55 μm^{-2} seems to be the most optimized configuration.

4.3.4 Influence of top layer thickness

During the fabrication of the vertically aligned ZnO NW array/polymer composite, the thickness of the top layer was a key parameter and required to be determined in advance. As suggested in the FEM simulation illustrated by Figure 4.20(a), the resulting charge generated from the array matrix gradually decreases as the thickness of the PMMA top layer is increased. On one hand, increasing the PMMA thickness leads to less ZnO concentration of the whole samples, provoking a decline in the piezoelectric response. More specifically, the decrease of the potential just arises from the fact that electric potential or field at a position generated from the charge, regarded as top of NW here, decreases with the distance between them in classical electrostatics [238,239]. This phenomenon is also can be simply attributed to the fact that the impedance of top insulating layer, as shown in the electrical circuit equivalent model (Figure 4.14), is increasing with the thickness of the top layer to reduce the output charge on the top electrode. On the other hand, the mechanical strain of the ZnO NW composite seems to be stable as a function of the PMMA thickness (cf. Figure 4.20 (b)), only very little fluctuation has been observed for the whole thickness range from 500 nm to 3000 nm. It therefore allowed to conclude that the Young's modulus of the composite is almost unchanged regardless of the top layer thickness. Similar to what was observed in Figure 4.17(d), a slightly increased slop occurs at small thickness of the top layer (i.e., 250-500 nm, Figure 4.20(b)), which is due to the non-homogenous structure of the bottom composite. Consequently, the decreasing effective

Cette thèse est accessible à l'adresse : http://theses.insa-lyon.fr/publication/2022LYSEI006/these.pdf
© [X. Zhang], [2022], INSA Lyon, tous droits réservés

piezoelectric sensitivity is not related to the strain variation, but rather caused by the diminution of the electric transmission generated within the top matrix layer.

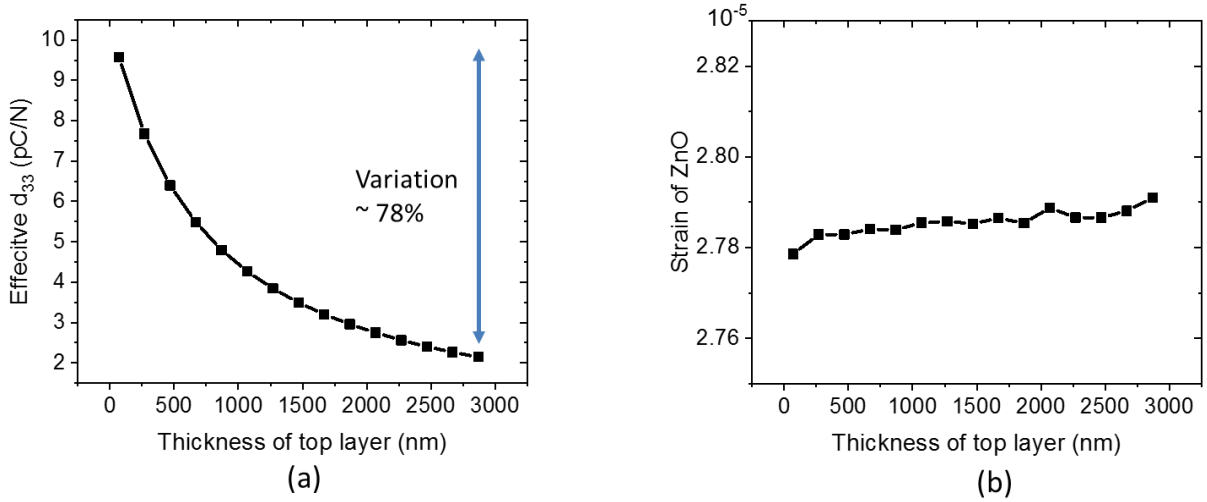

Figure 4.20. FEM simulation results on the effect of top layer thickness on the (a) generated effective d_{33}, (b) strain of ZnO.

4.3.5 Influence of NW dimensions

Besides the NW density, we demonstrate that the piezoelectric behavior also depends on the size of NW, which is assumed to be perfectly cylindrical shape. In practice, we fabricated NWs with dimension of around 42 nm radius and 1031 nm length. To better assess the effect of each parameter on the piezoelectric potential, two simulation trials are carried out, in which one parameter is varied while the other is fixed. In both tests, the unit cell is submitted to a static compressive stress of 1 MPa along the vertical z-axis. The results are displayed in Figure 4.21.

Seen in Figure 4.21(a), for a constant radius of 42 nm, we increase the NW length from 500 to 7000 nm and the thickness of top layer is coherently raised to keep a constant volume fraction of ZnO as well as NW density. In that case (Figure 4.21(c)), the effective Young's modulus of bottom composite is always fixed while the strain of ZnO increases with NW length at the beginning and then gradually reaches the saturation state. Then it is highly suspected that the main reason is the changing thickness of top layer as we discussed in the section 4.3.4. At small thickness of the top layer, the non-homogenous configuration around the interface between NW and PMMA causes a little rise in the strain response. As a consequence, the resultant effect d_{33} increases and converges to a maximum value with a variation around 5%. Figure 4.21 (b) shows the evolution of the piezoelectric effective d_{33} as a function of the NW radius, with a fixed length of 1031 nm. In order to keep the volume fraction of ZnO, a ratio α between the NW diameter and the unit cell width was fixed during the simulation. Indeed, with the radius increasing, the NW density coherently decreased and the strain of ZnO gradually decreases as displayed in Figure 4.21(d), resulting a decrease trend in the effective d_{33} of whole device. Nonetheless, varying a large span of radius or length only brings a small variation of the piezoelectric response (~ 5% and 8%, respectively) of ZnO NW composites. We can conclude that the NW geometry has few impacts on the piezoelectric sensitivity d_{33} of the whole composite when we keep the volume fraction of ZnO as a constant.

Cette thèse est accessible à l'adresse : http://theses.insa-lyon.fr/publication/2022LYSEI006/these.pdf
© [X. Zhang], [2022], INSA Lyon, tous droits réservés

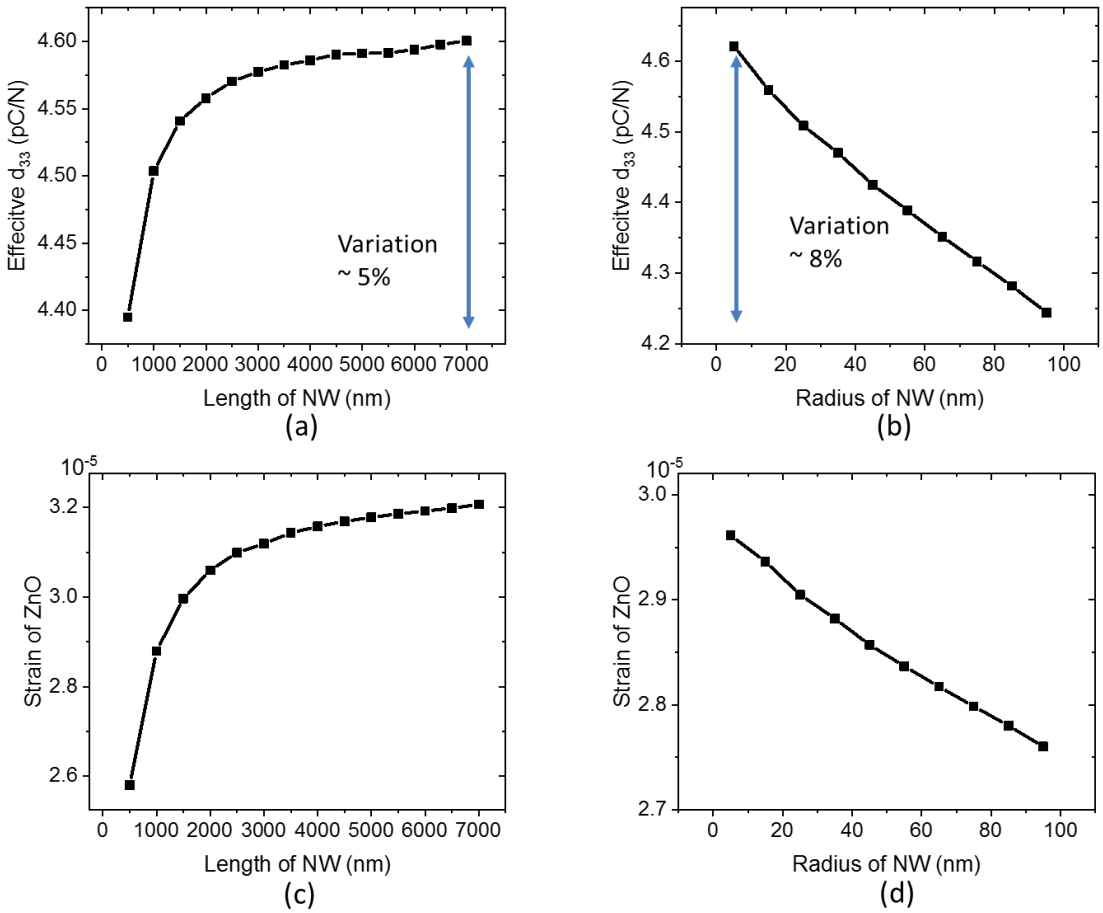

Figure 4.21. Effect of (a) NW length, and (b) radius on the effective d_{33} subjected to a constant compressive stress of 1 MPa; (c) and (d) the resulting strain of ZnO along the stress direction with respect to different effects.

4.3.6 Influence of surrounding environment

In order to simulate the realistic model, the NW unit cell was embedded in an infinite air environment to provide the zero electric field boundary condition at distance far away from the device (Figure 4.22(a)). Due to the strong edge effect and the electrostatic phenomena, the output voltage of one unit cell leads to much lower value (around 0.02 V) as opposed to the one (0.18 V) without considering the air effect (see Figure 4.16). In Figure 4.22(b), as the number of ZnO NW unit cells increases, the edge effects in classic electrostatics decrease, thus the output voltage coherently increase and then gently saturates at a maximum value when the cell number exceeds 600 NWs. For a large size of 33 × 33 cells (Figure 4.22(c)), the electric potential reaches 0.16 V, which is close to the reference value generated in a single cell without surrounding by the air. As a result, an array with at least 25×25 cells surrounded in the air is regarded as a suitable model to predict the theoretical performance in comparison with the experimental results.

Cette thèse est accessible à l'adresse : http://theses.insa-lyon.fr/publication/2022LYSEI006/these.pdf
© [X. Zhang], [2022], INSA Lyon, tous droits réservés

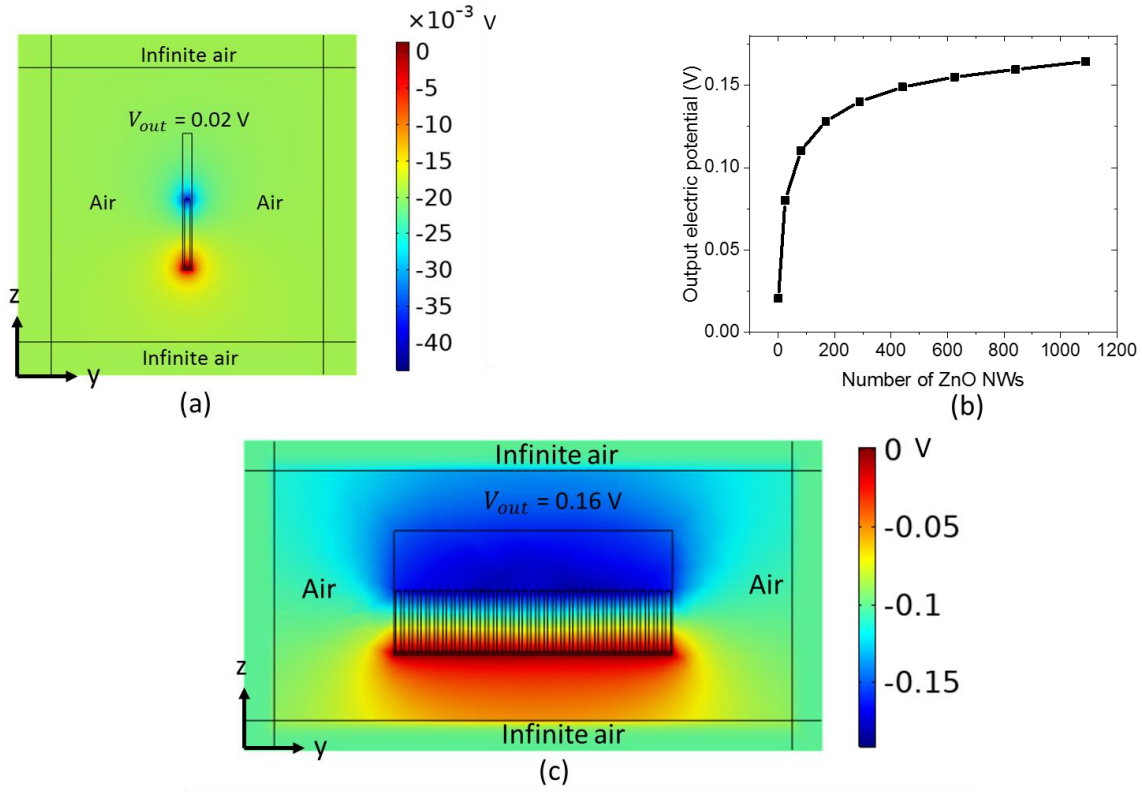

Figure 4.22. (a) FEM simulation of NW matrix subjected to an axial compressive stress of 1MPa, (b) Variation of the electric potential on the top electrode as a function of the matrix size. (c) In the 2D YZ center cut plane, the distribution of the electric potential for a 33×33 cell NW matrix surrounded by air.

Finally, the utilization of COMSOL simulation in this work provides basic optimization guidelines for the development of vertically aligned ZnO NW/polymer composite. This step allowed to better understand effects of the material properties (Young's modulus, relative permittivity) as well as geometric design of structure (NW shape and density, top layer thickness) to the piezoelectric sensor performance. However, in comparison with the actual experimental performance, the simulation still lacks several considerations like the semiconducting properties of ZnO.

4.4 Summary

In this work, single nanowire (NW) as the fundamental building structure of ZnO composite based device was firstly studied. Thanks to the perturbation theory proposed by the Gao *et al* [221], piezoelectric potential distribution was analytically calculated in a NW that is deflected by a lateral force or compressed by a compressive force. The electric potential in a bending mode is uniform along the z direction to behave as a 'parallel plate capacitor', while along the c-axis in a compressive mode. Due to the first-order approximation and limitation of Saint-Venant theory in deflected NW, the analytical solution leads to somewhat inaccurate estimation. Hence, a full numerical calculation-based FEM was introduced using COMSOL Multiphysics, which consists of two different models including bending and compression modes. External force and geometric parameters (shape and size of NW) were swept in both modes to figure out their relationship with the output potential, which were consistent with the analytical theory. It has been

Cette thèse est accessible à l'adresse : http://theses.insa-lyon.fr/publication/2022LYSEI006/these.pdf
© [X. Zhang], [2022], INSA Lyon, tous droits réservés

pointed out that, for a given external force, the compressive mode afforded higher piezoelectric sensitivity than the bending mode. This result shows an interest of operating the aligned NWs structure under the compression excitation so as to fulfill the medical's need, especially for the development of bio-environment sensors.

Similarly, both analytical and FEM simulation modeling were performed on the composite consisting of vertically ZnO nanowire arrays embedded PMMA matrix. Three mechanisms referring to the mechanical, electromechanical, and electrical models have been analyzed, providing a clear comprehension on the complex structure of the developed material. FEM simulations were then performed to figure out which and how some parameters affected on the piezoelectric response of the NWs based composite. This task involved in achieving an optimal design structure, which relied on the material properties and geometries so as to meet high sensing performance adapted to biological media in future applications. Simulation results revealed that the mechanical Young's modulus and the dielectric permittivity of the PMMA bottom matrix, as well as the dielectric permittivity and thickness of the top matrix layer had high impact on the effective piezoelectric coefficient d_{33}. In contrast, the Young's modulus of top layer and the geometric parameter of NW has been observed no worthy effect on the piezoelectric performance. Moreover, NWs density was also considered to get the best trade-off between the mechanical behavior and the piezoelectric sensor response.

The next chapter discusses on the experiment results of the ZnO NW arrays-based composite, allowing to validate the analytical model and the numerical predictions.

Cette thèse est accessible à l'adresse : http://theses.insa-lyon.fr/publication/2022LYSEI006/these.pdf
© [X. Zhang], [2022], INSA Lyon, tous droits réservés

Chapter 5. Piezoelectric vertically nano/micro arrays/PMMA composites

In order to enhance the piezoelectric and mechanical properties with superior flexibility, the developed composites are realized by the encapsulation of ZnO fillers in a polymer matrix. As previously described in Chapter 3, the particles composite elaborated via casting method can achieve higher performance, by increasing the filler content or reducing the interparticle distance through dielectrophoretic alignment of fillers. In this chapter, an alternative solution is proposed to further improve the material characteristics. Microrod (MR) fillers with higher aspect ratio (AR) are found to enhance the dielectric, piezoelectric, and mechanical performance of the composites as opposed to the correspondingly spherical particles. Significant effect of electric field magnitude and frequency on the dielectrophoretic assembly process for different filler shape will be explored.

However, the perfect full alignment of MR fillers is difficult to achieve through the casting method, especially at high filler content. A new fabrication process based chemical bath deposition (CBD) developed by LMGP leads to a creation of multi-layer composite with improved electromechanical performance. ZnO is spontaneously grown on silicon (Si) substrate to form vertically repetitive nanowires (NWs) with higher AR compared to the MR. Such an architecture exhibits higher aspect ratio and better anisotropic behavior, which is supposed to boost the piezoelectric sensitivity of the composite. To study the functionality of each individual layer of the whole sample, different designed structures were fabricated and characterized in terms of electrical and piezoelectric properties. Experimental and simulation tests are performed, indicating that the decreasing thickness of the top PMMA layer can substantially enhance the piezoelectric sensitivity of the ZnO NW composite. Finally, a time varying model is thoroughly explored to provide an estimation of the charge coefficient (d_{33}) for ZnO NWs. Despite of improvement in the piezoelectric response, this fabrication approach presents two major technical challenges: 1) high rigidity and fragility of the sample caused by Si substrate; and 2) non-negligibility of the conduction leakage induced in a thin top polymer layer, particularly under low-frequency excitation.

Accordingly, ZnO NWs vertically grown on flexible PDMS polymer substrate are envisaged to overcome the drawbacks provoked by the rigid Si substrate. From the application point of view, flexible piezoelectric sensors are of high interest for applications in implantable biomedical detection, particularly in the FFR technique [129]. Due to the semiconducting intrinsic property of ZnO, the piezoelectric polarization charges are assumed to be partially screened by the free charge carriers from native defects. A COMSOL simulation was performed to better understand the electromechanical coupling of the semiconductive NWs as well as other parameters relating to the doping concentration and the applied force. Thanks to the investigation of the crystal defects from spontaneously grown ZnO NWs, simple and effective strategies involving Sb-doping and thermal annealing are carried out by decreasing carrier concentration in ZnO, with the aim of weakening the screening effect. Finally, composite of NWs pretreated with Sb-doping and thermal annealing provide a greatly enhanced piezoelectric charge coefficient (d_{33}), i.e., 4 times compared to the one without any post-depositions.

Cette thèse est accessible à l'adresse : http://theses.insa-lyon.fr/publication/2022LYSEI006/these.pdf
© [X. Zhang], [2022], INSA Lyon, tous droits réservés

5.1 Flexible ZnO MR/PDMS composites using casting method

As described in Chapter 3, the flexible composites of ZnO microparticles (MPs) randomly embedded in the PMMA matrix have been confirmed to exhibit good dielectric constant, as opposed to the nano-size counterparts elaborated with the same filler content. Moreover, the dielectric property can be greatly enhanced by aligning the ZnO MPs via the dielectrophoretic technique. To further improve the dielectric and piezoelectric performance of the composites, the filler aspect ratio (AR), defined as the longest axis to the shorted axis, is considered as an effective optimization route. During the dielectrophoretic dynamics process, the fillers with a high AR will orient with their longest axis to the external electric field [94]. It has been predicted that the ability of high AR filler to increase the dielectric property of composites is superior to the spherical filler [162,240]. Regarding the analytical models developed by Bowen and Van den Ende [85][89], the dielectric and piezoelectric constants of the structured composites are proportionately related to the ratio (denoted γ) between the average particles size and the interparticle distance along the aligned chains. Thereby, increasing the particle's dimension in the field direction can minimize the number of interconnects, which can lead to decrease interparticle distance and thus increase γ ratio [94]. Hence, to reinforce the material structure, ZnO microrods (MRs), which have higher AR than spherical particles, are synthesized and dispersed in the PMMA polymer to form ZnO MRs/PMMA composite.

5.1.1 Morphological properties

Figure 5.1 presents the FESEM image of the synthesized ZnO MRs under a magnification of 10000 using a FEI Quanta 250 FESEM instrument. Through morphology analysis, the fillers have a rod shape with a 3.9±1.3 μm length and a 477 ± 270 nm diameter. Figure 5.2 (a) shows, at a volume fraction of either 2% or 8%, the random dispersion of the ZnO MRs. After being subjected to a sinusoidal electric field of 0.6 V/μm and 2 Hz, the MRs are aligned within the solidified PMMA matrix along the field direction (Figure 5.2(b)). It has been revealed that observation of MR's alignment at low volume fraction (i.e., 2%) is more obvious than the one of 8% vol.

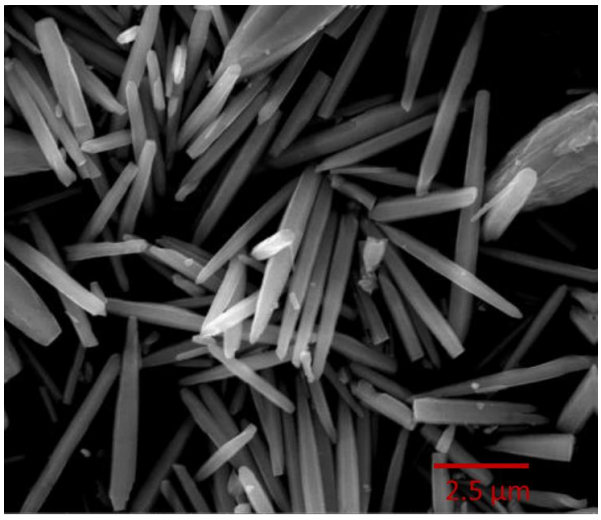

Figure 5.1. FESEM image of the top view of ZnO microrods

Cette thèse est accessible à l'adresse : http://theses.insa-lyon.fr/publication/2022LYSEI006/these.pdf
© [X. Zhang], [2022], INSA Lyon, tous droits réservés

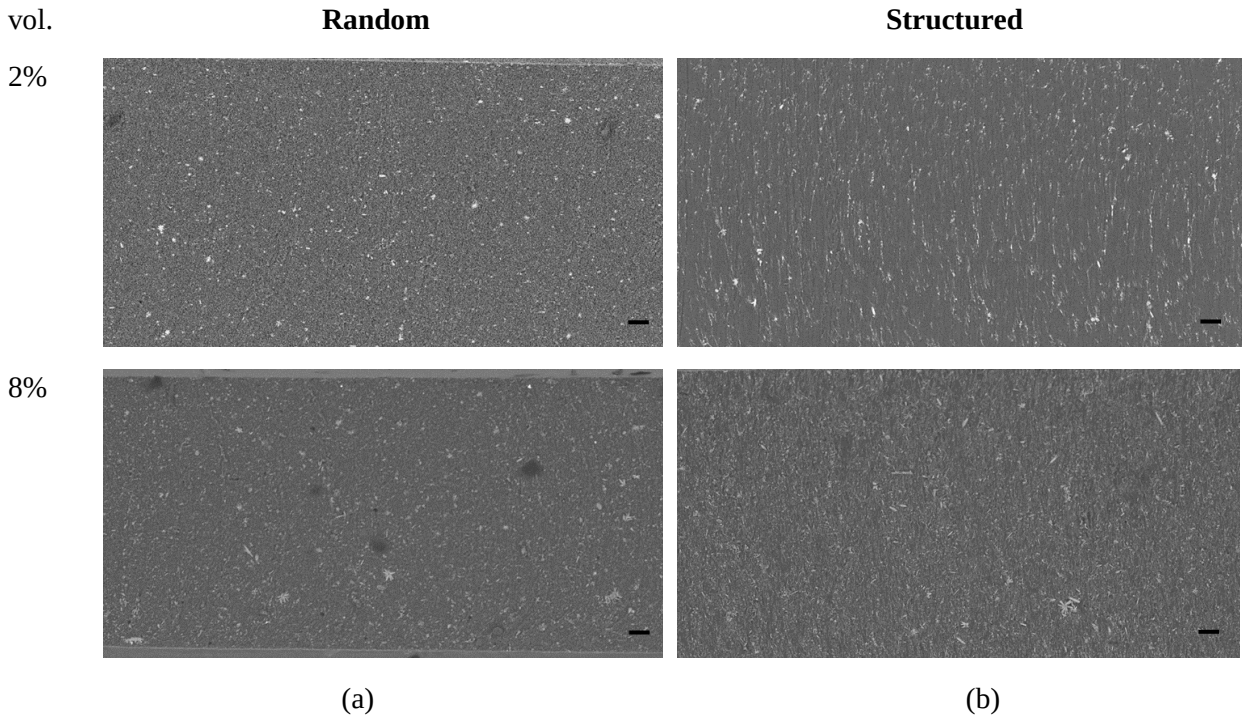

Figure 5.2. SEM images of (a) random and (b) structured MRs composites at different volume fractions, with a scale bar of 300 μm.

5.1.2 Dielectric properties

During the dielectrophoretic manipulation, the level of orientation is determined by the DEP force, which depends on the amplitude and frequency of the electric field acting on the composite. On one hand, the higher of the amplitude of the applied field, the better the dielectrophoretic alignment of the fillers will be achieved. On the other hand, effect of the frequency is much more complicated. Actually, the DEP force indirectly depends on the frequency through a function of the electric conductivity of the filler and matrix (see Eqs. (2.5) -(2.7)). Hence, the frequency tuning is not the same for different composites. Bowen *et al* have demonstrated that the optimum alignment condition of 22 vol.% $(Ba_{0.55}Sr0.45)TiO_3$(BST) filler composites is processed at a 10 Hz frequency since the molecular rotation cannot fellow the field direction at higher dynamics [89]. Van den Ende *et al* have reported that for dielectrophoretically structured PZT composites, the best dielectric and piezoelectric performances were found at a fixed structuring field of very high frequency, i.e. 4 kHz. This can be explained due to the fact that the conduction of epoxy hinders the formation of alignment at low frequency [85]. Therefore, based on the dielectric properties, it is necessary to verify the frequency and magnitude dependence of the MR's structuration. That allows to confirm whether or not MR long chains can successfully form within PMMA matrix.

Figure 5.3 indicates the relationship between the dielectric measurement and the field magnitude that probably influences on the alignment degree of the MRs. Keeping the same processing frequency (2 Hz), the orientation angle increases with electric field magnitude, which leads to a higher dielectric constant (Figure 5.3a). Similarly, in Figure 5.3(b), an increasing trend of loss tangent ($tan\delta$) was observed with respect to an increase in the field amplitude. Moreover, the variation in the spectroscopy is more obvious at lower frequencies (below 10 kHz), which is ascribed to the contribution of the electronic conduction as well

Cette thèse est accessible à l'adresse : http://theses.insa-lyon.fr/publication/2022LYSEI006/these.pdf
© [X. Zhang], [2022], INSA Lyon, tous droits réservés

as the interfacial polarization. As expected, the higher the electric field amplitude, the higher the permittivity constant and so is the $tan\delta$ loss. In practice, the amplitude value is set to not exceed 0.6 V/μm to prevent any electrical breakdown of PDMS polymer. Figure 5.3(c), (d) illustrate the frequency dependence of the dielectric parameters, which is not prominent as compared to the amplitude effect. For instance, measured at 0.1 Hz, changing amplitude from 0.2 V/μm to 0.6 V/μm leads to a threefold increase in ε (from 24 to 71) of the aligned composite. Contrarily, a smaller variation in ε (from 47 to 71) is recorded with a decreasing field frequency (from 2 kHz down to 2 Hz). Finally, the best processing parameters of the input electric field are found equal to 0.6 V/μm and 2 Hz, leading to considerably enhanced dielectric constant for the aligned composite (i.e., ε = 71 against 6 as in the case of the corresponding random sample).

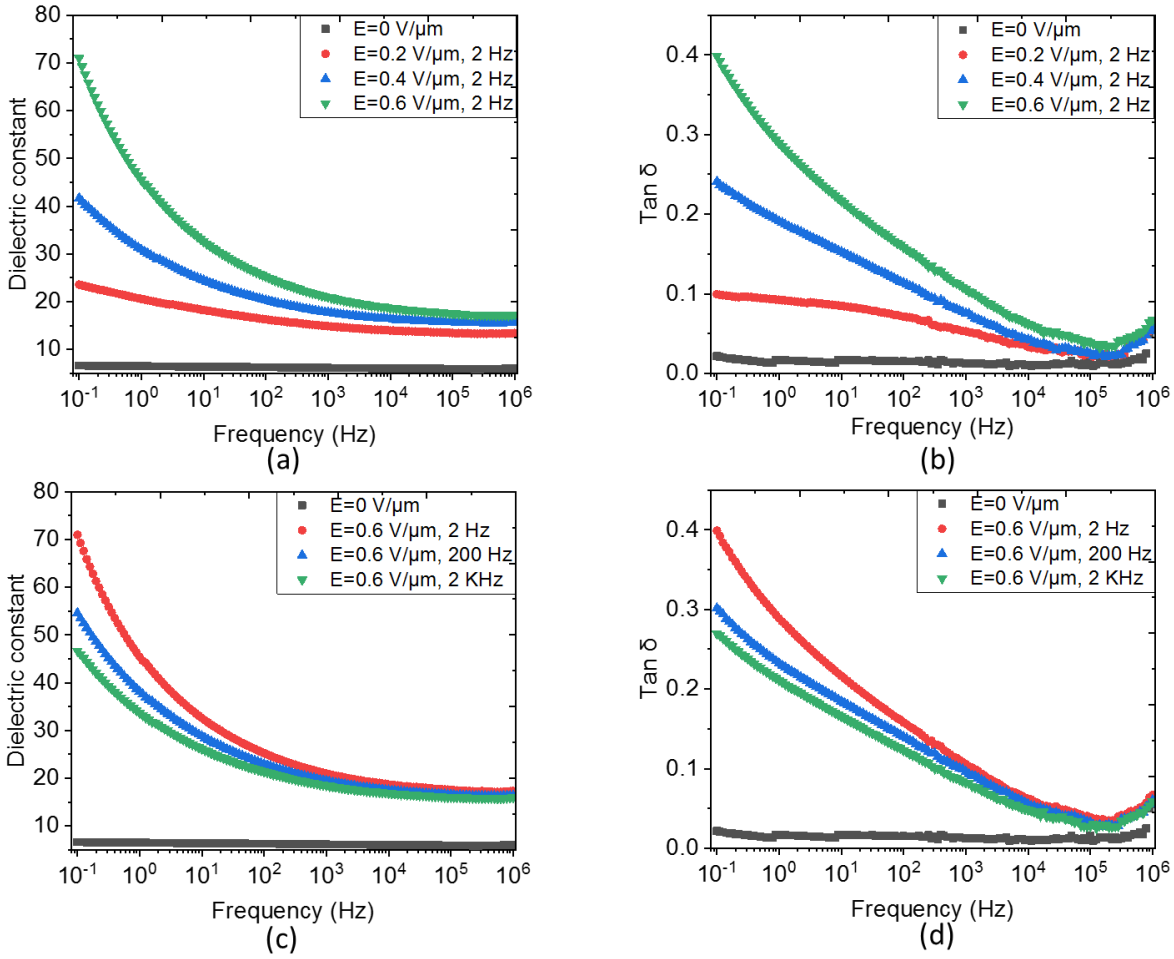

Figure 5.3. Broadband spectroscopy of an 8% vol. ZnO MRs composite under different parameters of the applied electric field: (a), (b) varied amplitude and fixed frequency of 2 Hz; and (c), (d) varied frequency and fixed amplitude of 0.6 V/μm.

In order to investigate the influence of the aspect ratio, composites of ZnO particles with a micro size (~10 μm diameter) incorporated into PDMS polymer were fabricated with the same volume fraction of 8%. As shown in Figure 5.4, similar to the ZnO MRs based composites, the dielectric constant (ε) of the microparticles (MPs) composites can be enhanced by either increasing the amplitude or reducing the

Cette thèse est accessible à l'adresse : http://theses.insa-lyon.fr/publication/2022LYSEI006/these.pdf
© [X. Zhang], [2022], INSA Lyon, tous droits réservés

frequency of the electric field. However, the improvement is drastically lower as compared to the MRs counterparts. More specifically, under the same optimal condition (E = 0.6 V/µm, 2 Hz), the MPs composites can achieve almost threefold increase in ε (measured at 0.1 Hz) with respect to the random one, while tenfold in the case of MRs composite with the higher AR. Interestingly, the random MRs/PDMS still have higher ε as opposed to the random MPs/PDMS with the same filler content, confirming that the dielectric behavior is strongly impacted by the filler geometry [240]. Indeed, during the dielectrophoretic dynamics process, the high-AR rods are found be to more aligned than the low-AR particles. Usually, spherical particles might be more easily attracted by their neighbors to form a corner-to-corner alignment, leading to an out-off-axis orientation effect [241]. Although high degree of alignment and fast orientation in the low AR particles seems to be easier to achieve compared to the high AR rods, which is due to the different hydrodynamic drag induced torques [241]. This behavior should be considered in a transient regime, but after a long-time application of thermal heating and low-dynamic input field, a steady state is well established. Observation in that state clearly verifies that the composite embedded with high AR rods leads to higher dielectric performance.

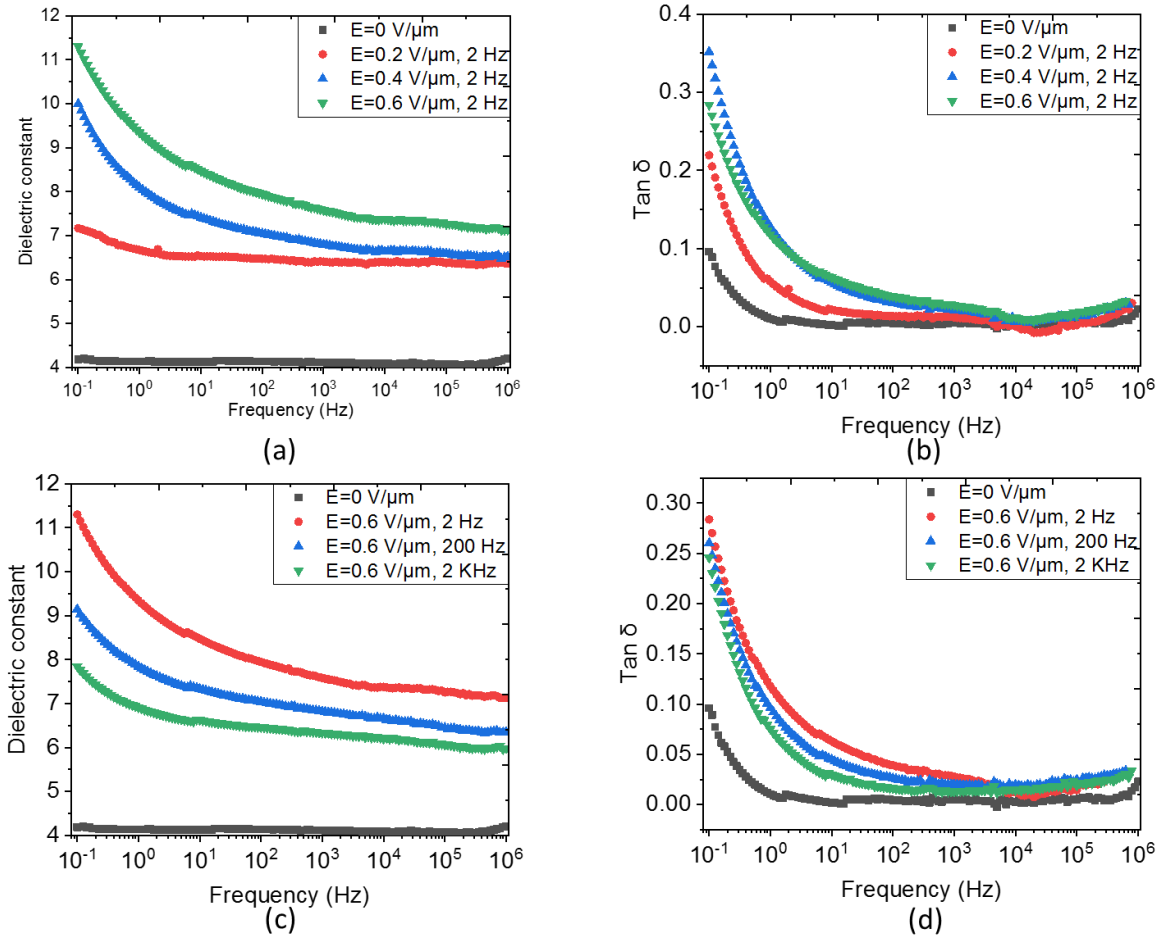

Figure 5.4. Broadband spectroscopy of an 8% vol. ZnO MPs composite under different parameters of the applied electric field: (a), (b) varied amplitude and fixed frequency of 2 Hz; and (c), (d) varied frequency and fixed amplitude of 0.6 V/µm.

Cette thèse est accessible à l'adresse : http://theses.insa-lyon.fr/publication/2022LYSEI006/these.pdf
© [X. Zhang], [2022], INSA Lyon, tous droits réservés

5.1.3 Mechanical properties

In order to further explore the effect of structuration, mechanical properties, which in turn impact the piezoelectric behaviors, were studied under monotonic tensile and compressive testing. Figure 5.5(a), (b) shows the tensile stress-strain curve of 8% vol. and 2% vol. ZnO MRs/PDMS composites, respectively, with and without dielectrophoretic treatment. A typical stress-strain curve consisting of elastic linear, nonlinear and fracture regions was observed from the tensile testing. Meanwhile, the compressive stress-strain curves of the random and structured 8% vol. composites are plotted in Figure 5.6 (a), (b), respectively. Under different strain loadings, both random and structured composites recover to the initial position, but with different slopes. As seen in Table 5.1, the tensile elastic modulus ($Y_{tensile}$) is calculated from the linear slope near the origin, while the compressive elastic modulus ($E_{compressive}$) is deduced from the linear slope of peak-stress-versus-peak-strain characteristics (Figure 5.6 (c)). It has been expected that the elastic modulus is improved with respect to an increase in the filler content (e.g, from 2% to 8%), whatever the applied force configuration (compressive or tensile). However, no obvious difference of $Y_{tensile}$ was observed between the random and structured composites, as the tensile force direction was perpendicular to the dielectrophoretic field. This configuration does not effectively favorize the benefit of the "preferred" aligned axis, in which the results are correlated to those described in Chapter 3 (subsection 3.3.1). In contrast, the $E_{compressive}$ of the aligned composites is enhanced and strengthened as opposed to the random one, since the compressive load is in the same direction of the dielectrophoretic field. In other words, the chain-like structure of the fillers makes the whole system stiffer in that direction. Additionally, under a volume fraction of 8%, composites of rod-shaped fillers are much stiffer than that of spherical-shaped fillers. Such an improvement is especially evident for $E_{compressive}$ of the structured composites (~17.535 MPa), manifested by higher continue phase of fillers, which in turn contribute to their excellent piezoelectric behaviors.

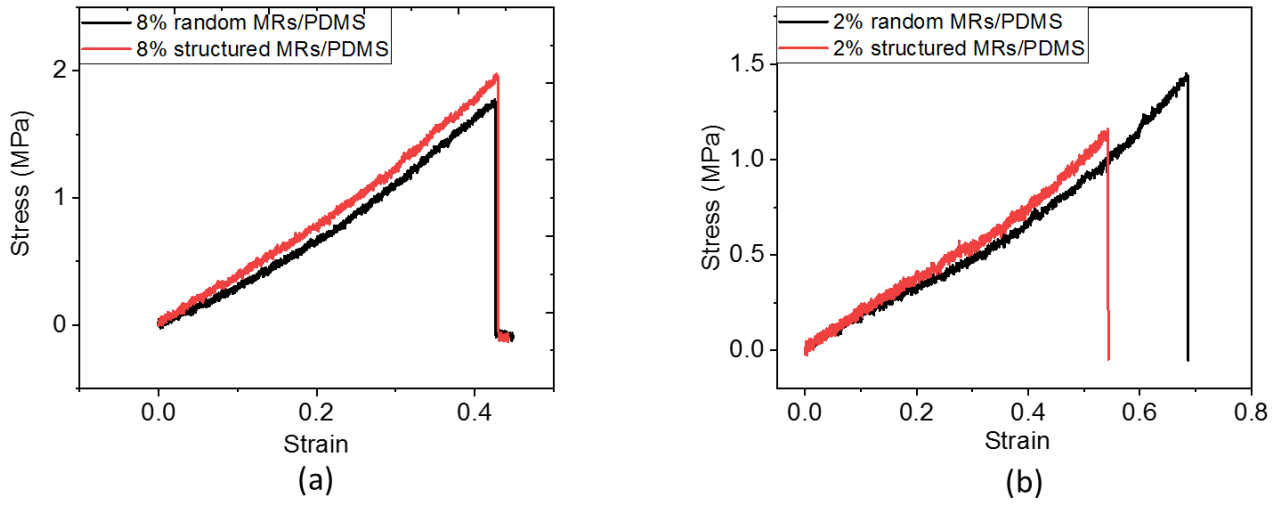

Figure 5.5. The tensile stress-strain response of (a) 8% vol. and (b) 2% vol. MRs/ PDMS composites.

Cette thèse est accessible à l'adresse : http://theses.insa-lyon.fr/publication/2022LYSEI006/these.pdf
© [X. Zhang], [2022], INSA Lyon, tous droits réservés

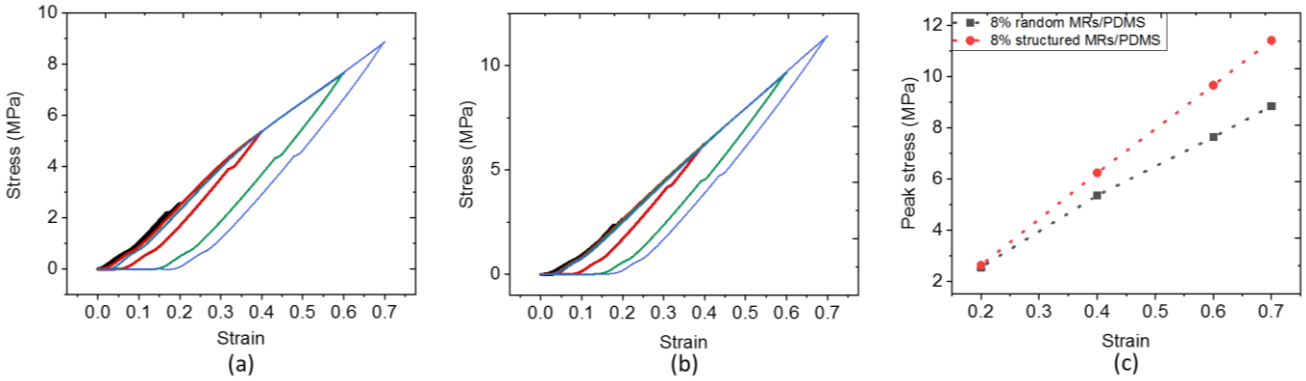

Figure 5.6. The compressive stress-strain curve of the 8% vol. (a) random and (b) structured ZnO MRs/PDMS composites; (c) peak stress *vs.* strain for the random and structured composites.

Table 5.1. The average tensile and compressive elastic modulus

	Random		Structured	
	$Y_{tensile}$ (MPa)	$E_{compressive}$ (MPa)	$Y_{tensile}$ (MPa)	$E_{compressive}$ (MPa)
8% vol. ZnO MRs/PDMS	3.284 ± 0.004	12.501 ± 0.438	3.785 ± 0.003	17.535 ± 0.151
2% vol. ZnO MRs/PDMS	1.598 ± 0.003	7.6 ± 0.451	1.873 ± 0.003	8.321 ± 0.775
8% vol. ZnO MPs/PDMS	2.957 ± 0.003	11.317 ± 0.302	2.971 ± 0.004	13.572 ± 0.233

5.1.4 Piezoelectric properties

Following the dielectric characterization, the piezoelectric measurements are performed as displayed in Figure 5.7. For a better comparison, composites with different volume fractions and shapes of fillers were investigated under the same optimized dielectrophoretic conditions (E = 0.6 V/μm, 2Hz). Oscillating stress with a 0.15 MPa magnitude and a 1 Hz frequency is subjected to the random and structured 8% vol. ZnO MRs/PDMS composites. Figure 5.7a highlights the linear piezoelectric effect of the composite where the resulting electric charges are somehow in phase with the input stress. A little phase shift is found perhaps due to the detection delay or the restore/discharge mechanism of the capacitive sample. Figure 5.7(b)-(d) illustrates the generated charge density versus the stress variation (ΔT) of the three samples: 2% vol. ZnO MRs, 8% vol. ZnO MRs, and 8% vol. ZnO MPs, respectively. A linear relationship has been recorded until a stress level of 0.3 MPa, above which an aberrant increase in the charge measurement was found, e.g. at ΔT = 0.35 MPa. This is due to the stress limitation in the test bench. The amplitude of the applied stress should not be close or larger than the initially static clamping stress (~ 0.2 MPa). Otherwise, the sample will slide from the test bench and become moveable.

In general, for the rigid piezoelectric material such as ceramics, the piezoelectric charge coefficient (d_{33}) is independent of the material deformation. On the other hand, for the soft PDMS-based composites with low Young's modulus (a few MPa), the contribution of deformation under high stress should be taken in

Cette thèse est accessible à l'adresse : http://theses.insa-lyon.fr/publication/2022LYSEI006/these.pdf
© [X. Zhang], [2022], INSA Lyon, tous droits réservés

account, that can lead to higher value of d_{33}. In that case, the applied stress dependence of d_{33} can be described as a second order polynomial [242]. In addition, due to the Poisson effect, the polymer material is compressed and thus deformed in all directions to arouse other piezoelectric operation modes. For instance, the lateral strain is induced to contribute to the output charge thanks to the transverse piezoelectric effect (relating to d_{31}), which makes the charge-versus-stress characteristics nonlinear and complicated for modeling. Therefore, d_{33} is calculated from the linear fitting of the ΔD-versus-ΔT curve where ΔT is within [0.15-0.3 MPa] interval. As displayed in Table 5.3, for all samples, the coefficient of determination (R^2) obtained from the linear regression is closed to 1, confirming the accurate prediction of the d_{33} coefficient under such a mechanical solicitation range. The results of Table 5.2 leads to conclude that:

- In both random and structured ZnO MRs/PDMS composites, increasing the filler content gives raise to increase piezoelectric response.
- With the same filler concentration, MRs composites with a higher AR definitely exhibit higher piezoelectric property than the MPs counterparts.
- Whatever AR of ZnO, dielectrophoretic alignment substantially enhances the piezoelectric performance of composites.

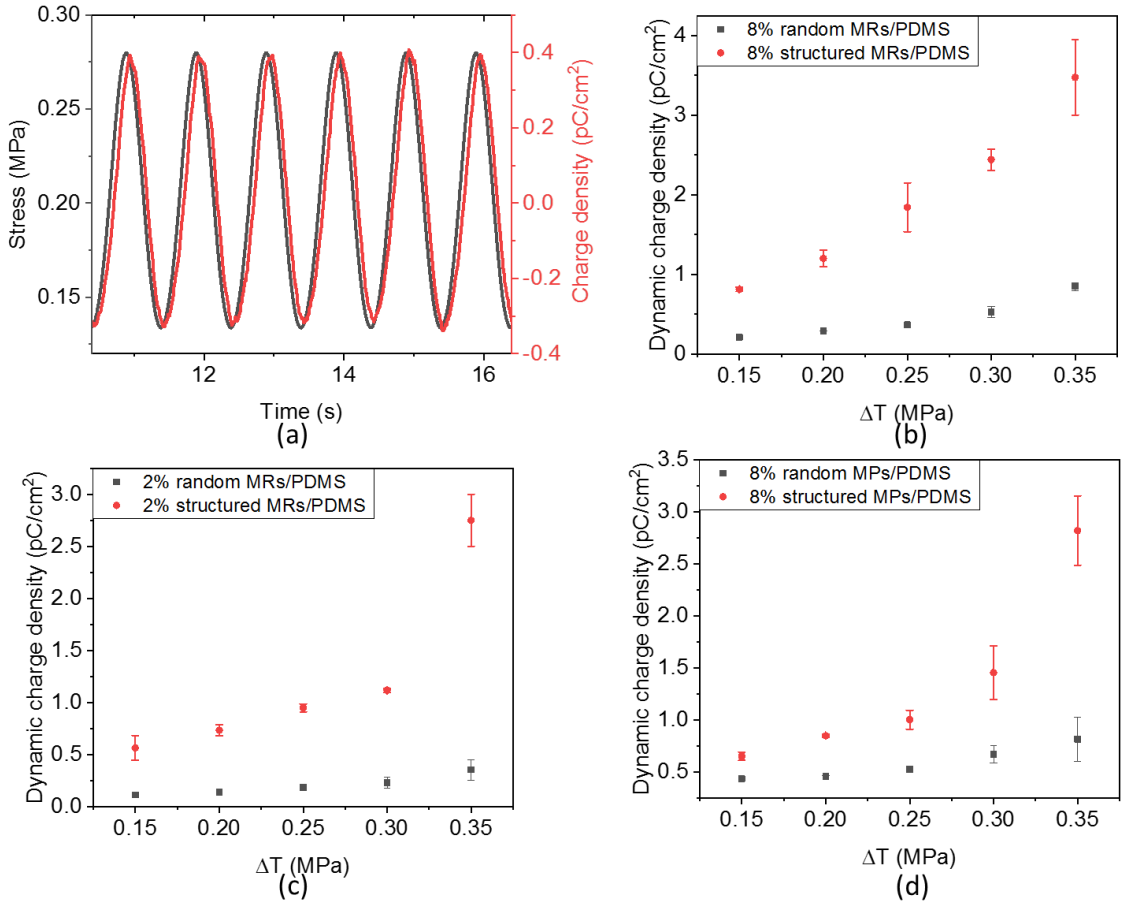

Figure 5.7. (a) Time evolution of the stress and generated charge density in the structured 8% vol. ZnO MRs composites under a dynamic stress of 0.15 MPa. The increasing dynamic change density versus the dynamic stress in

Cette thèse est accessible à l'adresse : http://theses.insa-lyon.fr/publication/2022LYSEI006/these.pdf
© [X. Zhang], [2022], INSA Lyon, tous droits réservés

(b) 8% vol. ZnO MRs/PDMS composites, (c) 2% vol. ZnO MRs/PDMS composites, and (d) 8% vol. ZnO MPs/PDMS composites.

Table 5.2. Piezoelectric coefficient (d_{33}) from experimental measurement

	Random d_{33} (pC/N)	R^2	Structured d_{33} (pC/N)	R^2
8% vol. ZnO MRs/PDMS	0.0173 ± 0.0022	0.969	0.1040 ± 0.0079	0.989
2% vol. ZnO MRs/PDMS	0.0073 ± 0.0008	0.973	0.0371 ± 0.0015	0.997
8% vol. ZnO MPs/PDMS	0.0086 ± 0.0020	0.903	0.0399 ± 0.0049	0.970

In order to observe the influence of the filler structuration on the composite performances, the permittivity and piezoelectric coefficient (d_{33}) are computed relatively to those of the random composites. As shown in Figure 5.8, the 8% vol. structured ZnO MRs/PDMS composites possess the largest enhancements in dielectric (~ sevenfold) and piezoelectric (~ sixfold) characteristics as compared with the random one. Increasing the volume fraction is another effective approach to obtain high piezoelectric conversion efficiency. However, during the fabrication process, higher filler content (more than 10%) can be challenging due to the agglomeration and high viscosity effect. Consequently, the thin-film casting method seems not to be the most adaptable technique to achieve high material performance. A new process based chemical bath deposition (CBD) developed by LMGP is investigated to better align ZnO wires in a vertical direction while increasing the ZnO density within the polymer matrix. Description of the CBD technique is found in Chapter 2. In the following sections, characterizations of the composites made by this technique are carried out, demonstrating a possibility to substantially enhance their piezoelectric behavior.

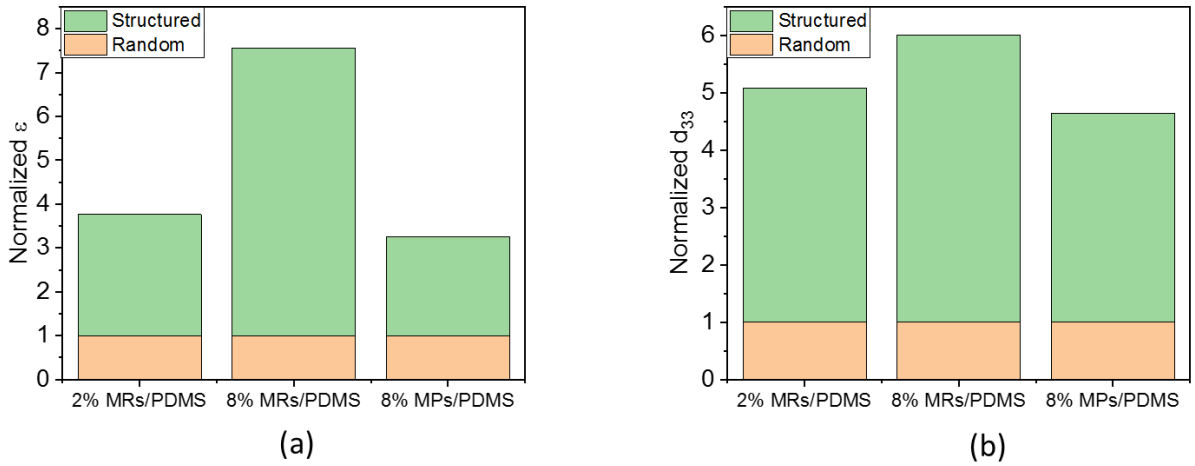

Figure 5.8. Dielectric and piezoelectric performances of three samples: (a) normalized dielectric constant values; (b) normalized d_{33} values.

Cette thèse est accessible à l'adresse : http://theses.insa-lyon.fr/publication/2022LYSEI006/these.pdf
© [X. Zhang], [2022], INSA Lyon, tous droits réservés

5.2 Rigid ZnO NW arrays composites using CBD method

When exerting dielectrophoresis to filler dispersed in uncured polymer, even with the optimized input parameters, it is difficult to achieve perfect alignment of fillers. For instance, particles tend to form a chain-like structure along the field direction, but are also disturbance by adjacent chains [153]. Moreover, considering the lateral interaction of neighboring fillers, corner-to-corner connections are created, provoking an off-axis situation of for certain chains [243]. Additionally, the high connectivity from filler orientation in turn causes the short-circuit problem and disrupt the continuity of filler phase along the field direction. Therefore, vertical ZnO NWs spontaneously grown by CBD are believed to have higher piezoelectric efficiency.

5.2.1 Morphological properties

The morphology of ZnO NWs was assessed by field-emission scanning electron microscopy (FESEM) imaging using a FEI Quanta 250 FESEM instrument. The coating of (001) Si substrate with a 40 nm-thickness ZnO seed layer (SL) was achieved by a dip coating process on a sol-gel solution. The polycrystalline SL strongly oriented along the polar c-axis and ZnO NWs by CBD is known to homoepitaxially grow on top of it [244]. The CBD growth was performed with an equimolar precursor solution of $Zn(NO_3)_2$ and HMTA at 85 °C and with a pH of around 5.5 [245,246]. The hexagonal shape typical of a wurtzite structure is presented in Figure 5.9(a) by FESEM imaging, showing that they are oriented along the polar c-axis. According to Figure 5.9(a-b), ZnO NWs exhibit a mean radius and length of 42 ± 8 nm and 1031 ± 16 nm, respectively. Additionally, Figure 5.9(c) depicts the ZnO NW arrays encapsulated in a PMMA matrix deposited by spin coating and exhibiting a thickness of ~1.5 µm on the top.

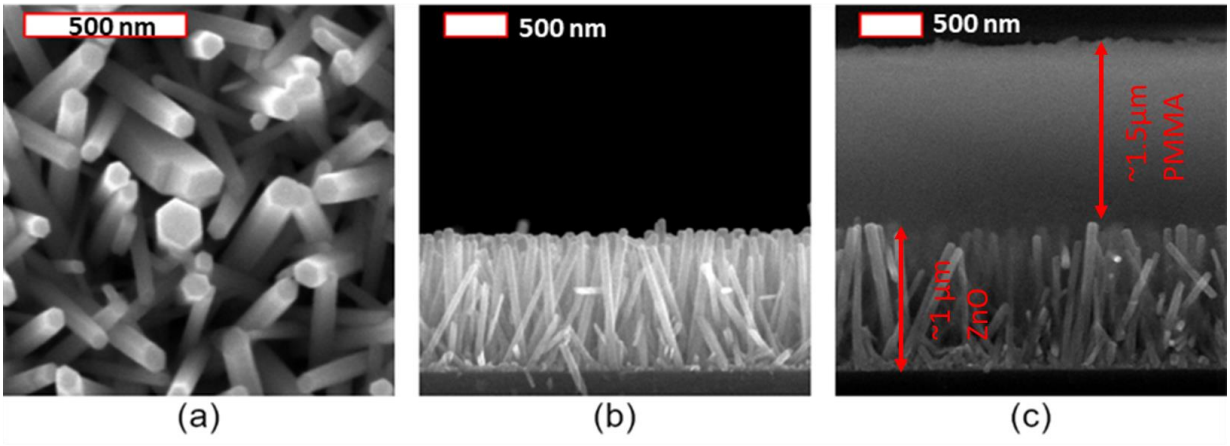

Figure 5.9. FESEM images of (a) top view and (b) cross-section view of ZnO NWs grown by CBD. (c) ZnO NW arrays with a PMMA matrix exhibiting a thickness of ~1.5 µm in the top.

5.2.2 Electrical properties

This study details the electrical characterization of our designed devices, which is represented by the current density-electric field (J-E) curve. The first column of Table 5.3 shows different materials tested on the experimental setup as described in subsection 2.3.3. To better understand the electrical behavior of the complex structure (consisting of 4 layers like Silicon (Si) substrate, ZnO seed layer (SL), ZnO NWs

Cette thèse est accessible à l'adresse : http://theses.insa-lyon.fr/publication/2022LYSEI006/these.pdf
© [X. Zhang], [2022], INSA Lyon, tous droits réservés

embedded in PMMA matrix, and top PMMA layer), simplified structures were investigated (e.g., with 1, 2, or 3 layers). All samples were subjected to an alternating electric field of 1 kHz frequency, and under static stress or dynamic stress.

Table 5.3. Electrical measurement of different samples

Sample	N° of layers	Resistivity (Ω·m) at 1 MPa	Surface capacitance ($nF \cdot cm^{-2}$)	Relative permittivity	Property
Si	1	2.144 ± 0.004	-	-	resistive
Si/SL	2	6.321 ± 0.009	-	-	resistive
Si/PMMA (1 µm)	2	-	3.212 ± 0.005	3.809 ± 0.006	capacitive
Si/SL/PMMA (1 µm)	3	-	3.195 ± 0.003	3.760 ± 0.004	capacitive
Si/SL/NWs/PMMA (1 µm)	4	-	-	-	-
Si/SL/NWs/PMMA (1.5 µm)	4	-	3.089 ± 0.009	5.108 ± 0.015	capacitive
Si/SL/NWs/PMMA (2 µm)	4	-	2.439 ± 0.004	5.509 ± 0.009	capacitive

5.2.2.1 Static characterization

As expected in Figure 5.10(a), the characteristic J-E curves of Si and Si/SL samples were perfectly linear and symmetric, which was indicated by a passive resistive behavior. The values of their resistivity, deduced from the J-E slopes, were displayed in Table 5.3. Logically, the bilayer Si/SL sample exhibits a superior resistivity than the pure Si sample due to the addition of one more resistive layer of 40 nm thickness. Figure 5.10(b) shows a circular-shaped J-E curve of the 3-layer and 4-layer samples containing the PMMA, reflecting that the capacitive property is dominant with respect to the resistive one. Interestingly, increasing the thickness of the PMMA layer from 1.5 µm to 2 µm in vertically aligned Si/SL/NWs/PMMA composite leads to moderate improvement in the permittivity (Table 5.3). From the surface capacitance value, it is possible to determine the equivalent dielectric permittivity of the capacitive materials. Since there is no difference in the electrical properties between the Si/PMMA (1 µm) and the Si/SL/PMMA (1 µm) samples, only the result of the Si/SL/PMMA (1 µm) is displayed in Figure 5.10(b), i.e., overlapped otherwise. It should be noticed that, in order to improve the accuracy, all parameters in Table 5.1 are the average values calculated on at least five periods of the alternative input. Among them, the Si/SL/NWs/PMMA (2 µm) showed unexpected properties which will be discussed later.

Cette thèse est accessible à l'adresse : http://theses.insa-lyon.fr/publication/2022LYSEI006/these.pdf
© [X. Zhang], [2022], INSA Lyon, tous droits réservés

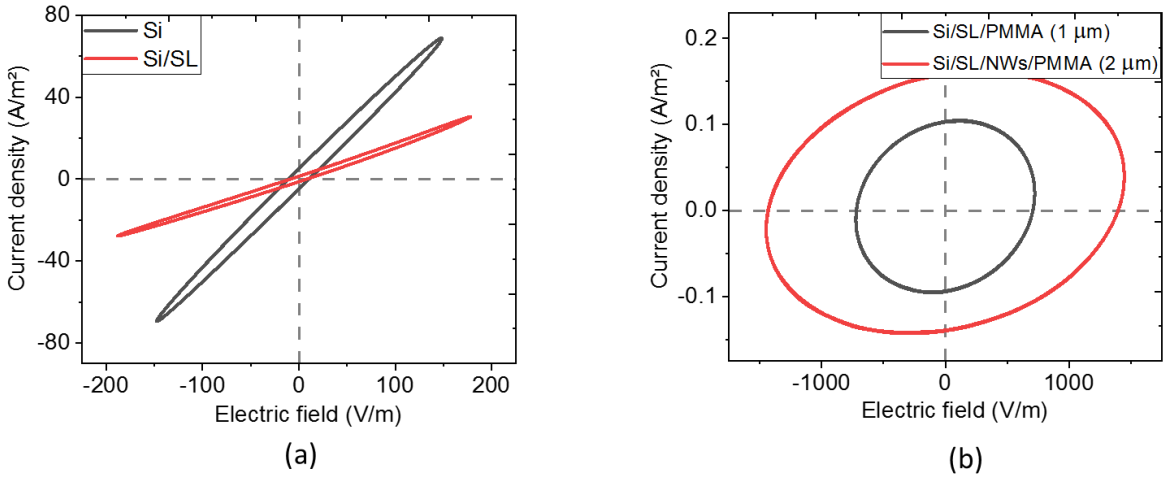

Figure 5.10. Representative current density versus electric field of (a) resistive-like samples including Si and Si/SL; (b) capacitive-like samples including Si/SL/PMMA (1 µm) and Si/SL/NWs/PMMA (2 µm).

5.2.2.2 Dynamic characterization

With the aim of evaluating the electrical properties under dynamic mechanical excitation, samples were subjected to a 1 Hz compressive stress, with magnitude $\Delta T = max_{load} - min_{load}$. Starting with the resistive samples: the electric response of the Si substrate as a function of the periodic compressive stress (ΔT= 1MPa) is displayed in Figure 5.11(a). When the stress increases, the impedance of Si coherently decreases. Due to the high Young's modulus of Si multi-crystalline structure (~130-188 GPa [247]), it is reasonable to assume that there is no deformation induced to the Si sample. As a result, its impedance variation is mainly caused by the piezoresistive effect, where the electric resistivity changes with the mechanical excitation [248] . Due to the crystalline nature of Si, the application of mechanical strain can alter the inter-atom distance to narrow or broaden the bandgap, finally changing the conductivity of Si. To date, numerous applications of Si sensors based piezoresistive effect have been developed in microelectronics and biomedical systems [249,250]. The sensitivity of these sensors mainly depends on the crystallographic orientation configuration, the applied stress, and the temperature condition.

As seen in Figure 5.11(b), regardless of the stress magnitude, for example at the position of "max load" corresponding to the maximum stress or "min load" corresponding to the minimum stress, the current density always has a linear relationship with the electric field. Both of them are perfectly in phase, reflecting the resistive behavior of the silicon (Figure 5.11c). Based on the resistivity-versus-dynamic stress characteristics displayed in Figure 5.11(d), it is possible to calculate the piezoresistive sensitivity of the Si sample (~0.081 ± 0.007 Ω·m/MPa), and the Si/SL sample (1.219 ± 0.309 Ω·m/MPa).

Cette thèse est accessible à l'adresse : http://theses.insa-lyon.fr/publication/2022LYSEI006/these.pdf
© [X. Zhang], [2022], INSA Lyon, tous droits réservés

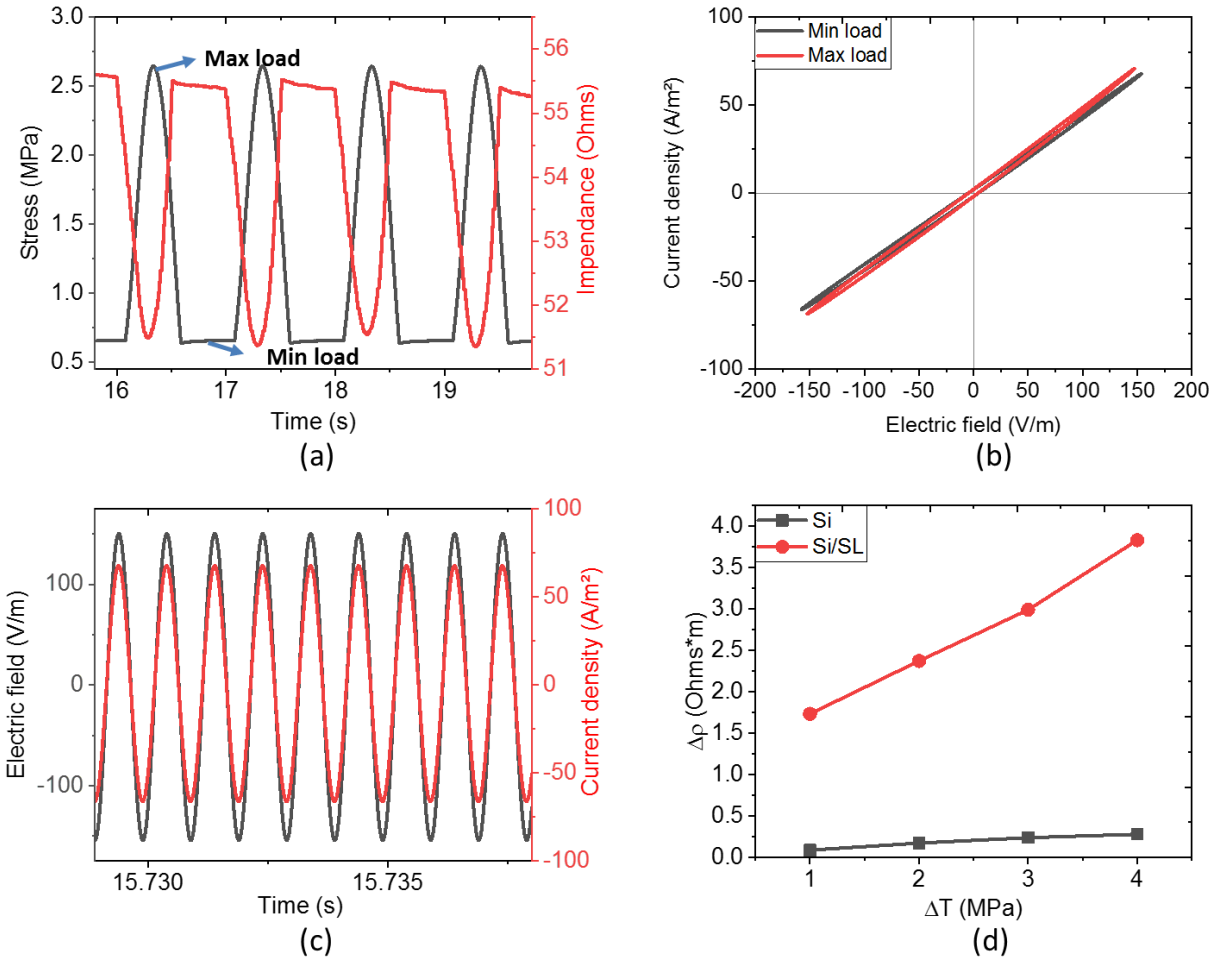

Figure 5.11. Electrical characterization, under dynamic stress of 1Hz and ΔT = 1 MPa, was carried out by applying a 1 kHz sinus electric field. For the Si sample, (a) time variation of stress and impedance; (b) at max and min load configurations, the current density is linear in response to the electric field; (c) and always keeps in phase. For the Si and Si/SL samples, (d) the variation of resistivity with respect to different dynamic stress.

For the sake of simplicity, among the capacitive samples, only the Si/SL/NWs/PMMA (2 µm) is presented in Figure 5.12(a)-(c). Figure 5.12(a) describes an inverse variation between the stress and the electrical impedance of the sample, which was induced by a slight change in the sample's thickness during mechanical solicitation owning to the small Young's modulus of PMMA (~3 GPa) [251]. Concretely, a peak of stress (i.e. "max load") corresponds to the minimum impedance as the sample thickness somewhat decreases due to the compression. On the other hand, "min load" leads to the maximum impedance as the sample is "less compressed". Interestingly, as displayed in Figure 5.12 (b), the current density still has a circular response with the electric field, regardless of variation in the mechanical excitation. For arbitrary stress, the current density and the applied electric field are 90-degree out of phase (Figure 5.12c), confirming the typical capacitive behavior. When slightly increasing the dynamic stress (ΔT from 0.1 to 0.4 MPa), the surface capacitance of the Si/SL/NWs/PMMA and the Si/SL/PMMA samples was almost constant (Figure 5.12d). Accordingly, the capacitive behavior of Si/SL/NWs/PMMA composite is revealed to be stable under a dynamic uniaxial compression less than 0.4 MPa, and so is the dielectric property.

Cette thèse est accessible à l'adresse : http://theses.insa-lyon.fr/publication/2022LYSEI006/these.pdf
© [X. Zhang], [2022], INSA Lyon, tous droits réservés

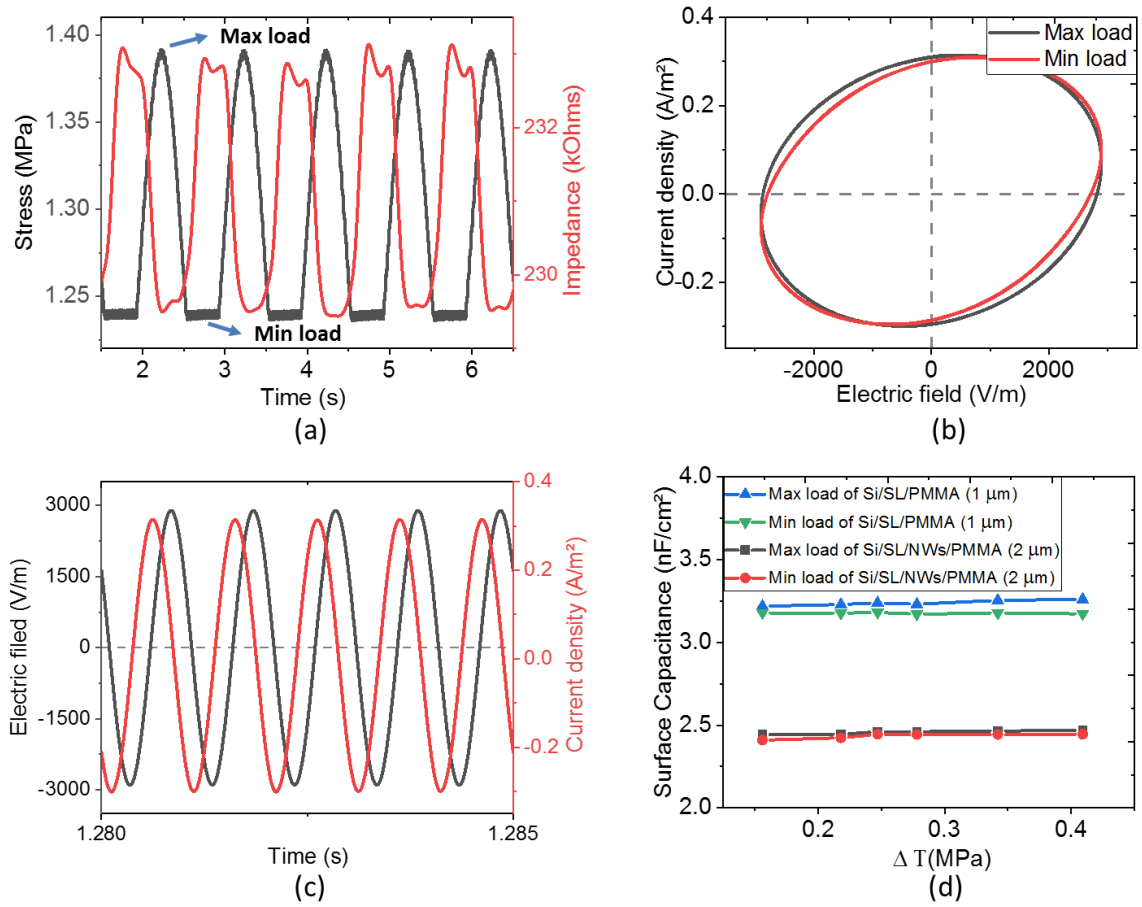

Figure 5.12. Electrical characterization under a dynamic stress of 1Hz and 0.15 MPa was carried out by applying a 1 kHz sinus electric field. For the Si/SL/NWs/PMMA (2 µm) sample, (a) time variation of stress and impedance; and (b) at max and min load configurations, the current circularly changes with the electric field, (c) and 90° out of phase. (d) Relative permittivity of the Si/SL/PMMA (1 µm) and Si/SL/NWs/PMMA (2 µm) sample is almost constant regardless of which dynamic stress level.

5.2.3 Dielectric properties

In order to further elucidate the dielectric properties of capacitor-like samples, the variation of the dielectric constant (ε), loss tangent (tanδ) versus frequency ranging from 1 Hz-1 MHz were plotted in Figure 5.13. For easier comparison, a pure PMMA sample without any substrate chosen as a reference sample, was fabricated in our lab based on a thin-film spin coating method. It was expected that the two "passive" samples (red and blue lines) exhibit similar dielectric behavior with respect to the pure one. Whatever the frequency range, both Si/SL/NWs/PMMA composites lead to an improvement in the relative permittivity, which may be due to the fact that the PMMA polymer might penetrate and sediment into the interstitial space between ZnO NWs. As observed in Figure 5.13(b), superior tanδ loss of Si/SL/NWs/PMMA composites occurs at low frequency range, which probably originates from the introduction of interfacial polarization between the NWs and the polymer matrix. While a raising trend of tanδ loss (beyond 1 MHz) is observed at high frequency for all samples, owning to the dipolar polarization. It is noticed that the values of the dielectric constant at 1 Hz measured through a dielectric spectrometer are consistent with those calculated in Table 5.3.

Cette thèse est accessible à l'adresse : http://theses.insa-lyon.fr/publication/2022LYSEI006/these.pdf
© [X. Zhang], [2022], INSA Lyon, tous droits réservés

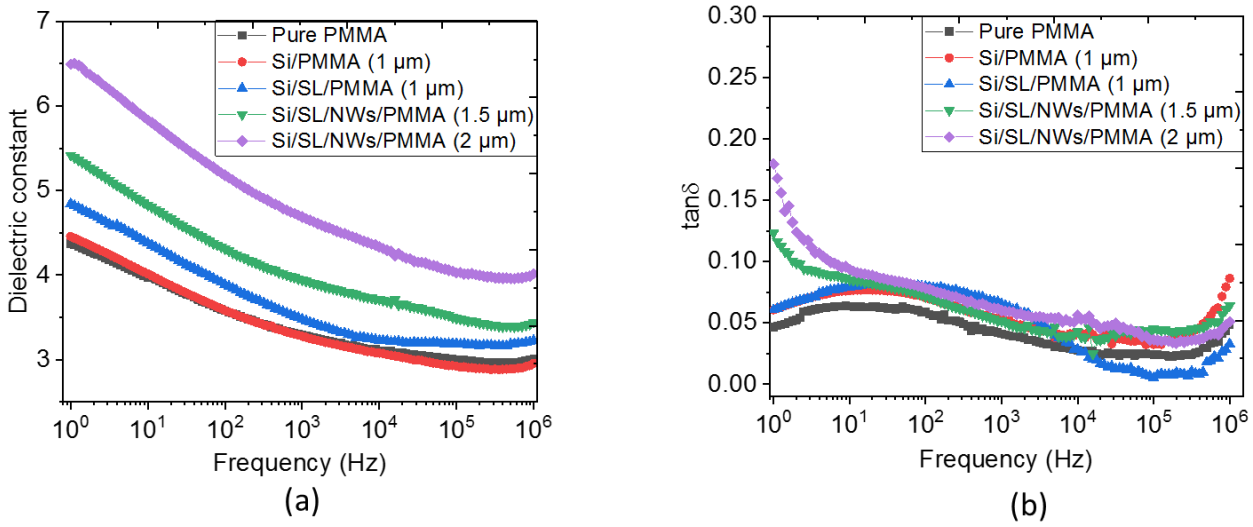

Figure 5.13. Variation of the (a) dielectric constant; and (b) loss tangent as a function of frequency for different samples.

5.2.4 Piezoelectric properties

As described in section 2.3.3, by applying dynamic mechanical stress on the sample in a short circuit, the electric charge can be collected and the piezoelectric coefficient d_{33} was then evaluated. Experimental tests were performed on the two "active" samples, consisting of ZnO NW arrays embedded into the PMMA matrix designed with different thickness of the dielectric top layer (i.e. 1.5 µm and 2 µm). The remaining "passive" samples, from which no charge signals were observed under mechanical excitation, are not worth being presented here. Figure 5.14 (a)-(d) describe the piezoelectric behavior of the Si/SL/NWs/PMMA (2 µm) under increasing dynamic stress, where the periodic variation of the generated charge density is in accordance with the applied stress. As increasing stress is applied to the samples and transferred through the polymer matrix into the piezoelectric NWs, compressed NW can generate electrical charges at the two ends of NWs. The PMMA matrix behaves as a capacitor that can store the electric charges on the surfaces of the two electrodes through the external circuit. During this process, an increasing trend of the charge density is monitored and measured via the charge meter. When the sample transfers from a compressed state to a relaxed state, a reverse polarization appears on the NWs and the electric charge decrease to a negative value due to the damping effect [252] (see Figure 5.14). More specifically, decreasing stress causes the formation of opposite polarization on the NWs. Thus, the stored electric charges will be consumed at the beginning and reach a negative peak at the end, explaining why the amplitude of negative charges is lower than that of positive charges. When a constant stress is followed, similar to the capacitor discharge process, no electric charge is generated but only a small exponential decay is observed in Figure 5.14. It is expected in Figure 5.15(a) that the variation of D linearly increases with the increasing ΔT, allowing an estimation of the piezoelectric coefficient (d_{33}) deduced from the slop of the ΔD-versus-ΔT characteristics. It has been pointed out that the Si/SL/NWs/PMMA (1.5 µm) gives rise to approximately 4-fold improvement in the piezoelectric response (d_{33} ~ 3.40 pC/N) compared to the 2 µm counterpart (d_{33} ~ 0.86 pC/N), displayed in Table 5.4. And a smallest piezoelectric response (d_{33} ~ 0.33 pC/N) was found in the Si/SL/PMMA (1 µm) sample.

Cette thèse est accessible à l'adresse : http://theses.insa-lyon.fr/publication/2022LYSEI006/these.pdf
© [X. Zhang], [2022], INSA Lyon, tous droits réservés

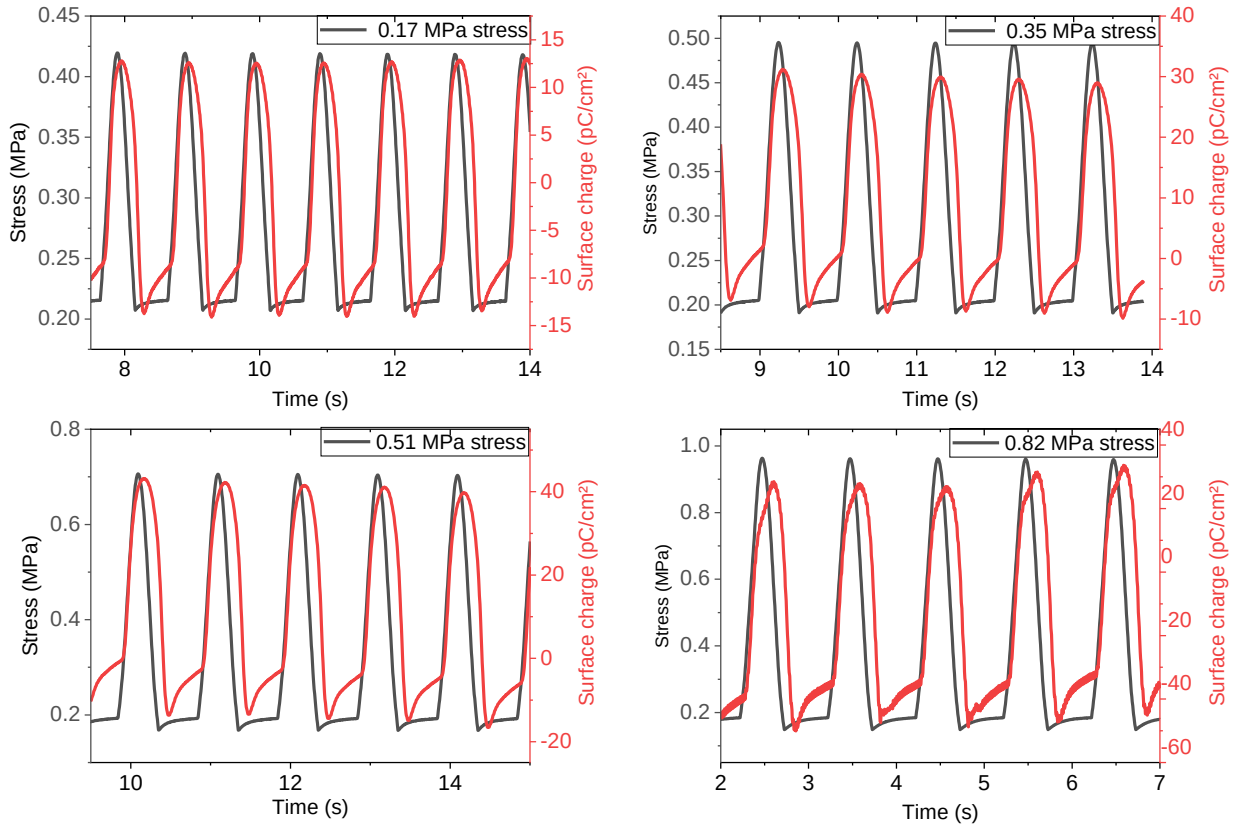

Figure 5.14. Piezoelectric characterization was performed under dynamic stress of 1 Hz. Time evolution of stress and charge density of the Si/SL/NWs/PMMA (2 µm) composite under different magnitude of dynamic stress: (a) 0.17 MPa, (b) 0.35 MPa, (c) 0.51 MPa and (d) 0.82 MPa.

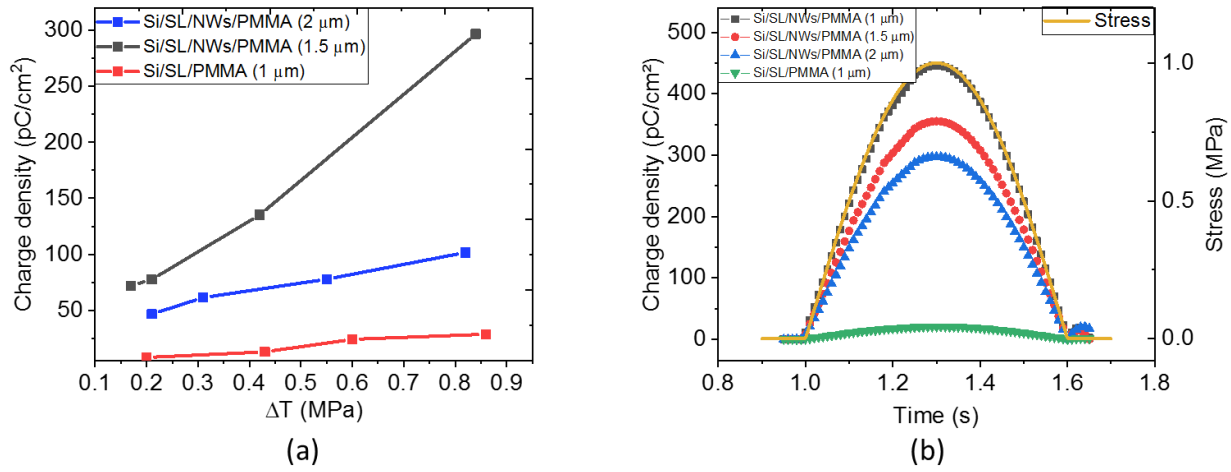

Figure 5.15. (a) Piezoelectric charge density versus dynamic stress of samples with different thicknesses of the top PMMA layer. (b) Theoretical piezoelectric response via FEM simulation performed in “Piezoelectricity module” coupled with “Electrical circuit module”.

Cette thèse est accessible à l'adresse : http://theses.insa-lyon.fr/publication/2022LYSEI006/these.pdf
© [X. Zhang], [2022], INSA Lyon, tous droits réservés

The d_{33} of the ZnO NW can be estimated by fitting the effective d_{33} from the FEM model with the corresponding experimental value. The model of NWs-based structure (Si/SL/NWs/PMMA) with different thickness of polymer, and the case without NWs (i.e., Si/SL/PMMA) were built to correlate with the experimental results. In order to achieve the best fitting between the experimental and simulation results, the piezoelectric coefficient of each ZnO NW was set at d_{33} =16.5 pC/N, approximately. It is highlighted in Figure 5.15(b) that when the stress increases, the composite generates increasing electric charges on the electrodes, which will be then stored in the external capacitor. On the other hand, the accumulated charges start to decrease when the composite is mechanically released. Table 5.4 compares the experimental and simulated piezoelectric coefficient of all four samples. Simulation results confirm that under identical compression mode, the NW composite with a thinner top PMMA layer provides higher instantaneous surface charges, giving rise to significantly improved piezoelectric coefficient (d_{33}). Unfortunately, the Si/SL/NWs/PMMA (1 µm) sample was electrical breakdown during experiment, that why no value of d_{33} is shown in Table 5.4. Logically, the sample without ZnO NWs shows every low piezoelectric response.

Table 5.4. Piezoelectric coefficient d_{33} from experimental and COMSOL simulation

	Measured effective d_{33} (pC/N)	R^2	Simulation effective d_{33} (pC/N)
Si/SL/NWs/PMMA (1 µm)	-	-	4.46
Si/SL/NWs/PMMA (1.5 µm)	3.40 ± 0.22	0.99	3.55
Si/SL/NWs/PMMA (2 µm)	0.86 ± 0.07	0.98	2.98
Si/SL/PMMA (1 µm)	0.33 ± 0.06	0.94	0.21

5.3 Flexible ZnO NW arrays composites using CBD method

Rigid NW arrays composites exhibit promising piezoelectric performance for the purpose of stress sensing. But charge leakage effect (see the below annexes) and low elasticity of these samples makes practical implement challenging, which could hinder their possible use in a medical environment. The ZnO MRs/PDMS composites-based casting method offers high flexibility and solves the leakage problem, meanwhile, the low piezoelectric coefficient was yielded, even with the help of dielectrophoresis (Section 5.1). As a matter of fact, the casting method seems not to be an efficient approach to favorize the piezoelectric properties of ZnO with high AR, either in nanoscale or microscale. Therefore, this section reports on flexible ZnO NW arrays structure developed with the CBD technique, i.e., similar to the case of the rigid composite (Section 5.2). However, NWs here are grown on a flexible PMMA substrate instead of a rigid silicon one, as shown in Figure 5.16.

In fact, ZnO is natural n-type semiconductor containing mobile negative electrons due to the existence of crystal defects. Irrespective of the physical or chemical deposition techniques of NW's synthesis, high electron density with a high conductivity still persists and impacts the intrinsic properties of ZnO NWs [253,254]. It has been demonstrated that the root reason for high electron density in unintentionally doped ZnO NWs grown by CBD is massive incorporation of hydrogen in the center [255,256], which typically generates a significant and detrimental screening potential. Actually, it leads to a creation of a mixed Zn- and O-polarity in the arrays, where the piezoelectric potential is partially generated with an opposite sign

Cette thèse est accessible à l'adresse : http://theses.insa-lyon.fr/publication/2022LYSEI006/these.pdf
© [X. Zhang], [2022], INSA Lyon, tous droits réservés

from O-polar to Zn-polar NWs [257]. Recently, Jose *et al.* has pointed out that the pristine ZnO NWs exhibits a high electron density in the range of 2.7 $\times 10^{18}$ to 3.1 $\times 10^{19}$ cm^{-3}. This is manifested by a large concentration of the H_{BC} and (V_{Zn}-3H) surface defects acting as two shallow donors, which is affected by the absorption of HMTA molecules [258]. All of these phenomena strongly reduce the output voltage of piezoelectric devices made of ZnO NWs and hence limiting their integration into real-world applications. Understanding the fundamental issues related to the properties of a semiconductive ZnO NW may help to optimize and enhance the electromechanical coupling of the piezoelectric sensor system, especially in a macroscopic scale.

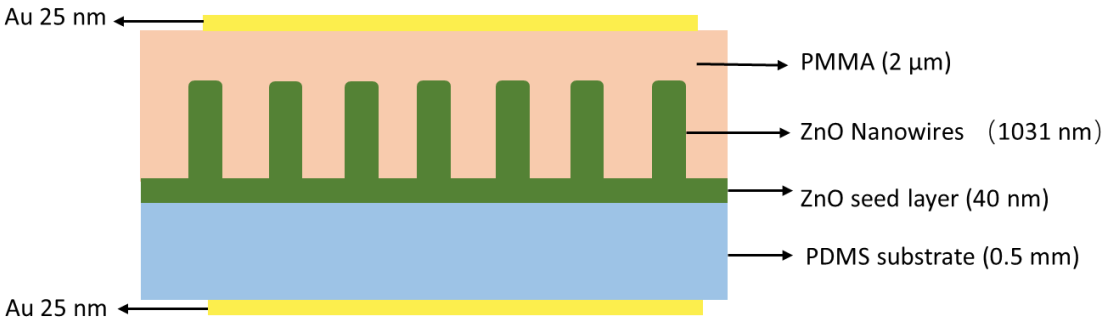

Figure 5.16. Schematics of flexible ZnO NW arrays-based structure

5.3.1 Screening effect

For the ZnO NWs applied by bending or compressive stress, free electrons can screen the generated polarization and thus reduce the piezoelectric potential. Thus, the output potential and the efficiency of devices can be enhanced by inhibiting the piezoelectric screening effect. In order to simulate the influence of free-charge concentration on the equilibrium electric potential as well as the electron distribution, a numerical approach via FEM was carried out.

First of all, the derivation of the theoretical equation will be introduced by considering the coupling between the piezoelectric and semiconducting properties of ZnO material. The free carriers interact with the piezoelectric field generated in the deformed ZnO NW and redistribute under thermodynamic equilibrium. The electric displacement (D) can be calculated according to Eqs. (4.3) – (4.4) while the free charge density (ρ_F) is given by:

$$\rho_F = e(p - n + N_D^+ - N_A^-) = e(N_D^+ - n) \tag{5.5}$$

where p is the valence-band hole concentration; n is the conduction-band electron concentration, N_D^+ and N_A^- are the ionized donor and acceptor concentration, respectively; and e denotes the electron charge (~ 1.602E–19 C). In the n-doped ZnO NW, ρ_F is the sum of the free electron and the ionized donor charges where $p = N_A^- = 0$. According to Fermi-Dirac statistics, the positively ionized donor concentration (N_D^+) can be calculated as [259]:

$$N_D^+ = N_D\left(\frac{1}{1+2\exp\left(\frac{E_F - E_D}{\kappa T}\right)}\right) \tag{5.6}$$

Cette thèse est accessible à l'adresse : http://theses.insa-lyon.fr/publication/2022LYSEI006/these.pdf
© [X. Zhang], [2022], INSA Lyon, tous droits réservés

where N_D is the donor concentration, κ is the Boltzmann constant, $T = 300\ K$ is the ambient temperature, E_D is the position-dependent donor energy level. The Fermi level (E_F) is set to be zero and a shallow donor level is assumed with $E_D = E_{c0} - \Delta E_D$, where $\Delta E_D = 35$ meV [260] and $E_{c0} = \kappa T * In(N_c/N_D)$ is the conduction-band energy. Similarly, the electron concentration *n* is expressed as [259]:

$$n = N_c F_{1/2}(-\frac{E_c(x)-E_F}{\kappa T}) \tag{5.7}$$

$$N_c = 2(\frac{2\pi m_e}{h^2})^{3/2} \tag{5.8}$$

where $F_{1/2}$ is the Fermi-Dirac integral of order ½ function; h is Planck's constant. N_c is the effective states density for electrons in the conduction band, i.e., dependent on the effective mass of electron (m_e) calculated as m_e = 0.628 m_0 where m_0 is the mass of electron (~9.11E-31 kg) [261]. $E_c(x)$ is the position of the conduction band edge that varies with the electric potential (φ) and deformation, as given by [262]:

$$E_c(x) = E_{c0} - e\varphi + \Delta E_{def}^c \tag{5.9}$$

where $\Delta E_{def}^c = a_c \frac{\Delta V}{V}$ is the band edge variation due to the mechanical loading, which is determined by the deformation constant $a_c = -0.61\ eV$ [263] and the relative volume variation $\frac{\Delta V}{V}$. As a consequence, the free charge density (ρ_F) is derived as a function of piezoelectric potential (φ). According to the Poisson equation, expressed as:

$$\varepsilon \nabla^2 \varphi = -(\rho_p - \rho_F) \tag{5.10}$$

where ρ_p is the piezoelectric charge density, the non-linear source term of the free charge density should be taken in account. In that case, direct calculation of the analytical solution is complicated. Thanks to the FEM, a fixed space charge density ρ_F, initially calculated and defined by combing Eqs. (5.5) – (5.9), can be coupled into the COMSOL Multiphysics software to solve those nonlinear partial differential equations.

The COMSOL model is defined as described in Chapter 4 (Figure 4.2), where a cylinder NW with 1031 nm length and 42 nm radius was subjected to a compressive force of -60 nN along the z-axis. The ambient air environment is provided to set a zero electric field at an infinite distance from the NW. The simulation is performed under a stationary state and the open-circuit voltage is analyzed. As seen in Figure 5.17(a) for the dashed red line, when the dielectric NW presenting no defect is subjected to a compressive deformation, a negative potential is produced across the whole NW with the electrical grounded condition on the bottom. Meanwhile, the magnitude of the generated potential gradually increases along the z-axis and reaches the maximum of around 250 mV (in absolute value) at the top. However, by incorporating impurity into the NW, the free electrons at the top are repelled by the electric field generated from piezoelectric polarization and accumulated at the bottom end, leaving immobile ionized donors at the tip. Those positive donors might screen the negative charge and a depletion region is formed close to the top, causing a drop in the output voltage with respect to an increase in the donor concentration (see Figure 5.17(a)). As revealed in Figure 5.18, the maximum magnitude of the electric potential (φ) dramatically decreases from 71 mV with a low charge concentration (1×10^{15} cm^{-3}) to 18.6 mV with a higher concentration (10^{17} cm^{-3}). Moreover, the depletion region width, corresponding to the rainbow area where a voltage drop is generated in Figure 5.18, decreases with an increasing trend of the donor concentration.

Cette thèse est accessible à l'adresse : http://theses.insa-lyon.fr/publication/2022LYSEI006/these.pdf
© [X. Zhang], [2022], INSA Lyon, tous droits réservés

In Eq. (5.9), the generated piezoelectric potential φ has a direct impact on the conduction energy level E_c. The conduction band level at the top of the NW is deflected by the mechanical deformation and the electric field introduced by the piezoelectric polarization (cf. Figure 5.17(b)). The higher the donor concertation, the lower the negative electric potential and so is the conduction band level. Indeed, the free electrons prefer to occupy the lower energy level of the conduction band [264]. As confirmed in Figure 5.17(c), a high conduction band indicates a low free charge carrier concentration of surface defects. In other words, for a shallow donor level, nearly all the donor atoms are ionized ($N_D^+ \sim N_D$), which is interpreted to be complete ionization. In that case, each donor donates a free electron to the conduction band with $n = N_D^+$. Thus, normally a higher free charge carrier density is obtained at high doping material. Except at the top of NW, a drop of free electron density is observed due to the existence of the electric field introduced by the piezoelectric polarization.

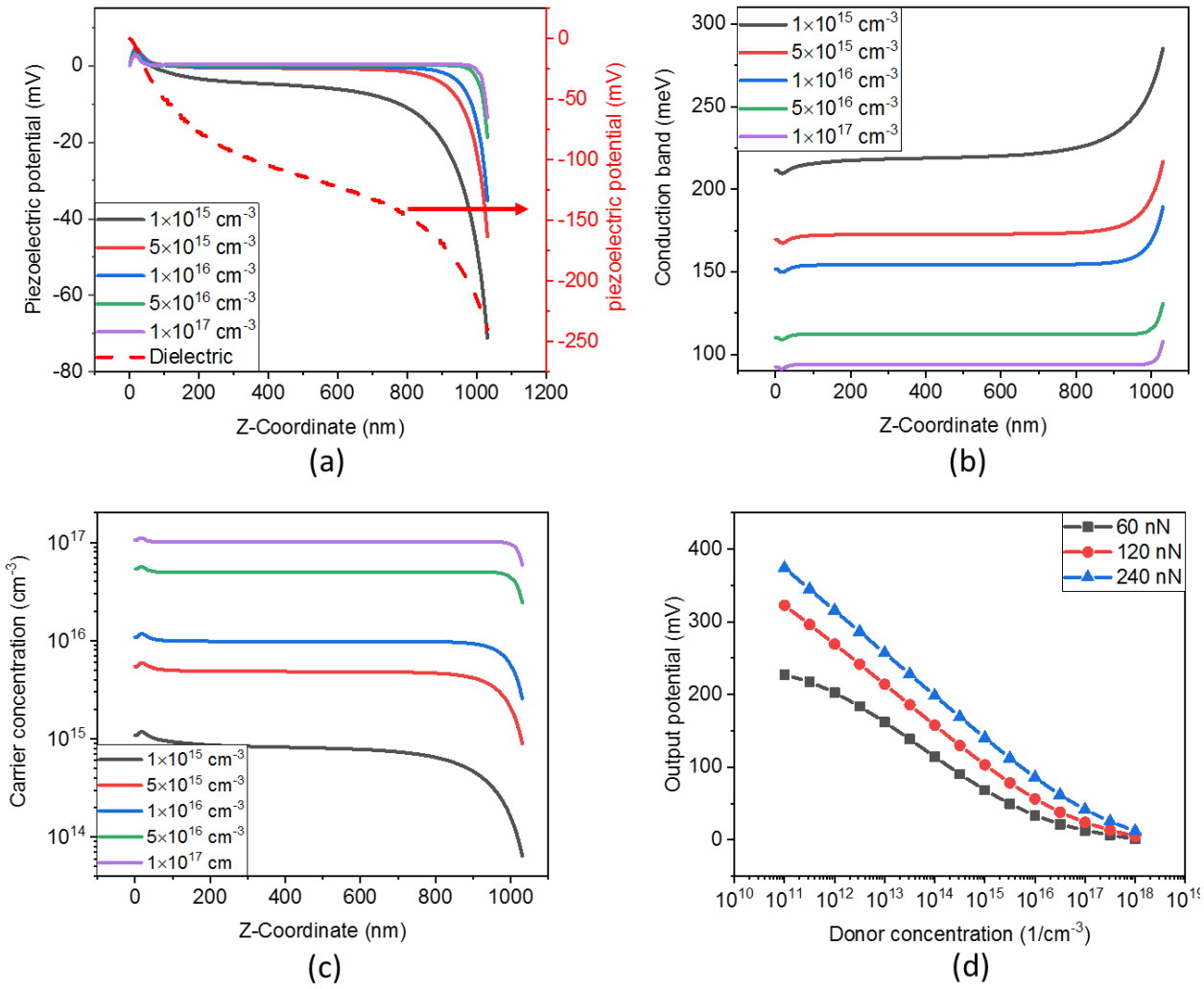

Figure 5.17. Simulation results of a single ZnO NW exerted by a force F = – 60 nN: (a) piezoelectric potential; (b) conduction band; (c) free carrier concentration along the central z-coordinate of the NW for different donor concentrations; (d) output voltage as a function of donor concentration with respect to different applied forces.

Here we used some assumptions (homogenous free charge, perfect vertical alignment of NW, etc.) in the simulation models, which could lead to a discrepancy between the numerical solution and the

Cette thèse est accessible à l'adresse : http://theses.insa-lyon.fr/publication/2022LYSEI006/these.pdf
© [X. Zhang], [2022], INSA Lyon, tous droits réservés

experimental results[226]. To improve the NW-based devices performance, several optimization guidelines can be outlined as follows:

Firstly, because the electric potential can be partially screened by the positive donor ions, the output voltage increases as the donor concentration decreases (Figure 5.17(d)). The output voltage will be completely screened to zero if a donor density around 1 $\times 10^{18}$ cm^{-3} is given.

Secondly, it can be concluded from the above discussions that the piezoelectric potential (φ) can regulate the carrier transport characteristics by tuning the conduction band and the free charge carrier amount. Hence parameters impacting on the output voltage of compressed piezoelectric NW should be thoroughly considered (e.g., external force; shape, size, AR, and density of NW). In Figure 5.17(d), when the exerting force increases and other parameters are kept constant (N_D, R, L), an increasing trend of the output potential is observed.

Thirdly, it always encounters technical challenges to improve the NW quality with the better growing procedure to decrease the defect concentration. Researchers have developed and designed a novel structure to cancel the screening effect in n-type ZnO NWs. It has been reported that forming a Schottky junction on the ZnO surface by introducing Au particles would weaken the screening effect and thus increase the remnant output potential [265]. Lee *et al*. have demonstrated that a p-type P3HT semiconductor polymer coated on the ZnO NWs can significantly reduce the screening effect and improve the piezoelectric output several times compared to pristine ZnO NWs-based nanogenerator [266]. However, it is difficult to experimentally alter the concentration of the positive charges in p-type polymer to equal the free electron density in the NWs, so as to achieve optimal output potential.

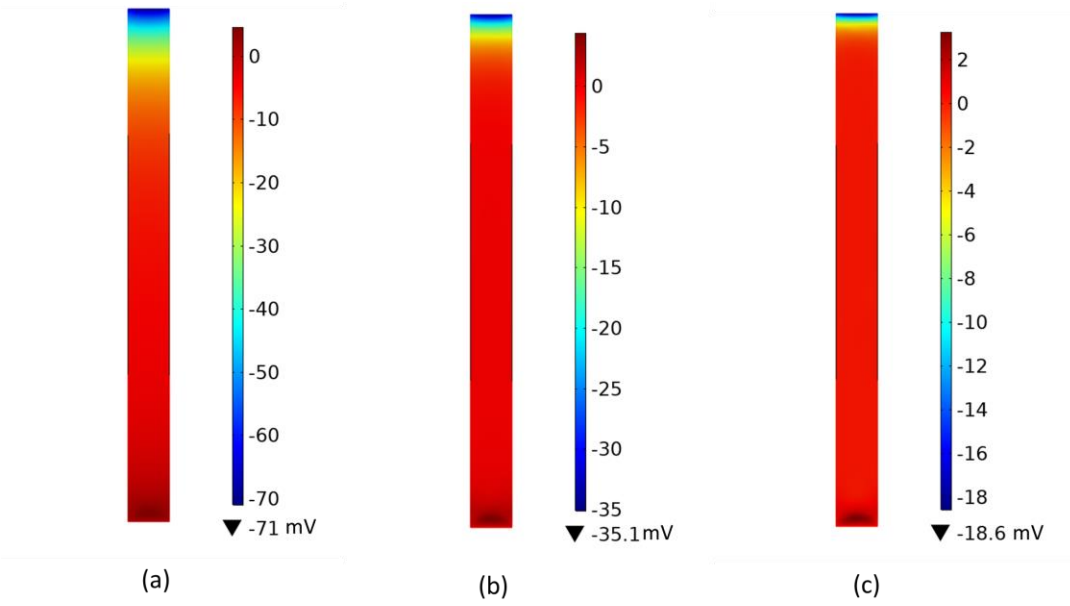

Figure 5.18. Electric potential in the longitudinal profile of single NW subjected to an axial compression viewed in 2D YZ cut plane with a donor concentration of (a) 1×10^{15} cm^{-3}; (b) 1×10^{16} cm^{-3}; (c) 1×10^{17} cm^{-3}.

In our case, as the nitrogen- and hydrogen-related defects have been identified as the major source of crystal defects in pristine ZnO NWs, a thermal annealing pretreatment strategy was proposed to dissociate those defects from their electrical properties [267]. For instance, an acceptable small free charge density of

Cette thèse est accessible à l'adresse : http://theses.insa-lyon.fr/publication/2022LYSEI006/these.pdf
© [X. Zhang], [2022], INSA Lyon, tous droits réservés

5.6×10^{17} cm^{-3} is obtained for ZnO NWs annealed at a moderated temperature of 300 °C [267]. Another optimized approach involves the incorporation of Sb doping into the p-ZnO NWs so as to boost their piezoelectric property that can be used in several applications dedicated to sensing devices and/or energy generators [268][269]. Zn atom is substituted by the Sb dopants in the ZnO lattice and attracts neighboring bounded electrons, resulting in the generation of positively charged holes. Accordingly, the positive charge carriers from Sn-doping would consume or recombine with the negative charge carriers from the hydrogen-related defects to have a compensation effect, yielding an improved electromechanical coupling.

5.3.2 Piezoelectric and dielectric properties

Figure 5.19(a)-(b) illustrates the broadband spectroscopic of the pristine ZnO composite and those with thermal post-annealing and/or Sb-doped pretreatment. The discrepancy of the dielectric constants and the shift of the loss tangent (i.e., $tan\delta$) peak of all samples emphasizes the main contribution of the Sb dopants. On one hand, the doped samples (blue and green curves) give raise to a substantial increase in the dielectric constant and the $tan\delta$ as well. Thermal annealing, on the other hand, has a small impact on the dielectric properties where similar behavior is observed between the pristine (black curve) and the annealed (red curve) composites. Particularly, the loss tangent measured at low frequencies (below 1 Hz) is found smaller than 0.1, indicating good dielectric behavior (without any leakage effect) of these samples as opposed to the rigid counterparts (see annexes).

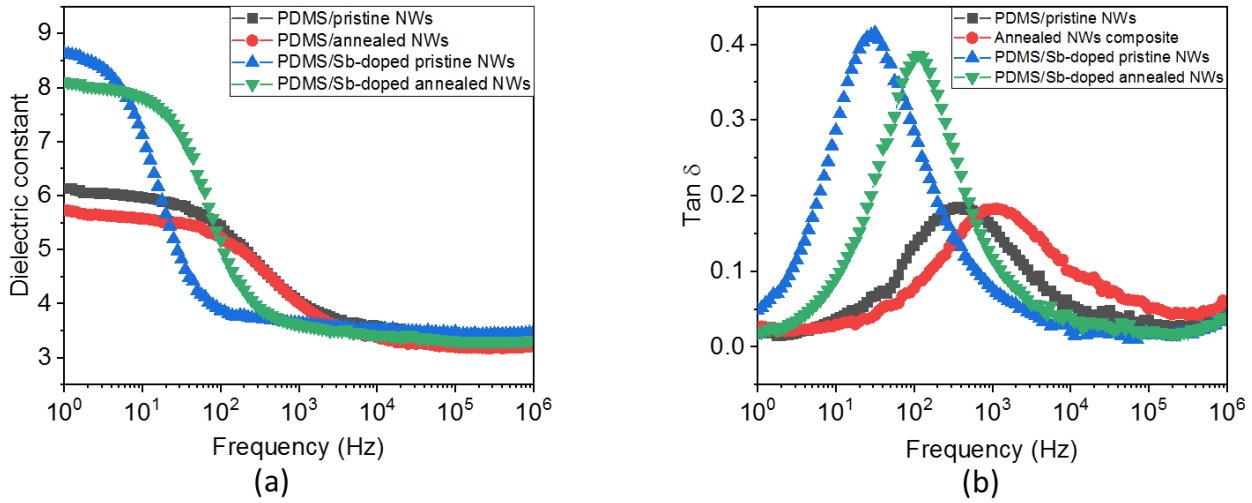

Figure 5.19. Effect of doping and annealing techniques on dielectric properties of NW composites: (a) Dielectric constant and (b) loss tangent as a function of frequency for different samples.

Figure 5.20(a) displays the piezoelectric charge variation (ΔD) in response to oscillating stress with 0.15 MPa magnitude and 1 Hz frequency. Specific generated charges were measured with respect to the increasing dynamic stress (ΔT) as shown in Figure 5.20(b). Thereby, the piezoelectric coefficient (d_{33}) can be accurately deduced from the linear fitting of the ΔD-versus-ΔT characteristics, i.e., corresponding to the slope of the linear regression. The numerical values of d_{33} together with the determination coefficient (R^2) are shown in Table 5.5. As observed, the piezoelectric response of the annealed composite is somewhat higher than that of the pristine composite, which was previously confirmed by the fact that there is no

Cette thèse est accessible à l'adresse : http://theses.insa-lyon.fr/publication/2022LYSEI006/these.pdf
© [X. Zhang], [2022], INSA Lyon, tous droits réservés

significant change in their dielectric properties. In contrast, Sb-doped implement can achieve 3 times improvement in d_{33} (~ 0.763 pC/N) compared to the pristine composite (~0.288 pC/N), and even 4 times increase (~1.055 pC/N) in the case of annealed and doped samples, simultaneously. Accordingly, the piezoelectric output is considerably enhanced by the doping and thermal annealing post-deposition, leading to a decrease in the screening effect that is essentially caused by a high density of free electrons.

Due to the addition of a flexible PDMS layer instead of the rigid Si substrate, the d_{33} coefficient of the PDMS/Sb-doped annealed NWs composite is lower than that of the Si/SL/NWs/PMMA (1.5 µm) (~3.4 pC/N). Indeed, both PDMS substrate and top PMMA layer act as an insulating layer for NWs to couple the piezoelectric effect and electrostatic induction. Thus, the reduction of d_{33} can be explained through FEM simulation as described in Subsection 4.3.4, where an increasing thickness of the polymer layer can lead to a drastic decrease in the electromechanical coupling. For the application point of view, the flexible structures, despite their lower piezoelectric sensitivity, exhibit further advantages in terms of implementation and reliability.

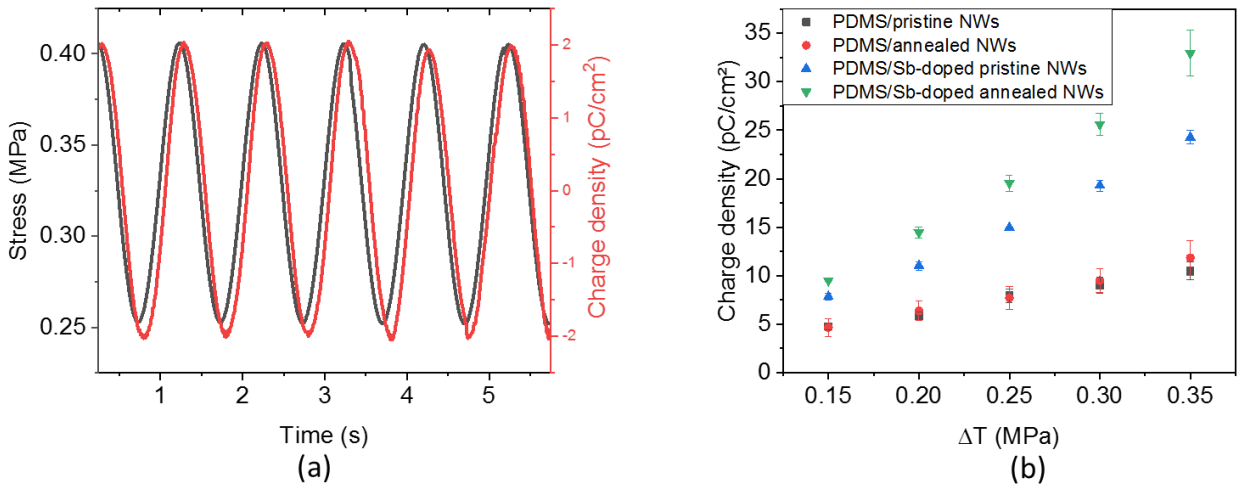

Figure 5.20. Piezoelectric characterization performed under a 1-Hz dynamic stress. (a) Time evolution of stress and charge density of the pristine ZnO NWs composite at a 0.15 MPa peak-to-peak. (b) Piezoelectric charge density versus dynamic stress for different samples.

Table 5.5. Piezoelectric charge coefficient (d_{33}) from experimental measurement

	Random d_{33} (pC/N)	**R^2**
PDMS/pristine NWs	0.288 ± 0.020	0.985
PDMS/annealed NWs	0.338 ± 0.018	0.991
PDMS/Sb-doped pristine NWs	0.763 ± 0.046	0.989
PDMS/Sb-doped annealed NWs	1.055 ± 0.035	0.996

Cette thèse est accessible à l'adresse : http://theses.insa-lyon.fr/publication/2022LYSEI006/these.pdf
© [X. Zhang], [2022], INSA Lyon, tous droits réservés

5.4 Summary

To sum up, there are several arrangements of the constituent phase in the ZnO piezoelectric composites as presented in Figure 5.21. It is noteworthy that the piezoelectric response depends on the connectivity pattern. Starting with the 0-3 or random particle composite whose process-based casting method is easy, but this structure leads to an extremely low piezoelectric coefficient (d_{33}). Thus, a dielectrophoretic technology is developed to form the alignment of particles within polymer matrix where the interparticle distance is reduced to improve the efficiency. Unfortunately, this improvement is limited due to the saturation of the microparticles (MP) concentration, in which beyond 40 vol.% is a real challenge. To further enhance the piezoelectric performance, microrod (MR) shaped fillers with a higher AR were suggested to substitute the spherical filler. Similarly, quasi 1-3 rod composites can be achieved via dielectrophoretic manipulation, but this technique still suffers from the limitation of the ZnO concentration and the non-perfect alignment as in the real 1-3 pattern. Actually, in the 1-3 composite, wires are vertically embedded in a polymer matrix and create a continuous connection from the bottom to the top electrodes, giving raise to the highest connectivity, and thereby yielding the largest d_{33}. Considering the semiconducting property of ZnO, a thin polymer layer should be coated between the top NW and the top electrode to avoid the leakage effect. Finally, based on the substrate materials, rigid and flexible ZnO NWs composites are fabricated via CBD technique to enhance the piezoelectric sensitivity. But the manufacturing process of CBD is more complex and higher cost compared to the traditional casting method.

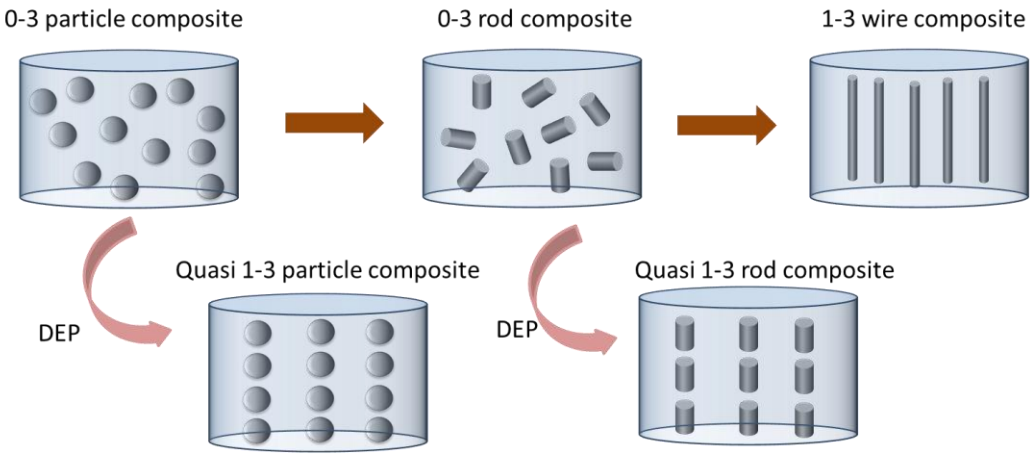

Figure 5.21. Representative of connectivity patterns used in the developed materials.

More specifically, for the flexible MR composites, the dielectrophoretic conditions were firstly investigated and compared to the particle composites. For all AR particles, the average orientation angle increases with the electric field magnitude, causing a rise in the dielectric constant and the piezoelectric coefficient. The field-amplitude dependence of the dielectric constant is prominent for the high AR of MR as opposed to the low AR of spherical particles. Therefore, under the same optimized external electric field (0.6 V/μm, 2 Hz), the 8% vol. structured ZnO MRs/PDMS composites exhibit substantial enhancements in the dielectric (~ sevenfold) and the piezoelectric (~ sixfold) responses as compared with the random one, while threefold and fivefold improvement in the case of the MP samples, correspondingly.

For the rigid ZnO NW arrays composites, one of the objectives aims to identify the characteristics of each layer as well as of the whole complex structure. Electrical characterizations were investigated on a set

Cette thèse est accessible à l'adresse : http://theses.insa-lyon.fr/publication/2022LYSEI006/these.pdf
© [X. Zhang], [2022], INSA Lyon, tous droits réservés

of designed configurations, allowing to confirm that the Si and ZnO seed layer performed like a resistor, while the other samples stacked with a PMMA layer behaved as a capacitor. Also, we demonstrated that the dielectric properties of these capacitors were perfectly stable under dynamic stress varied from 0.1 to 0.4 MPa. A small change in their electric impedance was originated from the thickness variation when the sample was subjected to a compressive force. Experimental measurements highlighted that ZnO NWs composite with a lower thickness of PMMA top layer gave rise to increased piezoelectric sensitivity. The effective charge coefficient (d_{33}) of the fabricated composite reached 3.4 pC/N when being stacked with a 1.5 µm-thick PMMA, as opposed to 0.86 pC/N in the case with the 2 µm-thick PMMA counterpart. This effect was to some extent correlated to the model predicted by COMSOL FEM. Accordingly, significant improvements in the piezoelectric behavior were achieved through optimization of the top-layer thickness (i.e., 1.5 µm).

Flexible PDMS polymer instead of stiff Si was utilized as the substrate of the ZnO NWs composite. Even though the piezoelectric charge coefficient (d_{33}) is inhibited, this structure with high mechanical flexibility can become a promising candidate in the self-powered piezoelectric sensors for implantable biomedical detection, particularly in the FFR technique. Concerning the high free electron density of ZnO NWs grown by the CBD technique, the induced screening effect can be decreased by applying a post-deposition thermal annealing or Sb-doping during the fabrication process. It has been confirmed in the experimental tests that d_{33} of the annealed and dopped NWs composite is significantly improved (~1.055 pC/N) compared to the pristine sample (~0.288 pC/N).

Cette thèse est accessible à l'adresse : http://theses.insa-lyon.fr/publication/2022LYSEI006/these.pdf
© [X. Zhang], [2022], INSA Lyon, tous droits réservés

Annexes: How to detect failure samples

As shown in Figure 5.22(a), applying a sinusoidal electric field, the measured impedance of Si/SL/NWs/PMMA (1 µm) sample has a periodical variation with respect to repeated deformation. However, unlike what we expect in the samples containing the PMMA insulating layer, either at the min or max mechanical load (Figure 5.22b), the current density of Si/SL/NWs/PMMA (1 µm) sample has a near-linear response to the electric field, reflecting the resistive property. The conducting behavior of the NWs-based sample causes a very small (even zero) output charge because of the charge leakage effect. The resistive device cannot store the generated piezoelectric charges but cancel and recombine the positive and negative electrons inside the structure.

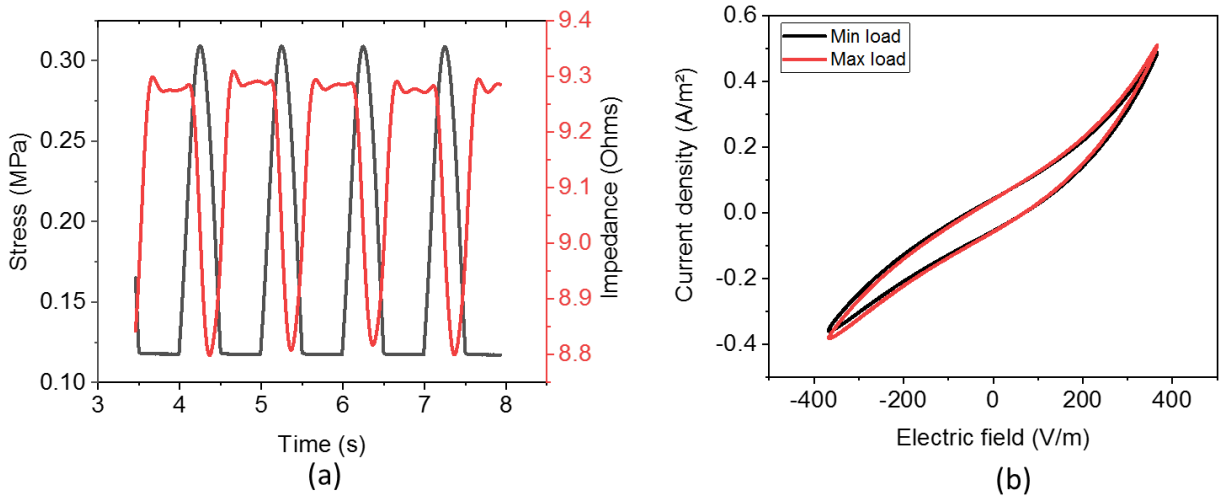

Figure 5.22. Electrical characterization under dynamic stress of 1Hz and 0.15 MPa was carried out by applying a 1 kHz sinus electric field. For the Si/SL/NWs/PMMA (1 µm) sample, (a) time variation of stress and impedance, and (b) at max and min load con-figurations, the current linearly changes with the electric field.

Indeed, the PMMA polymer, whose top PMMA layer is probably not a perfect homogeneous film, maybe involve some inevitable structural defects, charge traps, impurities. If PMMA thickness is small enough, the hopping conduction mechanism in the dielectric material can induce electron transportation through the tunneling effect of trapped electrons jumping from one site to another [105]. Therefore, dielectric measurement tests of Si/PMMA samples under different static stresses were performed to prove our assumption. In Figure 5.23(a), the measured dielectric constants under the static stress beyond 2 MPa are unstable and dramatically fluctuate at low frequency with the presence of high noises. Meanwhile, the loss tangent calculated as $tan\delta = \frac{\varepsilon''}{\varepsilon'} + \frac{\sigma}{\omega}$ depends on the conductivity σ. Hence, the abnormally large value of loss tangent (~10 at 1 Hz) with applied stress exceeding 2 MPa can be originated from the high conductivity. More specific, increasing the magnitude of applied stress can reduce the effective thickness of the PMMA layer, which raises the possibility of leakage effect. Additionally, high stress applied on the device possibly damages the dielectric layer which seems to be irreversible.

Cette thèse est accessible à l'adresse : http://theses.insa-lyon.fr/publication/2022LYSEI006/these.pdf
© [X. Zhang], [2022], INSA Lyon, tous droits réservés

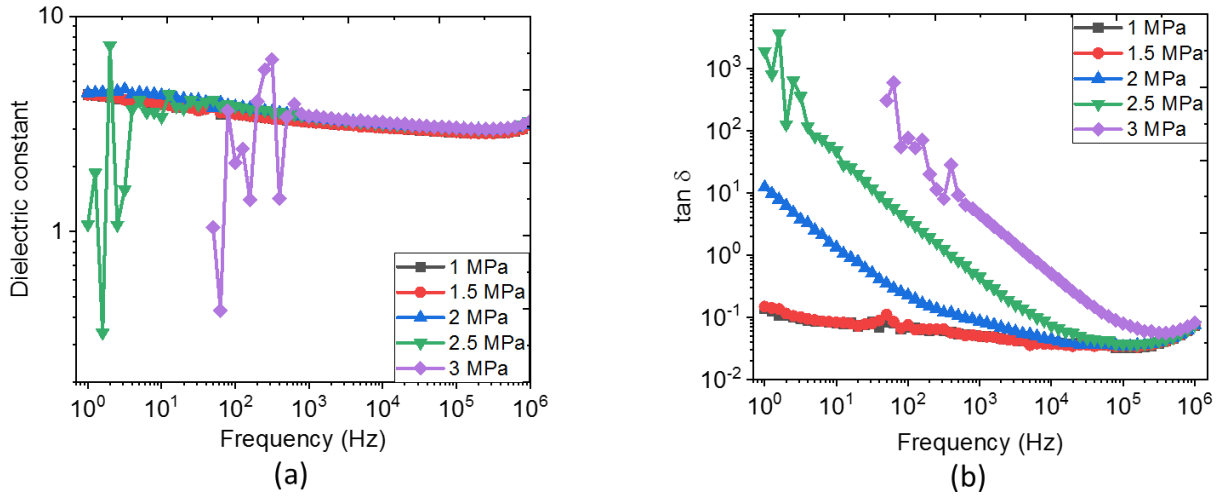

Figure 5.23. For the Si/PMMA (1.5 µm) sample, (a) the dielectric constant and (b) loss $tan\delta$ are measured as a function of frequency under increasing static stress.

In order to reduce the leakage effect that should result in a drastic decrease of the output performance, improvement of the device quality and optimization of the structural configuration were performed. Firstly, thermal annealing during the spin coating process is studied to verify the influence on the sample quality. PMMA films with Teflon as substrate were fabricated using the casting method. A pure PMMA thin film of ~ 47 µm thickness were elaborated after peeling off the Teflon, as displayed in Figure 5.24(a). Different annealing times and temperatures were utilized during the annealing procedure, but their loss tangents were almost identical (Figure 5.24b), implying the stable properties of the PMMA layer. On the other hand, a thin PMMA film with ~1.5 µm thickness was spin coated on two same Si wafers (label as A and B). Specifically, soft annealing of samples was performed on a hot plate at 180 °C for 1 min 30 seconds. Followed with the hard bake annealing, samples were placed on the hot plate at 180 °C with different annealing times, finally, we obtained a PMMA thickness of ~1.5 µm. As displayed in Figure 5.24(c)–(d), regardless of annealing time, most of the samples in the wafer A and B exhibit conductive characteristics overwhelming the capacitive property. Consequently, compared to the condition of annealing time, temperature, the thickness of the insulating layer has much more influence on the dielectric properties.

Another approach is to increase the thickness of the insulating layer to suppress the leakage effect. In Figure 5.25, the NWs-based samples with a thin thickness of the insulating layer (D < 2 µm) indicate strong conductive characteristics instead of capacitive behavior, while both two samples with thicker PMMA film (D= 3.81 µm, 3.86 µm) have good dielectric properties with low losses under large frequency range, which is highly consistent to the pure PMMA properties (seen in Figure 5.24). Consequently, it can be concluded that increasing the thickness of the top polymer layer can help to suppress the influence from the leakage effect. However, as simulated in section 4.3.4 (Figure 4.20), the generated charges drastically decrease with the thickness of the PMMA top layer. Moreover, during the PMMA spin coating process, this fluid polymer might penetrate and sediment into the interstitial space between ZnO NWs that can decrease the effective thickness of the insulating layer. Therefore, growing the ZnO NWs on a flexible dielectric matrix, instead of a rigid Si substrate, is an optimized method to guarantee the capacitive property of devices. Simultaneously, it can increase the flexibility of the device to versatile applications.

Cette thèse est accessible à l'adresse : http://theses.insa-lyon.fr/publication/2022LYSEI006/these.pdf
© [X. Zhang], [2022], INSA Lyon, tous droits réservés

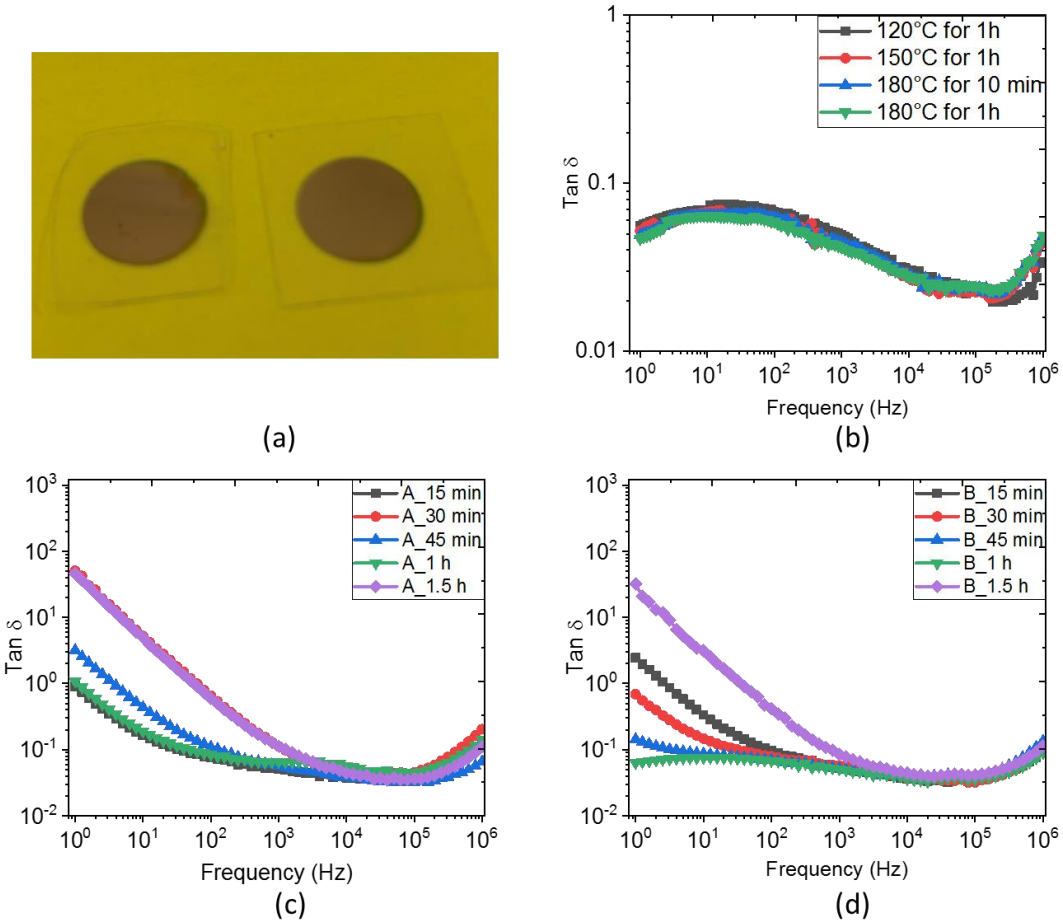

Figure 5.24. (a) Photograph of pure PMMA thin films with a thickness ~ 47 µm; and (b) evolution of its loss tangent at different annealing times and temperatures. The variation of loss tangent of Si/ PMMA (~1.5 µm) sample (c) A and (d) B as a function of frequency with different annealing times.

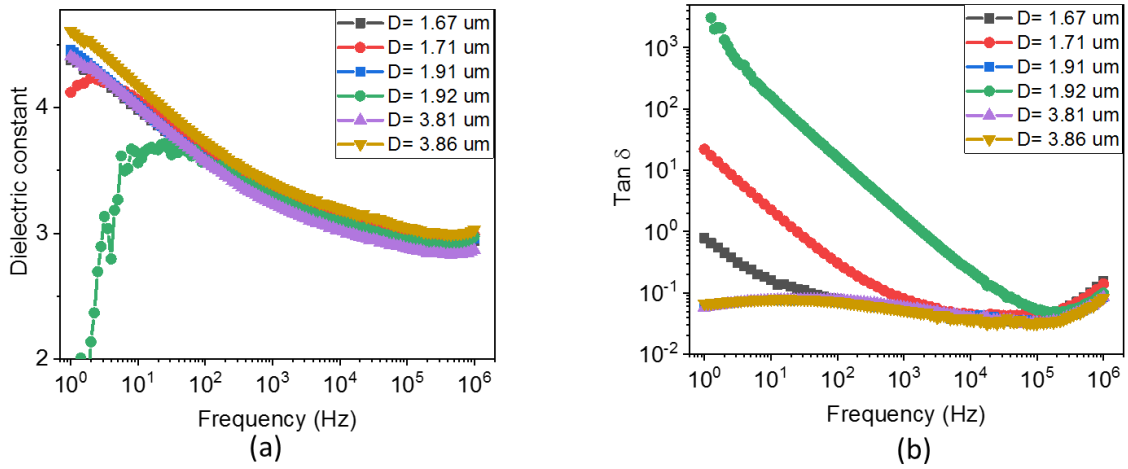

Figure 5.25. Frequency evolution of (a) dielectric constant and (b) loss tangent of Si/SL/NWs/PMMA sample with different PMMA thickness (D)

Cette thèse est accessible à l'adresse : http://theses.insa-lyon.fr/publication/2022LYSEI006/these.pdf
© [X. Zhang], [2022], INSA Lyon, tous droits réservés

General Conclusion

This thesis reported the exploration of enhancing the piezoelectric performance of ZnO-based composites for the potential application of implantable biomedical sensor. In order to achieve flexible, tiny and efficient sensor adopted to low-frequency biological media, the optimization guidelines were developed relying on the best tuning of material properties of individual phases as well as structural design.

Firstly, starting from the basic structure where ZnO particles are randomly embedded into the polymer matrix (PDMS), the conductive, mechanical and dielectric properties were sequentially investigated due to their contributions to the piezoelectric properties. COMSOL simulation allowed to confirm that the field distribution around the fillers was greatly affected by two factors including the filler concentration and the particles connectivity (i.e., aligned or randomly dispersed). A non-linear current density-electric field (J-E) characteristics were obtained under high DC and varying (sinusoidal) field tests. On one hand, DC nonlinear J-E characteristics indicated that the switch field decreases with the increasing filler concentration and dielectrophoretically aligned particles due to the creation of short conduction paths within the matrix. On the other hand, under different sinusoidal field levels, two different conduction mechanisms were illustrated and correlated with respective mathematical analysis models. Nevertheless, the conductivity derived from low voltage excitation the and the nonlinear coefficient extracted from high input voltage manifested the improvement of the conductive properties for composite with large filler content and aligned structuration. Subsequently, an increasing trend of Young's modulus with ZnO volume fraction was verified in the tensile and compression tests, leading an estimation of Young's modulus of ZnO (~163.4 GPa) with the help of Nielsen model. Especially, during the compressive tests, reinforcement along the particle's orientation from structured composites gave rise to improved mechanical properties. Afterwards, dielectric measurements revealed that a higher particle concentration increases dielectric permittivity of composites, especially when particles are aligned along dielectrophoretic direction. This can be explained by the fact that interfacial dipole moments at the ZnO/ZnO interface contribute to an increase in the dielectric constant. Meanwhile, the dielectric constant of ZnO was derived from both analytical models (~125) and COMSOL simulations (~ 250 with γ = 50). At the end, the piezoelectric charge coefficient (d_{33}) of structured composites were found to be much larger with respect to those randomly dispersed owing to the high ZnO/ZnO connectivity. Besides, based on the parameters (Young' modulus, dielectric constant) extracted from previous relevant measurements, the piezoelectric coefficient of the ZnO was predicted in a FEM model ($d_{33}\approx$0.5 pC·N^{-1}) and analytical models ($d_{33}\approx$1.45 pC·N^{-1}) via fitting to the experimental data.

Secondly, the piezoelectric performance can be further improved by adding microrod shape fillers with higher aspect ratio (AR) than the spherical microparticles (MPs). Significant improvement in the piezoelectric behavior of the MRs composite has been successfully achieved via dielectrophoretic alignment of ZnO filler. Additionally, it has been confirmed that the dielectric constant of both MPs and MRs composites can be enhanced by increasing the amplitude or reducing the frequency of dielectrophoretic field. Under the same optimized external electric field (E = 0.6 V/μm, 2 Hz), a six-fold increase in d_{33} was obtained for the aligned MRs composite as opposed to the random one, while a five-fold increase in the case of the MPs counterparts, under the same filler content (8% vol.). In spite of filler structuration (aligned or randomly

Cette thèse est accessible à l'adresse : http://theses.insa-lyon.fr/publication/2022LYSEI006/these.pdf
© [X. Zhang], [2022], INSA Lyon, tous droits réservés

dispersed), composites with MRs fillers exhibit higher piezoelectric response (twofold) than those with spherical fillers.

Thirdly, vertically aligned ZnO NWs were implemented so as to obtain 1-3 structure with optimal AR and perfect full alignment of fillers. By coupling the piezoelectric effect and the electrostatic induction, an insulating layer was stacked on the top of the ZnO NWs and the interstitial polymer between NWs. Starting from a single ZnO NW, both analytical and numerical FEM calculation suggested that operating the aligned NWs structure under the compression excitation had high efficiency compared to the bending model. Optimization strategies were then developed through adjustment of the key parameters such as Young's modules and dielectric constant of the constituent phases, together with density and dimension of NW. Thus, a multi-layer system grown on a rigid resistive Si substrate was firstly characterized in the experiments to identify the function of each layer as well as of the whole complex structure. The effective charge coefficient (d_{33}) of the fabricated composite reached 3.4 pC/N with a 1.5 µm-thick PMMA (11% vol.), as opposed to 0.86 pC/N in case of the 2 µm-thick PMMA counterpart (9.5% vol.), which agreed well with the FEM simulation results. Alternatively, a time varying model combining piezoelectricity and electric circuit modules performed an estimation of d_{33} for the ZnO NWs (16.5 pC/N). Due to the charge leakage effect, a flexible PDMS substrate was replaced the rigid Si one, yielding a lower piezoelectric sensitivity ($d_{33} \approx 0.288$ $pC \cdot N^{-1}$). Accordingly, it can be increased by almost 4 times with post-depositions (Sb-doping and thermal annealing) owning to a decrease in the carrier concentration in ZnO. From the application point of view, the developed structure is revealed to be high promising in implantable biomedical detection, particularly in FFR technique.

This thesis described an entire evolution route about how to boost the piezoelectric sensitivity for ZnO-based composites with specific considerations for medical applications. The result is very promising, confirming that ZnO NW composite, with further benefit of no polarization need, can reach comparable piezoelectric performance regarding conventional alternatives like $BaTiO_3$. In the future, several aspects would be considered as followed:

- conducting more advanced characterization to fully evaluate the piezoelectric performance. For instance, parameters involved to the external mechanical excitation (e.g. frequency and direction) and the external environment, especially the biological media;
- upgrading the flexible structure according to the optimization strategies derived from FEM simulations, such as thinner substrate;
- suppressing the screening effect of semiconductor via decreasing the charges in NWs such as coating a p-type polymer or forming Schottky junction on the ZnO surface;
- coating two metal contacts at the end of ZnO NWs to maximize its piezoelectric effect, by ensuring that at least on end of the NWs is Schottky contact;

Cette thèse est accessible à l'adresse : http://theses.insa-lyon.fr/publication/2022LYSEI006/these.pdf
© [X. Zhang], [2022], INSA Lyon, tous droits réservés

References

[1] J. Curie, P. Curie, Développement par compression de l'électricité polaire dans les cristaux hémièdres à faces inclinées, Bull. La Société Minéralogique Fr. 3 (1880) 90–93. https://doi.org/10.3406/bulmi.1880.1564.

[2] G.W. Taylor, Piezoelectricity, New York, 1985.

[3] J. Valasek, Piezo-Electric and Allied Phenomena in Rochelle Salt, Phys. Rev. 17 (1921) 475–481. https://doi.org/10.1103/PhysRev.17.475.

[4] N. Murayama, K. Nakamura, H. Obara, M. Segawa, The strong piezoelectricity in polyvinylidene fluroide (PVDF), Ultrasonics. 14 (1976) 15–24. https://doi.org/10.1016/0041-624X(76)90067-6.

[5] A. Arnau, D. Soares, Fundamentals of piezoelectricity, Piezoelectric Transducers Appl. (2008) 1–38. https://doi.org/10.1007/978-3-540-77508-9_1.

[6] 176-1987 IEEE Standard on Piezoelectricity., n.d. https://ieeexplore.ieee.org/document/26560 (accessed July 23, 2019).

[7] Z. Wang, X. Pan, Y. He, Y. Hu, H. Gu, Y. Wang, Piezoelectric Nanowires in Energy Harvesting Applications, Adv. Mater. Sci. Eng. 2015 (2015). https://doi.org/10.1155/2015/165631.

[8] H. Khanbareh, Expanding the Functionality of Piezo-Particulate Composites, (2016). https://doi.org/10.4233/UUID:AAB2497D-6EEC-4956-8C15-8F5FDEDC94F3.

[9] J.G. Webster, The measurement, instrumentation, and sensors handbook, 1999.

[10] M. Lines; A. Glass, Principles and applications of ferroelectrics and related materials, Clarendon Press, Oxford, 1979.

[11] K. Uchino, Piezoelectric ceramics for transducers, Ultrason. Transducers Mater. Des. Sensors, Actuators Med. Appl. (2012) 70–116. https://doi.org/10.1533/9780857096302.1.70.

[12] J.S. Wilson, Sensor Technology Handbook, Elsevier Inc., 2005. https://doi.org/10.1016/B978-0-7506-7729-5.X5040-X.

[13] H.D. MEGAW, Crystal structure of barium titanate, Nature. 155 (1945) 484–485.

[14] S. Jiansirisomboon, K. Songsiri, A. Watcharapasorn, T. Tunkasiri, Mechanical properties and crack growth behavior in poled ferroelectric PMN-PZT ceramics, Curr. Appl. Phys. 6 (2006) 299–302. https://doi.org/10.1016/j.cap.2005.11.004.

[15] P.K. Panda, Review: environmental friendly lead-free piezoelectric materials, (n.d.). https://doi.org/10.1007/s10853-009-3643-0.

[16] polymer | Description, Examples, & Types | Britannica, (n.d.). https://www.britannica.com/science/polymer (accessed May 14, 2020).

[17] H. Kawai, The Piezoelectricity of Poly (vinylidene Fluoride), Jpn. J. Appl. Phys. 8 (1969) 975–976. https://doi.org/10.1143/jjap.8.975.

[18] H. Lee, R. Cooper, K. Wang, H. Liang, Nano-Scale Characterization of a Piezoelectric Polymer (Polyvinylidene Difluoride, PVDF), Sensors. 8 (2008) 7359–7368. https://doi.org/10.3390/s8117359.

[19] T.T. Wang, J.M. Herbert, A.M. (Alastair M.. Glass, The Applications of ferroelectric polymers, Blackie, 1988.

Cette thèse est accessible à l'adresse : http://theses.insa-lyon.fr/publication/2022LYSEI006/these.pdf
© [X. Zhang], [2022], INSA Lyon, tous droits réservés

[20] H. Ohigashi, Electromechanical properties of polarized polyvinylidene fluoride films as studied by the piezoelectric resonance method, J. Appl. Phys. 47 (2008) 949. https://doi.org/10.1063/1.322685.

[21] N. Della Schiava, K. Thetpraphi, M.-Q. Le, P. Lermusiaux, A. Millon, J.-F. Capsal, P.-J. Cottinet, Enhanced Figures of Merit for a High-Performing Actuator in Electrostrictive Materials, Polym. 2018, Vol. 10, Page 263. 10 (2018) 263. https://doi.org/10.3390/POLYM10030263.

[22] K. Thetpraphi, M.Q. Le, A. Houachtia, P.J. Cottinet, L. Petit, D. Audigier, J. Kuhn, G. Moretto, J.F. Capsal, Surface Correction Control Based on Plasticized Multilayer P(VDF-TrFE-CFE) Actuator—Live Mirror, Adv. Opt. Mater. 7 (2019) 1900210. https://doi.org/10.1002/adom.201900210.

[23] K. Furusawa, K. Nagashima, C. Anzai, Synthetic process to control the total size and component distribution of multilayer magnetic composite particles, Colloid Polym. Sci. 272 (1994) 1104–1110. https://doi.org/10.1007/BF00652379.

[24] E. Duguet, M. Abboud, F. Morvan, P. Maheu, M. Fontanille, PMMA encapsulation of alumina particles through aqueous suspension polymerisation processes, Macromol. Symp. 151 (2000) 365–370. https://doi.org/10.1002/1521-3900(200002)151:1<365::AID-MASY365>3.0.CO;2-T.

[25] S. Hayashi, K. Fujiki, N. Tsubokawa, Grafting of hyperbranched polymers onto ultrafine silica: Postgraft polymerization of vinyl monomers initiated by pendant initiating groups of polymer chains grafted onto the surface, React. Funct. Polym. 46 (2000) 193–201. https://doi.org/10.1016/S1381-5148(00)00053-5.

[26] M.Q. Le, F. Belhora, A. Cornogolub, P.J. Cottinet, L. Lebrun, A. Hajjaji, Enhanced magnetoelectric effect for flexible current sensor applications, J. Appl. Phys. 115 (2014) 194103. https://doi.org/10.1063/1.4876910.

[27] M.Q. Le, J.F. Capsal, J. Galineau, F. Ganet, X. Yin, M.D. Yang, J.F. Chateaux, L. Renaud, C. Malhaire, P.J. Cottinet, R. Liang, All-organic electrostrictive polymer composites with low driving electrical voltages for micro-fluidic pump applications, Sci. Rep. 5 (2015) 1–13. https://doi.org/10.1038/srep11814.

[28] H. Gong, Y. Zhang, J. Quan, S. Che, Preparation and properties of cement based piezoelectric composites modified by CNTs, Curr. Appl. Phys. 11 (2011) 653–656. https://doi.org/10.1016/J.CAP.2010.10.021.

[29] A.K. Roy, Z. Ahmad, A. Prasad, K. Prasad, Concentration dependent dielectric properties of Barium Titanate / Polyvenylidene Fluoride (PVDF) and, Adv. Mater. Res. 1 (2012) 285–297.

[30] A.S. Tatarenko, V. Gheevarughese, G. Srinivasan, O. V. Antonenkov, M.I. Bichurin, Microwave magnetoelectric effects in ferrite—piezoelectric composites and dual electric and magnetic field tunable filters, J. Electroceramics 2007 241. 24 (2007) 5–9. https://doi.org/10.1007/S10832-007-9382-1.

[31] G. D'Ambrogio, O. Zahhaf, Y. Hebrard, M.Q. Le, P. Cottinet, J. Capsal, Micro-Structuration of Piezoelectric Composites Using Dielectrophoresis: Toward Application in Condition Monitoring of Bearings, Adv. Eng. Mater. (2020) 2000773. https://doi.org/10.1002/adem.202000773.

[32] D. Grinberg, S. Siddique, M.Q. Le, R. Liang, J.F. Capsal, P.J. Cottinet, 4D Printing based piezoelectric composite for medical applications, J. Polym. Sci. Part B Polym. Phys. 57 (2019) 109–115. https://doi.org/10.1002/polb.24763.

[33] Q. Liu, M.Q. Le, C. Richard, R. Liang, P.J. Cottinet, J.F. Capsal, Enhanced pseudo-piezoelectric dynamic force sensors based on inkjet-printed electrostrictive terpolymer, Org. Electron. 67 (2019) 259–271. https://doi.org/10.1016/j.orgel.2019.01.028.

[34] F. Ganet, M.Q. Le, J.F. Capsal, J.F. Gérard, S. Pruvost, J. Duchet-Rumeau, S. Livi, P. Lermusiaux,

Cette thèse est accessible à l'adresse : http://theses.insa-lyon.fr/publication/2022LYSEI006/these.pdf
© [X. Zhang], [2022], INSA Lyon, tous droits réservés

A. Millon, P.J. Cottinet, Haptic feedback using an all-organic electroactive polymer composite, Sensors Actuators, B Chem. 220 (2015) 1120–1130. https://doi.org/10.1016/j.snb.2015.06.071.

[35] D.C. Look, Recent advances in ZnO materials and devices, Mater. Sci. Eng. B. 80 (2001) 383–387. https://doi.org/10.1016/S0921-5107(00)00604-8.

[36] Ü. Özgür, Y.I. Alivov, C. Liu, A. Teke, M.A. Reshchikov, S. Doğan, V. Avrutin, S.-J. Cho, H. Morkoç, A comprehensive review of ZnO materials and devices, J. Appl. Phys. 98 (2005) 041301. https://doi.org/10.1063/1.1992666.

[37] S. Xu, Z.L. Wang, One-dimensional ZnO nanostructures: Solution growth and functional properties, Nano Res. 4 (2011) 1013–1098. https://doi.org/10.1007/s12274-011-0160-7.

[38] M.S. Arnold, P. Avouris, Z.W. Pan, Z.L. Wang, Field-effect transistors based on single semiconducting oxide nanobelts, J. Phys. Chem. B. 107 (2003) 659–663. https://doi.org/10.1021/jp0271054.

[39] M.H. Huang, S. Mao, H. Feick, H. Yan, Y. Wu, H. Kind, E. Weber, R. Russo, P. Yang, Room-temperature ultraviolet nanowire nanolasers, Science (80-.). 292 (2001) 1897–1899. https://doi.org/10.1126/science.1060367.

[40] A.O. Govorov, H.H. Richardson, C. Soci, A. Zhang, B. Xiang, S.A. Dayeh, D.P.R. Aplin, J. Park, X.Y. Bao, Y.H. Lo, D. Wang, ZnO nanowire UV photodetectors with high internal gain, Nano Lett. 7 (2007) 30–38. https://doi.org/10.1021/nl070111x.

[41] W.I. Park, G.-C. Yi, Electroluminescence in n-ZnO Nanorod Arrays Vertically Grown on p-GaN, Adv. Mater. 16 (2004) 87–90. https://doi.org/10.1002/adma.200305729.

[42] M. Law, L.E. Greene, J.C. Johnson, R. Saykally, P. Yang, Nanowire dye-sensitized solar cells, Nat. Mater. 4 (2005) 455–459. https://doi.org/10.1038/nmat1387.

[43] Z. Li, R. Yang, M. Yu, F. Bai, C. Li, Z.L. Wang, Cellular level biocompatibility and biosafety of ZnO nanowires, J. Phys. Chem. C. 112 (2008) 20114–20117. https://doi.org/10.1021/jp808878p.

[44] J. Zhou, N. Xu, Z.L. Wang, Dissolving behavior and stability of ZnO wires in biofluids: A study on biodegradability and biocompatibility of ZnO nanostructures, Adv. Mater. 18 (2006) 2432–2435. https://doi.org/10.1002/adma.200600200.

[45] S.B. Kulkarni, U.M. Patil, R.R. Salunkhe, S.S. Joshi, C.D. Lokhande, Temperature impact on morphological evolution of ZnO and its consequent effect on physico-chemical properties, J. Alloys Compd. 509 (2011) 3486–3492. https://doi.org/10.1016/J.JALLCOM.2010.12.036.

[46] H. Morkoç, Ü. Özgür, General Properties of ZnO, 2009. https://doi.org/10.1002/9783527623945.ch1.

[47] Z.L. Wang, ZnO nanowire and nanobelt platform for nanotechnology, Mater. Sci. Eng. R Reports. 64 (2009) 33–71. https://doi.org/10.1016/J.MSER.2009.02.001.

[48] P.W. Tasker, The stability of ionic crystal surfaces, J. Phys. C Solid State Phys. 12 (1979) 4977. https://doi.org/10.1088/0022-3719/12/22/036.

[49] V. Consonni, A.M. Lord, Polarity in ZnO nanowires: A critical issue for piezotronic and piezoelectric devices, Nano Energy. 83 (2021) 105789. https://doi.org/10.1016/j.nanoen.2021.105789.

[50] What It Is and How It Works | National Nanotechnology Initiative, (n.d.). https://www.nano.gov/nanotech-101/what (accessed October 5, 2021).

[51] Z.L. Wang, Zinc oxide nanostructures : growth , properties and applications, 16 (2004) 829–858. https://doi.org/10.1088/0953-8984/16/25/R01.

Cette thèse est accessible à l'adresse : http://theses.insa-lyon.fr/publication/2022LYSEI006/these.pdf
© [X. Zhang], [2022], INSA Lyon, tous droits réservés

[52] M. Fu, D. Pan, Y. Yang, T. Shi, Z. Zhang, J. Zhao, H.Q. Xu, Q. Chen, Electrical characteristics of field-effect transistors based on indium arsenide nanowire thinner than 10 nm, Appl. Phys. Lett. 105 (2014) 143101. https://doi.org/10.1063/1.4897496.

[53] M.-R. He, Y. Shi, W. Zhou, J.W. Chen, Y.J. Yan, J. Zhu, Diameter dependence of modulus in zinc oxide nanowires and the effect of loading mode: In situ experiments and universal core-shell approach, Appl. Phys. Lett. 95 (2009) 091912. https://doi.org/10.1063/1.3205102.

[54] C.Q. Chen, Y. Shi, Y.S. Zhang, J. Zhu, Y.J. Yan, Size Dependence of Young ' s Modulus in ZnO Nanowires, 075505 (2006) 1–4. https://doi.org/10.1103/PhysRevLett.96.075505.

[55] A. V. Desai, M.A. Haque, Mechanical properties of ZnO nanowires, Sensors Actuators, A Phys. 134 (2007) 169–176. https://doi.org/10.1016/j.sna.2006.04.046.

[56] R. Agrawal, H.D. Espinosa, Giant piezoelectric size effects in zinc oxide and gallium nitride nanowires. A first principles investigation, Nano Lett. 11 (2011) 786–790. https://doi.org/10.1021/nl104004d.

[57] J. Hong, D. Fang, Systematic study of the ferroelectric properties of Pb(Zr0.5Ti0.5)O3 nanowires, J. Appl. Phys. 104 (2008) 064118. https://doi.org/10.1063/1.2982090.

[58] Y. Zhang, J. Hong, B. Liu, D. Fang, Strain effect on ferroelectric behaviors of BaTiO3 nanowires: A molecular dynamics study, Nanotechnology. 21 (2010). https://doi.org/10.1088/0957-4484/21/1/015701.

[59] M. Riaz, J. Song, O. Nur, Z.L. Wang, M. Willander, Study of the piezoelectric power generation of ZnO nanowire arrays grown by different methods, Adv. Funct. Mater. 21 (2011) 628–633. https://doi.org/10.1002/adfm.201001203.

[60] Z.L. Wang, J. Song, Piezoelectric nanogenerators based on zinc oxide nanowire arrays, Science (80-.). 312 (2006) 242–246. https://doi.org/10.1126/science.1124005.

[61] P.X. Gao, J. Song, J. Liu, Z.L. Wang, Nanowire piezoelectric nanogenerators on plastic substrates as flexible power sources for nanodevices, Adv. Mater. 19 (2007) 67–72. https://doi.org/10.1002/adma.200601162.

[62] † Min-Hua Zhao, ‡ and Zhong-Lin Wang, † Scott X. Mao*, Piezoelectric Characterization of Individual Zinc Oxide Nanobelt Probed by Piezoresponse Force Microscope, (2004). https://doi.org/10.1021/NL035198A.

[63] D.A. Scrymgeour, J.W.P. Hsu, Correlated Piezoelectric and Electrical Properties in Individual ZnO Nanorods, Nano Lett. 8 (2008) 2204–2209. https://doi.org/10.1021/NL080704N.

[64] J.A. Christman, R.R. Woolcott, A.I. Kingon, R.J. Nemanich, Piezoelectric measurements with atomic force microscopy, Appl. Phys. Lett. 73 (1998) 3851–3853. https://doi.org/10.1063/1.122914.

[65] H.J. Fan, W. Lee, R. Hauschild, M. Alexe, G. Le Rhun, R. Scholz, A. Dadgar, K. Nielsch, H. Kalt, A. Krost, M. Zacharias, U. Gösele, Template-assisted large-scale ordered arrays of ZnO pillars for optical and piezoelectric applications, Small. 2 (2006) 561–568. https://doi.org/10.1002/smll.200500331.

[66] M. Minary-Jolandan, R.A. Bernal, I. Kuljanishvili, V. Parpoil, H.D. Espinosa, Individual GaN Nanowires Exhibit Strong Piezoelectricity in 3D, (2011). https://doi.org/10.1021/nl204043y.

[67] Zhaoyu Wang, Jie Hu, Abhijit P. Suryavanshi, and Kyungsuk Yum, M.-F. Yu*, Voltage Generation from Individual BaTiO3 Nanowires under Periodic Tensile Mechanical Load, Nano Lett. 7 (2007) 2966–2969. https://doi.org/10.1021/NL070814E.

[68] R. Steinhausen, T. Hauke, H. Beige, W. Watzka, U. Lange, D. Sporn, S. Gebhardt, A. Schönecker,

Cette thèse est accessible à l'adresse : http://theses.insa-lyon.fr/publication/2022LYSEI006/these.pdf
© [X. Zhang], [2022], INSA Lyon, tous droits réservés

Properties of fine scale piezoelectric PZT fibers with different Zr content, J. Eur. Ceram. Soc. 21 (2001) 1459–1462. https://doi.org/10.1016/S0955-2219(01)00041-3.

[69] V. Cauda, B. Torre, A. Falqui, G. Canavese, S. Stassi, T. Bein, M. Pizzi, Confinement in oriented mesopores induces piezoelectric behavior of polymeric nanowires, Chem. Mater. 24 (2012) 4215–4221. https://doi.org/10.1021/cm302594s.

[70] Z.L. Wang, Z.W. Pan, Z.R. Dai, Structures of Oxide Nanobelts and Nanowires, Microsc. Microanal. 8 (2002) 467–474. https://doi.org/10.1017/S1431927602010383.

[71] R.A. Laudise, A.A. Ballman, HYDROTHERMAL SYNTHESIS OF ZINC OXIDE AND ZINC SULFIDE1, J. Phys. Chem. 64 (2002) 688–691. https://doi.org/10.1021/J100834A511.

[72] M.A. Vergés, A. Mifsud, C.J. Serna, Formation of rod-like zinc oxide microcrystals in homogeneous solutions, J. Chem. Soc. Faraday Trans. 86 (1990) 959–963. https://doi.org/10.1039/FT9908600959.

[73] Y. Sun, G.M. Fuge, M.N.R. Ashfold, Growth of aligned ZnO nanorod arrays by catalyst-free pulsed laser deposition methods, Chem. Phys. Lett. 396 (2004) 21–26. https://doi.org/10.1016/J.CPLETT.2004.07.110.

[74] D. Lin, W. Pan, H. Wu, Morphological Control of Centimeter Long Aluminum-Doped Zinc Oxide Nanofibers Prepared by Electrospinning, J. Am. Ceram. Soc. 90 (2007) 71–76. https://doi.org/10.1111/J.1551-2916.2006.01366.X.

[75] L. Vayssieres, Growth of Arrayed Nanorods and Nanowires of ZnO from Aqueous Solutions, Adv. Mater. 15 (2003) 464–466. https://doi.org/10.1002/adma.200390108.

[76] S. Xu, C. Lao, B. Weintraub, Z.L. Wang, Density-controlled growth of aligned ZnO nanowire arrays by seedles chemical approach on smooth surfaces, J. Mater. Res. 23 (2008) 2072–2077. https://doi.org/10.1557/jmr.2008.0274.

[77] X. Li, M. Sun, X. Wei, C. Shan, Q. Chen, 1D piezoelectric material based nanogenerators: Methods, materials and property optimization, Nanomaterials. 8 (2018). https://doi.org/10.3390/nano8040188.

[78] S. Dai, M.L. Dunn, H.S. Park, Piezoelectric constants for ZnO calculated using classical polarizable core–shellpotentials, Nanotechnology. 21 (2010) 445707. https://doi.org/10.1088/0957-4484/21/44/445707.

[79] R.E. Newnham, D.P. Skinner, L.E. Cross, Connectivity and piezoelectric-pyroelectric composites, Mater. Res. Bull. 13 (1978) 525–536. https://doi.org/10.1016/0025-5408(78)90161-7.

[80] I. Babu, G. de With, Highly flexible piezoelectric 0-3 PZT-PDMS composites with high filler content, Compos. Sci. Technol. 91 (2014) 91–97. https://doi.org/10.1016/j.compscitech.2013.11.027.

[81] C.K. Wong, F.G. Shin, Effect of electrical conductivity on poling and the dielectric, pyroelectric and piezoelectric properties of ferroelectric 0–3 composites, Front. Ferroelectr. A Spec. Issue J. Mater. Sci. (2006) 229–249. https://doi.org/10.1007/978-0-387-38039-1_21.

[82] Y.T. Or, C.K. Wong, B. Ploss, F.G. Shin, Modeling of poling, piezoelectric, and pyroelectric properties of ferroelectric 0–3 composites, J. Appl. Phys. 94 (2003) 3319. https://doi.org/10.1063/1.1596718.

[83] X. Renxin, C. Wen, Z. Jing, L. Yueming, S. Huajun, Dielectric and piezoelectric properties of 0-3 PZT/PVDF composite doped with polyaniline, J. Wuhan Univ. Technol. Sci. Ed. 2006 211. 21 (2006) 84–87. https://doi.org/10.1007/BF02861478.

[84] A. Safari, Development of piezoelectric composites for transducers, J. Phys. III. 4 (1994) 1129–1149. https://doi.org/10.1051/jp3:1994191.

[85] D.A. Van Den Ende, B.F. Bory, W.A. Groen, S. Van Der Zwaag, Improving the d33 and g33

Cette thèse est accessible à l'adresse : http://theses.insa-lyon.fr/publication/2022LYSEI006/these.pdf
© [X. Zhang], [2022], INSA Lyon, tous droits réservés

properties of 0-3 piezoelectric composites by dielectrophoresis, J. Appl. Phys. 107 (2010) 0–8. https://doi.org/10.1063/1.3291131.

[86] T. Yamada, T. Ueda, T. Kitayama, Piezoelectricity of a high-content lead zirconate titanate/polymer composite, J. Appl. Phys. 53 (1982) 4328–4332. https://doi.org/10.1063/1.331211.

[87] D.Y. Wang, K. Li, H.L.W. Chan, High frequency 1-3 composite transducer fabricated using sol-gel derived lead-free BNBT fibers, Sensors Actuators, A Phys. 114 (2004) 1–6. https://doi.org/10.1016/j.sna.2004.02.024.

[88] A. Abrar, D. Zhang, B. Su, T.W. Button, K.J. Kirk, S. Cochran, 1-3 Connectivity piezoelectric ceramic-polymer composite transducers made with viscous polymer processing for high frequency ultrasound, in: Ultrasonics, 2004: pp. 479–484. https://doi.org/10.1016/j.ultras.2004.02.008.

[89] C.P. Bowen, R.E. Newnham, C.A. Randall, Dielectric properties of dielectrophoretically assembled particulate-polymer composites, J. Mater. Res. 13 (1998) 205–210. https://doi.org/10.1557/JMR.1998.0027.

[90] N.K. James, D.B. Deutz, R.K. Bose, S. van der Zwaag, P. Groen, High Piezoelectric Voltage Coefficient in Structured Lead-Free (K,Na,Li)NbO_3 Particulate-Epoxy Composites, J. Am. Ceram. Soc. 99 (2016) 3957–3963. https://doi.org/10.1111/jace.14428.

[91] A. Al Masud, N. D'Souza, P. Von Lockette, Z. Ounaies, On the dielectrophoretic and magnetic alignment of magnetoactive barium hexaferrite-pdms nanocomposites, ASME 2017 Conf. Smart Mater. Adapt. Struct. Intell. Syst. SMASIS 2017. 1 (2017). https://doi.org/10.1115/SMASIS2017-3988.

[92] C. Park, Z. Ounaies, K.A. Watson, R.E. Crooks, J. Smith, S.E. Lowther, J.W. Connell, E.J. Siochi, J.S. Harrison, T.L. St Clair, Dispersion of single wall carbon nanotubes by in situ polymerization under sonication, Chem. Phys. Lett. 364 (2002) 303–308. https://doi.org/10.1016/S0009-2614(02)01326-X.

[93] L. An, C.R. Friedrich, Process parameters and their relations for the dielectrophoretic assembly of carbon nanotubes, J. Appl. Phys. 105 (2009). https://doi.org/10.1063/1.3093975.

[94] M.A. Al Masud, Z. Ounaies, Dielectric properties of dielectrophoretically aligned ZNO-PDMS composites, in: ASME 2016 Conf. Smart Mater. Adapt. Struct. Intell. Syst. SMASIS 2016, American Society of Mechanical Engineers, 2016. https://doi.org/10.1115/SMASIS2016-9128.

[95] X. Zhang, M.Q. Le, O. Zahhaf, J.F. Capsal, P.J. Cottinet, L. Petit, Enhancing dielectric and piezoelectric properties of micro-ZnO/PDMS composite-based dielectrophoresis, Mater. Des. 192 (2020) 108783. https://doi.org/10.1016/j.matdes.2020.108783.

[96] J. He, Introduction of Varistor Ceramics, Met. Oxide Varistors. (2019) 1–30. https://doi.org/10.1002/9783527684038.ch1.

[97] M. Oxide, Z.V. Ceramics, Metal Oxide ZnO-Based Varistor Ceramics, (n.d.).

[98] M.M. Saadeldin, O.A. Desouky, M. Ibrahim, G.E. Khalil, Investigation of structural and electrical properties of ZnO varistor samples doped with different additives, NRIAG J. Astron. Geophys. 7 (2019) 201–207. https://doi.org/10.1016/j.nrjag.2018.06.002.

[99] S. Ishibe, M. Mori, M. Kozako, A New Concept Varistor With Epoxy / Microvaristor Composite, 29 (2014) 677–682.

[100] K. Eda, Zinc Oxide Varistors, IEEE Electr. Insul. Mag. 5 (1989) 28–30. https://doi.org/10.1109/57.44606.

[101] L. Donzel, F. Greuter, T. Christen, Nonlinear resistive electric field grading part 2: Materials and

Cette thèse est accessible à l'adresse : http://theses.insa-lyon.fr/publication/2022LYSEI006/these.pdf
© [X. Zhang], [2022], INSA Lyon, tous droits réservés

applications, IEEE Electr. Insul. Mag. 27 (2011) 18–29. https://doi.org/10.1109/MEI.2011.5739419.

[102] D. Weida, C. Richter, M. Clemens, Design of ZnO microvaristor material stress-cone for cable accessories, IEEE Trans. Dielectr. Electr. Insul. 18 (2011) 1262–1267. https://doi.org/10.1109/TDEI.2011.5976125.

[103] K.P. Donnelly, B.R. Varlow, Non-linear dc and ac conductivity in electrically insulating composites, IEEE Trans. Dielectr. Electr. Insul. 10 (2003) 610–614. https://doi.org/10.1109/TDEI.2003.1219645.

[104] C.C. Lin, W.S. Lee, C.C. Sun, W.H. Whu, A varistor-polymer composite with nonlinear electrical-thermal switching properties, Ceram. Int. 34 (2008) 131–136. https://doi.org/10.1016/j.ceramint.2006.09.018.

[105] F. Chiu, A Review on Conduction Mechanisms in Dielectric Films, 2014 (2014).

[106] F.C. Chiu, C.Y. Lee, T.M. Pan, Current conduction mechanisms in Pr2 O3 /oxynitride laminated gate dielectrics, J. Appl. Phys. 105 (2009) 074103. https://doi.org/10.1063/1.3103282.

[107] Z. Yang, J. Zu, Comparison of PZN-PT, PMN-PT single crystals and PZT ceramic for vibration energy harvesting, Energy Convers. Manag. 122 (2016) 321–329. https://doi.org/10.1016/j.enconman.2016.05.085.

[108] P. Kramar, D. Miklavčič, L.M. Mir, Electroporation-based Technologies and Treatments Proceedings of the Electroporation-based Technologies and Treatments International SCIENTIFIC WORKSHOP and POSTGRADUATE COURSE, n.d. www.ebtt.org (accessed February 1, 2021).

[109] F.D. Ramirez, V.Y. Reddy, R. Viswanathan, M. Hocini, P. Jaïs, Emerging Technologies for Pulmonary Vein Isolation, Circ. Res. 127 (2020) 170–183. https://doi.org/10.1161/CIRCRESAHA.120.316402.

[110] V.Y. Reddy, P. Neuzil, J.S. Koruth, J. Petru, M. Funosako, H. Cochet, L. Sediva, M. Chovanec, S.R. Dukkipati, P. Jais, Pulsed Field Ablation for Pulmonary Vein Isolation in Atrial Fibrillation, J. Am. Coll. Cardiol. 74 (2019) 315–326. https://doi.org/10.1016/j.jacc.2019.04.021.

[111] X. Jing, Z. Guo, Fabrication of biocompatible super stable lubricant-immobilized slippery surfaces by grafting a polydimethylsiloxane brush: Excellent boiling water resistance, hot liquid repellency and long-term slippery stability, Nanoscale. 11 (2019) 8870–8881. https://doi.org/10.1039/c9nr01556f.

[112] Y. Chen, W.H. Tse, L. Chen, J. Zhang, Ag nanoparticles-decorated ZnO nanorod array on a mechanical flexible substrate with enhanced optical and antimicrobial properties, Nanoscale Res. Lett. 10 (2015) 106. https://doi.org/10.1186/s11671-014-0712-3.

[113] S. Jakmuangpak, T. Prada, W. Mongkolthanaruk, V. Harnchana, S. Pinitsoontorn, Engineering Bacterial Cellulose Films by Nanocomposite Approach and Surface Modification for Biocompatible Triboelectric Nanogenerator, ACS Appl. Electron. Mater. 2 (2020) 2498–2506. https://doi.org/10.1021/acsaelm.0c00421.

[114] Y. Ateş, C.A. Yücesoy, M.A. Ünlü, B. Saygin, N. Akkaş, The Mechanical Properties of Intact and Traumatized Epidural Catheters, Anesth. Analg. 90 (2000) 393. https://doi.org/10.1213/00000539-200002000-00029.

[115] L. Blanc, A. Delchambre, P. Lambert, Flexible medical devices: Review of controllable stiffness solutions, Actuators. 6 (2017). https://doi.org/10.3390/act6030023.

[116] Y. Shirasaki, K. Yoshizawa, T. Tateishi, Changes in the mechanical properties of silicone catheter in degrading process, Nihon Reoroji Gakkaishi. 29 (2001) 9–13. https://doi.org/10.1678/rheology.29.9.

Cette thèse est accessible à l'adresse : http://theses.insa-lyon.fr/publication/2022LYSEI006/these.pdf
© [X. Zhang], [2022], INSA Lyon, tous droits réservés

[117] A.S. Barnett, T.D. Bahnson, J.P. Piccini, Recent Advances in Lesion Formation for Catheter Ablation of Atrial Fibrillation, Circ. Arrhythmia Electrophysiol. 9 (2016). https://doi.org/10.1161/CIRCEP.115.003299.

[118] A. Aryana, S.M. Singh, G. Mugnai, C. de Asmundis, M. Kowalski, D.K. Pujara, A.I. Cohen, S.K. Singh, C.E. Fuenzalida, N. Prager, M.R. Bowers, P.G. O'Neill, P. Brugada, A. d'Avila, G.B. Chierchia, Pulmonary vein reconnection following catheter ablation of atrial fibrillation using the second-generation cryoballoon versus open-irrigated radiofrequency: results of a multicenter analysis, J. Interv. Card. Electrophysiol. 47 (2016) 341–348. https://doi.org/10.1007/s10840-016-0172-z.

[119] C. Falconi, G. Mantini, A. D'Amico, Z.L. Wang, Studying piezoelectric nanowires and nanowalls for energy harvesting, Sensors Actuators, B Chem. 139 (2009) 511–519. https://doi.org/10.1016/j.snb.2009.02.071.

[120] Y. Li, Z. Çelik-Butler, D.P. Butler, An integrated piezoelectric zinc oxide nanowire micro-energy harvester, Nano Energy. 26 (2016) 456–465. https://doi.org/10.1016/j.nanoen.2016.05.008.

[121] K.Y. Lee, B. Kumar, J.S. Seo, K.H. Kim, J.I. Sohn, S.N. Cha, D. Choi, Z.L. Wang, S.W. Kim, P-type polymer-hybridized high-performance piezoelectric nanogenerators, Nano Lett. 12 (2012) 1959–1964. https://doi.org/10.1021/nl204440g.

[122] R. Tao, M. Parmar, G. Ardila, P. Oliveira, D. Marques, L. Montès, M. Mouis, Performance of ZnO based piezo-generators under controlled compression, Semicond. Sci. Technol. 32 (2017) 64003. https://doi.org/10.1088/1361-6641/aa691f.

[123] R. Yang, Y. Qin, L. Dai, Z.L. Wang, Power generation with laterally packaged piezoelectric fine wires, Nat. Nanotechnol. 4 (2009) 34–39. https://doi.org/10.1038/nnano.2008.314.

[124] S. Xu, Y. Qin, C. Xu, Y. Wei, R. Yang, Z.L. Wang, Self-powered nanowire devices, Nat. Nanotechnol. 5 (2010) 366–373. https://doi.org/10.1038/nnano.2010.46.

[125] Y. Hu, C. Xu, Y. Zhang, L. Lin, R.L. Snyder, Z.L. Wang, A nanogenerator for energy harvesting from a rotating tire and its application as a self-powered pressure/speed sensor, Adv. Mater. 23 (2011) 4068–4071. https://doi.org/10.1002/adma.201102067.

[126] N.H.J. Pijls, B. De Bruyne, Coronary pressure measurement and fractional flow reserve, (n.d.).

[127] System and method for FFR guidewire recovery, (2014).

[128] N.H.J. Pijls, B. de Bruyne, K. Peels, P.H. van der Voort, H.J.R.M. Bonnier, J. Bartunek, J.J. Koolen, Measurement of Fractional Flow Reserve to Assess the Functional Severity of Coronary-Artery Stenoses, Http://Dx.Doi.Org/10.1056/NEJM199606273342604. 334 (2009) 1703–1708. https://doi.org/10.1056/NEJM199606273342604.

[129] G. D'Ambrogio, O. Zahhaf, M. Bordet, M.Q. Le, N. Della Schiava, R. Liang, P.-J. Cottinet, J.-F. Capsal, Structuring BaTiO3 /PDMS Nanocomposite via Dielectrophoresis for Fractional Flow Reserve Measurement, Adv. Eng. Mater. (2021) 2100341. https://doi.org/10.1002/ADEM.202100341.

[130] T. Sharma, K. Aroom, S. Naik, B. Gill, J.X.J. Zhang, Flexible Thin-Film PVDF-TrFE Based Pressure Sensor for Smart Catheter Applications, (n.d.). https://doi.org/10.1007/s10439-012-0708-z.

[131] C. Pouillot, S. Fournier, J. Glasenapp, G. Rambaud, K. Bougrini, R. Vi Fane, C. Geyer, J. Adjedj, Pressure wire versus microcatheter for FFR measurement: A head-to-head comparison, Arch. Cardiovasc. Dis. Suppl. 10 (2018) 25–26. https://doi.org/10.1016/J.ACVDSP.2017.11.048.

[132] B.C. Reuben, M.G. Whitten, M. Sarfati, L.W. Kraiss, Increasing use of endovascular therapy in acute arterial injuries: Analysis of the National Trauma Data Bank, J. Vasc. Surg. 46 (2007) 1222-1226.e2.

Cette thèse est accessible à l'adresse : http://theses.insa-lyon.fr/publication/2022LYSEI006/these.pdf
© [X. Zhang], [2022], INSA Lyon, tous droits réservés

https://doi.org/10.1016/J.JVS.2007.08.023.

[133] P. Rheaume, J. Chen, P. Casey, Open vs endovascular repair of blunt traumatic thoracic aortic injuries, J. Vasc. Surg. 51 (2010) 763–769. https://doi.org/10.1016/J.JVS.2009.12.014.

[134] Z. Wang, Nanogenerators for self-powered devices and systems, 2011. http://smartech.gatech.edu/handle/1853/39262.

[135] R. Yang, Y. Qin, C. Li, G. Zhu, Z.L. Wang, Converting biomechanical energy into electricity by a muscle-movement- driven nanogenerator, Nano Lett. 9 (2009) 1201–1205. https://doi.org/10.1021/nl803904b.

[136] Y. Mao, Y. Zhu, T. Zhao, C. Jia, M. Bian, X. Li, Y. Liu, B. Liu, A portable and flexible self-powered multifunctional sensor for real-time monitoring in swimming, Biosensors. 11 (2021) 1–11. https://doi.org/10.3390/bios11050147.

[137] S. Lee, R. Hinchet, Y. Lee, Y. Yang, Z.-H. Lin, G. Ardila, L. Montès, M. Mouis, Z.L. Wang, Ultrathin Nanogenerators as Self-Powered/Active Skin Sensors for Tracking Eye Ball Motion, Adv. Funct. Mater. 24 (2014) 1163–1168. https://doi.org/10.1002/adfm.201301971.

[138] Z. Li, G. Zhu, R. Yang, A.C. Wang, Z.L. Wang, Muscle-driven in vivo nanogenerator, Adv. Mater. 22 (2010) 2534–2537. https://doi.org/10.1002/adma.200904355.

[139] Z.L. Wang, Progress in piezotronics and piezo-phototronics, Adv. Mater. 24 (2012) 4632–4646. https://doi.org/10.1002/adma.201104365.

[140] † Xudong Wang, †,‡ Jun Zhou, † Jinhui Song, † Jin Liu, ‡ and Ningsheng Xu, † Zhong L. Wang*, Piezoelectric Field Effect Transistor and Nanoforce Sensor Based on a Single ZnO Nanowire, Nano Lett. 6 (2006) 2768–2772. https://doi.org/10.1021/NL061802G.

[141] J.H. He, C.L. Hsin, J. Liu, L.J. Chen, Z.L. Wang, Piezoelectric Gated Diode of a Single ZnO Nanowire, Adv. Mater. 19 (2007) 781–784. https://doi.org/10.1002/ADMA.200601908.

[142] Q. Yang, W. Wang, S. Xu, Z.L. Wang, Enhancing Light Emission of ZnO Microwire-Based Diodes by Piezo-Phototronic Effect, Nano Lett. 11 (2011) 4012–4017. https://doi.org/10.1021/NL202619D.

[143] Zinc Oxide ZnO MicroPowder, ZnO, 99.9+%, (n.d.). https://www.us-nano.com/inc/sdetail/734 (accessed June 11, 2021).

[144] SYLGARD™ 184 Silicone Elastomer Kit | Dow Inc., (n.d.). https://www.dow.com/en-us/pdp.sylgard-184-silicone-elastomer-kit.01064291z.html (accessed June 11, 2021).

[145] Y. Zhang, V. Perrin, L. Seveyrat, L. Lebrun, On a better understanding of the electromechanical coupling in electroactive polyurethane, Smart Mater. Struct. 29 (2020) 055007. https://doi.org/10.1088/1361-665X/AB7947.

[146] Y. Zhang, L. Seveyrat, L. Lebrun, Correlation between dielectric, mechanical properties and electromechanical performance of functionalized graphene / polyurethane nanocomposites, Compos. Sci. Technol. 211 (2021) 108843. https://doi.org/10.1016/J.COMPSCITECH.2021.108843.

[147] H.A. Pohl, J.S. Crane, Dielectrophoresis of Cells, Biophys. J. 11 (1971) 711–727. https://doi.org/10.1016/S0006-3495(71)86249-5.

[148] R. Pethig, G.H. Markx, Applications of dielectrophoresis in biotechnology, Trends Biotechnol. 15 (1997) 426–432. https://doi.org/10.1016/S0167-7799(97)01096-2.

[149] K. Khoshmanesh, S. Nahavandi, S. Baratchi, A. Mitchell, K. Kalantar-zadeh, Biosensors and Bioelectronics Dielectrophoretic platforms for bio-microfluidic systems, Biosens. Bioelectron. 26 (2011) 1800–1814. https://doi.org/10.1016/j.bios.2010.09.022.

Cette thèse est accessible à l'adresse : http://theses.insa-lyon.fr/publication/2022LYSEI006/these.pdf
© [X. Zhang], [2022], INSA Lyon, tous droits réservés

[150] H. Zhang, H. Chang, P. Neuzil, DEP-on-a-Chip : Dielectrophoresis Applied to Microfluidic Platforms, (2019) 1–22.

[151] S.A. Wilson, R.W. Whatmore, ELECTRIC-FIELD STRUCTURING OF PIEZOELECTRIC COMPOSITE MATERIALS, Cranfield University, 1999. http://dspace.lib.cranfield.ac.uk/handle/1826/3373 (accessed June 21, 2021).

[152] R.E. Randall, C. A., Bowen, C. P., Shrout, T. R., Messing, G. L., Newnham, Dielectrophoretic assembly: a novel concept in advanced composite fabrication, Proc. 4th Int. Conf. Electrorheological Fluids. World Sci. (1994) 516–25.

[153] S.A. Wilson, G.M. Maistros, R.W. Whatmore, Structure modification of 0-3 piezoelectric ceramic/polymer composites through dielectrophoresis, J. Phys. D. Appl. Phys. 38 (2005) 175–182. https://doi.org/10.1088/0022-3727/38/2/001.

[154] T.B. Jones, Electromechanics of Particles, Cambridge University Press, 1995. https://doi.org/10.1017/cbo9780511574498.

[155] AC electrokinetics: colloids and nanoparticles - Enlighten: Publications, (n.d.). https://eprints.gla.ac.uk/33024/ (accessed June 24, 2021).

[156] N. Siva Kumar Gunda, S. Bhattacharjee, S.K. Mitra, Study on the use of dielectrophoresis and electrothermal forces to produce on-chip micromixers and microconcentrators, Biomicrofluidics. 6 (2012). https://doi.org/10.1063/1.4749827.

[157] F. Pedroli, A. Flocchini, A. Marrani, M.Q. Le, O. Sanseau, P.J. Cottinet, J.F. Capsal, Boosted energy-storage efficiency by controlling conduction loss of multilayered polymeric capacitors, Mater. Des. 192 (2020) 108712. https://doi.org/10.1016/j.matdes.2020.108712.

[158] C.Y. Liu, A.J. Bard, Pressure-induced insulator-conductor transition in a photoconducting organic liquid-crystal film, Nature. 418 (2002) 162–164. https://doi.org/10.1038/nature00875.

[159] H. Ahmad, A. Haddad, H. Griffiths, S. Robson, T. Nishimura, N. Tsukamoto, Electrical characterisation of ZnO microvaristor materials and compounds, in: Annu. Rep. - Conf. Electr. Insul. Dielectr. Phenomena, CEIDP, Institute of Electrical and Electronics Engineers Inc., 2015: pp. 688–692. https://doi.org/10.1109/CEIDP.2015.7352035.

[160] S. Del Gobbo, J. Poolwong, V. D'Elia, M. Ogawa, Simultaneous Controlled Seeded-Growth and Doping of ZnO Nanorods with Aluminum and Cerium: Feasibility Assessment and Effect on Photocatalytic Activity, Cryst. Growth Des. 20 (2020) 5508–5525. https://doi.org/10.1021/ACS.CGD.0C00694.

[161] K.J. Loh, D. Chang, Zinc oxide nanoparticle-polymeric thin films for dynamic strain sensing, J. Mater. Sci. 46 (2011) 228–237. https://doi.org/10.1007/s10853-010-4940-3.

[162] A. Sihvola, Mixing Rules with Complex Dielectric Coefficients, Subsurf. Sens. Technol. Appl. 1 (2000) 393–415. https://doi.org/10.1023/A:1026511515005.

[163] K. Goc, K. Gaska, K. Klimczyk, A. Wujek, W. Prendota, L. Jarosinski, A. Rybak, G. Kmita, C. Kapusta, Influence of magnetic field-aided filler orientation on structure and transport properties of ferrite filled composites, J. Magn. Magn. Mater. 419 (2016) 345–353. https://doi.org/10.1016/j.jmmm.2016.06.046.

[164] H. Khanbareh, S. Van Der Zwaag, W.A. Groen, Effect of dielectrophoretic structuring on piezoelectric and pyroelectric properties of lead titanate-epoxy composites, Smart Mater. Struct. 23 (2014). https://doi.org/10.1088/0964-1726/23/10/105030.

[165] X. Yang, X. Zhao, H. Jinliang, Grading Electric Field in High Voltage Insulation Using Composite Materials, (2018). https://doi.org/10.1109/MEI.2018.8246118.

Cette thèse est accessible à l'adresse : http://theses.insa-lyon.fr/publication/2022LYSEI006/these.pdf
© [X. Zhang], [2022], INSA Lyon, tous droits réservés

[166] X. Yang, J. Hu, S. Chen, J. He, Understanding the Percolation Characteristics of Nonlinear Composite Dielectrics, Sci. Rep. 6 (2016) 1–11. https://doi.org/10.1038/srep30597.

[167] J.S. Dodds, F.N. Meyers, K.J. Loh, Piezoelectric characterization of PVDF-TrFE thin films enhanced with ZnO nanoparticles, IEEE Sens. J. 12 (2012) 1889–1890. https://doi.org/10.1109/JSEN.2011.2182043.

[168] A. Morel, G. Pillonnet, Y. Wanderoild, A. Badel, Dielectric losses considerations for piezoelectric energy harvesting, J. Low Power Electron. 14 (2018) 244–254. https://doi.org/10.1166/jolpe.2018.1562.

[169] G. Liu, S. Zhang, W. Jiang, W. Cao, Losses in ferroelectric materials, Mater. Sci. Eng. R Reports. 89 (2015) 1–48. https://doi.org/10.1016/J.MSER.2015.01.002.

[170] F. Pedroli, A. Marrani, M.-Q. Le, C. Froidefond, P.-J. Cottinet, J.-F. Capsal, Processing optimization: A way to improve the ionic conductivity and dielectric loss of electroactive polymers, J. Polym. Sci. Part B Polym. Phys. 56 (2018) 1164–1173. https://doi.org/10.1002/polb.24636.

[171] J. Maiz, P. Loxq, P. Fau, K. Fajerwerg, M.L. Kahn, G. Fleury, G. Hadziioannou, G. Guégan, J. Majimel, M. Maglione, al Ferreoelectricity, Ferreoelectricity in undoped ZnO nanorods, ZnO Nanorods. J. Phys. Chem. C. 123 (2019). https://doi.org/10.1021/acs.jpcc.9b08247ï.

[172] H. Moriwake, A. Konishi, T. Ogawa, K. Fujimura, C.A.J. Fisher, A. Kuwabara, T. Shimizu, S. Yasui, M. Itoh, Ferroelectricity in wurtzite structure simple chalcogenide, Appl. Phys. Lett. 104 (2014) 242909. https://doi.org/10.1063/1.4884596.

[173] M. Laurenti, G. Canavese, A. Sacco, M. Fontana, K. Bejtka, M. Castellino, C.F. Pirri, V. Cauda, Nanobranched ZnO Structure: p-Type Doping Induces Piezoelectric Voltage Generation and Ferroelectric–Photovoltaic Effect, Adv. Mater. 27 (2015) 4218–4223. https://doi.org/10.1002/ADMA.201501594.

[174] L.Z. Hasse, S. Babicz, L. Kaczmarek, J.M. Smulko, V. Sedlakova, Low-frequency noise in ZnO varistor structures Microelectronics Reliability Quality assessment of ZnO-based varistors by 1 / f noise, Microelectron. Reliab. (2011) 1–9. https://doi.org/10.1016/j.microrel.2013.09.007.

[175] R. Hinchet, J. Ferreira, J. Keraudy, G. Ardila, E. Pauliac-Vaujour, M. Mouis, L. Montes, Scaling rules of piezoelectric nanowires in view of sensor and energy harvester integration, Tech. Dig. - Int. Electron Devices Meet. IEDM. (2012) 119–122. https://doi.org/10.1109/IEDM.2012.6478988.

[176] C. Miehe, S. Göktepe, J. Méndez Diez, Finite viscoplasticity of amorphous glassy polymers in the logarithmic strain space, Int. J. Solids Struct. 46 (2009) 181–202. https://doi.org/10.1016/j.ijsolstr.2008.08.029.

[177] I.D. Johnston, D.K. McCluskey, C.K.L. Tan, M.C. Tracey, Mechanical characterization of bulk Sylgard 184 for microfluidics and microengineering, J. Micromechanics Microengineering. 24 (2014). https://doi.org/10.1088/0960-1317/24/3/035017.

[178] C. Outline, Fundamentals of Polymer Matrix Composites Containing CNTs, 2015. https://doi.org/10.1016/B978-1-4557-3195-4.00005-9.

[179] Z. Fan, P. Tsakiropoulos, A.P. Miodownik, Prediction of Young's modulus of particulate two phase composites, Mater. Sci. Technol. (United Kingdom). 8 (1992) 922–929. https://doi.org/10.1179/mst.1992.8.10.922.

[180] P.H. Ashton, J. E., Halpin, J. C., & Petit, Primer on Composite Materials: Analysis Technomic, Stamford Conn. (1969).

[181] J.C. Halpin, Stiffness and Expansion Estimates for Oriented Short Fiber Composites, (n.d.).

Cette thèse est accessible à l'adresse : http://theses.insa-lyon.fr/publication/2022LYSEI006/these.pdf
© [X. Zhang], [2022], INSA Lyon, tous droits réservés

[182] C.L. Tucker, E. Liang, Stiffness predictions for unidirectional short-fiber composites: Review and evaluation, Compos. Sci. Technol. 59 (1999) 655–671. https://doi.org/10.1016/S0266-3538(98)00120-1.

[183] L.E. Nielsen, Generalized Equation for the Elastic Moduli of Composite Materials, J. Appl. Phys. 41 (2003) 4626. https://doi.org/10.1063/1.1658506.

[184] J.M. Keith, J.A. King, I. Miskioglu, S.C. Roache, Tensile modulus modeling of carbon-filled liquid crystal polymer composites, Polym. Compos. 30 (2009) 1166–1174. https://doi.org/10.1002/PC.20673.

[185] H. Tavman, Thermal and Mechanical Properties of Aluminum Powder-Filled High-Density Polyethylene Composites, (n.d.).

[186] M.Y. Soomro, I. Hussain, N. Bano, E. Broitman, O. Nur, M. Willander, Nanoscale elastic modulus of single horizontal ZnO nanorod using nanoindentation experiment, Nanoscale Res. Lett. 7 (2012) 146. https://doi.org/10.1186/1556-276X-7-146.

[187] J.E. Bradby, S.O. Kucheyev, J.S. Williams, C. Jagadish, M. V. Swain, P. Munroe, M.R. Phillips, Contact-induced defect propagation in ZnO, Appl. Phys. Lett. 80 (2002) 4537. https://doi.org/10.1063/1.1486264.

[188] T.H. Fang, W.J. Chang, C.M. Lin, Nanoindentation characterization of ZnO thin films, Mater. Sci. Eng. A. 452–453 (2007) 715–720. https://doi.org/10.1016/J.MSEA.2006.11.008.

[189] N. Yamamoto, H. Makino, T. Yamamoto, Young's modulus and coefficient of linear thermal expansion of ZnO conductive and transparent ultra-thin films, Adv. Mater. Sci. Eng. 2011 (2011). https://doi.org/10.1155/2011/136127.

[190] F. Gaudi, Soft Matter with biomimetic Layer-by-Layer nanofilms, (2012). https://doi.org/10.1039/C2SM25614B.

[191] M. Akram, A. Javed, T.Z. Rizvi, Dielectric properties of industrial polymer composite materials, Turkish J. Phys. 29 (2005) 355–362. https://doi.org/10.22401/jnus.13.1.10.

[192] W.A. Hussain, A.A. Hussein, J.M. Khalaf, A.H. Al-Mowali, A.A. Sultan, Dielectric Properties and a.c. Conductivity of Epoxy/Alumina Silicate NGK Composites, Adv. Chem. Eng. Sci. 05 (2015) 282–289. https://doi.org/10.4236/aces.2015.53028.

[193] J.C.M. Garnett, Colours in Metal Glasses and in Metallic Films, Philos. Trans. R. Soc. A Math. Phys. Eng. Sci. 203 (1904) 385–420. https://doi.org/10.1098/rsta.1904.0024.

[194] K. Mazur, Polymer-ferroelectric ceramic composites, Plast. Eng. YORK. 28 (1995) 539.

[195] N. Jayasundere, B. V. Smith, Dielectric constant for binary piezoelectric 0-3 composites, J. Appl. Phys. 73 (1993) 2462–2466. https://doi.org/10.1063/1.354057.

[196] S. Liu, S. Xiu, B. Shen, J. Zhai, L.B. Kong, Dielectric properties and energy storage densities of poly(vinylidenefluoride) nanocomposite with surface hydroxylated cube shaped Ba0.6Sr0.4TiO3 nanoparticles, Polymers (Basel). 8 (2016) 10–14. https://doi.org/10.3390/polym8020045.

[197] T.S. Velayutham, W.H. Abd Majid, W.C. Gan, A. Khorsand Zak, S.N. Gan, Theoretical and experimental approach on dielectric properties of ZnO nanoparticles and polyurethane/ZnO nanocomposites, J. Appl. Phys. 112 (2012). https://doi.org/10.1063/1.4749414.

[198] Y. Thakur, T. Zhang, C. Iacob, T. Yang, J. Bernholc, L.Q. Chen, J. Runt, Q.M. Zhang, Enhancement of the dielectric response in polymer nanocomposites with low dielectric constant fillers, Nanoscale. 9 (2017) 10992–10997. https://doi.org/10.1039/c7nr01932g.

[199] C.-W. Nan, A. Tschöpe, S. Holten, H. Kliem, R. Birringer, Grain size-dependent electrical properties

Cette thèse est accessible à l'adresse : http://theses.insa-lyon.fr/publication/2022LYSEI006/these.pdf
© [X. Zhang], [2022], INSA Lyon, tous droits réservés

of nanocrystalline ZnO, J. Appl. Phys. 85 (1999) 7735. https://doi.org/10.1063/1.370578.

[200] H.K. Park, K.Y. Lee, J.S. Seo, J.A. Jeong, H.K. Kim, D. Choi, S.W. Kim, Charge-generating mode control in high-performance transparent flexible piezoelectric nanogenerators, Adv. Funct. Mater. 21 (2011) 1187–1193. https://doi.org/10.1002/adfm.201002099.

[201] S.C. Tjong, G.D. Liang, Electrical properties of low-density polyethylene/ZnO nanocomposites, Mater. Chem. Phys. 100 (2006) 1–5. https://doi.org/10.1016/j.matchemphys.2005.11.029.

[202] J.I. Hong, P. Winberg, L.S. Schadler, R.W. Siegel, Dielectric properties of zinc oxide/low density polyethylene nanocomposites, Mater. Lett. 59 (2005) 473–476. https://doi.org/10.1016/j.matlet.2004.10.036.

[203] L. Ramajo, M. Reboredo, M. Castro, Dielectric response and relaxation phenomena in composites of epoxy resin with BaTiO3 particles, Compos. Part A Appl. Sci. Manuf. 36 (2005) 1267–1274. https://doi.org/10.1016/j.compositesa.2005.01.026.

[204] N. Hadik, A. Outzourhit, A. Elmansouri, A. Abouelaoualim, A. Oueriagli, E.L. Ameziane, Dielectric behavior of ceramic (BST)/epoxy thick films, Act. Passiv. Electron. Components. 2009 (2009) 1–7. https://doi.org/10.1155/2009/437130.

[205] M.K. Gupta, N. Sinha, B.K. Singh, N. Singh, K. Kumar, B. Kumar, Piezoelectric , dielectric , optical and electrical characterization of solution grown fl ower-like ZnO nanocrystal, Mater. Lett. 63 (2009) 1910–1913. https://doi.org/10.1016/j.matlet.2009.06.003.

[206] S. Bhattacharrya, S.K. Saha, D. Chakravorty, Nanowire formation in a polymeric film, Appl. Phys. Lett. 76 (2000) 3896–3898. https://doi.org/10.1063/1.126813.

[207] J. Belovickis, J. Macutkevic, Š. Svirskas, V. Samulionis, J. Banys, Ferroelectrics Dielectric Spectroscopy of Polymer Based PDMS Nanocomposites with ZnO Nanoparticles, (2015) 37–41. https://doi.org/10.1080/00150193.2015.1012016.

[208] C. Zhang, D. Wang, J. He, M. Liu, G.H. Hu, Z.M. Dang, Synthesis, nanostructures and dielectric properties of novel liquid crystalline block copolymers, Polym. Chem. 5 (2014) 2513–2520. https://doi.org/10.1039/c3py01522j.

[209] G.L. Wang, Y.Y. Zhang, J. Zhang, K.H. Ding, Z.F. Wang, M. Zhang, Preparation and electrodeformation of silicone dielectric elastomers containing poly(propylene glycol diacetate) with different molecular weights, J. Appl. Polym. Sci. 134 (2017) 45329. https://doi.org/10.1002/app.45329.

[210] X. Huang, H. Zhang, Y. Lai, J. Li, The lowered dielectric loss tangent and grain boundary effects in fluorine-doped calcium copper titanate ceramics, Appl. Phys. A 2017 1235. 123 (2017) 1–7. https://doi.org/10.1007/S00339-017-0947-9.

[211] B.E. Schubert, Electronic Supplementary Information (ESI): Variable stiffness mate- rial based on rigid low-melting-point-alloy-microstructures embedded in soft poly (dimethylsiloxane) (PDMS), (2013) 3–5.

[212] R. Strümpler, J. Glatz-Reichenbach, Conducting polymer composites, J. Electroceramics. 3 (1999) 329–346. https://doi.org/10.1023/A:1009909812823.

[213] Y.P. Varshni, Temperature dependence of the energy gap in semiconductors, Physica. 34 (1967) 149–154. https://doi.org/10.1016/0031-8914(67)90062-6.

[214] F.H. Abd El-kader, S.A. Gaafer, K.H. Mahmoud, S.I. Mohamed, M.F.H. Abd El-kader, Electrical conduction in (polyvinyl alcohol/glycogen) blend films, Polym. Compos. 30 (2009) 214–220. https://doi.org/10.1002/pc.20553.

Cette thèse est accessible à l'adresse : http://theses.insa-lyon.fr/publication/2022LYSEI006/these.pdf
© [X. Zhang], [2022], INSA Lyon, tous droits réservés

[215] A. Chaipanich, Dielectric and piezoelectric properties of PZT-cement composites, Curr. Appl. Phys. 7 (2007) 537–539. https://doi.org/10.1016/j.cap.2006.10.015.

[216] R. Li, Z. Zhao, Z. Chen, J. Pei, Novel BaTiO3/PVDF composites with enhanced electrical properties modified by calcined BaTiO3 ceramic powders, Mater. Express. 7 (2017) 536–540. https://doi.org/10.1166/mex.2017.1393.

[217] J. Song, J. Zhou, Z.L. Wang, Piezoelectric and semiconducting coupled power generating process of a single ZnO belt/wire. A technology for harvesting electricity from the environment, Nano Lett. 6 (2006) 1656–1662. https://doi.org/10.1021/nl060820v.

[218] L. Wang, X. Tian, S. Yang, Z. Xu, W. Wang, X. Bai, Dynamic nanomechanics of zinc oxide nanowires, Appl. Phys. Lett. 100 (2012) 163110. https://doi.org/10.1063/1.4704919.

[219] Z.C. Tu, X. Hu, Elasticity and piezoelectricity of zinc oxide crystals, single layers, and possible single-walled nanotubes, Phys. Rev. B. 74 (2006) 035434. https://doi.org/10.1103/PhysRevB.74.035434.

[220] P.J. Michalski, N. Sai, E.J. Mele, Continuum Theory for Nanotube Piezoelectricity, Phys. Rev. Lett. 95 (2005) 116803. https://doi.org/10.1103/PhysRevLett.95.116803.

[221] Y. Gao, Z.L. Wang, Electrostatic potential in a bent piezoelectric nanowire. The fundamental theory of nanogenerator and nanopiezotronics, Nano Lett. 7 (2007) 2499–2505. https://doi.org/10.1021/nl071310j.

[222] J.. SYNGE, Principles Of Mechanics, 1948.

[223] J.M. TIMOSHENKO, Stephen P., GERE, Theory of elastic stability, Courier Corporation, 2009.

[224] N.N. Bologyubov, V.N. Plechko, Perturbation theory in the polaron model at finite temperature, Theor. Math. Phys. 65 (1985) 1255–1263. https://doi.org/10.1007/BF01036135.

[225] R.W. Soutas-Little, Elasticity, Courier Corporation, 2012.

[226] G. Romano, G. Mantini, A. Di Carlo, A. D'Amico, C. Falconi, Z.L. Wang, Piezoelectric potential in vertically aligned nanowires for high output nanogenerators, Nanotechnology. 22 (2011). https://doi.org/10.1088/0957-4484/22/46/465401.

[227] S. Hoffmann, F. Östlund, J. Michler, H.J. Fan, M. Zacharias, S.H. Christiansen, C. Ballif, Fracture strength and Young's modulus of ZnO nanowires, Nanotechnology. 18 (2007). https://doi.org/10.1088/0957-4484/18/20/205503.

[228] R. Hinchet, Electromechanical study of semiconductor piezoelectric nanowires, University of Grenoble, 2014.

[229] H.S. Kim, On the rule of mixtures for the hardness of particle reinforced composites, Mater. Sci. Eng. A. 289 (2000) 30–33. https://doi.org/10.1016/S0921-5093(00)00909-6.

[230] O. Graton, G. Poulin-Vittrant, L.P. Tran Huu Hue, M. Lethiecq, Strategy of modelling and simulation of electromechanical conversion in ZnO nanowires, Adv. Appl. Ceram. 112 (2013) 85–90. https://doi.org/10.1179/1743676112Y.0000000029.

[231] M.A. Schubert, S. Senz, M. Alexe, D. Hesse, U. Gösele, Finite element method calculations of ZnO nanowires for nanogenerators, Appl. Phys. Lett. 92 (2008) 5–7. https://doi.org/10.1063/1.2903114.

[232] O. Graton, G. Poulin-Vittrant, A.S. Dahiya, N. Camara, L.P. Tran Huu Hue, M. Lethiecq, Evaluation of the performance of a piezoelectric nanowire-based composite microgenerator, 2013 Jt. IEEE Int. Symp. Appl. Ferroelectr. Work. Piezoresponse Force Microsc. ISAF/PFM 2013. (2013) 298–301. https://doi.org/10.1109/ISAF.2013.6748701.

Cette thèse est accessible à l'adresse : http://theses.insa-lyon.fr/publication/2022LYSEI006/these.pdf
© [X. Zhang], [2022], INSA Lyon, tous droits réservés

[233] W.A. Smith, B.A. Auld, Modeling 1–3 Composite Piezoelectrics: Thickness-Mode Oscillations, IEEE Trans. Ultrason. Ferroelectr. Freq. Control. 38 (1991) 40–47. https://doi.org/10.1109/58.67833.

[234] N. Doumit, G. Poulin-Vittrant, A New Simulation Approach for Performance Prediction of Vertically Integrated Nanogenerators, Adv. Theory Simulations. 1 (2018) 1–8. https://doi.org/10.1002/adts.201800033.

[235] R. Hinchet, S. Lee, G. Ardila, L. Montès, M. Mouis, Z.L. Wang, Performance optimization of vertical nanowire-based piezoelectric nanogenerators, Adv. Funct. Mater. 24 (2014) 971–977. https://doi.org/10.1002/adfm.201302157.

[236] R. Tao, R. Hinchet, G. Ardila, M. Mouis, Evaluation of vertical integrated nanogenerator performances in flexion, J. Phys. Conf. Ser. 476 (2013). https://doi.org/10.1088/1742-6596/476/1/012006.

[237] R. Hinchet, S. Lee, G. Ardila, L. Montes, M. Mouis, Z.L. Wang, Design and guideline rules for the performance improvement of vertically integrated nanogenerator, Proc. PowerMEMS. 7 (2013) 4.

[238] R. Tao, G. Ardila, M. Parmar, L. Michaud, M. Mouis, Flexible piezoelectric transducers based on a PMMA/ZnO nanowire composite, Jt. Int. EUROSOl Work. Int. Conf. Ultim. Integr. Silicon-ULIS, EUROSOI-ULIS 2017 - Proc. (2017) 188–191. https://doi.org/10.1109/ULIS.2017.7962558.

[239] M. FARADAY, Experimental Researches In Electricity-Volume 1, 2005.

[240] Z. Wang, J.K. Nelson, J. Miao, R.J. Linhardt, L.S. Schadler, H. Hillborg, S. Zhao, Effect of high aspect ratio filler on dielectric properties of polymer composites: A study on barium titanate fibers and graphene platelets, IEEE Trans. Dielectr. Electr. Insul. 19 (2012) 960–967. https://doi.org/10.1109/TDEI.2012.6215100.

[241] D.A. Van Den Ende, S.E. Van Kempen, X. Wu, W.A. Groen, C.A. Randall, S. Van Der Zwaag, Dielectrophoretically structured piezoelectric composites with high aspect ratio piezoelectric particles inclusions, J. Appl. Phys. 111 (2012). https://doi.org/10.1063/1.4729814.

[242] I. Babu, Piezoelectric composites: design, fabrication and performance analysis, 2013. https://doi.org/10.6100/IR760468.

[243] W.M. Chirdon, W.J. O'Brien, R.E. Robertson, Diffuse reflectance of short-fiber-reinforced composites aligned by an electric field, Dent. Mater. 22 (2006) 57–62. https://doi.org/10.1016/J.DENTAL.2005.03.004.

[244] S. Guillemin, E. Appert, H. Roussel, B. Doisneau, R. Parize, T. Boudou, G. Bremond, V. Consonni, Controlling the Structural Properties of Single Step, Dip Coated ZnO Seed Layers for Growing Perfectly Aligned Nanowire Arrays, J. Phys. Chem. C. 119 (2015) 21694–21703. https://doi.org/10.1021/acs.jpcc.5b06180.

[245] C. Lausecker, B. Salem, X. Baillin, V. Consonni, Modeling the Elongation of Nanowires Grown by Chemical Bath Deposition Using a Predictive Approach, J. Phys. Chem. C. 123 (2019) 29476–29483. https://doi.org/10.1021/acs.jpcc.9b08958.

[246] R. Parize, J. Garnier, O. Chaix-Pluchery, C. Verrier, E. Appert, V. Consonni, Effects of Hexamethylenetetramine on the Nucleation and Radial Growth of ZnO Nanowires by Chemical Bath Deposition, J. Phys. Chem. C. 120 (2016) 5242–5250. https://doi.org/10.1021/acs.jpcc.6b00479.

[247] L. Zhao, A. Maynadier, D. Nelias, Stiffness and fracture analysis of photovoltaic grade silicon plates, Int. J. Solids Struct. 97–98 (2016) 355–369. https://doi.org/10.1016/J.IJSOLSTR.2016.07.013.

[248] J.C. Suhling, R.C. Jaeger, Silicon Piezoresistive Stress Sensors and Their Application in Electronic Packaging, 1 (2001) 14–30.

Cette thèse est accessible à l'adresse : http://theses.insa-lyon.fr/publication/2022LYSEI006/these.pdf
© [X. Zhang], [2022], INSA Lyon, tous droits réservés

[249] P. Alpuim, V. Correia, E.S. Marins, J.G. Rocha, I.G. Trindade, S. Lanceros-Mendez, Piezoresistive silicon thin film sensor array for biomedical applications, Thin Solid Films. 519 (2011) 4574–4577. https://doi.org/10.1016/J.TSF.2011.01.300.

[250] V. Mosser, J. Suski, J. Goss, E. Obermeier, Piezoresistive pressure sensors based on polycrystalline silicon, Sensors Actuators A Phys. 28 (1991) 113–132. https://doi.org/10.1016/0924-4247(91)85020-O.

[251] A. Boger, A. Bisig, M. Bohner, P. Heini, E. Schneider, Variation of the mechanical properties of PMMA to suit osteoporotic cancellous bone, Http://Dx.Doi.Org/10.1163/156856208785540154. 19 (2012) 1125–1142. https://doi.org/10.1163/156856208785540154.

[252] S. Xu, Y. Yeh, G. Poirier, M.C. Mcalpine, R.A. Register, N. Yao, Flexible Piezoelectric PMN − PT Nanowire-Based Nanocomposite and Device, (2013) 1–6.

[253] A.M. Lord, T.G. Maffeis, A.S. Walton, D.M. Kepaptsoglou, Q.M. Ramasse, M.B. Ward, J. Köble, S.P. Wilks, Factors that determine and limit the resistivity of high-quality individual ZnO nanowires, Nanotechnology. 24 (2013) 435706. https://doi.org/10.1088/0957-4484/24/43/435706.

[254] A. De Luna Bugallo, F. Donatini, C. Sartel, V. Sallet, J. Pernot, Metallic core conduction in unintentionally doped ZnO nanowire, Appl. Phys. Express. 8 (2015) 025001. https://doi.org/10.7567/APEX.8.025001.

[255] J.L. Lyons, J.B. Varley, D. Steiauf, A. Janotti, C.G. Van de Walle, First-principles characterization of native-defect-related optical transitions in ZnO, J. Appl. Phys. 122 (2017) 035704. https://doi.org/10.1063/1.4992128.

[256] C.G. Van de Walle, Hydrogen as a Cause of Doping in Zinc Oxide, Phys. Rev. Lett. 85 (2000) 1012. https://doi.org/10.1103/PhysRevLett.85.1012.

[257] T. Cossuet, H. Roussel, J.-M. Chauveau, O. Chaix-Pluchery, J.-L. Thomassin, E. Appert, V. Consonni, Well-ordered ZnO nanowires with controllable inclination on semipolar ZnO surfaces by chemical bath deposition, Nanotechnology. 29 (2018) 475601. https://doi.org/10.1088/1361-6528/aadf62.

[258] J. Villafuerte, F. Donatini, J. Kioseoglou, E. Sarigiannidou, O. Chaix-pluchery, J. Pernot, V. Consonni, J. Villafuerte, F. Donatini, J. Kioseoglou, E. Sarigiannidou, O. Chaix-pluchery, Zinc Vacancy-Hydrogen Complexes as Major Defects in ZnO Nanowires Grown by Chemical Bath Deposition To cite this version : HAL Id : hal-03025863 Zinc Vacancy - Hydrogen Complexes as Major Defects in ZnO Nanowires Grown by Chemical Bath Deposition, 2020.

[259] S.M. Sze and Kwok K. Ng, Physics of Semiconductor Devices (3rd edition), Wiley, 2007.

[260] N. Ashkenov, B.N. Mbenkum, C. Bundesmann, V. Riede, M. Lorenz, D. Spemann, E.M. Kaidashev, A. Kasic, M. Schubert, M. Grundmann, G. Wagner, H. Neumann, V. Darakchieva, H. Arwin, B. Monemar, Infrared dielectric functions and phonon modes of high-quality ZnO films, J. Appl. Phys. 93 (2002) 126. https://doi.org/10.1063/1.1526935.

[261] K. C, ZnO: material, physics and applications, Chemphyschem. 8 (2007) 782–803. https://doi.org/10.1002/CPHC.200700002.

[262] Y. Gao, Z.L. Wang, Equilibrium potential of free charge carriers in a bent piezoelectric semiconductive nanowire, Nano Lett. 9 (2009) 1103–1110. https://doi.org/10.1021/nl803547f.

[263] W. Shan, W. Walukiewicz, J.W.A. III, K.M. Yu, Y. Zhang, S.S. Mao, R. Kling, C. Kirchner, A. Waag, Pressure-dependent photoluminescence study of ZnO nanowires, Appl. Phys. Lett. 86 (2005) 153117. https://doi.org/10.1063/1.1901827.

[264] O. Graton, G. Poulin-Vittranta, L.-P.T.H. Huea, M. Lethiecqb, Modelling tools for the simulation of

Cette thèse est accessible à l'adresse : http://theses.insa-lyon.fr/publication/2022LYSEI006/these.pdf
© [X. Zhang], [2022], INSA Lyon, tous droits réservés

microgenerators based on piezo-semiconducting nanowires, Acoust. 2012 …. (2012) 129–134. http://hal.archives-ouvertes.fr/hal-00811263/.

[265] S. Lu, Q. Liao, J. Qi, S. Liu, Y. Liu, Q. Liang, G. Zhang, Y. Zhang, The enhanced performance of piezoelectric nanogenerator via suppressing screening effect with Au particles/ZnO nanoarrays Schottky junction, Nano Res. 9 (2016) 372–379. https://doi.org/10.1007/s12274-015-0916-6.

[266] K.Y. Lee, J. Bae, S.M. Kim, J.H. Lee, G.C. Yoon, M.K. Gupta, S. Kim, H. Kim, J. Park, S.W. Kim, Depletion width engineering via surface modification for high performance semiconducting piezoelectric nanogenerators, Nano Energy. 8 (2014) 165–173. https://doi.org/10.1016/j.nanoen.2014.06.008.

[267] J. Villafuerte, O. Chaix-pluchery, J. Kioseoglou, F. Donatini, J. Pernot, V. Consonni, Engineering nitrogen- and hydrogen-related defects in ZnO nanowires using thermal annealing, (n.d.) 1–36.

[268] C. Cao, X. Xie, Y. Zeng, S. Shi, G. Wang, L. Yang, C.Z. Wang, S. Lin, Highly efficient and stable p-type ZnO nanowires with piezotronic effect for photoelectrochemical water splitting, Nano Energy. 61 (2019) 550–558. https://doi.org/10.1016/J.NANOEN.2019.04.098.

[269] K.C. Pradel, W. Wu, Y. Zhou, X. Wen, Y. Ding, Z.L. Wang, Piezotronic E ff ect in Solution-Grown p - Type ZnO Nanowires and Films, (2013).

Cette thèse est accessible à l'adresse : http://theses.insa-lyon.fr/publication/2022LYSEI006/these.pdf
© [X. Zhang], [2022], INSA Lyon, tous droits réservés

List of Figures

Cette thèse est accessible à l'adresse : http://theses.insa-lyon.fr/publication/2022LYSEI006/these.pdf
© [X. Zhang], [2022], INSA Lyon, tous droits réservés

Cette thèse est accessible à l'adresse : http://theses.insa-lyon.fr/publication/2022LYSEI006/these.pdf
© [X. Zhang], [2022], INSA Lyon, tous droits réservés

Cette thèse est accessible à l'adresse : http://theses.insa-lyon.fr/publication/2022LYSEI006/these.pdf
© [X. Zhang], [2022], INSA Lyon, tous droits réservés

Cette thèse est accessible à l'adresse : http://theses.insa-lyon.fr/publication/2022LYSEI006/these.pdf
© [X. Zhang], [2022], INSA Lyon, tous droits réservés

Cette thèse est accessible à l'adresse : http://theses.insa-lyon.fr/publication/2022LYSEI006/these.pdf
© [X. Zhang], [2022], INSA Lyon, tous droits réservés

Cette thèse est accessible à l'adresse : http://theses.insa-lyon.fr/publication/2022LYSEI006/these.pdf
© [X. Zhang], [2022], INSA Lyon, tous droits réservés

Cette thèse est accessible à l'adresse : http://theses.insa-lyon.fr/publication/2022LYSEI006/these.pdf
© [X. Zhang], [2022], INSA Lyon, tous droits réservés

List of tables

Cette thèse est accessible à l'adresse : http://theses.insa-lyon.fr/publication/2022LYSEI006/these.pdf
© [X. Zhang], [2022], INSA Lyon, tous droits réservés

List of publications

Peer-reviewed publications:

1. X. Zhang, M.Q. Le, O. Zahhaf, J.F. Capsal, P.J. Cottinet, L. Petit, “Enhancing dielectric and piezoelectric properties of micro-ZnO/PDMS composite-based dielectrophoresis,” *Mater. Des.*, vol. 192, p. 108783, Jul. 2020.

2. X. Zhang, M.Q. Le, V.C. Nguyen, J.F. Mogniotte, J.F. Capsal, D. Grinberg, P.J. Cottinet, L. Petit, “Characterization of micro-ZnO/PDMS composite structured via dielectrophoresis – Toward medical application,” *Mater. Des.*, vol. 208, p. 109912, Oct. 2021.

3. X. Zhang, J. Villafuerte, V. Consonni, J.F. Capsal, P.J. Cottinet, L. Petit, M.Q. Le, “Characterizing and Optimizing Piezoelectric Response of ZnO Nanowire/PMMA Composite-Based Sensor,” *Nanomater. 2021, Vol. 11, Page 1712*, vol. 11, no. 7, p. 1712, Jun. 2021.

4. “Boosting piezoelectric properties of flexible ZnO nanowire/PMMA composite using annealing and doping techniques, ” in preparation.

Conference publications:

5. X. Zhang, M.Q. Le, J. Mogniotte, J.F. Capsal, P.J. Cottinet, and L. Petit, “Effect of dielectrophoretic structuring on dielectric and piezoelectric behaviors of ZnO/PDMS microcomposite,” 2021, vol. 11587, p. 41.

Conferences participation:

- ENHANCE event - Workshop “From Molecular Engineering to Advanced Materials”. May 2019. Cologne, Germany
- IWPMA 2019: International Workshop on Piezoelectric Materials and Applications in Actuators, Lyon, October 2019
- 21st World Congress on Materials Science and Engineering, Online, June 2020
- SPIE Smart Structures + Nondestructive Evaluation, Online, March 20

Cette thèse est accessible à l'adresse : http://theses.insa-lyon.fr/publication/2022LYSEI006/these.pdf
© [X. Zhang], [2022], INSA Lyon, tous droits réservés

FOLIO ADMINISTRATIF

THESE DE L'UNIVERSITE DE LYON OPEREE AU SEIN DE L'INSA LYON

NOM : ZHANG DATE de SOUTENANCE : 01 /Février/ 2022

Prénom : Xiaoting

TITRE: Characterization and structuration of piezoelectric ZnO-based composites: Toward medical applications

NATURE : Doctorat Numéro d'ordre : 2022LYSEI006

Ecole doctorale : E.E.A.

Spécialité : Electronique - Génie électrique

RESUME : Grâce à ses multiples fonctionnalités, l'oxyde de Zinc (ZnO) est déjà utilisé dans de nombreuses applications du domaine de l'optoélectronique, des capteurs physico-chimiques, des composants électroniques ou encore des micro-dispositifs électromécaniques. Son excellente biocompatibilité et sa biosécurité permettent en particulier d'envisager des procédés technologiques innovants exploitant ses propriétés piézoélectriques en milieu biologique. Un matériau composite utilisant des charges ZnO incorporées dans une matrice polymère offre ainsi de nombreux avantages potentiels tels qu'une flexibilité élevée, un faible coût, une réelle recyclabilité et une intégration aisée, de plus adaptée à la fabrication additive sous toutes formes et dimensions. Ces composites se présente donc comme une intéressante alternative dans le domaine des capteurs flexibles compacts pour détecter les variations de pression ou de déformation élastique de tissus ou liquides biologiques.

L'objectif de ces travaux est de mener une caractérisation complète à l'échelle macroscopique de composites piézoélectriques intégrant des structures micro/nano ZnO afin d'aboutir à une meilleure compréhension du couplage électromécanique ainsi que des propriétés diélectriques, électriques et mécaniques intrinsèques de la matrice et de la charge, qu'elles soient individuelles ou combinées. Un autre point se concentre sur le développement de stratégies optimisées basées sur la caractérisation expérimentale et la méthode des éléments finis (FEM), dans le but d'augmenter les performances piézoélectriques des micro/nano composites ZnO.

Dans ce but, la présente étude s'est d'abord orientée vers la mise au point d'un process de fabrication de composite, à faible cout, à l'élaboration simple et parfaitement maitrisée, basé sur l'utilisation des particules de ZnO encapsulées dans une matrice de polydiméthylsiloxane (PDMS). Les résultats expérimentaux ont montré qu'une concentration de particule élevée entraîne une augmentation de la permittivité diélectrique, de la conductivité, du module élastique de compression et de la constante piézoélectrique. Plus important encore, une amélioration significative de ces caractéristiques a été obtenue avec succès grâce à l'alignement diélectrophorétique de microparticules de ZnO à concentration plus faible. Une étude de l'influence de la forme et de la taille des charges sur les propriétés des composites a également été menée en utilisant des particules sphériques, des microtubes ou des nanofils. Les composites utilisant un réseau vertical ordonné de nanofils ZnO obtenu par dépôt en bain chimique présente au final le couplage piézoelectrique le plus élevé. Des simulations par la méthode des éléments finis ont été utilisées dans ce sens pour optimiser l'activité piézoélectrique d'un composite à nanofils ZnO en fonction du module d'élasticité et de la constante diélectrique des éléments constitutifs ainsi que de la densité et des dimensions des nanofils. Il a également été établi que l'apparition de défauts cristallins lors de la croissance des nanofils de ZnO génère des porteurs de charges électriques qui ont un effet masquant sur l'effet piézoelectrique. Cette dégradation peut être atténuée par un dopage à l'Antimoine (Sb) ou par un recuit thermique qui permet de diminuer la concentration de ces porteurs parasites. Au final, des composites flexibles piézoélectriques à nanofils ZnO ont été developpé en utilisant un substrat de type polymère PDMS au lieu d'un substrat rigide silicium. L'ensemble des résultats expérimentaux obtenus confirme l'excellent potentiel des matériaux développés pour toute application de biodétection in vivo nécessitant impérativement des dispositifs médicaux flexibles et extensibles.

Directeur de thèse: PETIT Lionel

Co-directrice de thèse : LE Minh Quyen

Président de jury : Georges BREMOND

Composition du jury : DEMOLY Frédéric (rapporteur de thèse), GUIFFARD Benoit (rapporteur de thèse), BREMOND Georges (examinateur), LIANG Zhiyong (examinateur), CONSONNI Vincent (Invité), DELLA SCHIAVA Nellie (Invitée), PETIT Lionel (directeur de thèse), LE Minh Quyen (co-directrice de thèse).

Cette thèse est accessible à l'adresse : http://theses.insa-lyon.fr/publication/2022LYSEI006/these.pdf
© [X. Zhang], [2022], INSA Lyon, tous droits réservés